CHARACTERIZATION OF DEFECT STRUCTURE OF EPITAXIAL CDTE FILMS

**A Thesis Submitted to
the Graduate School of Engineering and Sciences of
Izmir Institute of Technology
in Partial Fulfillment of Requirement for Degree of**

MASTER OF SCIENCE

in Physics

**by
Selin ÖZDEN**

**July 2014
İZMİR**

We approve the thesis of **Selin ÖZDEN**

Examining Committee Members:

Assoc. Prof. Dr. Yusuf SELAMET
Department of Physics, İzmir Institute of Technology

Assist. Prof. Dr. Cem ÇELEBİ
Department of Physics, İzmir Institute of Technology

Prof. Dr. Salih OKUR
Department of Material Science and Engineering, İzmir Katip Celebi University

07 July 2014

Assoc. Prof. Dr. Yusuf SELAMET
Supervisor, Department of Physics
İzmir Institute of Technology

Prof. Dr. Nejat BULUT
Head of the Department of Physics

Prof. Dr. R. Tuğrul SENGER
Dean of the Graduate School of
Engineering and Sciences

ACKNOWLEDGEMENTS

I would like to thank all of those people who helped me through this thesis work. I would like to thank my advisor Assoc. Prof. Dr. Yusuf Selamet for his endless support, expertise, help and patience through the whole period of my study. I am very grateful to him for guidance and giving me a chance to working with him. He always trusted me and encouraged me throughout this study. Without his support, kindness and invaluable advises, I would never have been able to complete this study.

I would also like to thank my co-advisor Assist. Prof. Dr. Enver Tarhan for his advises and support. I am thankful to him for his help, comments on my research, teaching me MonoVista Raman system and also for giving me the opportunity to use Raman system. I gratefully thank Prof. Dr. Salih Okur and Assist. Prof. Dr. Cem Çelebi for being on my committee, for suggestions and comments on my study.

I would like to thank all my friends and colleagues for their continuous support and friendly encouragement. Especially; I would like to thank Elif Bilgilisoy for her friendship and help in etching CdTe epitaxial films and also Merve Günnar for Spectroscopic Ellipsometry analysis. In addition, thanks to Mustafa Polat and Ozan Arı for XRD measurements. I would like to thank Hasan Aydın and Nesli Tekgüzel Yağmurcukardeş for teaching me AFM. In addition, I would like to thank Zebih Çetin and Hasan Yasin Ergunt for their great friendship and support.

Thank to IYTE Material Research Center staff for performing SEM and EDX analysis. I also would like to thank SSM and ASELSAN for providing technical and financial support for my thesis.

The last thanks go to my small family; my mother, grandfather and grandmother. They supported me everytime and encouraged me to continue my academic life. Without all of you I could not have achieved any of this.

Throughout my study, lots of people were of roles in one or the other way. I would like to thank all them whose names I might have forgotten to mention here.

ABSTRACT

CHARACTERIZATION OF DEFECT STRUCTURE OF EPITAXIAL CDTE FILMS

Mercury Cadmium Telluride (HgCdTe) is widely used material for infrared detection. Epitaxial growths carried on Gallium arsenide (GaAs) substrates gained more attention in recent years due to commercially availability of epi-ready wafers. However, large lattice mismatch between the HgCdTe epilayer and GaAs substrates, and Gallium (Ga) diffusion into HgCdTe layers during growth limit the device performance. In order to decrease large lattice mismatch and hereby dislocations formed at HgCdTe epilayer, a closely lattice matched Cadmium Telluride (CdTe) is preffered buffer layer for Molecular Beam Epitaxial (MBE) growth of HgCdTe.

This thesis focuses on a study of defects on (211)B CdTe buffer layers grown on (211)B oriented GaAs substrates by MBE. Prior to epitaxial growth of CdTe layers, to understand the effect of wet cleaning procedure on chemical composition of epi-ready GaAs wafers, piranha solution-based wet chemical etching and oxide removal processes using diluted hydrofluoric acid (HF) were performed on undoped 625±25 μm thick GaAs(211)B wafers. The surfaces of GaAs wafers were investigated by Atomic Force Microscopy (AFM) and Scanning Electron Microscopy (SEM). The variation of As_2O_3 and Ga_2O_3 contents on GaAs (211)B wafers studied by Raman spectroscopy. Following the growth of CdTe (211)B epitaxial films, the quality of CdTe layers were investigated in detail by various characterization techniques such as AFM, SEM, Nomarski Microscopy, X-ray Diffraction (XRD), Fourier Transform Infrared Spectroscopy (FTIR) and Raman Spectroscopy. Thicknesses of CdTe layers were calculated via intensity oscillations in the transmittance spectrum of the films.

ÖZET

EPİTAKSİYEL CDTE FİLMLERİNİN KUSUR YAPILARININ KARAKTERİZASYONU

Cıva Kadmiyum Tellür (HgCdTe) kızılötesi algılamada yaygın bir şekilde kullanılan bir malzemedir. Epi-hazır Galyum Arsenik (GaAs) alttaşlarının ticari olarak bulunmasından dolayı son yıllarda GaAs alttaşlarının kullanıldığı epitaksiyel büyütmeler bir hayli dikkat çekicidir. Ancak HgCdTe epi-katmanlarıyla GaAs alttaşlarının arasındaki yüksek örgü uyumsuzluğu ve büyütme sırasında HgCdTe epi-katmanlarına Ga difüzyonu foto algılayıcı performansını önemli ölçüde sınırlar. Yüksek örgü uyumsuzluğunu ve bu örgü uyumsuzluğundan kaynaklı HgCdTe epi-katmanlarında oluşan dislokasyonları azaltmak için örgü uyumu bir hayli yüksek olan Kadmiyum Tellür (CdTe) tampon katmanları HgCdTe'nin moleküler demet (ışın) epitaksisinde (MBE) büyütülmesinde tercih edilir.

Bu tez çalışmasında, MBE'de (211)B yüzey yönelimine sahip GaAs alttaşlar üzerine büyütülmüş (211)B CdTe tampon katmanlarındaki kusurların incelenmesine yer verilmiştir. CdTe katmanlarının epitaksiyel büyütülmesi öncesi kimyasal temizliğin epi-hazır GaAs alttaşların kimyasal kompozisyonuna etkisinin anlaşılması için katkılanmamış, 625±25 µm kalınlığında GaAs(211)B alttaşlarına pirana solüsyonu tabanlı kimyasal aşındırma ve seyreltik hidroflorik asit kullanılarak oksit kaldırma işlemleri gerçekleştirilmiştir. GaAs alttaşlarının yüzeyleri atomik kuvvet mikroskobu (AFM) ve taramalı electron mikroskobu (SEM) ile incelenmiştir. GaAs alttaşlarındaki As_2O_3 ve Ga_2O_3 içeriğinin değişimi Raman spektroskopisiyle gösterilmiştir. CdTe(211)B epitaksiyel filmlerin büyütülmesinden sonra bu filmlerin kalitesi, AFM, SEM, Nomarski mikroskobu, X-ışını kırınımı (XRD), Fourier dönüşümlü kızılötesi spektroskopisi (FTIR) ve Raman spektroskopisi gibi çeşitli karakterizasyon teknikleriyle incelenmiştir. CdTe katmanlarının kalınlıkları filmlerin geçirgenlik spektrumundaki şiddet değerleri dalgalanmalarıyla hesaplanmıştır.

Dedicated to;

My Grandfather

TABLE OF CONTENTS

LIST OF FIGURES X

LIST OF TABLES XXVI

CHAPTER 1. INTRODUCTION 1

CHAPTER 2. CADMIUM TELLURIDE 3

2.1. FUNDAMENTAL PROPERTIES OF CDTE 3

2.1.1. Band Structure 3

2.1.2. Crystal Structure 11

2.1.3. Polar Surfaces of CdTe 13

2.1.4. Optical Properties 15

2.1.4.1. Photoluminescence 18

2.1.4.1.1. Excitonic Transitions in CdTe 21

2.1.4.1.1.1. Free Excitons 21

2.1.4.1.1.2. Bound Excitons 23

2.1.4.1.2. Radiative and Non-Radiative Recombination Mechanisms 26

2.1.4.1.2.1. Band to Band Transition 26

2.1.4.1.2.2. Donor-Acceptor Pair Transition 28

2.1.4.1.2.3. Free to Bound Transition 29

2.1.4.1.2.4. Phonon-Assisted Recombinations (Exciton-Phonon Interaction) 31

2.1.4.1.2.5. Auger Recombination 33

2.1.4.1.2.6. Shockley-Read-Hall Recombination 35

2.1.4.1.2.7. Surface Recombination 36

2.1.4.1.2.8. Total Recombination Lifetime 37

2.2. CDTE GROWTH TECHNIQUES 37

2.2.1. Bulk Crystal Growth Techniques 38

2.2.1.1. Bridgman Method 39

2.2.1.2. Czochralski Method 41

2.2.1.3. Traveling Heater Method (THM) 42
2.2.2. Epitaxial Growth Techniques 44
2.2.2.1. Molecular Beam Epitaxy (MBE) 44
2.2.2.2. Metalorganic Vapour Phase Epitaxy (MOVPE) 49
2.2.2.3. Atomic Layer Epitaxy (ALE) 50
2.2.2.4. Pulsed Laser Deposition (PLD) 51
2.2.2.5. Hot Wall Epitaxy (HWE) 53
2.2.3. Alternative Substrates For Epitaxial Growth of CdTe 53
2.3. DEFECTS IN CDTE 58
2.3.1. Point Defects 58
2.3.2. Line Defects 63
2.3.3. Surface Defects 66
2.3.4. Volumetric Defects 69

CHAPTER 3. EXPERIMENTAL TECHNIQUES AND PROCEDURES 71
3.1. MBE SYSTEM CONFIGURATION 71
3.2. CHARACTERIZATION TECHNIQUES 75
3.2.1. OPTICAL CHARACTERIZATION TECHNIQUES 75
3.2.1.1. Raman Spectroscopy 75
3.2.1.1.1. Raman Scattering in Zincblende Structures of CdTe and GaAs 81
3.2.1.2. Fourier Transform Spectroscopy (FTRs) 90
3.2.1.2.1. Basic Theory of FT Spectroscopy 93
3.2.1.3. Nomarski Interference Microscopy (NIM) 98
3.2.2. STRUCTURAL CHARACTERIZATION TECHNIQUES 102
3.2.2.1. Atomic Force Microscopy (AFM) 102
3.2.2.2. Scanning Electron Microscopy (SEM) And Energy Dispersive X-Ray Spectroscopy (EDX) 106

CHAPTER 4. SURFACE PREPARATION PRIOR TO MOLECULAR BEAM EPITAXIAL GROWTH 111
4.1. EX-SITU SURFACE PREPARATION 111
4.1.1. Wet-Chemical Etching and Chemically Oxide Removal Processes of GaAs(211)B Wafers 112

4.1.2. Results 114
4.1.2.1. AFM and SEM Resuts 114
4.1.2.2. Raman Spectroscopy Resuts 154
4.2. IN-SITU SURFACE PREPARATION 172
4.2.1. Thermal Oxide Desorption 172

CHAPTER 5. CHARACTERIZATION OF MBE-GROWN CDTE EPITAXIAL FILMS 176
5.1. STRUCTURAL CHARACTERIZATIONS 176
5.1.1. AFM and SEM Results 176
5.1.2. XRD Results 184
5.2. OPTICAL CHARACTERIZATIONS 188
5.2.1. Infrared Spectroscopy Results 188
5.2.2. Spectroscopic Ellipsometry Results 191
5.2.3. Raman Spectroscopy Results 193
5.3. DISLOCATION DENSITY ANALYSIS 214

CHAPTER 6. CONCLUSIONS 240

REFERENCES 244

LIST OF FIGURES

Figure **Page**

Figure 2.1. Electronic band structure of CdTe [4] 4
Figure 2.2. The first brillouin zone of the fcc lattice, including important symmetry points and lines [5]. 4
Figure 2.3. Schematic diagram of the band structure of CdTe about the point Γ in the Brillouin zone at room temperature in which the conduction, heavy hole(hh), light hole(lh) and split off (so) valence bands are shown. E_c and E_v are conduction and valence enegy levels, respectively and Δ is spin-orbit splitting energy. 5
Figure 2.4. The change of conduction band effective mass with bandgap energy for some semiconductors from $\vec{k}.\vec{p}$ theory 8
Figure 2.5. Change of bandgap energy with temperature of CdTe material where the solid line represents experimentally obtained bandgap energy and dot line represents the calculated band gap energy of CdTe [7]. 11
Figure 2.6. Three dimensional view of CdTe zincblende structure. 12
Figure 2.7. Two polar (211) and ($\bar{2}\bar{1}\bar{1}$) CdTe surfaces. 14
Figure 2.8. Absorption coefficients of various semiconductors at 300K [17]. 16
Figure 2.9. Dielectric constant ε_1 and ε_2 observed for CdTe by D.T.F Marple and H. Ehrenreich. Dashed curves are calculated values [18]. 17
Figure 2.10. The change of (a) Extinction coefficient with the annealing temperature of CdTe films, (b) Absorption coefficients with the annealing temperature of CdTe films [20]. 18
Figure 2.11. Schematic representation of fluorescence and phosphorescence processes 20
Figure 2.12. Free exciton energy levels within the bandgap energy. Green arrow show optical transition within the bandgap energy, pink and purple circles denote holes and electrons, respectively. 23
Figure 2.13. Schematic representation of band to band transitions in semiconductors for (a) diret and (b) indirect bandgaps. Blue circles and pink circles represent electrons and holes, respectively. 27

Figure 2.14. Schematic representation of (1) before and (2) after donor-acceptor pair transition; blue and pink circles denote electrons and holes, respectively. Hollow circles represent unoccupied states. 29
Figure 2.15. Representation of various radiative transitions in CdTe 31
Figure 2.16. Zero, first and second order LO replica shifts of free exciton away from absorption lines [53]. 32
Figure 2.17. Schematic representation of Auger-1 (left) recombination and Auger-7 recombination (right); blue and pink circles denote electons and holes, respectively. 34
Figure 2.18. Schematic representation of (1) before and (2) after Schockley-Read-Hall recombination processes. Blue and pink circles denote electrons and holes, respectively. 35
Figure 2.19. Cd-Te binary phase diagram [2] 39
Figure 2.20. Schematic illustration of a Vertical Bridgman (VB) method [66] 40
Figure 2.21. Schematic illustration of a Czochralski method [75] 42
Figure 2.22. Schematics of (a) Cold Traveling Heater Method (CTHM) and (b) Sublimation Traveling Heater Method (STHM) [83] 43
Figure 2.23. Schematic drawing of the MBE growth chamber [5] 45
Figure 2.24. Growth modes (a) 2D Layer by layer growth (Frank-Van der Merwe), (b) Layer plus island growth (Stranski-Kastranov), (c) 3D Island growth (Volmer-Weber) 46
Figure 2.25. Simplified schematic representation of deposition of a film where $\gamma_{film}, \gamma_{int}$ and γ_{sub} are surface free energy of film, the interfacial energy between the epitaxial layer and the substrate interface and surface free energy of substrate, respectively. 47
Figure 2.26. Schematic representation of the surface processes during Molecular Beam Epitaxial growth 48
Figure 2.27. Schematic diagram of (a) an organometallic cylinder and (b) Horizontal reaction chamber [91]. 50
Figure 2.28. A schematic representation of the Pulsed Laser Deposition Technique [99]. 52
Figure 2.29. Cost and largest available areas of substrates for the growth of HgCdTe [2] 56

Figure 2.30. Energy gap versus lattice parameter for several semiconductor materials [117] 57
Figure 2.31. Some of defects in zincblende structure of CdTe (a) Cation vacancy (V_{Cd}), (b) Anion vacancy (V_{Te}), (c) Tellurium antisite (Te_{Cd})........ 61
Figure 2.32. Schematic representation of comparasion of perfect lattice with some point defect types; (a) Perfect lattice (b) Interstitial impurity, (c) Cation vacancy (d) Anion Vacancy (e) Schottkey Imperfection (f) Frenkel Imperfection........ 61
Figure 2.33. Point defect densities as a function of Cd partial pressure. H and e are holes and electrons, and RT refers room temperature [82]........ 62
Figure 2.34. Growth of heteroepitaxial layer on a lattice mismatched substrate. (a) Strained layer below the critical thickness, (b) Partially relaxed layer above the critical thickness by forming misfit dislocations which it is shown in red color........ 64
Figure 2.35. The perfect crystal is cut and an extra half plane of atoms is inserted in (a) and forms extra half plane is an edge dislocation in (b) where Burger's vector b is perpendicular to dislocation line. In (c) the perfect crystal is cut and sheared one atom spacing, and formed screw dislocation in (d) where Burger's vector b is parallel to dislocation line [135]........ 65
Figure 2.36. On the left the ABABAB stacking sequence of close-packed planes of the HCP structure and on the right the ABCABCABC stacking sequence of close-packed planes of the FCC structure [135]........ 67
Figure 2.37. Examples of intrinsic and extrinsic stacking faults in close-spaced sublimation (CSS) grown polycrystalline CdTe/CdS film of [110] zone axis HRTEM images of an (a) intrinsic stacking fault and (b) extrinsic stacking fault. The insets are simulations of faults [136]........ 67
Figure 2.38. (a) Perfect cystal and (b) Formation of twin and twin boundaries [135] ... 68
Figure 2.39. Cross-sectional electron micrograph of CdTe(211)B/ZnTe/Si(211) interface where (111)-type stacking faults and twinning defects originating at the Si substrate surface. Inset shows electron diffraction pattern where approximately 3.5^{o} rotation between CdTe/Si crystal lattices [137]........ 68

Figure 2.40. (a) Three grains with different orientations and spacing seperated by grain goundary (b) Low angle grain boundary [135] 69
Figure 2.41. High-Pressure Bridgman (HPB) grown CdZnTe (a) Infrared micrograph of Te inclusions (b) Image of macroscopic cracks [139]. 70
Figure 3.1. Functional Diagram of Gen-20MZ MBE system. 1. Effusion cells, 2. Growth module, 3. Storage module gate valve, 4. X-axis transfer rod, 5. Storage module elevator, 6. Storage module, 7. Y-axis transfer rod, 8. Storage module gate valve, 9. Heated station for substrate outgassing, 10. Preparation module, 11. Preperation module gate valve, 12. Load lock module, 13. Load lock casette elevator, 14. Load lock door, 15. Venting/roughing manifold, 16. Z-axis manipulator [140] 72
Figure 3.2. (a) A typical effusion cell image (b) Different crucible types where number 1 is SUMO, 2 is conical and 3 is cylindrical crucible [143]. 73
Figure 3.3. Gen-20MZ MBE system facility in the department of physics at Iztech. 74
Figure 3.4. Top: A typical spectrum for Anti-Stokes, Rayleigh, and Stokes scattered photons ordered from left to right respectively. Bottom: Quantum excitations and de-excitations of the vibrational levels for the corresponding peaks. 77
Figure 3.5. MonoVista Raman system components in the department of physics at Iztech 81
Figure 3.6. Calculated electronic band structure of GaAs [5]. 82
Figure 3.7. Phonon dispersion curves in GaAs. Experimental data shown as points were measured at 12 K by neutron scattering and continuous lines were calculated with a 15-parameter rigid-ion model [150]. 83
Figure 3.8. Phonon dispersion curves in CdTe where solid lines were calculated from a first principles binding force model in comparison with neutron scattering data [151] 83
Figure 3.9. Γ_1 and Γ_{15} components of the second-order Raman spectrum of GaAs with an excitation photon energy of 2.81 eV [159]. 87
Figure 3.10. (a) Raman spectrum of bulk $Cd_{1-x}Zn_xTe$ at 80K with composition x of (a) 1, (b) 0.5, (c) 0.40, (d) 0.30, (e) 0.20, (f) 0.10, (g) 0.03, (h) 0.01, (i) 0.005 and (b) Variation of LO and TO frequencies in $Cd_{1-x}Zn_xTe$ as a function of composition x [180] 90

Figure 3.11. Michelson Interferometer 92
Figure 3.12. Interferogram (top) and spectrum (bottom) of water vapor in air. 93
Figure 3.13. Spectrum of a monochoromatic line with a wavenumber σ0. Instrumental effect leads to a sinc(z) function. With a proper apodization sinc2(z) function is obtained [183]. 97
Figure 3.14. (a) Design of Wollastron and Nomarski prisms, (b) Working principle of Nomarski Interference Microscope [188]. 100
Figure 3.15. Main components of the A13.1013 DIC Metallurgical Microscope at Iztech. 101
Figure 3.16. Main components of AFM [191] 102
Figure 3.17. The force of interaction between the tip and a sample as a function of the tip-sample distance where proper modes of operation are also indicated [191]. 103
Figure 3.18. Scanning Probe Microscopy instrument (Solver Pro 7 from NT-MDT, Russia) 106
Figure 3.19. Schematic representation of Bragg reflection from crystal planes where d_{hkl} is the distance between a set of parallel crystal planes (interplanar spacing) and θ is the angle of incidence. 109
Figure 3.20. Schematic illustration of a typical X-ray triple axis rocking curve peak 109
Figure 3.21. Thin Film Philips X'Pert Pro MRD System components in High Resolution X-ray diffraction configuration in the department of physics at Iztech 110
Figure 4.1. (a) and (c) are AFM 2D topographic images, (c) and (f) are AFM 3D topografic images of not chemically-etched GaAs wafer, (b) Profile line analysis of (a), and (e) Profile line analysis of (d) 115
Figure 4.2. (a) AFM 2D Topographic image and (b) AFM 3D Topographic image of sample G1C1-A1 and profile line analysis of (c) XS1 (line 157), (d) XS2 (line 240), (e) S1 line of 1.92 μm width and (f) S2 line of 1.45 μm width 116
Figure 4.3. (a) and (b) are SEM micrographs of sample G1C1-A1 with 10 000 and 50 000 magnifications where spectra show the regions that EDX analysis were performed in SEM image (b) and the table shows the percentage of distributions of Ga, As and O in spectrum 13 and 15. 117

Figure 4.4. (a) AFM 2D Topographic image and (b) AFM 3D Topographic image of sample G1C1-A2 and profile line analysis of (c) XS1 (line 86), (d) XS2 (line 15), (e) S1 line of 3,10 μm width and (f) S2 line of 2,67 μm width 118
Figure 4.5. (a) and (b) are SEM micrographs of sample G1C1-A2 with 50 000 and 100 000 magnifications where spectra show the regions that EDX analysis were performed in SEM images and the table shows the percentage of distributions of Ga, As and C in spectrum 5 and 8. 119
Figure 4.6. (a) AFM 2D and (b) AFM 3D Topographic images of sample G1C1-A3 and profile line analysis of (c) X2(line 26), (d) XS2 (line 144) 121
Figure 4.7. Left side of the figure is SEM micrograph of sample G1C1-A3 with 100 000 magnification where spectra show the region that EDX analysis were performed in SEM image and the table shows the percentage of distributions of Ga, As, C and O in spectrum 3. 122
Figure 4.8. (a) AFM 2D Topographic image and (b) AFM 3D Topographic image of sample G1C1-B1 and profile line analysis of (c) XS1 (line 185), (d) YS1 (line 58), (e) S1 and (f) S2 line of 1.3 μm width 123
Figure 4.9. The figure is SEM micrograph of sample G1C1-B1 with 100 000 magnification where spectra show the region that EDX analysis were performed in SEM image and the table shows the percentage of distributions of Ga, As, C and O in spectrum 1 and 3. 124
Figure 4.10. (a) AFM 2D Topographic image and (b) AFM 3D Topographic image of sample G1C1-B2 and profile line analysis of (c) XS1(line 64) and (d) S1 line of 2.83 μm width 125
Figure 4.11. (a), (b) and (c) are SEM micrographs of sample G1C1-B2 with 10 000 and 100 000 magnifications where spectra show the regions that EDX analysis were performed in SEM image (a) and (b), the table shows the percentage of distributions of elements in spectrum 6, 7, 9 and 11. 126
Figure 4.12. (a) AFM 2D Topographic image and (b) AFM 3D Topographic image of sample G1C1-B3 and profile line analysis of (c) XS1 (line 38), (d) YS1 (line 140), (e) S1 line of 3.17 μm width and (f) S2 line of 1.48 μm width 127

Figure 4.13. (a), (b) are SEM micrographs of sample G1C1-B3 with 10 000 and 100 000 magnifications where spectra show the regions that EDX analysis were performed in SEM image (b), the table shows the percentage of distributions of elements in spectrum 14 and 16. 128
Figure 4.14. (a) AFM 2D Topographic image and (b) AFM 3D Topographic image of sample G1C1-C1 and profile line analysis of (c) XS1 (line 64) and (d) S1 line of 2.17 μm width 129
Figure 4.15. SEM micrograph of sample G1C1-C1 with 25 000 magnification where spectra show the region that EDX analysis were performed in SEM image and the tables show the percentage of distributions of Ga and As in spectrum 16, 17, 18 and 19. 130
Figure 4.16. (a) AFM 2D Topographic image and (b) AFM 3D Topographic image of sample G1C1-C2 and profile line analysis of (c) YS1 (line 217) and (d) S1 line of 0.98 μm width 131
Figure 4.17. SEM micrograph of sample G1C1-C2 with 50 000 magnification where spectra show the region that EDX analysis were performed in SEM image and the tables show the percentage distributions of Ga and As in spectrum 22 and 23 132
Figure 4.18. (a) AFM 2D Topographic image and (b) AFM 3D Topographic image of sample G1C1-C3 and profile line analysis of (c) XS1 (line 110), (d) YS1 (line 117), (e) S1 line of 2.17 μm width and (f) S2 line of 1.60 μm width 133
Figure 4.19. SEM micrograph of sample G1C1-C3 with 100 000 magnification where spectra show the region that EDX analysis were performed in SEM image and the tables show the percentage distributions of Ga and As in spectrum 24 and 27. 134
Figure 4.20. (a) AFM 2D Topographic image and (b) AFM 3D Topographic image of sample G1C1-E1 and profile line analysis of (c) XS1 (line 224) and (d) YS1 (line 58).. 135
Figure 4.21. SEM micrograph of sample G1C1-E1 with 100 000 magnification where spectra show the region that EDX analysis were performed in SEM image and the tables show the percentage distributions of Ga, As and C in spectrum 18 and 20. 136

Figure 4.22. (a) AFM 2D Topographic image and (b) AFM 3D Topographic image of sample G1C1-E2 and profile line analysis of (c) XS1 (line 180) and (d) S1 line of 0,70 µm width 137
Figure 4.23. SEM micrograph of sample G1C1-E2 with 100 000 magnification where spectra show the region that EDX analysis were performed in SEM image and the tables show the percentage distributions of Ga, As, C and O in spectrum 23 and 25. 138
Figure 4.24. (a) AFM 2D Topographic image and (b) AFM 3D Topographic image of sample G1C1-E3 and profile line analysis of (c) XS1 (line 227) and (d) S1 line of 0,50 µm width 139
Figure 4.25. SEM micrograph of sample G1C1-E3 with 100 000 magnification where spectra show the region that EDX analysis were performed in SEM image and the tables show the percentage distributions of Ga, As and C in spectrum 28 and 29. 140
Figure 4.26. (a) AFM 2D Topographic image and (b) AFM 3D Topographic image of sample G1C1-F1 and profile line analysis of (c) XS2 (line 99) and (d) XS1 (line 252).. 141
Figure 4.27. Left side of the figure is SEM micrograph of sample G1C1-F1 with 100 000 magnification where spectra show the region that EDX analysis were performed in SEM image and the table shows the percentage of distributions of Ga, As, C and O in spectrum 18 and 19... 142
Figure 4.28. (a) AFM 2D Topographic image and (b) AFM 3D Topographic image of sample G1C1-F2 and profile line analysis of (c) XS2 (line 125) and (d) S1 line of 2,91 µm width 143
Figure 4.29. SEM micrograph of sample G1C1-F2 with 100 000 magnification where spectra show the region that EDX analysis were performed in SEM image and the tables show the percentage distributions of Ga, As, C and O in spectrum 23 and 24. 144
Figure 4.30. (a) AFM 2D Topographic image and (b) AFM 3D Topographic image of sample G1C1-G1 and profile line analysis of (c) XS1 (line 213) and (d) S1 line of 1,93 µm width 145
Figure 4.31. (a) and (b) are SEM micrographs of sample G1C1-G1 with 100 000 magnification where spectra show the region that EDX analysis were

performed in SEM image (b) and the tables show the percentage distributions of Ga, As, C and O in spectrum 4 and 5. 146
Figure 4.32. (a) AFM 2D Topographic image and (b) AFM 3D Topographic image of sample G1C1-G2 and profile line analysis of (c) XS1 (line 234) and (d) S1 line of 4,81 μm width 147
Figure 4.33. SEM micrograph of sample G1C1-G2 with 100 000 magnification where spectra show the region that EDX analysis were performed in SEM image and the tables show the percentage distributions of Ga, As, C and O in spectrum 10 and 13. 148
Figure 4.34. (a) AFM 2D Topographic image and (b) AFM 3D Topographic image of sample G1C1-G3 and profile line analysis of (c) XS1 (line 121) and (d) S1 line of 2,36 μm width 149
Figure 4.35. SEM micrograph of sample G1C1-G3 with 100 000 magnification where spectra show the region that EDX analysis were performed in SEM image and the tables show the percentage distributions of Ga, As, C and O in spectrum 14 and 17. 150
Figure 4.36. (a) and (b) are AFM 2D and 3D Topographic images before oxide removal, (c) and (d) are AFM 2D and 3D Topographic images and (d) and (e) are profile line analysis of XS1 (line 121) and (d) YS1 (line 40) of sample G2W24A after oxide removal process 152
Figure 4.37. (a) and (b) are AFM 2D and 3D Topographic images before oxide removal, (c) and (d) are AFM 2D and 3D Topographic images and (d) and (e) are profile line analysis of XS1 (line 202) and (d) YS1 (line 147) of sample G2W25A after oxide removal process 153
Figure 4.38. Room temperature Raman spectrum of powdered As_2O_3 and Ga_2O_3 [204] 155
Figure 4.39. Raman spectra of As vapour at 610 ºC [207] 156
Figure 4.40. (a) and (b) are the Raman spectra under 488 nm excitation for the GaAs(211)B wafer before the wet-chemical etching................................ 157
Figure 4.41. Experimentally obtained and Lorentzian fitted whole range Raman spectra of samples G1C1-A1, G1C1-A2 and G1C1-A3 under 488 nm excitation.. 158

Figure 4.42. Experimentally obtained and Lorentzian fitted whole range Raman spectra of samples G1C1-B1, G1C1-B2 and G1C1-B3 under 488 nm excitation 160
Figure 4.43. Experimentally obtained and Lorentzian fitted whole range Raman spectra of samples G1C1-C1, G1C1-C2 and G1C1-C3 under 488 nm excitation 161
Figure 4.44. Experimentally obtained and Lorentzian fitted whole range Raman spectra of samples G1C1-E1, G1C1-E2 and G1C1-E3 under 488 nm excitation 162
Figure 4.45. Experimentally obtained and Lorentzian fitted whole range Raman spectra of samples G1C1-G1, G1C1-G2 and G1C1-G3 under 488 nm excitation 163
Figure 4.46. Experimentally obtained and Lorentzian fitted whole range Raman spectra of sample G2W24A before and after oxide removal procedure under 488 nm excitation 164
Figure 4.47. Experimentally obtained and Lorentzian fitted whole range Raman spectra of sample G2W25A before and after oxide removal procedure under 488 nm excitation 165
Figure 4.48. (a) Optical microscope image of 2x2 μm^2 scanned area on sample G1C1-A1, Raman intensity change of (b) As_2O_3 phonon mode and (c) As_4 phonon mode 168
Figure 4.49. (a) Optical microscope image of 20x20 μm^2 scanned area on sample G1C1-A2, Raman intensity change of (b) As_2O_3 phonon mode, (c) LO phonon mode and (d) As_4 phonon mode 169
Figure 4.50. (a) Optical microscope image of 2x2 μm^2 scanned area on sample G1C1-A2, Raman intensity change of (b) As_2O_3 phonon mode, (c) LO phonon mode and (d) As_4 phonon mode 170
Figure 4.51. (a) Optical microscope image of 10x10 μm^2 scanned area on sample G1C1-B1 and (b) Raman intensity change of As_2O_3 phonon mode on scanned area 171
Figure 4.52. (a) Optical microscope image of 20x20 μm^2 scanned area on sample G1C1-B2 and (b) Raman intensity change of As_2O_3 phonon mode on scanned area 171

Figure 4.53. (a) Optical microscope image of 10x10 μm^2 scanned area on sample G1C1-G1, Raman intensity change of (b) As_2O_3 phonon mode on scanned area and (c) LO phonon mode.. 172
Figure 4.54. The change of BFM reading with As cracker cell valve position and time during flux calibration prior to oxide removal........................... 173
Figure 4.55. Obtained GaAs(211)B wafer temperature by kSA Bandit and vacuum reading during oxide removal process 174
Figure 4.56. RHEED diffraction pattern of (a) and (b) before oxide desorption, (c), (d), (e) and (f) during oxide desorption at 582 ^oC of GaAs wafer....... 175
Figure 5.1. (a) AFM 2D Topographic image and (b) AFM 3D Topographic image of sample CdTe18 and profile line analysis of (c) YS1 (line 193) and (d) XS1 (line 202)... 177
Figure 5.2. (a) and (c) are SEM micrographs of sample CdTe18 with 50 000 magnifications, (b) and (d) are EDX-map of SEM micrographs of (a) and (c), respectively and tables show the percentage distributions of Cd, Te, Ga and As in scanned area of (b) and (d), respectively. 178
Figure 5.3. (a) AFM 2D Topographic image and (b) AFM 3D Topographic image of sample CdTe23 and profile line analysis of (c) XS1 (line 38) and (d) YS1 (line 215)... 179
Figure 5.4. (a) and (c) are SEM micrographs of sample CdTe23 with 50 000 magnifications, (b) and (d) are EDX-map of SEM micrographs of (a) and (c), respectively and tables show the percentage distributions of Cd, Te, Ga and As in scanned area of (b) and (d), respectively. 180
Figure 5.5. (a) AFM 2D Topographic image and (b) AFM 3D Topographic image of sample CdTe24 and profile line analysis of (c) XS1 (line 231) and (d) YS1 (line 170) 181
Figure 5.6. (a) and (b) are SEM micrographs of sample CdTe24 with 50 000 magnifications, (c) and (d) are EDX-map of SEM micrographs of (a) and (b), respectively and tables show the percentage distributions of Cd, Te, Ga and As in scanned area of (c) and (d), respectively. 183
Figure 5.7. Cross-sectional SEM micrographs of (a) CdTe18, (b) CdTe23 and (c) CdTe24 184
Figure 5.8. A typical (422) GaAs XRD rocking curve which was used as a substrate for epitaxially growth of CdTe(211)B films.............................. 185

Figure 5.9. XRD rocking curve of (422) CdTe for CdTe18 sample 186
Figure 5.10. XRD rocking curve of (422) CdTe for CdTe24 sample 187
Figure 5.11. X-ray reflectivity curve of CdTe18 sample where blue line represents measured curve and red line represent fitted curve by X-pert XRD data sorftware 188
Figure 5.12. Room temperature IR transmission curves of MBE-grown CdTe epitaxial films 190
Figure 5.13. Room temperature transmittance curves of CdTe samples in the range of 3800 to 13 000 cm^{-1} taken with UV/VIS/NIR spectrometer. 191
Figure 5.14. Ex-situ spectroscopic ellipsometry data of experimentally obtained and fitted using oscillator model refractive index and extinction coefficient of CdTe18, CdTe23 and CdTe24 192
Figure 5.15. Temperature dependence Raman spectra of CdTe18 sample under 488 nm excitation 194
Figure 5.16. Raman scattering spectra of CdTe18 at various temperatures. The spectra were normalized to the first order TO phonon mode of CdTe 194
Figure 5.17. The whole range Raman spectra of CdTe18 at 300 K and 250 K. The insets show experimentally obtained and Lorentzian fitted Raman spectra at 300 K and 250 K. 196
Figure 5.18. The whole range Raman spectra of CdTe18 at 200 K and 150 K. The insets show experimentally obtained and Lorentzian fitted Raman spectra at 200 K and 150 K. 197
Figure 5.19. The whole range Raman spectra of CdTe18 at 120 K and 100 K. The insets show experimentally obtained and Lorentzian fitted Raman spectra at 120 K and 100 K. 198
Figure 5.20. Experimentally obtained and Lorentzian fitted the whole range Raman spectra of CdTe18 at 80 K. 199
Figure 5.21. The change of Te specific E-symmetry and A_1-symmetry modes with the temperature for CdTe18 sample 199
Figure 5.22. The change of CdTe-like TO, LO and 2LO phonon modes with the temperature for CdTe18 sample 200
Figure 5.23. The change of calculated intensity ratios of observed phonon modes for CdTe18 sample.. 200

Figure 5.24. Temperature dependent Raman spectra of CdTe23 sample under 488 nm excitation 201
Figure 5.25. Raman scattering spectra of CdTe23 at various temperatures. The spectra were normalized to Raman active TO phonon mode of GaAs 202
Figure 5.26. The whole range Raman spectra of CdTe23 at 300 K and 250 K. The insets show experimentally obtained and Lorentzian fitted Raman spectra at 300 K and 250 K. 203
Figure 5.27. The whole range Raman spectra of CdTe23 at 200 K and 150 K. The insets show experimentally obtained and Lorentzian fitted Raman spectra at 200 K and 150 K. 204
Figure 5.28. The whole range Raman spectra of CdTe23 at 120 K and 100 K. The insets show experimentally obtained and Lorentzian fitted Raman spectra at 120 K and 100 K. 205
Figure 5.29. Expeimentally obtained and Lorentzian fitted the whole range Raman spectra of CdTe23 at 80 K. 206
Figure 5.30. Temperature dependent Raman spectra of CdTe24 sample under 488 nm excitation 207
Figure 5.31. Raman scattering spectra of CdTe24 at various temperatures. The spectra were normalized to first-order TO phonon mode of CdTe 207
Figure 5.32. The whole range Raman spectra of CdTe24 at 300 K and 250 K. The insets show experimentally obtained and Lorentzian fitted Raman spectra at 300 K and 250 K. 208
Figure 5.33. The whole range Raman spectra of CdTe24 at 200 K and 150 K. The insets show experimentally obtained and Lorentzian fitted Raman spectra at 200 K and 150 K. 210
Figure 5.34. The whole range Raman spectra of CdTe24 at 100 K and 120 K. The insets show experimentally obtained and Lorentzian fitted Raman spectra at 100 K and 120 K. 211
Figure 5.35. Experimentally obtained and Lorentzian fitted the whole range Raman spectra of CdTe24 at 80 K. 212
Figure 5.36. Variation of Te specific E-symmetry and A_1-symmetry modes with the temperature for CdTe24 sample. 213

Figure 5.37. The change of CdTe-like TO, LO and 2LO phonon modes depending on the temperature for CdTe24 sample 213
Figure 5.38. The change of calculated intensity ratios of observed phonon modes for CdTe24 sample.. 214
Figure 5.39. (a) SEM micrograph with 50 000 magnifications, (b) and (c) are AFM 2D Topographic image from 20x20 μm^2 and 2x2 μm^2 scanned areas, (d) AFM 3D Topographic image and (e) and (f) are profile line analysis of XS1 (line 65) and S1 line of 0,140 µm width of Everson defect decorated CdTe18-1 sample 217
Figure 5.40. (a) and (b) are AFM 2D Topographic image from 20x20 μm^2 and 2x2 μm^2 scanned areas, (e) AFM 3D Topographic image and (c) and (d) are profile line analysis of XS1 (line 93) and (d) S1 line of 0,157 µm width of Everson defect decorated CdTe18-2 sample 219
Figure 5.41. SEM micrographs of sample CdTe18-2 with 10 000 and 2500 magnifications where spectra show the region that EDX analysis were performed in SEM image and the tables show the percentage distributions of Cd, Te, Ga and As in spectrum 18 and 19. 220
Figure 5.42. (a) SEM micrograph with 100 000 magnifications, (b) and (c) are AFM 2D Topographic image from 20x20 μm^2 and 2x1.7 μm^2 scanned areas, (d) AFM 3D Topographic image and (e) and (f) are profile line analysis of XS1 (line 82) and S1 line of 0,096 µm width of Everson defect decorated CdTe18-3 sample... 221
Figure 5.43. Nomarski images of CdTe18 sample (a) before dislocation decoration and (b) after Everson etch with 0.5HF+4HNO3+25Lactic acid mixture during 30 s 222
Figure 5.44. Everson etched CdTe23-1 sample of (a) SEM micrograph with 50 000 magnification, (b) AFM 2D Topographic image, (c) AFM 3D Topographic image and (d) Profile line analyse of XS1 (line 55)... 223
Figure 5.45. Everson etched CdTe23-2 sample of (a) SEM micrograph with 100 000 magnification, (b) and (c) are AFM 2D Topographic images, (c) AFM 3D Topographic image, (d) Profile line analyses of YS1 (line 208) and (e) S1 line of 0,132 µm width 224

Figure 5.46. (a) SEM micrograph with 50 000 magnification, (b) and (c) are AFM 2D Topographic images, (d) AFM 3D Topographic image, (e) Profile line analyses of XS1 (line 215) and (f) S1 line of 0,315 μm width of Everson etched CdTe23-3 sample 225
Figure 5.47. (a) SEM micrograph with 10 000 magnification, (b) AFM 2D Topographic image, (c) Profile line analysis of XS1 (line 146) and (d) AFM 3D Topographic image of Everson etched CdTe23-4 sample 227
Figure 5.48. Nomarski images of CdTe23 sample (a) before dislocation decoration and (b) after Everson etch with 1HF+4HNO3+25Lactic acid mixture during 60 s 228
Figure 5.49. Benson decoration etched CdTe23-5 sample of (a) and (b) AFM 2D Topographic images for 5 μm^2 and 2 μm^2 scanned areas, (c) and (d) Profile line analysis of XS1 (line 136) and S1 line of 0,206 μm width 229
Figure 5.50. SEM micrograph of CdTe23-5 with 50 000 magnifications and EDX elemental analyses results 230
Figure 5.51. Everson etched CdTe24-1 sample of AFM 2D topographic images for (a) 5 μm^2 scanned area and (b) 2 μm^2 scanned area, (c) Profile line analyses of XS1 (line 123), (d) S1 line of 0,243 μm width and (e) AFM 3D topographic image 231
Figure 5.52. Everson etched CdTe24-1 sample of SEM micrographs with 50 000 and 2 500 magnifications and EDX analyses results in spectrums 14 and 15 232
Figure 5.53. Everson etched CdTe24-2 sample of AFM 2D topographic images for (a) 10x10 μm^2 scanned area and (b) 2x2 μm^2 scanned area, (c) Profile line analyses of XS1 (line 199), (d) S1 line of 0,235 μm width and (e) AFM 3D topographic image 233
Figure 5.54. SEM micrographs of CdTe24-2 with 50 000, 100 000 and 2 500 magnifications and table shows EDX spectrum results in 2 500 magnification SEM image 234
Figure 5.55. Everson etched CdTe24-3 sample of AFM 2D topographic images for (a) 20x20 μm^2 scanned area and (b) 2x2 μm^2 scanned area, (c) Profile line analyses of S1 line of 0.714 μm width and (d) AFM 3D topographic image 235

Figure 5.56. SEM micrographs of CdTe24-3 with (a) 50 000 and (b) 2 500 magnifications, and EDX analyses results of spectrum 2 in (b) 236
Figure 5.57. Nomarski images of CdTe24 sample (a) before dislocation decoration, after Everson etch with (b) 1HF+4HNO3+50Lactic acid mixture for 40 s, (c) and (d) 1HF+4HNO3+25Lactic acid mixture for 20 s 237
Figure 5.58. a) Optical microscope image of 10 μmx10 μm scanned area on sample CdTe24-2, Raman intensity change of (b) A_1-symmetry mode, (c) CdTe-like TO phonon mode, (d) CdTe-like LO phonon mode, (e) GaAs-like TO phonon mode and (f) GaAs-like LO phonon mode.. 238

LIST OF TABLES

Table **Page**

Table 2.1. The change of lattice parameter with temperature for CdTe [13] 13

Table 2.2. Refractive index values for different wavelengths 18

Table 2.3. Bound exciton PL amission band energies for donor and acceptor impurities in CdTe [43, 46] 25

Table 2.4. Comparison of Alternative Substrates for HgCdTe/CdTe [110] 55

Table 2.5. Ionization energies of point defects in CdTe 62

Table 3.1. The selection rules for the zincblende structure according to Birman 86

Table 3.2. Combined phonon modes in wave numbers (cm^{-1}) at 293 K of CdTe from dispersive Fourier transform spectroscopy [171] 89

Table 4.1. Wet-chemically etched samples with sample IDs, degreasing processes, H_2SO_4:H_2O_2:H_2O volume ratios, implementation times, drying processes 113

Table 4.2. Oxide removal processes of GaAs wafers with sample IDs, volume ratios and implementation time 114

Table 4.3. The change of RMS roughness average depending on the mixture volume ratios and implementation times 151

Table 4.4. Average RMS roughness value change of before and after oxide removal 154

Table 4.5. Behavior of the Raman peaks depending on the wet-chemical etching by piranha solution 166

Table 4.6. Behavior of the Raman peaks before and after oxide removal process....... 168

Table 5.1. Obtained density, thickness and roughness of CdTe18 sample layers from XRR fitted curve.. 188

Table 5.2. CdTe layer thicknesses obtained from spectroscopic ellipsometry (SE) and calculated using FTIR transmittance curves.. 191

Table 5.3. chemical composition, volume ratios, implementation times of performed defect decoration methods with sample IDs.............................. 216

CHAPTER 1

INTRODUCTION

The ternary alloy Mercury Cadmium Telluride ($Hg_{1-x}Cd_xTe$) is commonly used material for infrared (IR) imaging since the first discovery in 1958 by Lawson and co-workers [1]. The band gap energy tunability depending on the Cd composition makes it a versalite material for infrared detector applications in the short wavelength IR (SWIR: 1-3 μm), mid-wavelength IR (MWIR: 3-5 μm), long wavelength (LWIR: 8-14 μm) and very long wavelength (VLWIR: 14-30 μm) ranges. Despite the growth of HgCdTe material has been performed on the alternative substrates such as Si, GaAs, InSb and Ge for years, defects created due to large lattice and thermal expansion coefficient mismatch between HgCdTe and these substrates deleteriously affects the performance of HgCdTe devices. After the first synthesis of bulk $Cd_{1-x}Zn_xTe$ material in mid-1980s, it became a preferred substrate for HgCdTe IR detectors due to lower lattice, thermal expansion coefficient and valence mismatch with %4 Zn concentration. However, high cost, limited available size and large thermal mismatch with the Si readout integrated circuit (ROIC) of CdZnTe necessities the need for new alternatives for the growth of high quality HgCdTe materials [2].

GaAs substrates can be found commercially epi-ready and easily removal of protective oxide layers makes it a convenient substrate for epitaxial growth of $Hg_{1-x}Cd_xTe$. However, diffusion of gallium and arsenic atoms into the growing layer degrades the device performance. Nowadays, Cadmium Telluride (CdTe) growth on GaAs substrate as a buffer layer for the subsequent growth epitaxial $Hg_{1-x}Cd_xTe$ draws attention due to relatively small lattice mismatch between CdTe and $Hg_{1-x}Cd_xTe$. It also prevents impurity atom migration into the $Hg_{1-x}Cd_xTe$ layers. Despite favourable effects of CdTe buffer layers, propagation of crystalline defects into the growing epitaxial layers deleteriously effects the quality of $Hg_{1-x}Cd_xTe$ layers.

Throughout this study, defect structures of Molecular Beam Epitaxy (MBE)-grown CdTe epitaxial films were investigated via structural and optical characterizations. The overview of this thesis can be summarized with the main objectives as follows;

- The first part of this study, Chapter 2, gives background information about the fundamental properties of CdTe such as its crystal structure, electronic and optical properties. Widely used bulk and epitaxial growth techniques for the growth of CdTe material and also the possible imperfections will be briefly explained in this chapter.
- In the second part of the thesis, Chapter 3, MBE growth technique and structural and optical characterization techniques such as Atomic Force Microscopy (AFM), Scanning Electron Microscopy (SEM), Nomarski Microscopy, X-ray Diffraction (XRD), Fourier Transform Infrared Spectroscopy (FTIR) and Raman Spectroscopy used in this study explained in detail.
- The next part of the thesis, Chapter 4, includes the in-situ and ex-situ preparation processes of GaAs (211)B wafers prior to MBE growth of CdTe epitaxial films. In ex-situ preparation processes; wet-chemical etching and chemically oxide removal methods are explained in detail and the quality of the surfaces characterized by AFM and SEM, and oxide complexes of GaAs wafers such as As_2O_3 and Ga_2O_3 were investigated via Raman scattering technique.
- Chapter 5 focuses on the discussion of the quality of CdTe layers grown on GaAs wafers. The structural and optical properties of produced samples are discussed in this chapter.
- Summary of significant parts of this study, conclusions and prospects for future investigations will be discussed in Chapter 6.

CHAPTER 2

CADMIUM TELLURIDE

In this chapter, we are going to briefly review the fundamental properties of CdTe such as its crystal structure, electronic and optical properties which will be necessary to take into account for the understanding the defect structures in CdTe. In addition, widely used bulk and epitaxial growth techniques and also the possible imperfections or defects will be briefly discussed for the growth of bulk CdTe and epitaxial CdTe films.

2.1. Fundamental Properties of CdTe

2.1.1. Band Structure

CdTe has a direct band gap at a minimum of the conduction band and maximum of the valence band in the centre of Brillouin zone, Γ point, which means an electron recombine with a hole and can directly emit a photon. The forbidden bandgap energy of CdTe is about 1.529 eV at room temperature (300 K) and 1.606 eV at liquid He temperature (4 K) [3]. In Figure 2.1, the electronic band structure of CdTe and in Figure 2.2 the first Brillouin zone for zinc-blende lattice with symmetry points and lines are shown.

In Figure 2.2, the high-symmetry points of the first Brillouin zone of Fcc lattice is shown. High symmetry points and lines inside the Brillouin zone are shown by Greek letters and the points on the surfaces of Brillouin zone are shown by Roman letters. The center of Brillouin zone is Γ symmetry point. Lines between Γ and X points, Γ and L points and Γ and K points are denoted by Δ, Λ and Σ lines in [100], [111] and [110] directions, respectively. The Brillouin zone of Fcc lattice has eight hexagonal faces and all faces contain L point in center. In addition, the Brillouin zone of Fcc lattice is highly symmetrical which is unchanged by rotations and invariant under reflection.

Figure 2.1. Electronic band structure of CdTe [4]

Figure 2.2. The first brillouin zone of the fcc lattice, including important symmetry points and lines [5].

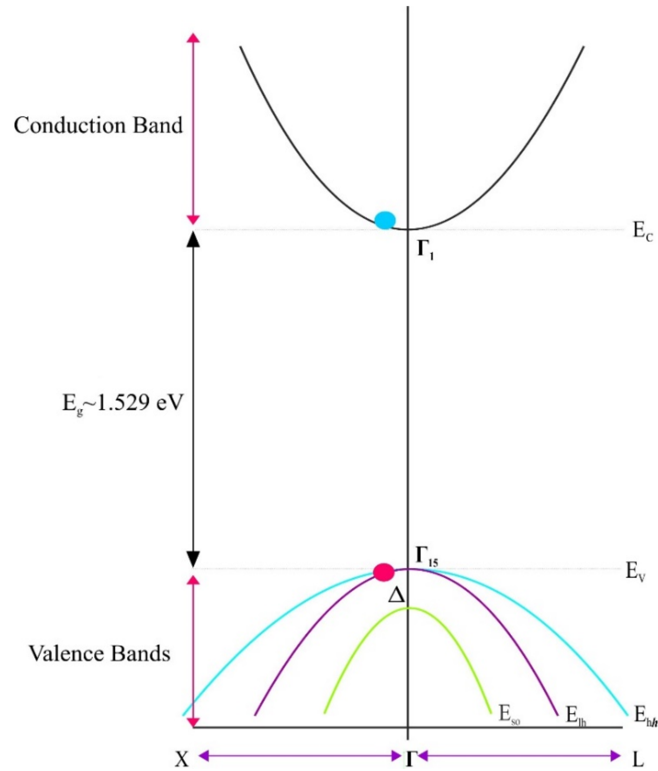

Figure 2.3. Schematic diagram of the band structure of CdTe about the point Γ in the Brillouin zone at room temperature in which the conduction, heavy hole(hh), light hole(lh) and split off (so) valence bands are shown. E_c and E_V are conduction and valence enegy levels, respectively and Δ is spin-orbit splitting energy.

In Figure 2.3, the schematic diagram of conduction and valance bands of CdTe at room temperature is shown. The valance band of CdTe consists of heavy hole, light hole and split off bands which have different effective masses. In most semiconductors, due to spin-orbit interaction, the valence band splits into three bands, a light-hole band, a heavy hole band and a split-off band. Even though hole states exist in all bands, holes are generally confined to valence band due to the large spin-orbit splitting energy. Split off valance band is shifted by the spin-orbit splitting energy, Δ. Analytic expressions for band dispersion and effective masses around high-symmetry points can be calculated using **k.p** perturbation method. In this method, the energy near a band maximum or minimum is calculated using perturbation of wavenumber. The **k.p** method can be derived from the one electron Schrödinger equation and using Bloch theorem, condition for $|k| \ll 2\pi/a$ that far from Brillouin zone edges. The one electron Schrödinger equation can be given by;

$$H\phi_n(\vec{r})=\left(\frac{p^2}{2m}+V(\vec{r})\right)\phi_n(\vec{r})=E_n\phi_n(\vec{r}) \qquad (2.1)$$

And Bloch theorem solution for the reduced scheme is;

$$\phi_{nk}=exp(i\vec{k}\vec{r})u_{nk}(\vec{r}) \qquad (2.2)$$

where $u_{nk}(\vec{r})$ is the Bloch lattice function, ϕ_{nk} is the Bloch wavefunction, n is band index and $\vec{k}$ is wavevector. When ϕ_{nk} is substituted into eq. 2.1, computing the action of $\vec{p}$ on $\vec{\phi}$;

$$\vec{p}.\left(e^{i\vec{k}\vec{r}}u_{nk}\left(\vec{r}\right)\right)=-i\hbar\vec{\nabla}.\left(e^{i\vec{k}\vec{r}}u_{nk}\left(\vec{r}\right)\right)$$

$$=\hbar\vec{k}e^{i\vec{k}\vec{r}}u_{nk}\left(\vec{r}\right)+e^{i\vec{k}\vec{r}}\vec{p}u_{nk}\left(\vec{r}\right) \qquad (2.3)$$

Then, it is obtained from this equation;

$$\left(\frac{p^2}{2m}+\frac{\hbar\vec{k}\vec{p}}{m}+\frac{\hbar^2k^2}{2m}+V\right)u_{nk}=E_{nk}u_{nk} \qquad (2.4)$$

and where;

$$\vec{k}.\vec{p}=k_x\left(-i\hbar\frac{\partial}{\partial x}\right)+k_y\left(-i\hbar\frac{\partial}{\partial y}\right)+k_z\left(-i\hbar\frac{\partial}{\partial z}\right) \qquad (2.5)$$

When k=(0, 0, 0), equation (2.3) reduces to;

$$\left(\frac{p^2}{2m}+V\right)u_{no}=E_{no}u_{no}\ ,\ (n=1, 2, 3,...) \qquad (2.6)$$

If we write Hamiltonian as the sum of two terms in equation (2.4);

$$\left(\underbrace{\left(\frac{P^2}{2m}+V\right)}_{H_0}+\underbrace{\left(\frac{\hbar\vec{k}\vec{p}}{m}+\frac{\hbar^2k^2}{2m}\right)}_{H_k'}\right)u_{nk}=E_{nk}u_{nk} \tag{2.7}$$

we can obtain unperturbed Hamiltonian 'H_0' and perturbed Hamiltonian 'H_k'' terms. Without spin-orbit interaction, the three valence bands degenerate at $\vec{k}$ =0. Then, the nth perturbed eigenvalue can be obtained as;

$$E_n \approx E_n(0)+\left(\frac{\hbar^2k^2}{2m_0}\right)\frac{\hbar^2}{m_0^2}\sum_{m\neq n}\frac{\left|\left\langle u_{n0}(\vec{r})\middle|\vec{k}.\vec{p}\middle|u_{m0}(\vec{r})\right\rangle\right|^2}{E_n(0)-E_m(0)} \tag{2.8}$$

Simplifying equation (2.8);

$$E_n(k)=E_n(0)+\left(\frac{\hbar^2k^2}{2m^*}\right) \tag{2.9}$$

where;

$$\frac{1}{m_n^*}=\frac{1}{m_0}\left[1+\frac{2}{m_0k^2}\sum_{m\neq n}\frac{\left|\left\langle u_{n0}(\vec{r})\middle|\vec{k}.\vec{p}\middle|u_{m0}(\vec{r})\right\rangle\right|^2}{E_n(0)-E_m(0)}\right] \tag{2.10}$$

m_n^* is the effective mass of the nth band and m_0 is free electron mass. And, ignoring spin-orbit interaction, conduction band effective mass can be given as;

$$\frac{1}{m_c^*}=\frac{1}{m_0}\left[1+\frac{2}{m_0k^2}\left[\frac{1}{2}\left(\frac{k^2p^2}{E_g}\right)+\frac{1}{6}\left(\frac{k^2p^2}{E_g}\right)+\frac{1}{3}\left(\frac{k^2p^2}{E_g}\right)\right]\right] \tag{2.11}$$

With an approximation of $\frac{2p^2}{m_0}=\frac{8\pi^2\hbar^2}{m_0a^2}\approx 20$ eV in eq. 2.11, where a is lattice constant, conduction band effective mass can be obtained as;

$$m_c^* \approx \frac{m_0}{1+\frac{20eV}{E_g}} \tag{2.12}$$

In Figure 2.4, the change of effective mass in conduction band depending on the bandgap energy in eV is shown. As can be seen, the effective mass of electrons increases as the bandgap energy increase. As shown in Figure 2.4, according to **k.p** theory, the effective mass of the conduction band for CdTe can be found as ~0.11m_0. Finally, band structure of the conduction band can be given as;

$$E_c(k) \approx E_g + \frac{\hbar^2 k^2}{2m_c^*} \tag{2.13}$$

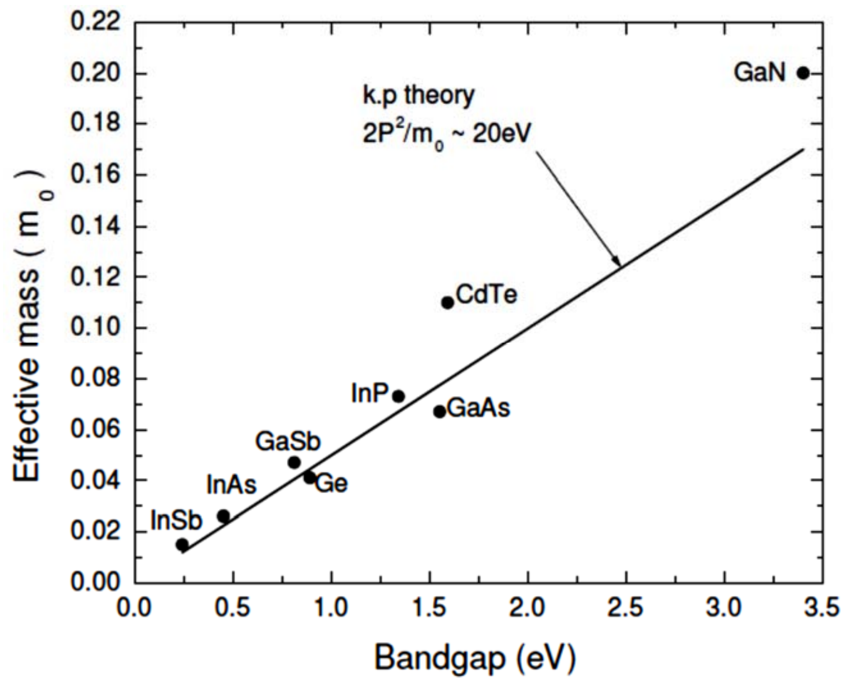

Figure 2.4. The change of conduction band effective mass with bandgap energy for some semiconductors from ***k.p*** theory

To calculate effective mass and bandstructure of the valence bands, spin-orbit (SO) interaction should be taken into consideration. SO interaction can be explained briefly as the interaction between particle's spin and its orbital angular momentum. SO coupling

directly affects the energy bandstructure which gives rise to splitting of the valence band. It is due to, the valence electrons are close to the nucleus and they move around the positively charged nucleus at relativistic speeds. The Hamiltonian for the SO interaction can be given by;

$$H_{SO} = \frac{\hbar}{4c^2 m^2}\left(\nabla\vec{V} \times \vec{p}\right).\vec{\sigma} \tag{2.14}$$

where m is electron mass, c is the speed of light, V is the electric potential, p is the momentum of electron and $\vec{\sigma} = \left(\sigma_x, \sigma_y, \sigma_z\right)$ is the vector of Pauli spin matrices. And, when the SO interaction is taken into account, equation 2.4 becomes;

$$\left[\frac{p^2}{2m} + \frac{\hbar\vec{k}\vec{\pi}}{m} + \frac{\hbar^2 k^2}{2m} + V + \frac{\hbar}{4c^2 m^2}\vec{p}.\vec{\sigma} \times \left(\nabla\vec{V}\right)\right]u_{nk} = E_{nk}u_{nk} \tag{2.15}$$

where

$$\vec{\pi} = \vec{p} + \frac{\hbar}{4c^2 m^2}\vec{\sigma} \times \nabla\vec{V} \tag{2.16}$$

Using the same results as for the case without SO interaction, the bandstructures and effective masses of four band can be obtained. For the conduction band, the band structure is;

$$E_c\left(k\right) \approx E_g + \frac{\hbar^2 k^2}{2m_c^*} \tag{2.17}$$

where the effective mass of conduction band is;

$$\frac{1}{m_c^*} = \frac{1}{m_0}\left[1 + \frac{2}{m_0 k^2}\left[\frac{1}{2}\left(\frac{k^2 p^2}{E_g}\right) + \frac{1}{6}\left(\frac{k^2 p^2}{E_g}\right) + \frac{1}{3}\left(\frac{k^2 p^2}{E_g + \Delta}\right)\right]\right] \tag{2.18}$$

where P is the Kane's matrix element ($P=8x10^{-8}$ $eV.cm$). The band structures of heavy hole, light-hole and split off can be given respectively as;

$$E_{hh}\left(k\right)=-\frac{\hbar^2 k^2}{2m_0} \tag{2.19}$$

$$E_{lh}\left(k\right)=-\frac{\hbar^2 k^2}{2m_{lh}^*} \tag{2.20}$$

$$E_{SO}\left(k\right)=-\Delta-\frac{\hbar^2 k^2}{2m_{SO}^*} \tag{2.21}$$

Effective mass of heavy hole valence band is the same as free-electron mass. And the effective mass of light-hole and split off valence band can be given respectively as [6];

$$m_{lh}^* = \frac{m_0}{1+\frac{4p^2}{3m_0E_g}} \tag{2.22}$$

$$m_{so}^* = \frac{m_0}{1+\frac{2p^2}{3m_0\left(E_g+\Delta\right)}} \tag{2.23}$$

where spin-orbit splitting energy value is 0.91 eV [4].

Bandgap value changes with the temperature. The change of bandgap energy in eVs with temperature for CdTe material is shown in Figure 2.5 and can be emprically given by;

$$E_g = 1.622 - 3.5x10^{-4}T - 1.1x10^{-7}T^2 \tag{2.24}$$

where T is the measured temperature in Kelvin.

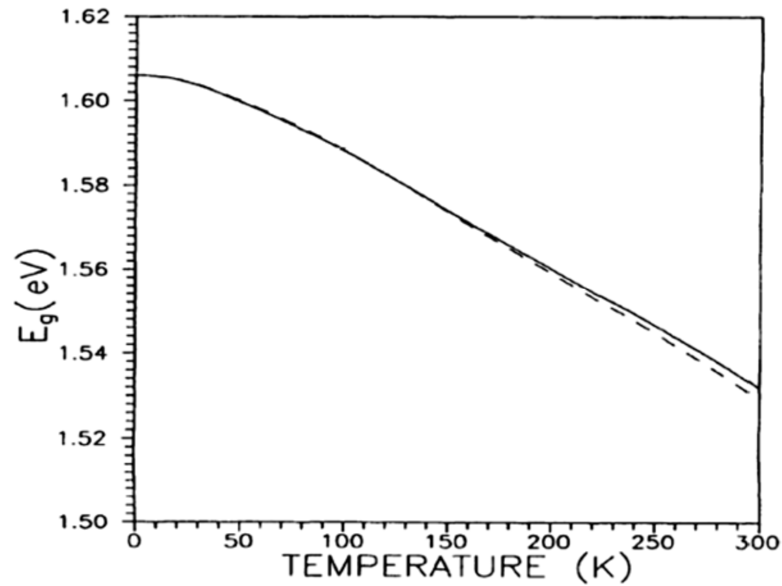

Figure 2.5. Change of bandgap energy with temperature of CdTe material where the solid line represents experimentally obtained bandgap energy and dot line represents the calculated band gap energy of CdTe [7].

2.1.2. Crystal Structure

CdTe is a II-VI compound which can be crystallize in zincblende (ZB), hexagonal and wurtzite (WZ) structures depending on the growth technique. At atmospheric pressure, bulk CdTe can be stabilized in zincblende structure. Wurtzite and especially zincblende structures are common for CdTe films. However; hexagonal structure is not certain for thin films of CdTe which depends on the substrate material grown on and its orientation [8-10]. Under the perfect growth conditions of MBE, CdTe has the cubic zincblende (sphalerite) crystal structure with the cubic space group $F\bar{4}3m$ (T_d^2) as class symbol which is short definition and $(3\bar{A}_4, 4A_3, 6m)$ as symmetry parameters in Hermann-Mauguin notation or number 216 within all 230 combined translations 3D space groups. According to Hermann-Mauguin notation; F symbolizes lattice type as Face-centered in class symbol and this structure has three 4-fold rotoinversion axes, four 3-fold rotational axes and 6 mirror planes [11].

Hybridization in diamond structure gives the zincblende structure. The zincblende structure is similar to diamond structure except that zincblende structure of CdTe has two types of atoms with equal numbers of cadmium (Cd, Group II) and tellurium (Te, Group VI) atoms while diamond structure has just one type. CdTe crystal structure has two the

face centered cubic (Fcc) lattices with one of Fcc lattice is formed by Cd atoms and the second one is formed by Te atoms. The zincblende structure of CdTe consists of two interpenetrating fcc Bravais lattices in which the coordinates of the Te atoms being (0,0,0), $(0,\frac{1}{2},\frac{1}{2})$, $(\frac{1}{2},0,\frac{1}{2})$, $(\frac{1}{2},\frac{1}{2},0)$ and the coordinates of the Cd atoms being $(\frac{1}{4},\frac{1}{4},\frac{1}{4})$, $(\frac{1}{4},\frac{3}{4},\frac{3}{4})$, $(\frac{3}{4},\frac{1}{4},\frac{3}{4})$,$(\frac{3}{4},\frac{3}{4},\frac{1}{4})$ as shown in Figure 2.6.

Cd and Te atoms are bonded to each other via ionic (heteropolar) and covalent (homopolar) bonding. In CdTe, the nearest neighbours have unequal numbers of valance electrons. CdTe has high atomic number (Z_{Cd}=48 and Z_{Te}=52). The atomic structure of Cd is kryptonlike-$4d^{10}5s^2$ and the atomic structure of Te is kryptonlike-$4d^{10}5s^25p^4$. As a result, when the Cd and Te atoms are bonded each other, they leave the net charges of Cd^{2+} and Te^{6+} on the atomic cores. On the other hand, ionic bonding between Cd and Te atoms formed when the cadmium atoms lose two electrons by forming cations (Cd^{2+}) and the tellurium atoms gain two electrons by forming anions (Te^{2-}). Changes between these bonding types can be represented by the mass of the electron cloud.

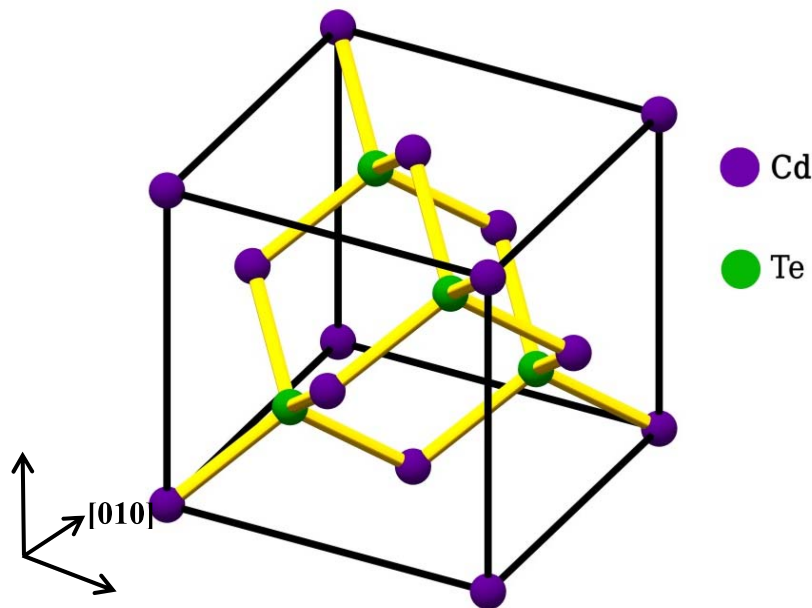

Figure 2.6. Three dimensional view of CdTe zincblende structure.

Shifting of the center of mass closer to the anion results in ionic bonding and shifting of the center of mass closer to the midpoint of electron cloud results covalent

bonding. CdTe has the largest lattice constant within all II-VI compounds. In 1960, Lawson reported the best value for lattice parameter is 6.481Å [12]. And then, in 1969, temperature dependence of CdTe lattice parameter have been found empirically by William *et al.* which is given by this equation:

$$a_t = 6.4802 + \left(31.94 \ x \ 10^{-6} T\right) + \left(7.55 \ x \ 10^{-9} T^2\right) + \left(9.25 \ x \ 10^{-12} T^3\right) \quad (2.25)$$

where a_t is the lattice parameter in Å and *T* is the temperature in ^{o}C. The change of CdTe lattice parameter with the temperature is given in Table 2.1 for both calculated and measured values [13]. The binding energy depends on the ionicity of the material. For most covalent tetrahedral structures, the binding energy decreases with increasing ionicity. The Phillips ionicity of CdTe is the highest value for any of the II-VI compounds, whose ionicity is 0.717 [14]. As a consequence, CdTe has large lattice constant and a high degree of ionicity with a small binding energy among all II-VI semiconductors.

Table 2.1. The change of CdTe lattice parameter with temperature [13].

Temperature (^{o}C)	a_t (Å) Calculated Values	a_t (Å) Measured Values
20	6.4808	6.4809
110	6.4838	6.4835
132	6.4846	6.4848
206	6.4827	6.4870
238	6.4884	6.4886
305	6.4909	6.4910
315	6.4913	6.4912
382	6.4940	6.4936
420	6.4956	6.4955

2.1.3. Polar Surfaces of CdTe

Ternary and quaternary of III-V and II-VI compounds, such as CdTe, GaAs, CdZnTe, HgCdTe, etc., exhibit different chemical characteristics depending on what atom terminated at the surface and hence their surfaces are called ‘polar’. Due to having the same bonding configuration of the surfaces such as (100) and (110) for these compounds, they are called the ‘non-polar surfaces’in this case charge and atomic

composition imbalance does not occur. However, the single crystal elements such as Si and Ge do not have a polar surface.

When the surface of CdTe terminated by cation (group II, Cd,) atoms, it is called 'A' surface and if it is terminated by anion (group VI, Te) atoms, it is called 'B' surface. For example, the (211) surface of CdTe can be written as (211)A while the ($\overline{2}\overline{1}\overline{1}$)surface is called (211)B. The polar faces of (211) and ($\overline{2}\overline{1}\overline{1}$) for CdTe are shown in Figure 2.7. In (111) and (211) planes, the orientation of Cd atoms aligned by 180° across the Te atoms. (211)B oriented CdTe surface has (100) terraces and (111) step edges.

Polar surfaces are less stable, so that the top-most atoms try to make maximum number of bonds with the other atoms. As can be seen, along [111] and [211] directions Cd atoms have three bonds with Te atoms and along the opposite direction Te atoms have three bonds with Cd.

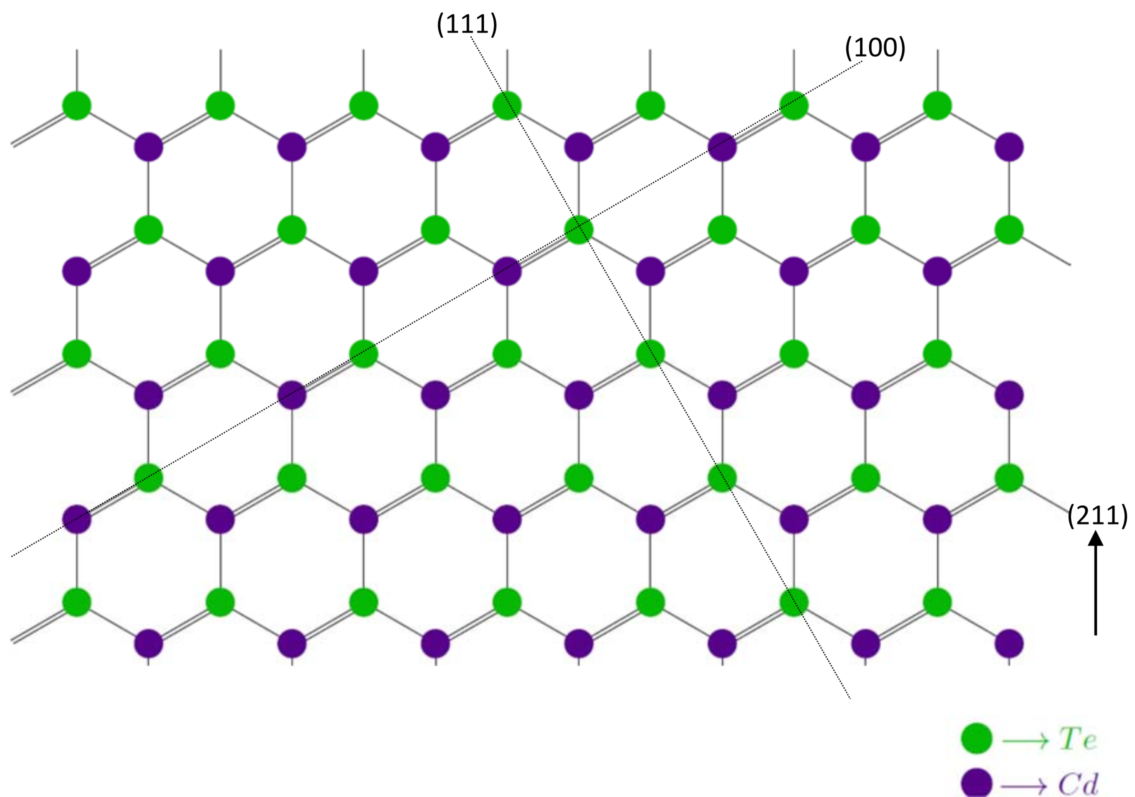

Figure 2.7. Two polar (211) and ($\overline{2}\overline{1}\overline{1}$) CdTe surfaces.

2.1.4. Optical Properties

CdTe material has a number of optical applications due to being a wide bandgap semiconductor. CdTe is a good absorber with high optical absorption coefficient $>10^4$ cm^{-1} [15]. The absorption coefficient depends on the material and strongly on the wavelength of light which is being absorbed. The absorption coefficient (α) of CdTe can be calculated as a function of incident photon energy $h\nu$ as

$$\alpha h\nu = A_0 (h\nu - E_g)^P \tag{2.26}$$

where P changes depending on whether the transition is direct or indirect and allowed or forbidden. For direct cases, P is integer. However, for indirect cases, it is rational number. For direct and allowed case; P has the value of 1/2 and for forbidden case has the value of 3/2. For indirect and allowed case has the value of 2 and forbidden case, it is 3. And in eq. 2.26, A_0 constant can be given by;

$$A_0 = \left(\frac{e^2}{neh^2 m_e^*} \right) \left(2m_r \right)^{3/2} \tag{2.27}$$

where m_e^* and m_r effective and reduced masses of charge carriers, respectively. In Figure 2.8, the absorption coefficient of various semiconductor materials are shown. And, in the 2 to 15 microns region the extinction coeffient is approximately 0.20 [16].

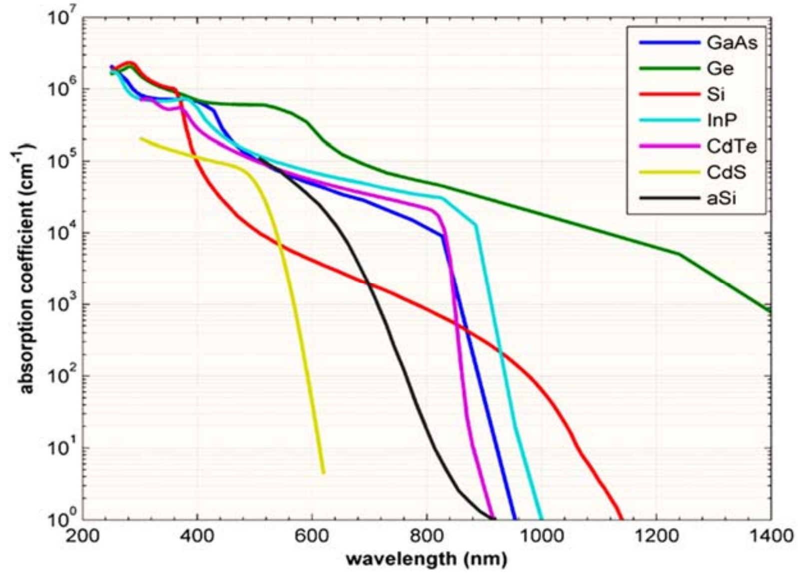

Figure 2.8. Absorption coefficients of various semiconductors at 300K [17].

When the single surface reflectance at normal incidence is taken into account, the relation between reflectivity (R), refractive index (n), and extinction coefficient (κ) can be given as

$$R = \frac{\left[(n-1) + \kappa^2 \right]}{\left[(n+1) + \kappa^2 \right]} \tag{2.28}$$

and the absorption coefficient, α, and the extinction coefficient, κ, relation is

$$\alpha = \frac{4\pi\kappa}{\lambda} \tag{2.29}$$

where λ is the wavelenght in nanometers. The complex forms of dielectric function (*ε*) and the refractive index (*n*) can be given by;

$$\varepsilon = \varepsilon_1 + i\varepsilon_2 \tag{2.30}$$

$$n_c = n + ik \tag{2.31}$$

$$n = \sqrt{\varepsilon_1 + i\varepsilon_2} \tag{2.32}$$

The measured and calculated dielectric constants at 300 K and 25 K of single-crystal CdTe by D.T.F Marple and H. Ehrenreich are shown in Figure 2.9.

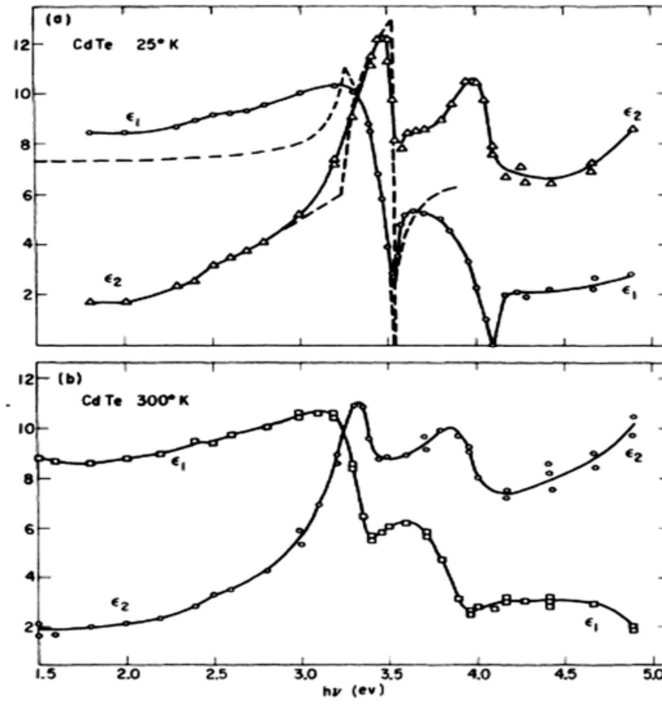

Figure 2.9. Dielectric constant ε_1 and ε_2 observed for CdTe by D.T.F Marple and H. Ehrenreich. Dashed curves are calculated values [18].

In addition, the extinction coefficient and absorption coefficients of CdTe films changes depending on the annealing temperature [19, 20]. In Figure 2.10, the change of extinction coefficient and the absorption coefficients with annealing temperature of CdTe are shown, respectively. Furthermore, refractive index value is 2.64 at 10.6 μm [21]. The reported refractive index values for CdTe material are given in Table 2.2.

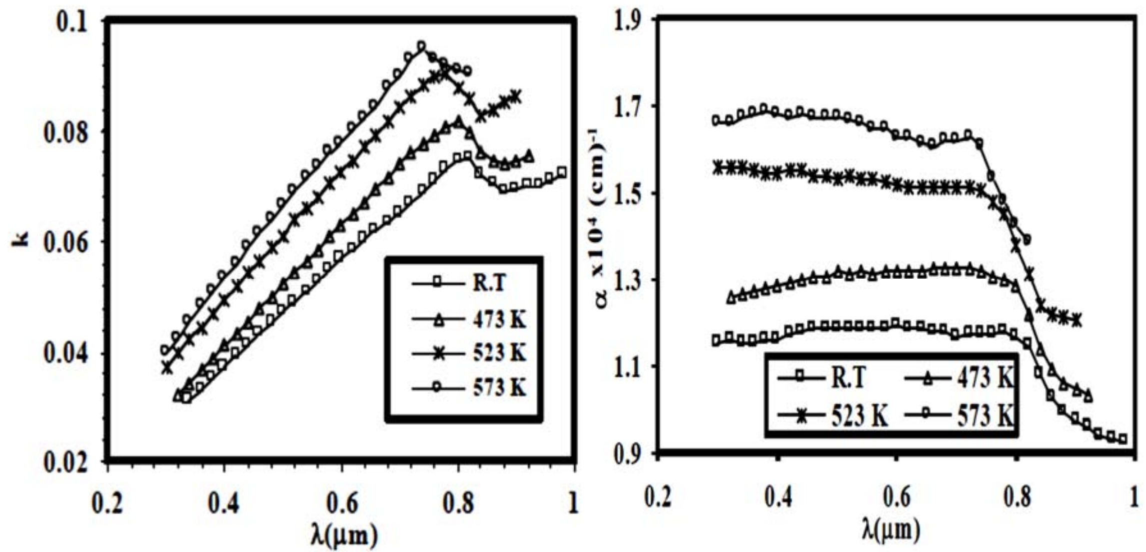

Figure 2.10. The change of (a) Extinction coefficient with the annealing temperature of CdTe films, (b) Absorption coefficients with the annealing temperature of CdTe films [20].

Table 2.2. Refractive index values for different wavelengths.

Wavelenght, λ (μm)	Refractive Index, n	Reference
0.903	3.47±0.05	[22]
1.10	3.13	[22]
1.0	2.83±0.03	[23]
1.0-1.3	3.27±0.05	[24]
7-10	2.75±0.01	[25]
10	2.81	[26]
14	2.76	[27]

2.1.4.1. Photoluminescence

The term *luminescence*, comes from *lumin* which means light in Latin, was first introduced as '*luminescenz'* by Eilhard Wiedeman in 1888 [28]. Luminescence is the phenomenon of emission of electromagnetic radiation which occurs when excited electron loses its excess energy as a photon. Luminescence is generally divided into three

classes of fluorescence, phosphorescence and delayed fluorescence depending on the duration of emission. Luminescence is called as fluorescence, if the emission of light occurs less than about 10^{-8} seconds ($\tau_c<10^{-8}$), and called as phosphorescence if the emission of light occurs higher than about 10^{-8} seconds which can take hours or days. Delayed fluorescence shows the same characteristic emission spectrum as fluorescence, but the emission of light occurs only somewhat shorter than phosphorescence. In phosphorescence, unlike fluorescence, the emission of electromagnetic radiation is delayed by traps (unoccupied states). Traps are generally formed in the forbidden gap due to the presence of defects such as lattice defects, vacant sites, irregularities in the lattice atoms and impurities. Analysis of the phosphorescence decay curves gives information about the trap levels, depths and the lifetime of carriers in the presence of the trapping states. The schematic representations of fluorescence and phosphorescence processes are shown in Figure 2.11. τ_c shows the lifetime of the excited atoms in the gaseous state.

Luminescence can be classified depending on the type of excitation. Some of important luminescence classes are photoluminescence, electroluminescence, cathodoluminescence, thermoluminescence, crystalloluminescence, triboluminescence, bioluminescence and chemiluminescence. Every luminescence process includes excitation or absorption, emission and storage of excitation energy which is lost when the electrons return to their ground state or interact with phonons. The most common luminescence type is Photoluminescence in which photons are absorbed and re-emitted by excitation of carriers to higher electronic states by exposing the material to light. The other common luminescence type is Electroluminescence. It is a process involving non-thermal emission of light due to radiative recombination of electrons and holes caused by electric field or electric current. Cathodoluminescence is also a type of an electroluminescence, but in this case the source of excitation is high-energy electrons (cathode rays). On the other hand, Thermoluminescence is emission of light due to heated material that is not the same process as black body radiation and incandescence. Chemiluminescence is the emission of light by a chemical reaction and bioluminescence is a type of chemiluminescence in which emission of light as a result of chemical reactions in living organisms. Crystalloluminescence is also a type of chemiluminescence which is generated during crystallization and used to determine the size of the crystal nucleus. Triboluminescence is not well understood process up to now, it can be described as generation of light as a result of the breaking of chemical bonds in a material [29, 30].

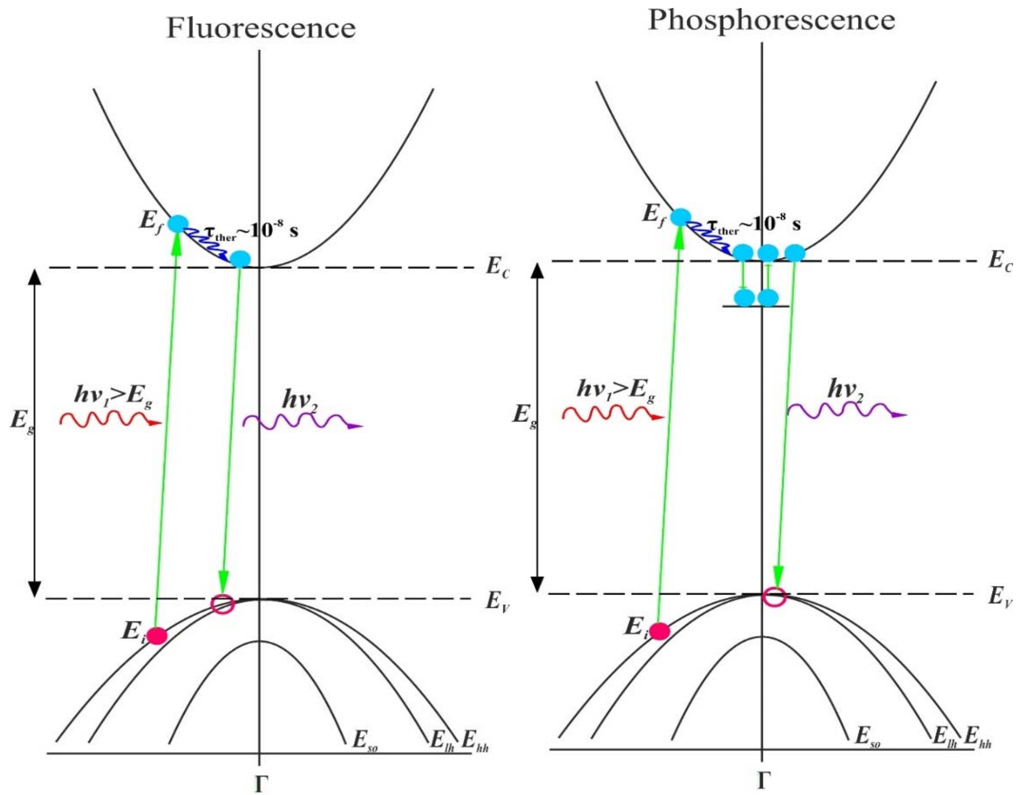

Figure 2.11. Schematic representation of fluorescence and phosphorescence processes

Photoluminescence (PL) is a non-destructive and an efficient optical characterization techique for measuring crystal quality of semiconductors, especially CdTe films. Analysis of photoluminescence emission spectrum helps to understand of recombination mechanisms, determination of band gap energy, localized defect and impurity levels and their types that affect the material quality and subsequently device performance. The first and major event in the history of photoluminescence was the publication by G. G. Stokes in 1852. In the paper of Stokes which entitled '*On the Change of Refrangibility of Light*', states that the wavelengths of the emitted radiation is equal or longer than the exciting light which is known as famous '*Stoke's law*' today [31]. However, the Stoke's law is not always valid. In some cases, the wavelengths of the emitted radiation is less than the exciting light which is known as '*anti-Stokes*'.

When material is subjected to electromagnetic radiation, the incident monochromatic photon beam can be reflected, absorbed and/or transmitted by the material. In this process, absorption of light occurs by raising of an electron from valence band up to higher energy levels within the bandgap or in conduction band. In the case of the photon has the higher energy than the bandgap of material, electron in the valence

band raise up to the higher energy levels in the conduction band and excess energy is given by electron, then electron falls back to lower energy states within the bandgap or to the valence band and photon is emitted by the material. This photon emission process is called photoluminescence. During absorption and excitation of light process, coulomb interaction between electrons and holes create electron-hole pairs (excitons). Creation of electron-hole pairs is called generation, whereas the annihilation or destruction of electron-hole pairs in which electrons and holes turn back to their equilibrium positions is recombination process. Electrons and holes can recombine energy by emitting as non-radiative and radiative emission.When material exposed to photon with higher energy than bandgap energy, photons are emitted via various radiative recombination mechanisms. However, in the case of non-radiative recombination, the excess energy due to electron-hole pair dissipates in the lattice in the form of phonons. Types of excitonic transitions, radiative and non-radiative recombination mechanisms and possible trap levels in CdTe will be detailed in this chapter.

2.1.4.1.1. Excitonic Transitions in CdTe

2.1.4.1.1.1. Free Excitons

A free electron in the conduction band and a free hole in the valence band can attract each other by Coulombic interaction and form a composite quasi-particle as a pair of opposite charges of electrons and holes named ‘exciton’. For high purity and crystal quality semiconductors, exciton is not trapped by defect or impurity which is referred as free exciton. Emitted photon energy is less than the bandgap energy by the amount of the exciton binding energy;

$$h\nu = E_g - E_x \quad (2.33)$$

E_x is the Coulomb energy of the free exciton and can be defined as;

$$E_x = E_g - \frac{2\pi^2 m_r^* q^4}{h^2 \varepsilon_0^2 n^2} \quad (2.34)$$

where E_g is the bandgap energy of the semiconductor, h is the Planck's constant, ε_0 is the vacuum permittivity constant, m_r^* is the reduced effective mass of the exciton, q is the electronic charge and n is the integer defining the various allowed states of the free excitons. Reduced effective mass of exciton is;

$$\frac{1}{m_r^*} = \frac{1}{m_e^*} + \frac{1}{m_h^*} \tag{2.35}$$

where m_e^* and m_h^* are effective masses of electrons and holes, respectively.

In eq. 2.34, the second term is the inner binding energy of exciton where binding energy of exciton has various values with the "n" number which is the numbering of discrete energy levels has for the case of the ground state n corresponds to *1*, and excited states corresponds to *2,3*,.. In addition to eq. 2.34, the binding energy of the exciton can be calculated using hydrogen model. According to this model, the allowed energy levels of a free exciton can be represented by;

$$E_x = E_g - \frac{R_H m_r}{\varepsilon_0 m_o n^2} \tag{2.36}$$

where R_H is the Rydberg constant of the hyrogen atom (13.6 eV) and m_0 is free electron mass. Exciton Rydberg constant can be defined as;

$$R_X = \left(\frac{m_r}{m_0 \varepsilon_r^2} \right) R_H \tag{2.37}$$

ε_r=10.6 is the relative permittivity constant for CdTe [32]. Calculated exciton Rydberg constant for CdTe is 12 meV [33]. And exciton Bohr radius is;

$$a_x = \left(\frac{m_0 \varepsilon_r}{m_r} \right) a_H \tag{2.38}$$

where a_H is the Bohr radius of the hyrogen atom. Exciton Bohr radius is 6.7 nm for CdTe material [33]. In addition, binding energy of excitons changes between 5 to 50 meV in a material and CdTe has the binding energy of free excitons is about 10 meV [34].

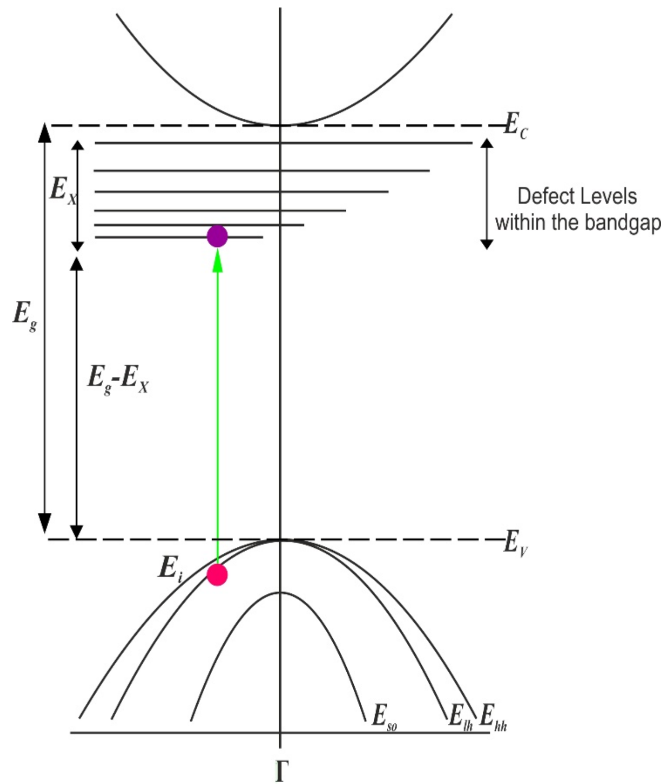

Figure 2.12. Free exciton energy levels within the bandgap energy. Green arrow show optical transition within the bandgap energy, pink and purple circles denote holes and electrons, respectively.

2.1.4.1.1.2. Bound Excitons

In a semiconductor, impurities and defects can introduce discrete electronic states called traps within the bandgap. Traps are formed if the impurity concentration is large, an overlap of the electron wavefunctions of neighboring impurity centers occur and this causes a broadening of the electron or hole levels [35]. Bound excitons are formed when exitons are trapped in these impurity levels via van der Walls interaction by neutral and ionized donors or acceptors [36]. When an exciton is trapped at an impurity or defect related state, the total energy of the system is reduced and exciton creates a photon with lower energy than free excitons. PL emission spectrum of bound excitons are important to characterize defects and impurities in a material. In this case, the photon emission decreases with the binding energy of the exciton to the defect (E_B);

$$hv = E_g - E_X - E_B \tag{2.39}$$

The first cosideration of possible formation of excitons was by Lampert [37]. After his study, large number of calculations of bound excitons were carried [38, 39]. Depending on whether the trapped location of excitons, bound excitons are called as donor-bound or acceptor bound. Generally, bound excitons can be classified as; excitons bound to neutral donors (D^o, X), excitons bound to neutral acceptors (A^o, X), excitons bound to ionized donors (D^+, X) and excitons bound to ionized acceptors (A^-,X). (D^o,X) contains a donor ion, two electrons and a hole; (D^+,X) contains a donor ion, an electron and a hole; (A^o,X) contains an acceptor ion, an electron and two holes and (A^-,X) contains a acceptor ion, an electron and a hole.

However, there cannot exist simultaneously both (D^+, X) and (A^-, X). The detection of these two PL emission bands depends on the ratio of electron and hole effective masses (m_e/m_h). (D^+, X) emission band can be observed when the ratio of the electron and hole effective masses is lower than 1.4. Additionally, the observation of (A^-, X) is possible when masses ratio is higher than the 1.4 [36, 40]. For CdTe, if accepted the electron effective mass and hole effective mass values are $0.11m_0$ and $0.4m_0$, respectively, the effective mass ratio becomes 0.28 [41]. Therefore, it is likely observe (D^+, X) PL emission band in CdTe. In general, the observation of (A^-, X) is not possible for any given material, because hole is usually heavier than the electron [42].

Bound exciton PL emission energies for various donor and acceptor impurities and their binding energies in CdTe is shown in Table 2.3. In the literature, acceptor impurity atoms related (A^o, X) emission lines in bulk CdTe reported in the range of 1.588-1590 eV [43]. However, when CdTe is grown on GaAs, As from the substrate can incorporate into CdTe epilayers as As_{Te}. Unlike to bulk CdTe, arsenic related (A^o, X) emission line should be observed at 1.5897 eV [44]. In addition to incorporation of arsenic in (211)B CdTe/(211)B GaAs, Ga diffusion in CdTe epilayers can form a defect which gives emission composed of free exciton recombination and electron-hole recombition at 1.594 eV [45].

Table 2.3. Bound exciton PL amission band energies for donor and acceptor impurities in CdTe [43, 46]

Donor	(D°,X) (eV)	ε_B (meV)	ε_D (meV)
F	1.59314	3.36	13.67
Ga	1.59309	3.41	13.88
Al	1.59305	3.46	14.05
In	1.59302	3.48	14.15
Cl	1.59296	3.54	14.48
I	1.5927	3.8	~15.1
Acceptor	**(A°,X) (eV)**	**ε_B (meV)**	**ε_A (meV)**
O	-	-	46
N	1.5892	7.2	56.0
Li	1.58923	7.17	58.0
Na	1.58916	7.24	58.7
As	1.58970	6.70	92.0
Ag	1.58848	7.92	107.5

2.1.4.1.2. Radiative and Non-Radiative Recombination Mechanisms

2.1.4.1.2.1. Band to Band Transition

Band to band transition is a radiative transition which generally can used for estimation of bandgap energy (E_g) of direct semiconductors. For a direct bandgap semiconductor, the energy of the emitted photon in a (e, h) transition is given by;

$$h\nu = E_f - E_i \tag{2.40}$$

where energy of the emitted phonon energy in (e, h) transition equals to the difference between the excited and ground states. In direct transition process, photon emission is equal or higher than the bandgap energy. Because, elecron-hole pairs can jump to excited states in the conduction band when exposed to higher energy photons than bandgap energy. This transition type is less probable to observe for indirect semiconductors because electrons in the conduction band need a change in momentum to fall into the valence band. In the case of indirect emission of photons, a creation of phonons and for the case of absorption process, destruction of phonons occur with frequency Ω and has much weaker intensity than direct transition. In this case, emitted photon energy with a phonon contribution ($h\Omega$) can be given as;

$$h\nu = E_f - E_i \pm h\Omega \tag{2.41}$$

In Figure 2.13, schematic representation of direct and indirect transition process is shown. Luminescence intensity of (e, h) recombination can be expressed by**;**

$$I_{PL} = A\sqrt{h\nu - E_g}\, e^{-\left(h\nu - E_g\right)/kT} \tag{2.42}$$

Luminescence intensity can be defined for free excitons at ground (n=1), x1, and first excited (n=2) states, x2, as;

$$I_{PL} = Ce^{-(h\nu - E_{X1})/kT} e^{-(h\nu - E_{X1})^2/2\sigma^2} \tag{2.43}$$

$$I_{PL} = Be^{-(h\nu - E_{X2})^2/2\sigma^2} \tag{2.44}$$

where hv is the emitted photon energy, E_g is the bandgap of CdTe, A, B and C are constants, σ is the temperature dependent standart deviation for Gaussian line shapes, k is Boltzmann constant, T is temperature in Kelvin, and E_{X1} and E_{X2} are free exciton at ground and first excited state recombination energies, respectively. Free-exciton binding energy is given before as 10 meV for CdTe. In addition, ground state binding energy of exciton is E_{X1}=1.503 eV and first excited binding energy of exciton is E_{X2}=1.5105 eV. Bandgap energy of CdTe is 1.513 eV at high temperatures [47, 48].

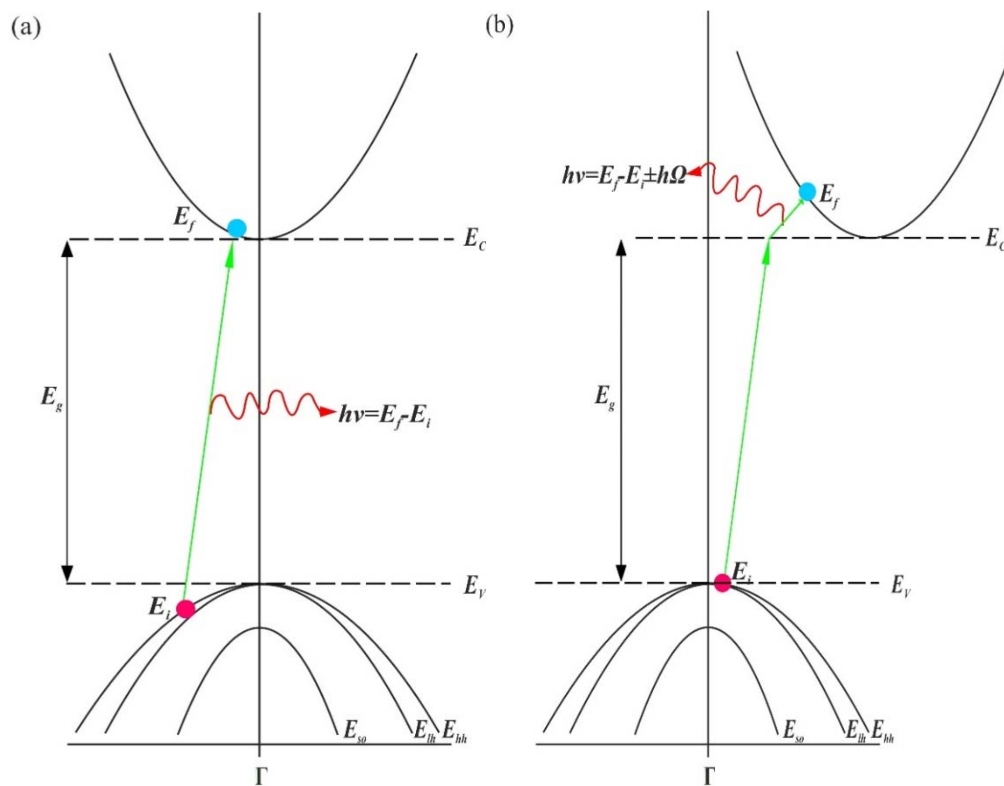

Figure 2.13. Schematic representation of band to band transitions in semiconductors for (a) diret and (b) indirect bandgaps. Blue circles and pink circles represent electrons and holes, respectively.

2.1.4.1.2.2. Donor-Acceptor Pair Transition

If a semiconductor contains simultaneously both donor and acceptor impurities, Coulomb interaction between donor and acceptor impurities can form pairs. In this case, electrons and holes are intercepted by ionized donor (D^+) and acceptor (A^-) and forms neutral donor (D^o) and acceptor (A^o). This transition is called donor-acceptor pair (DAP) emission. This radiative recombination can be represented by;

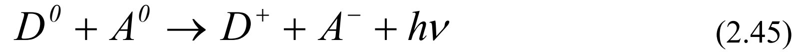

$$D^0 + A^0 \rightarrow D^+ + A^- + h\nu \tag{2.45}$$

and, the energy of the emitted photon in a DAP transition can be given by;

$$h\nu = E_g - E_A - E_D + \frac{e^2}{4\pi\varepsilon_0\varepsilon R} \tag{2.46}$$

where E_g is the bandgap energy, E_A is the acceptor ionization energy, E_D is the donor ionization energy, e is electronic charge, ε is the dielectric constant of the material, ε_o is the vacuum permittivity constant and R is the distance between the donor and acceptor pair. At high excitation intensities, most donors and acceptors are excited and distance between donor and acceptor pair becomes closer. As the pair distance decreases emission inceases due to high Coulomb interaction. In addition, as the pair distance increases, less overlap between electron and hole wavefunctions occurs with a lower transition probability. In this case, transition occur at longer lifetimes. Therefore, DAP emission line shifts to higher energies with increasing intensity of excitation light [49].

The power and time dependent PL experiments are helpful to understand whether a transition is DAP or not. In time-dependent PL experiments, emission band intensity shifts to lower energies as time elapses. However, in power-dependent PL experiments, as the excitation power increases, peak energy moves to higher energies due to saturation of distant donor-acceptor pairs. In addition, in time-dependent PL experiments, as the sample temperature increases shallow donor and acceptors become ionized which results in recombination of (D^o, h) or (e, A^o). The evolution from DAP to the corresponding recombinations with temperature of CdTe thin films will be discussed later.

Generally, DAP emission line is in the energy range from 1.4 to 1.55 eV for CdTe. In literature, the observed DAP band is related to Ga_{Cd} donor (E_D=14 meV) and As_{Te}

acceptor (E_A=92 meV) occur at 1.51 eV in bulk and CdTe films for grown on GaAs substrates. In addition, the shift of DAP emission band can be observed with increasing intensity of excitation source or excitation occured for longer time causes heating of the sample to 1.587 eV [43-45].

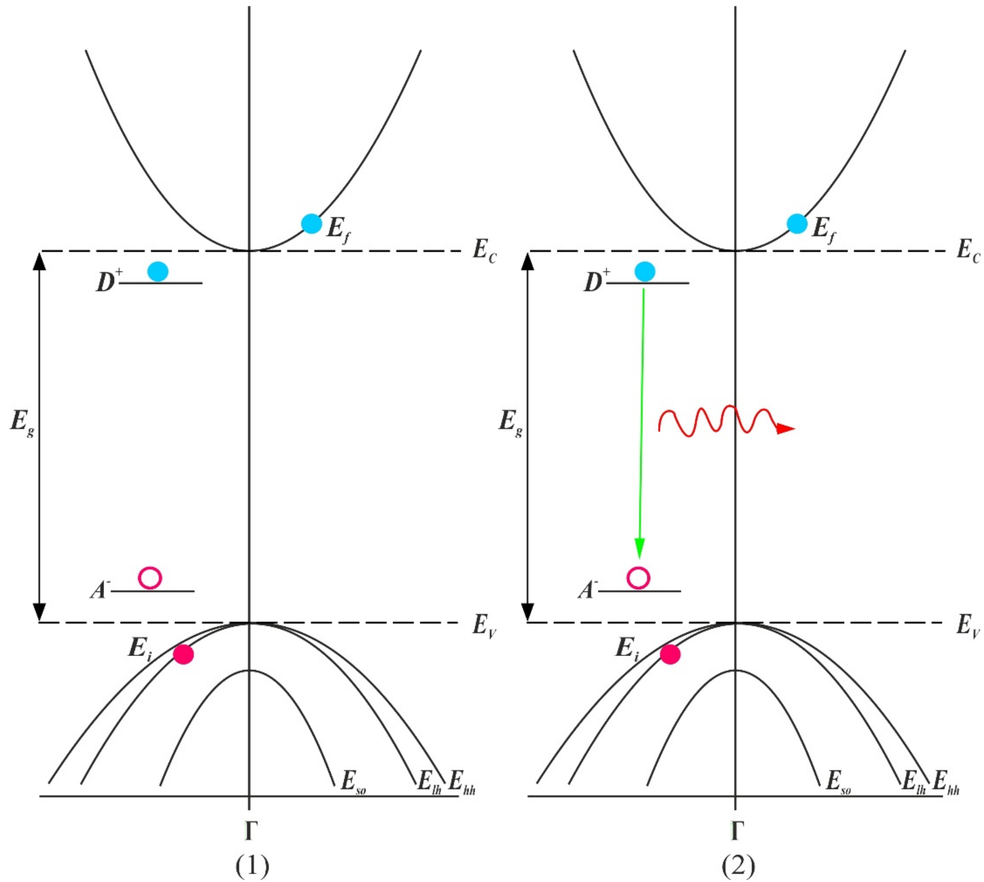

Figure 2.14. Schematic representation of (1) before and (2) after donor-acceptor pair transition; blue and pink circles denote electrons and holes, respectively. Hollow circles represent unoccupied states.

2.1.4.1.2.3. Free to Bound Transition

Free to bound transition are consist of radiative or non-radiative recombination of free electrons with trapped holes on neutral acceptor levels (e, A^o) or recombination of free holes with trapped electrons on neutral donor levels (D^o, h). In this case, the emitted photon energy from the transition of donor impurity level to valence band (D^o, h) is;

$$h\nu = E_g - E_D \tag{2.47}$$

and from the transition of conduction band to acceptor impuriy level (e, A^o) is;

$$h\nu = E_g - E_A + \frac{1}{2}k_B T_e \tag{2.48}$$

where E_g is the bandgap energy, E_D is the ionization energy of the donor impurity, E_A is the ionization energy of the acceptor impurity, k_B is the Boltzmann's constant and T_e is the temperature of electron. The term $(1/2)k_B T_e$ comes from the population distribution of electrons and density-of-states function in the conduction band [50]. In this transition type, phonon-assisted transitions can also be observed. In this case, the emitted photon energy with a phonon contribution ($h\Omega$) from the transition of donor impurity level to valence band (D^o, h) becomes;

$$h\nu = E_g - E_D - h\Omega \tag{2.49}$$

In addition to free cariers and ionized impurity recombinations, excitons can also bound to ionized impurities ((D$^+$, X), (A$^-$, X)), as mentioned above. The relation of binding energies between both free to bound recombinations can be given by [5];

$$E_{(D^+,X)} + E_X = E_{(D^0,h)} + E_D \tag{2.50}$$

where $E_{(D^+,X)}$ and E_D are binding energies of (D^o, h) and that of the electron to the donor ion.

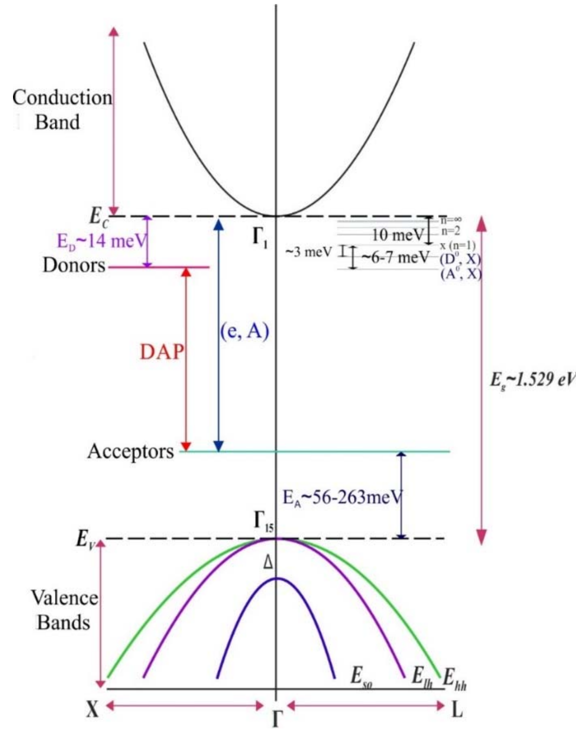

Figure 2.15. Representation of various radiative transitions in CdTe.

2.1.4.1.2.4. Phonon-Assisted Recombinations (Exciton-Phonon Interaction)

In some cases, phonons must be involved to provide momentum conservation in transitions in direct or indirect semiconductors. This transition type is generally observed for free excitonic transitions to satisfy the momentum conservation in both the optical and acoustic modes and observed as combinated emission bands. For low temperature PL experiments phonon replicas are resolved. However, for high temperature PL experiments, the phonon replicas blend into one broad peak. At low temperatures, intensity of phonon-assisted transition can be given by [45, 51];

$$I\left(hv-nE_{LO}\right)=e^{-S}\frac{S^{n}}{n!}g\left(E_{0}-n\hbar w_{LO}-E\right) \tag{2.51}$$

where hv is the zero-phonon transition energy, E_{LO} is the energy of radiative transition involving LO lattice vibration, S is the Huang-Rhys factor, g is the line shape of the transition, ω_{LO} longitudinal optical phonon frequency and n is the number of phonons

emitted. For CdTe, frequency of first-order optical phonon mode is in the range of 168-170 cm^{-1} [14, 52]. To determine PL emission band of free exciton recombination, first-order longitudional phonon (LO) replica of free exciton should be taken into account. LO phonon energy (E_{LO}) in CdTe is 21.3 meV. At low temperatures, free exciton recombination occurs at 1.5964 eV which is the ground state emission of free exciton in undoped CdTe [53]. As seen in Figure 2.16, the zero LO replica of free exciton shifts from absorption line by Boltzmann factor to lower energy and first and second order phonon replicas shift to the higher enery by (2/3)kT and (1/2)kT at low temperatures, respectively. However, PL emission of excited state of free exciton does not shift [36]. In addition, first order phonon replica of excited state of free exciton (X-1LO) is at 1.6038 eV and second order phonon replica of free exciton (X-2LO) is at 1.574 eV [53] .

For PL emission between 1.45 and 1.49 eV in CdTe, Huang-Rhys factor is higher than 1. In this range, the reported DAP emission due to Ag_{Te} is at 1.492 eV with S=1 and Cu_{Cd} is at 1.45 eV with S=2 [54]. However, emission band at 1.47 eV for (211)B CdTe/(211)B GaAs layers has low Huang-Rhys factor with S=0.4 corresponding structural defects [45, 54]. In literature, the observation of 1.47 eV emission band is also reported by CdTe epilayers grown on InSb and sapphire substrates [54, 55]. However, the reported S factor for the epitaxial growth of CdTe on InSb substrate is 0.2 which has much lower value than the epitaxial CdTe/GaAs films [54]. It can be concluded that 1.47 eV emission band is not specific to growth of CdTe on GaAs, it is defect related emission band as a result of epitaxial growth.

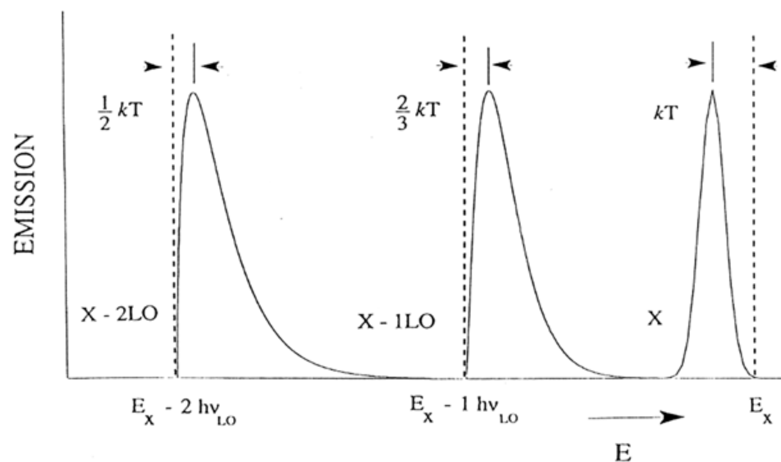

Figure 2.16. Zero, first and second order LO replica shifts of free exciton away from absorption lines [53].

2.1.4.1.2.5. Auger Recombination

Auger recombination is a tree-particle Coulomb interaction where electron-hole pairs are recombined and the excess energy is transferred to a third carrier in either conduction band or valence band. After the interaction, third carrier loses its excess energy to phonons. There are ten types of photon-less Auger recombination mechanisms which are common for semiconductor materials [56]. However, for wide-bandgap semiconductors such as CdTe, this non-radiative recombination type is not dominant.

The probability of Auger recombination depends on carrier concentration and doping density in a given material. Depending on the carrier concentration, Auger recombination consists of electron-electron-hole (n-type) or electron-hole-hole (p-type) interactions. n and p-type Auger mechanisms generally called respectively as Auger-1 and Auger-7 recombinations which are both most probable Auger recombination mechanisms within whole Auger mechanisms. Figure 2.17 illustrates shematic diagrams of Auger-1 and Auger-7 recombination processes. Auger-1 consists of recombination of a heavy-hole and an electron in the heavy-hole valence band. After the recombination of electron and hole, electron transfers its excess energy to another electron in the conduction band which excites to higher energy state in the conduction band. In Auger-7, an electron in the conduction band and a heavy-hole recombines in the heavy-hole valence band and excess energy transfered a hole in the light-hole valence band which excites to heavy-hole valence band.

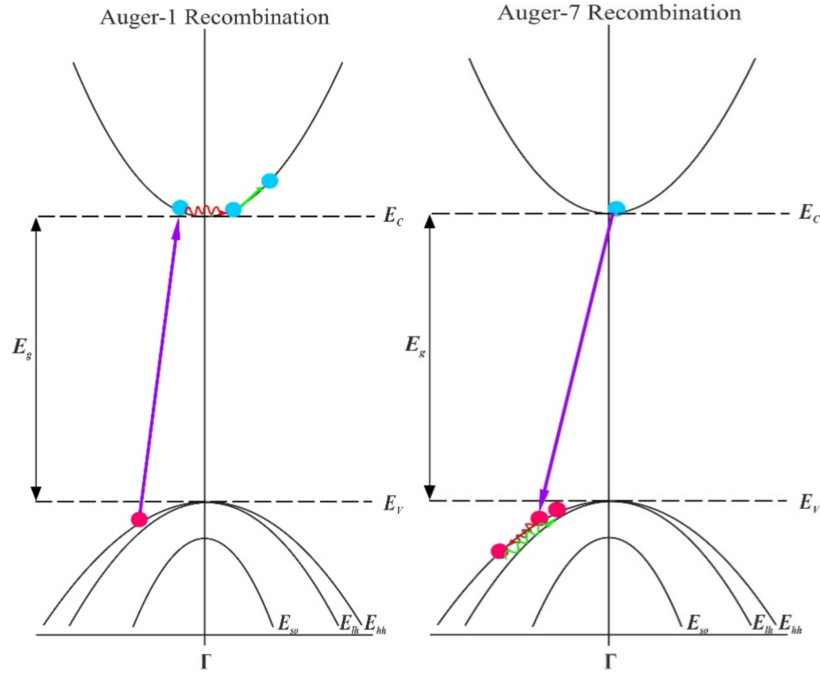

Figure 2.17. Schematic representation of Auger-1 (left) recombination and Auger-7 recombination (right); blue and pink circles denote electons and holes, respectively.

The recombination rates for n-type and p-type can be given respectively as [57];

$$U^{n}_{Auger} = C_n \Delta p N_D^2 \tag{2.52}$$

$$U^{p}_{Auger} = C_p \Delta n N_A^2 \tag{2.53}$$

C_n and C_p are Auger coefficients for n-type and p-type doped material which changes with a given material, Δn and Δp are density of electrons and holes in excess per unit volume for n-type and p-type doped material, and N_D and N_A are donor and acceptor doping concentration. And, Auger lifetimes in the case of low and high injections are given respectively as;

$$\tau^{low}_{Auger} = \frac{1}{C_n N_D^2} \;,\; \tau^{low}_{Auger} = \frac{1}{C_p N_A^2} \tag{2.54}$$

$$\tau^{high}_{Auger} = \frac{1}{C_a \Delta n^2} \;,\; C_a = C_n + C_p \tag{2.55}$$

where C_a is the ambipolar Auger coefficient. As seen in equations 2.54 and 2.55, the Auger lifetime highly depends on the carrier consentration; it decreases as carrier concentration increases in both low and high injection cases.

2.1.4.1.2.6. Shockley-Read-Hall Recombination

The Shockley-Read-Hall (SRH) recombination involves the recombination of electron-hole pairs via defect levels within the bandgap energy for a given material and excess energy released via photons. This localized defect states can either be crystallographic imperfections or impurities. The theory of this non-radiative recombination type was first developed by Shockley and Read [58], and Hall [59]. SRH recombination is an important process to determine carrier lifetimes for semiconductors. SRH has four possible transition of electrons and holes. Figure 2.18 shows the four probable SRH recombinations. Trap can be neutral, positively charged or negatively charged state. If the trap state is neutral, it can capture an electron from conduction band or capture a hole from valence band. If the trap state is negatively charged, emission of electron can be occured to the conduction state. If the trap state is positively charged, emission of hole can be occured to valence band.

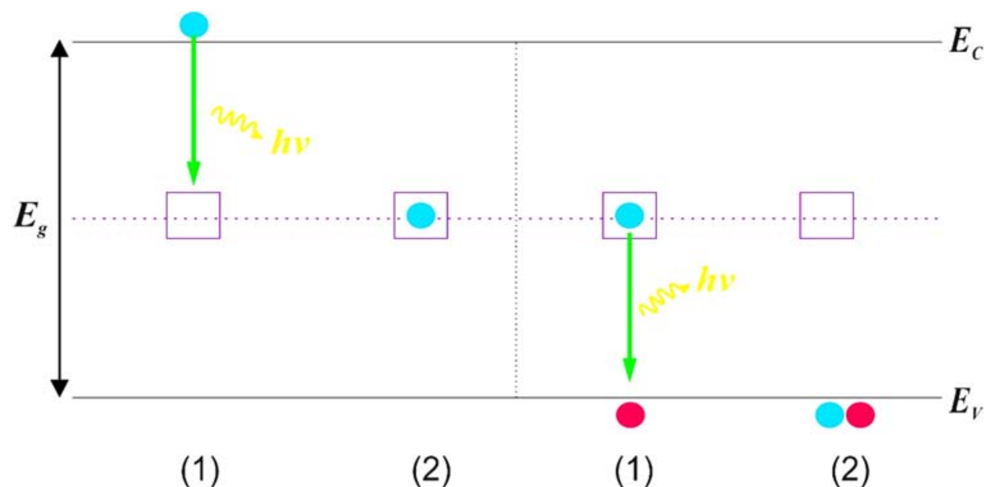

Figure 2.18. Schematic representation of (1) before and (2) after Schockley-Read-Hall recombination processes. Blue and pink circles denote electrons and holes, respectively.

In SRH recombination, for steady-state condition the net recombination rate can be given by [60];

$$U_{SRH} = \frac{(np - n_i^2)}{\tau_{p0}\left(n + n_1\right) + \tau_{n0}\left(p + p_1\right)} \tag{2.56}$$

where τ_{p0} and τ_{n0} are respectively minority hole lifetime for n-type semiconductor and minority electron lifetimes for p-type semiconductor and can be described by;

$$\tau_{p0} = \frac{1}{C_p N_t} \tag{2.57}$$

$$\tau_{n0} = \frac{1}{C_n N_t} \tag{2.58}$$

where N_t is the trap density, C_p and C_n are respectively hole and electron capture coefficients. In addition, n_1 and p_1 denote electron and hole densities, n_0 and p_0 are electron and hole concentrations at equilibrium, E_f is Fermi level and E_t is trap level,

$$n_1 = n_0 e^{\left(E_t - E_f\right)/k_B T} \tag{2.59}$$

$$p_1 = p_0 e^{\left(E_f - E_t\right)/k_B T} \tag{2.60}$$

And, carrier lifetime in SRH process can be described by the following;

$$\tau_{SRH} = \frac{\tau_{n0}\left(p + p_1\right) + \tau_{p0}\left(n + n_1\right)}{n + p} \tag{2.61}$$

2.1.4.1.2.7. Surface Recombination

Surface recombination is a type of SRH recombination. However, unlike SRH recombination, the trap states in surface recombination distributed various energy levels within the bandgap. Discontinuity of crystal lattice which forms unsaturated surface (or dangling) bonds causes an increase of active defect levels on the surface or near the surface of semiconductor. Surface passivation ensures the reduction of the number of

dangling bonds and hence surface recombination. In the process of surface passivation, a layer is grown on top of the semiconductor surface to eliminate dangling bonds and to passivate the localized surface states in the bandgap. The surface recombination rate depends on the electron and hole recombination velocities, carrier diffusion coefficient and semiconductor thickness [61]. For a surface with no recombination, the movement of minority carriers towards surface is zero. The surface recombination rate can be given by [62];

$$U_{SRH}^{surface} = \frac{np - n_i^2}{\left(\frac{n + n_1}{\nu_p}\right) + \left(\frac{p + p_1}{\nu_n}\right)} \tag{2.62}$$

where ν_n and ν_p are the electron and hole surface recombination velocities, respectively and, n_1 and p_1 are the same for the single localized state condition (SRH recombination).

2.1.4.1.2.8. Total Recombination Lifetime

For a given material, radiative and non-radiative recombination mechanisms can happen simultaneosly. In this case, total recombination mechanisms called effective lifetime for a material (τ_{eff}) can be obtained from the independent lifetime of each recombination;

$$\frac{1}{\tau_{eff}} = \frac{1}{\tau_{radiative}} + \frac{1}{\tau_{Auger}} + \frac{1}{\tau_{SRH}} + \frac{1}{\tau_{Surface}} \tag{2.63}$$

2.2. CdTe Growth Techniques

Compared to other semiconductors, CdTe is suitable material for many applications. Its high average atomic number of 50, wide bandgap, high absorption coefficient in the visible range of the solar spectrum and preparation in n-type and p-type forms, makes it convenient material for optoelectronic devices such as x-ray detectors, γ-ray detectors and solar cells [63]. In addition, CdTe demonstrates an excellent buffer layer

characteristic and can be used as a substrate for fabrication of HgCdTe-based infrared (IR) detectors and focal-plane arrays (FPAs) [64]. Due to wide range of applications, bulk and epitaxial growth of CdTe material has great interest for years. In this part, commonly used bulk and epitaxial growth techiques will be briefly introduced for the growth of CdTe material.

2.2.1. Bulk Crystal Growth Techniques

Bulk growth of CdTe includes growth from melt, solution, vapor phase and solid state. The most widely used growth techniques from melt are Bridgman, Zone refining and Czochraski methods. Traveling heater method can be given as an example of solution growth. Physical vapor and chemical vapor transport techniques are vapor growth methods and growth in solid state includes solid state recrystallization for the growth of bulk CdTe.

In both melt and vapor growth techniques, CdTe is molten to get compact ingots. Thus, in order to grow high quality film and bulk crystal of CdTe, it is important to understand the phase diagram. Melting point is 1092 ^{o}C for CdTe and gives %50 Te solid composition at this temperature. Melting points for Cd and Te are 320.9 ^{o}C and 450 ^{o}C, respectively. Phase diagram of CdTe is given in Figure 2.19. Due to high melting point of CdTe, crystal growth from the vapor or Te-rich solutions at lower temperatures are alternative methods to avoid high temperatures.

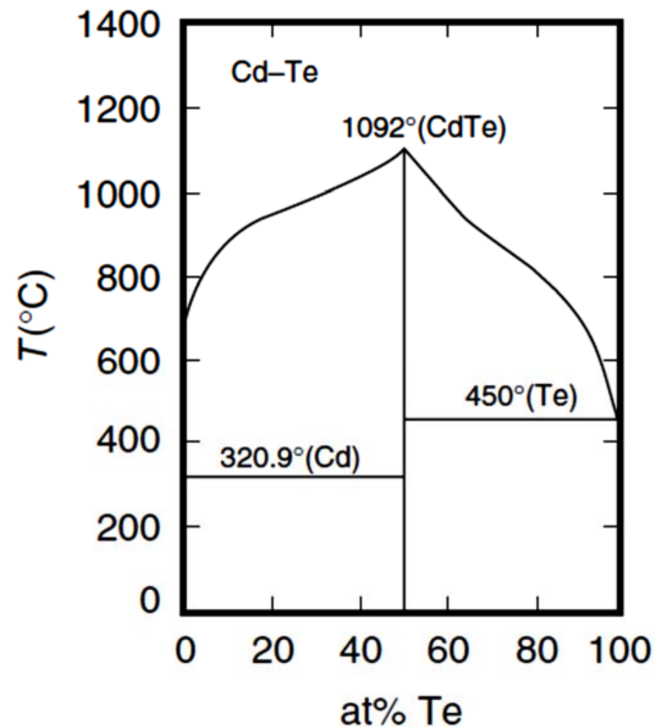

Figure 2.19. Cd-Te binary phase diagram [2].

2.2.1.1. Bridgman Method

The Bridgman growth technique was developed in 1925 by P.W. Bridgman [65]. The Bridgman method is most extensive method for the growth of II-VI wide-bandgap semiconductors such as CdTe, ZnTe and ZnSe crystals. The Bridgman technique have two different geometries as vertical and horizontal depending on configuration of the crucible. These two versions of Bridgman's method called as Vertical Bridgman method (Bridgman-Stockbarger technique), if material is placed in a vertically mounted tubular furnace, and called as Horizontal Bridgman method (Chalmer's technique), if material is placed in a horizontally mounted tubular furnace. Figure 2.20 is a schematic illustration of a Vertical Bridgman (VB) growth technique. In both cases, the system consists of three heating zones (solidification zone, melt zone and vapor pressure control zone) controlled individually and the material is placed in a glass, silica or quartz ampoule. After melting the material, it is gradually moved to colder zone (solidification zone).

The growth of bulk CdTe by Bridgman method consists of Cd and Te elements which are loaded generally into a fused silica or quartz ampoule. The furnace is heated to above melting point of CdTe and elements inside the ampoule begin to melt which lead

to a chemical reaction between the elements and formation of the CdTe material. Liquid of the material passes through colder part of the ampoule (solidification zone) in which the material is in solid phase. Once the material is solidified, it is cooled down to room temperature and the growth of bulk CdTe accomplished.

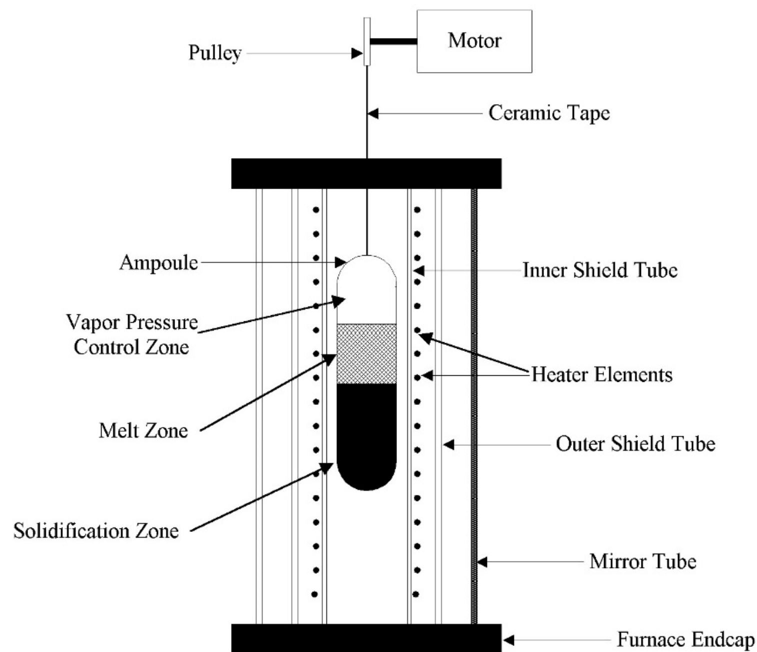

Figure 2.20. Schematic illustration of a Vertical Bridgman (VB) method [66].

On the other hand, CdTe Bridgman growth has not been very successful so far due to lack of homogenization which leads to grain boundaries and twins. To overcome defects in bulk CdTe, N.R. Kyle developed ‘modified Bridgman technique’ [67]. In modified Bridgman technique, the overheated melt is seperated from the seed crystal by a baffle and during the formation of the material, the furnace is oscillated by a transverse axis. Baffle between the heating zones controls temperature fluctations. Oscillation process is called as accelarated crucible rotation technique (ACRT) which reduces the segregation of metals inside the ampoule providing homogenization [68]. In addition to ACRT method, a coupled vibrational stirring method was applied to the Vertical Bridgman growth of CdTe in which low amplitude (0-100 Hz) mechanical vibrations applied to the ampoule. Despite improving homogenization, this technique decreased crystal quality [69].

In addition, to enable a better control of the stoichiometry several versions of Bridgman process such as low pressure and high pressure Bridgman techniques have been reported. The higher Cd vapor pressure than Te_2 causes the loss of Cd during crystal growth which causes Te-rich growth even if both Cd and Te are stoichiometric. The growth of semiconductor crystals under inert gas pressure by Bridgman method (High Pressure Bridgman, HPB) has become popular especially for bulk CdTe and CZT to loss of Cd during growth or to dope CdTe with shallow donors [70]. However, some studies showed that CdTe grown by HPB technique still lead to Cd loss and the incorporation of large concentration of Te precipitates and inclusions [71]. On the other hand, the growth of good quality CdTe crystal by low pressure Bridgman technique (LPB) occur under small excess tellurium which reduces Te precipitates and inclusions when compared to HPB [72].

2.2.1.2. Czochralski Method

The Czochralski method was first developed by Jan Czochralski in 1916. He invented this method when measuring the crystallization velocity of metals and published his study in 1918 [73]. However, Czochralski technique did not become widely known until Teal to grow 203 mm long and 19 mm diameter germanium (Ge) [74]. The Czochralski growth method is based on the crystallization by pulling from the melt. In this method, a seed crystal is attached on a rod and dipped into the molten material. Molten material is contained in a heated cylindrical crucible. And then, large oriented crystalline ingots are obtained by rotating and pulling rod upwards. Schematic illustration of a Czochralski growth method is given in Figure 2.21. However, this bulk growth technique is not suitable for CdTe growth due to high Cd vapor pressure. In order to minimize the vapor losses for the growth of CdTe at temperatures of about 1100 ^{o}C, the most widely used technique is liquid encapsulation technique (LEC) in which the melt is encapsulated with boric oxide (B_2O_3).

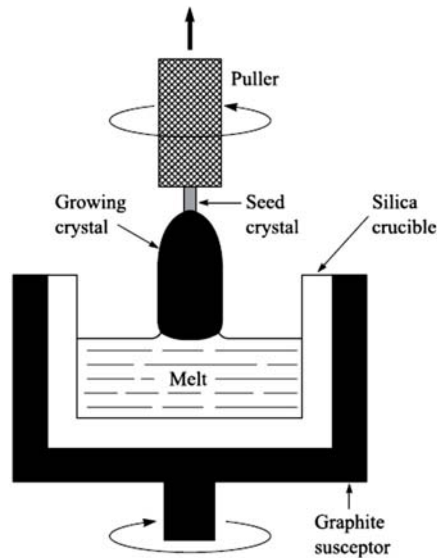

Figure 2.21. Schematic illustration of a Czochralski method [75].

LEC technique prevents the evaporation of volatile elements and generally used for growth of III-V semiconductors such as GaP, InP and GaAs [76-78]. However, the growth of CdTe by LEC method exhibits low angle grain boundaries, lamellar twins, dislocations and precipitates [79].

2.2.1.3. Traveling Heater Method (THM)

Traveling Heater Method (THM) was first developed by Weinstein and Mlavsky in 1962 [80]. THM is a preferred growth technique for bulk CdTe due to possibility grow at lower temperatures compared to other bulk growth methods which reduces contamination and vapor pressure related problems. Generally, the system consists of an ampoule at the bottom and it is surmounted by an appropriate amount of solvent material. Ampoule with solvent material is then placed in a furnace which surrounded by a heater. The growth temperature and the amount of the solvent depends on the phase diagram of the material. Growth of bulk CdTe by THM is based on the use of cadmium rod in an ampoule which is surrounded by Te pieces and powder. The furnace can be vertical or horizontal and the ampoule can be stationary or rotating about its horizontal or vertical axis depending on the configuration. The operating temperature is below melting point of CdTe. After

melting both Cd and Te elements, the ampoule or the heater around the ampoule is moved through the lower temperatures to get molten zone.

However, the growth of large crystal CdTe and CdZnTe could not obtained by THM, because, for large diameters (typically in excess of 25 mm diameter), undesirable composition and defects can occur [81]. To overcome limitations in quantity, cold-Traveling Heater Method (CTHM) and sublimation-Traveling Heater Method (STHM) has been developed. Two types of THM (Cold and Sublimation THM) is illustrated in Figure 2.22. In cold-THM, cylindrical rod of cadmium is placed in tellurium pieces and dissolved in the solvent. In sublimation-THM, molten zone in THM is replaced by empty space and source material is moved relative to the heater. Temperature difference between two zones allows the continuous growth over long distances [82].

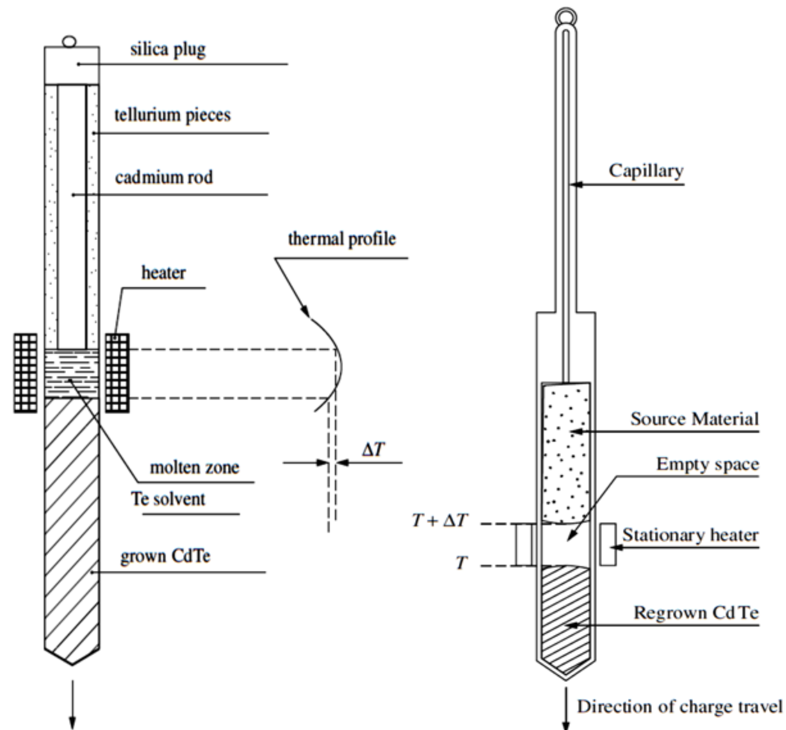

Figure 2.22. Schematics of (a) Cold Traveling Heater Method (CTHM) and (b) Sublimation Traveling Heater Method (STHM) [83].

2.2.2. Epitaxial Growth Techniques

In addition to bulk growth of CdTe, most widely used growth techniques are epitaxial techniques. These are Molecular Beam Epitaxy (MBE), Metalorganic Chemical Vapour Deposition (MOCVD), Atomic Layer Epitaxy (ALE), Pulsed Laser Deposition (PLD) and Hot Wall Epitaxy (HWE). In this part, in addition to MBE method, commonly used epitaxial growth techiques will be briefly introduced for the growth of CdTe material.

2.2.2.1. Molecular Beam Epitaxy (MBE)

Epitaxy is briefly the growth of crystal film on a crystalline substrate and comes from the two Greek words '*epi*' and '*taxis*'. '*Epi*' means placed or resting upon and '*taxis*' means arrangement. Epitaxy can be divided as homoepitaxy and heteroepitaxy. If the film and the substrate are the same material, it is called homoepitaxy. When the film and substrate are different materials the growth is called heteropitaxy.

Molecular Beam Epitaxy (MBE) is an epitaxial growth process in which molecular beams deposit epitaxial films on heated substrates under ultra-high vacuum conditions (UHV). MBE was first used in 1970s and since then it is most widely used growth technique for the growth of epitaxial layers of metals, insulators, superconductors and semiconductors [84]. MBE is a versatile growth technique which permits to produce high purity and crystalline thin films with the precise control of the composition, doping of the growing structure and lateral uniformity. The precise control of the beam fluxes and UHV growth environment enables to produce high purity and high crystalline structure thin films when compared to MBE with other growth techniques. When compared to other epitaxial growth techniques, MBE has an important advantage which UHV environment allows the control and analysis during growth with in situ characterization tools such as Reflection High Energy Electron Diffraction (RHEED) and ellipsometry. An MBE system usually consists of four main parts; load-lock, preparation, storage and growth chambers. Each chamber has their own pumping system. Figure 2.23 illustrates schematic diagram of a typical MBE growth chamber. The growth chamber includes effusion cells, sample holder, beam flow chamber and fluorescent screen for Reflection high energy

electron diffraction (RHEED) analysis. Growth chamber also contains cryopanel providing continuos cooling of the system by liquid N_2 which increases the vacuum level.

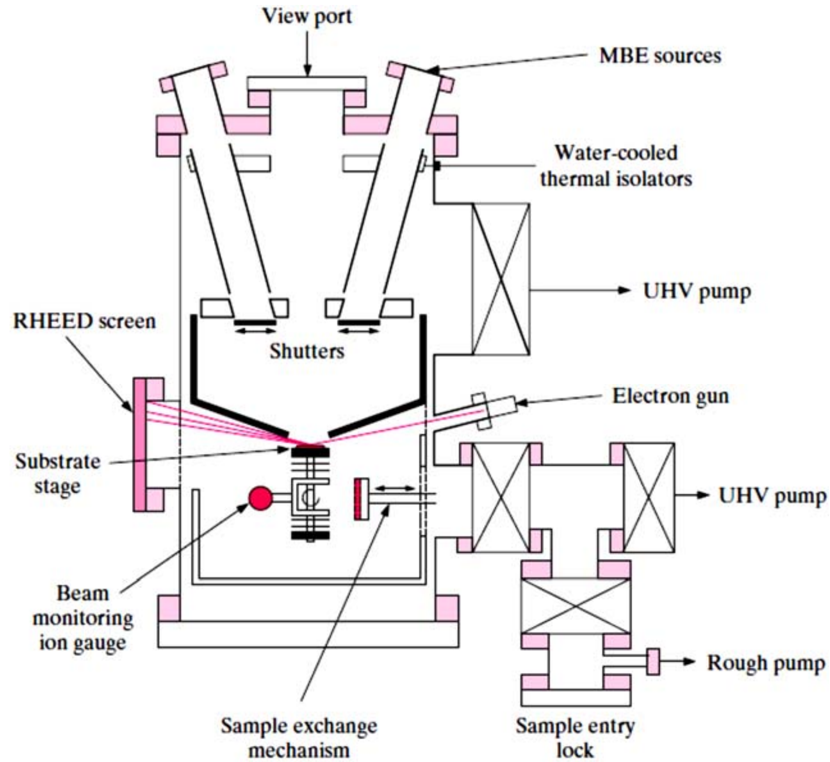

Figure 2.23. Schematic drawing of the MBE growth chamber [5].

UHV can be defined as the condition of total pressures of the residual gas in the reactor (p) as ≤$1.33\text{x}10^{-7}$ Pa (10^{-9} Torr). To calculate the total pressure in the reactor, it is important to take into account the mass flow from sources toward the substrate. There are two important parameters in the calculation of total pressure. The first one is the mean free path of the gas molecules and the second one is the concentration of the gas molecules. The mean free path of the gas molecules ℓ can be given by [85];

$$\ell = \frac{1}{\sqrt{2}\pi n d^{2}} \tag{2.64}$$

where d is the molecular diameter and n is the concentration of the gas molecules in the vacuum. The relation n with pressure (p) and temperature (T) is;

$$n = \frac{p}{k_B T} \tag{2.65}$$

where k_B is Boltzmann constant. Substituting this expression into 4.1, mean free path of the gas molecules ℓ can be obtained as;

$$\ell = 3.11x10^{-24} \frac{T}{pd^2} \tag{2.66}$$

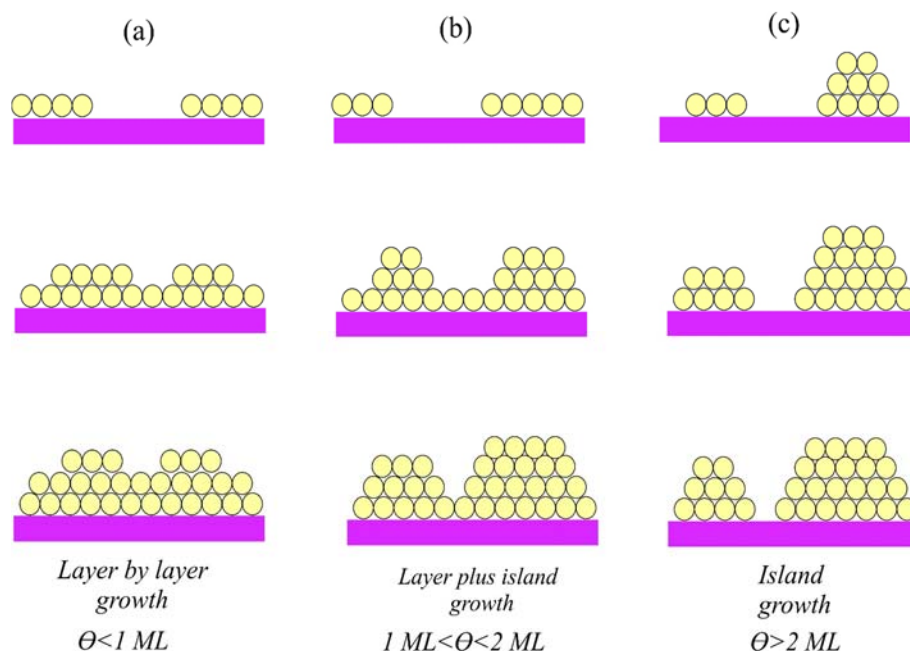

Figure 2.24. Growth modes (a) 2D Layer by layer growth (Frank-Van der Merwe), (b) Layer plus island growth (Stranski-Kastranov), (c) 3D Island growth (Volmer-Weber).

Film growth modes for a heteroepitaxial growth can be distinguished by the migration rates as shown in Figure 2.24. MBE is an atomic layer-by-layer crystal growth techique and can have very low grow rate of 1 μm/h (about 1 monolayer (ML) per second. When compared to 2D layer by layer growth (Frank-Van der Merwe) with other heteroepitaxial growth modes, such as layer plus island growth (Stranski-Kastranov) and 3D island growth (Volmer-Weber), the interatomic interactions between substrate and film are stronger. In this growth mode, new layer starts to grow after last layer growth finishes. Films with layer by layer growth have high structural quality. However, in 3D

island growth (Volmer-Weber) film atoms bound strongly together than the substrate and forms islands on the substrate material. In addition, there is a mixed growth mode in a heteroepitaxial growth called layer plus island growth mode (Stranski-Kastranov) is an intermediate case in which after the formation of a few monolayers by layer by layer growth mode, islands occur on the top of the surface.

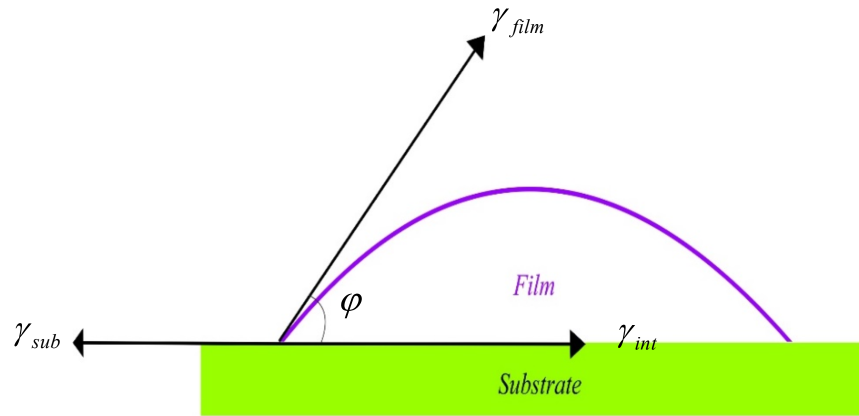

Figure 2.25. Simplified schematic representation of deposition of a film where $\gamma_{film}, \gamma_{int}$ and γ_{sub} are surface free energy of film, the interfacial energy between the epitaxial layer and the substrate interface and surface free energy of substrate, respectively.

Growth modes depend on the surface energies of the substrate and the epitaxial layer and also the interfacial energy between the epitaxial layer and the substrate interface. For thermodynamic equilibrium, the growth morphology gives the total surface tension ($\Delta\gamma$) which is force per unit length equals according to Young's equation;

$$\Delta\gamma = \gamma_{film} \cos\varphi + \gamma_{int} - \gamma_{sub} \tag{2.67}$$

$$\cos\varphi = \frac{\gamma_{sub} - \gamma_{film}}{\gamma_{int}} \tag{2.68}$$

where $\gamma_{film}, \gamma_{int}$ and γ_{sub} are respectively free energies of film, interface and substrate. However, growths occur in near or far from thermodynamic equilibrium, deposition does

not occur under thermodynamic equilibrium. For the layer by layer growth case, the sum of the film and interface free energy is smaller than the substrate free energy;

$$\varphi = 0 ; \quad \Delta\gamma = \gamma_{film} + \gamma_{int} - \gamma_{sub} \leq 0 \tag{2.69}$$

and, for the case of 3D island growth, the sum of the film and interface free energy is larger than the substrate free energy;

$$0 < \varphi < 90 ; \quad \Delta\gamma = \gamma_{film} + \gamma_{int} - \gamma_{sub} > 0 \tag{2.70}$$

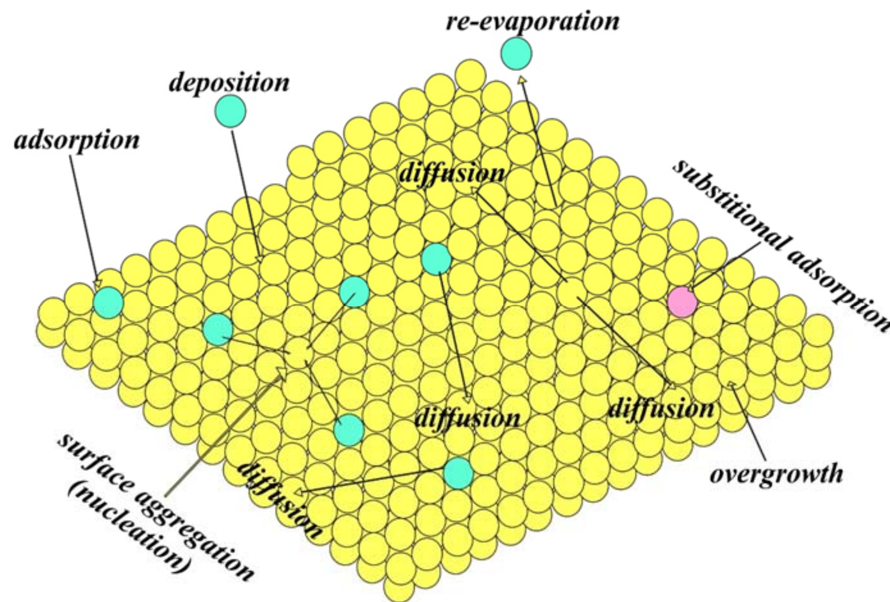

Figure 2.26. Schematic representation of the surface processes during Molecular Beam Epitaxial growth

Some surface processes involved in epitaxial growth of MBE is illustrated in Figure 2.26. During deposition, aggregation of adatoms, step or surface diffusion of adatoms and re-evaporation of adatoms at high temperatures can be occurred. In addition, adsorption occur during growth which is called physisorbed when atoms weakly bound to substrate by van der Waals force and called chemisorbed when atoms bound to substrate by stronger chemical bonds such as metallic, ionic or covalent bonding [86]. The rate of desorption processes *R* can be expressed by Arrhenius exponential [86];

$$R \propto exp\left(\frac{-E_d}{k_B T}\right) \quad (2.71)$$

where E_d is activation energy of desorption, k_B is Boltzmann constant and T is surface temperature.

2.2.2.2. Metalorganic Vapour Phase Epitaxy (MOVPE)

Metalorganic Vapour Phase Epitaxy (MOVPE) is major deposition method for epitaxial CdTe films since its introduction in 1968 and is referred also as metalorganic vapour phase deposition (MOVPD) and organometallic chemical vapour deposition (OMCVD) [87]. When compared to MBE, MOVPE growth occurs in the gas phase, not under high vacuum conditions (typically 15 to 750 Torr) but has very low growth rate of 1 μm/h (about 1 monolayer (ML) per second and it is also non-equilibrium growth technique similar to MBE. Due to operation in the gas phase, it has limited usage of in-situ characterization equipments such as RHEED and ellipsometry. Unlike MBE, MOVPE use various combinations of organometallic compounds, hybrides and other gas sources rather than elemental or compound sources.

An MOVPE system is consists of reactant storage, gas handling manifold and reaction chamber. The sources are sent into reaction chamber at near room temperature and decomposed generally in the presence of H_2 by a hot susceptor. For the case of CdTe growth, most widely used source precursors are di-methyl cadmium (DMCd, $(C_2H_5)_2Cd$) for cadmium and dimethyltelluride (DMTe, $(CH_3)_2Te$) or di-iso-propyl telluride (DIPTe, $(C_3H_7)_2Te$) for tellurium. High pressure sources of CdTe are located in organometallic cylinders in order to eliminate the possibility of condensation of chemical on the walls which allows the growth of high vapor pressure materials. The walls of the reaction chamber are cold to reduce the probability of chemical reactions at the walls and are generally made of either fused silica or stainless steel. The chamber is designed as either vertical geometry or horizontal geometry. A schematic drawing of an organometallic cylinder and horizontal reaction chamber is given in Figure 2.27.

Growth of II-VI materials by MOVPE technique depends on the input ratios between II and VI sources in which VI source ratio should be greater due to high vapour pressure of II materials. The proper growth temperatures for growth of II-VI materials are

between 350 and 550 °C due to their large diffusion coefficients and it is reported in the literature that 380 °C is the most suitable temperature for the growth of CdTe on GaAs substrate with (422) rocking-curve FWHM value of 80 arcsec [88]. Also, the lowest (422) rocking-curve FWHM value of 64 arc-sec and the lowest Everson EPD of $3x10^5$ cm^{-2} observed MOVPE grown (211)B CdTe films on (211)B ZnTe/Ge/Si layers [89]. In addition, HgCdTe can be grown by MOVPE technique, but direct growth of HgCdTe is difficult due to different thermodynamic properties of CdTe and HgTe. In order to grow HgCdTe by MOVPE, two common methods as direct allow growth (DAG) and interdiffuse multilayer process (IMP) techniques have been reported in the literature. DAG technique is a direct growth method of the ternary alloys and IMP technique is used for the growth of individual layers of HgTe and CdTe [90].

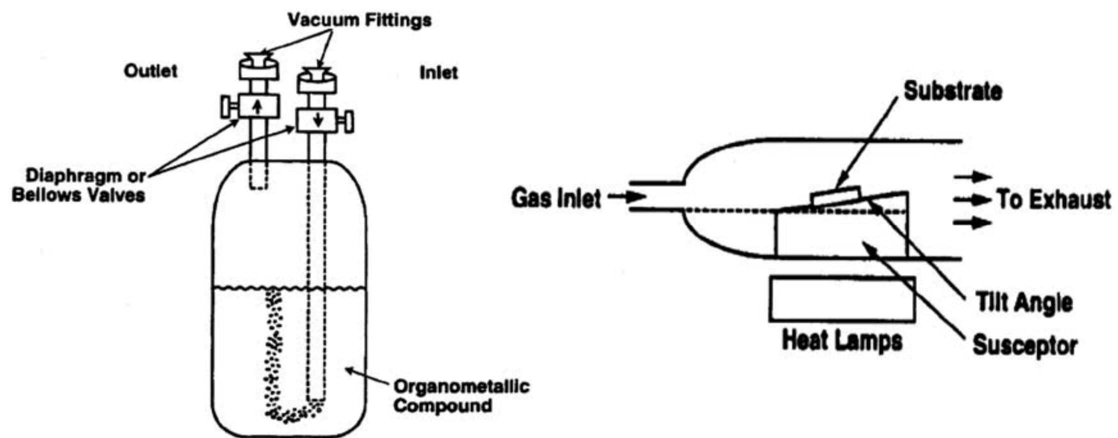

Figure 2.27. Schematic diagram of (a) an organometallic cylinder and (b) Horizontal reaction chamber [91].

2.2.2.3. Atomic Layer Epitaxy (ALE)

Atomic Layer Epitaxy (ALE) or Atomic Layer Chemical Vapor Deposition (ALCVD) was introduced to grow ZnS:Mn by Tuomo Suntola and patented in 1977 [92]. ALE technique is a combination of chemical reaction (i.e. Chemical Vapor Deposition) and physical reaction (i.e. Molecular Beam Epitaxy) processes. ALE provides precise control of film thickness and composition at atomic layer level. ALE uses precursors similar to MOVPE technique but it can be performed under either high vacuum conditions

or in the gas phase. UHV-ALE systems are compatible with in-situ characterization equipments which enables precise control of the growth process.

In ALE method, firstly the substrate surface is activated by chemical reaction and then chemical bond formation begins on the substrate surface as the precursor molecules intoduced into the growth chamber. Growth rate of ALE method is low that it changes between 0.5 ML and 1 ML per cycle under suitable growth conditions. Several growth modes occur in ALE growth technique in which for growth of one monolayer per cycle layer by layer growth mode is expected and for the growth of less than one monolayer other growth modes can be utilized. The growth mode in ALE technique can also be changed during growth [93]. Growth of layers by ALE consists of four major steps as; a self-terminating reaction of the first reactant (Reactant A), a purge to remove the non-reacted reactants, a self-terminating reaction of the second reactant (Reactant B) and finally a purge to remove the non-reacted reactants, again. For the case of CdTe; dimethyl cadmium ($(C_2H_5)_2Cd$) as Reactant A and hydrogen selenide (H_2Se) as Reactant B or Cd and Te can be used as Reactant A and B, respectively [94, 95]. Studies showed that the growth of CdTe films on GaAs substrate using Cd and Te as source materials, after four reaction cycles the bulk lattice constant of CdTe can be observed and high quality smooth layers of CdTe can be obtained by ALE method [96].

2.2.2.4. Pulsed Laser Deposition (PLD)

Pulsed Laser Deposition (PLD) is widely used growth techique for developing thin films of insulators, semiconductors, metals and superconductors. Lasers have been used for the first time for the growth of thin films in 1965 by H.M. Smith and A.F. Turner. In their experiments, H.M. Smith and A.F. Turner used a ruby laser; however, thickness of the grown films were not uniform [97]. The growth of thin films by PLD technique has not been successful until 1987. After the laser technology have been improved, first successful growth of $YBa_2Cu_3O_{7-x}$ superconductor thin films was obtained in 1987 [98]. A PLD system consists of an excimer laser which is a type of ultraviolet laser that produces high-power laser pulses. Laser wavelengths changes between 200 nm and 400 nm for thin film growth by PLD. Most PLD systems use excimer lasers formed by a combination of a noble gas such as argon (Ar), krypton (Kr) or xenon (Xe) and a reactive gas as fluorine (F) or chlorine (Cl). Also, as an infrared laser; neodymium-doped yttrium

aluminum garnet (Nd:YAG) laser with wavelength at 1064 nm has been used in many growths by PLD. Growths carried by PLD can be done under high vacuum conditions or in the presence of background gas depending on the process. Also, the chamber is compatible with in-situ characterization techniques such as RHEED. Schematic representation of a Pulsed Laser Deposition System is illustrated in Figure 2.28.

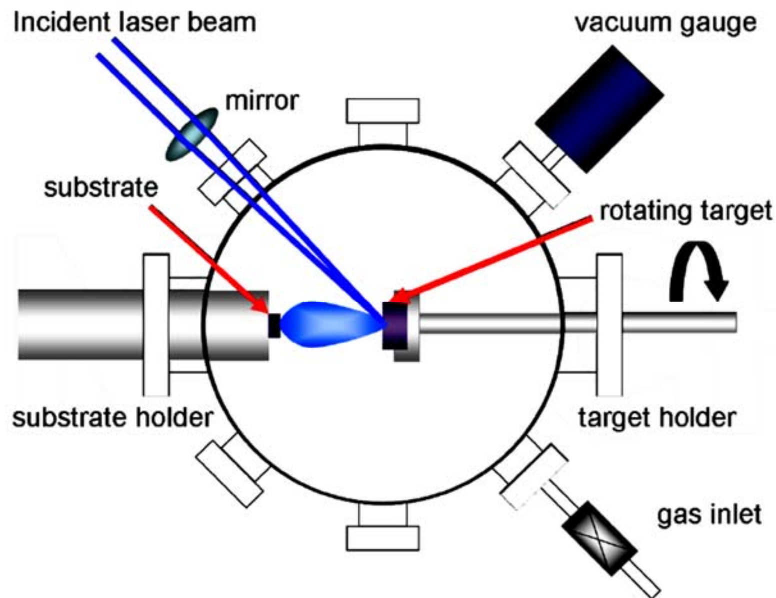

Figure 2.28. A schematic representation of the Pulsed Laser Deposition Technique [99].

PLD system configuration consists of a target and a substrate holder that aligned on the same line. In addition, many systems are compatible with multiple targets which permits the multilayer growth of thin films. The growth of CdTe thin films would be carried by powdered crystals of CdTe which are pressed to form target material. In addition, it is possible to grow CdZnTe using CdZnTe target which can be prepared from CdZnTe powder or from the mixture of CdTe and ZnTe powders [100]. In the principle of PLD, pulsed laser is focused on the target material and the material is vaporized from the target forming a plasma plume which is a combination of atoms, molecules, ions and electrons. Rotation of target holder provide homogenous growth of thin film. If the plasma plume is in contact with the substrate surface with repeated pulses, material grows on the substrate surface forming thin film. Laser penetration into the target material depends on the laser wavelength and material’s attenuation coefficient.

The growth of II-VI compounds by PLD technique has been a popular technique after the first successful growth by PLD. High quality CdTe films have been deposited on a variety of substrates using PLD technique [101]. However, it is not useful technique to grow CdTe nanoparticles due to limited plume distance by high background gas pressure [102].

2.2.2.5. Hot Wall Epitaxy (HWE)

Hot Wall Epitaxy (HWE) is introduced in 1978 for the epitaxial growth of CdTe [103]. HWE technique is also a successful growth technique for the growth of other II-VI compounds on many crystalline substrates. When compared to MOVPE and VPE methods, the HWE has many advantages such as; low cost of operation, simplicity and high growth rate. Improved type of HWE called multitube physical vapor transport (MTPVT) system can reach growth rates up to 150 μm/h on substrates such as GaAs [104, 105]. HWE is based on the evaporation of CdTe source under high vacuum conditions for the epitaxial growth of CdTe. Additional source can be placed into the chamber for doping or stoichometric control. The growth chamber of HWE consists of source furnace at the bottom of the chamber, the substrate furnace top on the source and a shutter between them. The shutter between the two furnaces called as hot wall which provides a nearly uniform and isotropic flux onto the substrate surface. Three parts of system (source furnace, hot wall and substrate furnace) are at different temperatues during growth. Despite having large lattice mismatch, it is possible to grow high quality epitaxial films of CdTe by HWE with FWHM value of 118 arcsec [106].

2.2.3. Alternative Substrates For Epitaxial Growth of CdTe

The substrate choice is the primary factor for the MBE growth of CdTe and HgCdTe which play an important role for the performance of MCT-based infrared (IR) detectors and focal-plane arrays (FPAs). However, substrate surface quality is less important for the growth of CdTe and HgCdTe by Liquid Phase Epitaxy (LPE), Vapor Phase Epitaxy (VPE) and Metalorganic Chemical Vapour Deposition (MOCVD) due to growth at much higher temperatures. Because of this reason, to have high quality CdTe and HgCdTe

films, substrate choice is a major factor for MBE based growth. There are important factors for the choice of proper substrate for the growth of CdTe and HgCdTe; such as lattice parameter matching, thermal expansion coefficient maching, valence matching, substrate, buffer and layer surface defect densities, maximum available size of substrate, cost, diffusion from the substrate to layers, high substrate thermal conductivity, rigidity, strength and hardness, easiness of substrate surface preparation.

The key factor for the growth of high quality epitaxial films is to grow on a lattice-matched substrate to avoid strain and dislocation formation during growth of epilayer. $Cd_{1-x}Zn_xTe$ with Zn concentration of %4 or %3.5 is a preferred substrate for MBE-grown HgCdTe infrared detectors and focal-plane arrays (FPAs) due to being almost perfect lattice, good thermal expansion coefficient and valence matching with HgCdTe [107, 108]. Despite having advantages of CdZnTe for the growth of HgCdTe material, being both brittle and soft makes it fragile and easily damaged during fabrication. In addition; high cost, lack of large area and large thermal mismatch with the Si readout integrated circuit (ROIC) of CdZnTe substrates give rise to necessity of growth over alternative substrate to CdZnTe.

Si, Ge, InSb, and GaAs have all were studied as alternate substrates for MBE growth of HgCdTe during years due to lower cost and much larger available sizes. Cost and largest available areas of CdZnTe, InSb, GaAs, Ge and Si substrates for the growth of HgCdTe material are compared in Table 2.4. Si and GaAs have lower cost and larger available size when compared to CdZnTe substate. When the size of bulk CdZnTe becomes large Zn segregation, increased greatly causing lattice parameter variations [107]. However, due to large lattice mismatch of alternative substrates to CdZnTe with HgCdTe, the usage of alternative substrates is limited [109].

In Figure 2.30, the lattice parameters of various semiconducting materials including alternative substrates are given. As seen from the graph, InSb has near perfect lattice match to LWIR HgCdTe (0.19% mismatch with $Cd_{0.3}Hg_{0.7}Te$) and has nearly the same thermal expansion coefficient.

Table 2.4. Comparison of Alternative Substrates for HgCdTe/CdTe [110].

	CdZnTe	Si	Ge	GaAs
Cost (US$/cm²)	~200	~1	~8	~5
Maximum Available Size (cm²)	~50	~700	~180	~180
Structure	ZB	Diamond	Diamond	ZB
EPD (/cm²)	10^4	$<10^2$	$<10^3$	$<10^3$
Lattice Parameter (Å)	6.48	5.43	5.66	5.65
Misfit (w/CdTe)	-	-19.3%	-14.6%	-14.6%
Thermal Ex. Coeff. (α)(x10⁻⁶ °C⁻¹)	5.0	2.6	5.8	5.8
α-Mismatch (w/CdTe)	-	-92.3%	13.8%	13.8%

InSb wafers are available with diameters up to 4 in, as seen in Figure 2.29. HgCdTe grown on InSb buffer layers can reach x-ray diffraction-full-width at half-maximum (XRD-FWHM) values as low as 18-22 arcsec and CdTe grown on InSb substrates have values of 20-30 arcsec [108, 111]. However, there are problems practically usage of InSb as an alternative substate. Low melting point (527 °C) and diffucuIty of removing oxide layer without substantial surface damage limits its successful use in epitaxial growth of HgCdTe layer. In addition, low thermal stability of InSb leads to In and In_2Te_3 diffusions to CdTe and HgCdTe epilayers [112].

Si and GaAs alternative substrates have easier surface preparation procedures when compared to InSb. However, having large lattice mismatches between HgCdTe, limits to growth of high quality layers. Between Si substrate and HgCdTe epilayers, lattice

mismatch has the value of 19.4% and the coefficient of thermal expansion mismatch of this system is 92%. Si substrates can be found commercially large area (2 to 16 in diameter), low cost of this substrate, easy removal of oxide layers at 850 ºC and reliability during thermal cycling makes Si substrates popular [113]. The first MBE growth of CdTe on Si was performed in 1983 by Yawcheng Lo, et al [114]. They found FWHM values as 7.26' and 2.13' after the growth of CdTe films on (100) and (111)Si substrates, respectively. In this study, Nomarski micrographs showed CdTe films are uniformly free of voids and microcracks. After the first growth of CdTe films on Si substrates, studies on CdTe/Si films were accelerated. In 1989, the first successful MBE growth on (100)Si substrates performed using ZnTe buffer layers to preserve the homo-orientation of CdTe growth on Si [115]. Today, it is possible to achieve higher quality CdTe/Si films with XRD triple axis rocking curve FWHM value of 50 to 60 arcsec range and $1.5x10^5$ cm^{-2} etch pit density (EPD) value [109, 116].

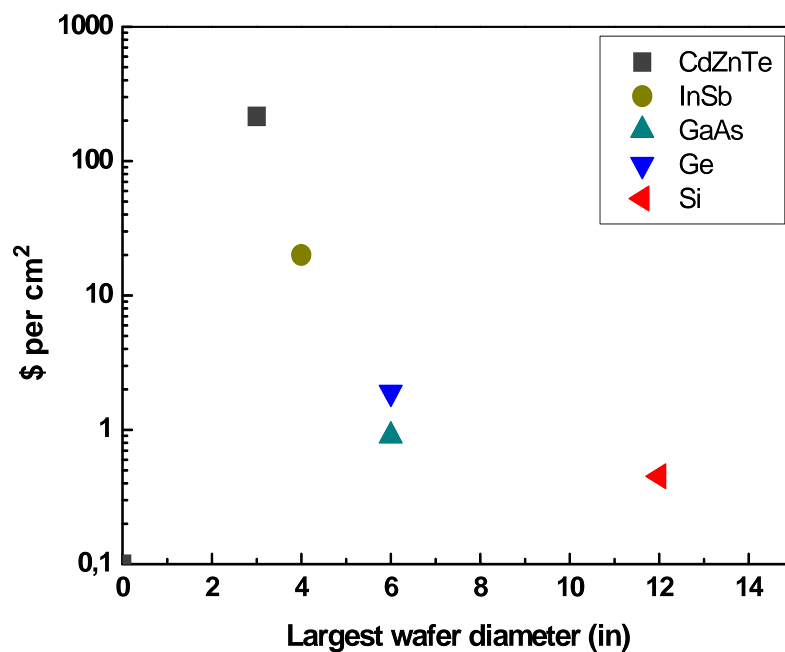

Figure 2.29. Cost and largest available areas of substrates for the growth of HgCdTe [2].

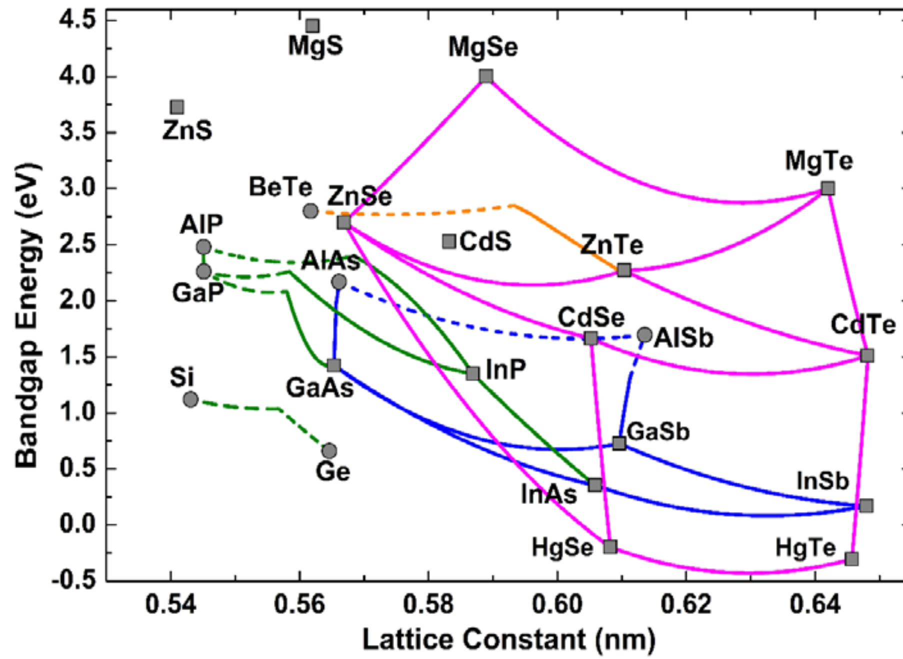

Figure 2.30. Energy gap versus lattice parameter for several semiconductor materials [117].

In 1988, R. Koestner and H. Schaake, to investigate best orientation for HgCdTe, (100), (111)B, (211)A and (211)B substrates used and found that (211)B growth suppress twin formation, gives best surface morphology and higher Hg sticking coefficients [118]. Nowadays, almost all growth is carried out over (211) substrates. Today it is possible to achieve higher quality (211)B CdTe/(211)B GaAs films than CdTe grown on Si substrates with XRD double crystal rocking curve (DCRC)-FWHM value of lower than 50 arcsec [107].

Since 1984, low-cost GaAs substrates are generally used as a substrate for the growth of HgCdTe. Lattice mismatch between GaAs substrate and HgCdTe epilayer is 13.6% and between CdTe and GaAs is %14.6 [119]. The thermal expansion coefficient mismatch between GaAs substrate and HgCdTe epilayer is 13.8% and between CdTe and GaAs is %27.5 [120]. Despite having large lattice mismatch with CdTe and HgCdTe materials, oxide layers of GaAs substrates can be removed easily around 580 ^{o}C. In addition, GaAs substrates can be found commercially epi-ready which do not need any preperation before the growth. Protective oxide capping of the epiready GaAs wafers can be removed thermally before the growth process. Oxide removal process of epiready GaAs wafers includes loss of volatile As_2O_x species at 400-500 ^{o}C and desorption of Ga_2O_3 species at approximately 572 ^{o}C under As_4 flux [119].

Growths carried on GaAs wafers, especially on the (211)B orientation which has the ability to suppress twin defect formation and minimize macroscopic defects, gained more attention in recent years due to advances in wafer processing [45]. However, owing to large lattice mismatch between the HgCdTe layer and GaAs substrate, to decrease the effects of lattice mismatch such as large dislocation concentration and strain effects, a closely lattice matched to HgCdTe buffer layer such as CdTe can be used for MBE-grown HgCdTe. However, during growth on GaAs substrates, diffusion of gallium and arsenic atoms into the growing CdTe layer was reported which is an important problem for the growth on GaAs substrates [45].

2.3. Defects in CdTe

The surface defects of substrate material and growth conditions can limit the crystal quality of CdTe epitaxial films. CdTe as a buffer layer for HgCdTe infrared detectors play an important role for the growth of HgCdTe films and fabrication processes. However, cyrstal quality of substrate material and surface of ZnTe and CdTe buffer layers affect the performance of HgCdTe detectors. In this part, the possible imperfections or defects will be briefly discussed for the growth of bulk CdTe and epitaxial CdTe films.

2.3.1. Point Defects

Point defects is sometimes called as zero dimensional defect have a significant effect on the material and it is common for semiconductors. Point defects are formed when the regular arrangement of the perfect crystal is not exist. It can be divided to two categories as intrinsic and extrinsic point defects depending on the type of atoms in the arrangement of the crystal. It is called intrinsic when no additional foreign atom involved in the cyrstal and called extrinsic when another species of atoms involved. Intrinsic point defects include vacancies, self-interstitials, Schottkey imperfections and Frenkel imperfections. However, substitutional impurities are extrinsic point defects.

The most significant point defect type is vacancy for the growth of CdTe epitaxial films. Due to vacancies, diffusions can occur during the growth. A missing atom in the regular arrangement of the crystal called as vacancy. At high temperatures, atoms change

their positions and leaves empty positions. The number of vacancies N_v can be estimated by Boltzmann distribution as [121];

$$N_v = N_s \left(-\frac{E_v}{k_B T} \right) \tag{2.72}$$

where N_s is the number of regular lattice sites, E_v is the energy required to form a vacant lattice site in a perfect crystal (activation energy), T is absolute temperature in Kelvin and k_B is Boltzmann constant.

There are two types of vacancies appearing in CdTe. They are a vacancy on the anion (tellurium) sublattice, V_{Te}, and a vacancy on the cation sublattice, V_{Cd}. Lack of an atom forms local distortions in the lattice. Antisites are defects which occur in ordered alloy and formed when atoms of different type exchange positions. In CdTe, cation antisite is formed when a cadmium atom occupies a tellurium lattice site (Cd_{Te}) and anion antisite is formed when a tellurium atom occupies a cadmium lattice site (Te_{Cd}).

Interstitial defects form when an additional anion or cation atom occupy a site other than lattice site in the cystal. This defect type can stand alone or can bound together to form complexes. Self-interstitials are formed when an extra atom which is the same type as the lattice atoms in the crystal lattice. It is generally called as cation interstitial when an additional cation atom is located in the crystal lattice and called as anion interstitial when an extra anion atom is located in the crystal lattice.

Occupation of a different type of atom in the regular site of crystal lattice is called substitutional impurity. CdTe has a high degree of ionicity with 0.717. Due to high ionicity, the Coulombic forces are very large and charge imbalance results the tendency to balance. To keep charge neutrality, some point defects can be formed in a perfect crystal of CdTe such as Frenkel and Schottkey defects. Schottkey imperfection is a type of vacancy which can be formed when an atom migrates from regular location in lattice site to the crystal surface. It is a pair of anion vacancy and cation vacancy. Frenkel defect is a pair of cation vacancy and a cation or an anion interstitial.

In Figure 2.33, calculated point defect and free-carrier consentrations by M.A. Berding are shown. As shown in the graph, the possible point defect type is cadmium vacancy under tellurium-rich conditions and the dominant point defect type is cadmium interstitial (Cd_I) under cadmium-rich conditions. In addition, the possible complex defect to occur in CdTe is Te_{Cd}-V_{Cd} [122]. Possible point defect ionization energy values in CdTe

are given in Table 2.5. In addition to CdTe, in HgCdTe, there are two types of cation interstitials. First one is, a mercury atom occupies a tellurium lattice site (Hg_{Te}) and the second one is, a cadmium atom occupies a tellurium lattice site (Cd_{Te}). In addition, anion antisite is referred as Te_{Hg} and Te_{Cd}. During the growth of HgCdTe, a Hg atom may evaporate leaving a V_{Hg} on the surface which then diffuses into the interior of crystal and forms Shottky defect. Generally found impurities in bulk HgCdTe are Al, Te, Ca, Mg, Ti, Cu and B impurities.

Generally, the impurities in CdTe and HgCdTe material are electrically active. However, some of them are not active and induce deep levels in the band gap. These deep levels in the material reduce the lifetime of minority carriers and affect badly the performance of device. In some conditions, vacancies can be filled and reduced by adding substitutional impurities (doping). For example, Indium (In) is a accepted n-type dopant for MBE HgCdTe and it was first reported in 1988 [123]. Annealing under Hg atmosphere at 250 ^{o}C, fills Hg vacancies. In order to fill the Hg vacancies, In can be used as a n-type dopant and As can be used as a p-type dopant for the MBE growth of HgCdTe [124, 125]. However, when In doped, In can combine with Te and form In_2Te_3 [126]. In addition, In atom impurities are fast diffusers, diffusion coefficient is approximately $5x10^{14}$ cm^2/Vs at 300K [127]. Because of that, p-n junction's stability changes when In is used as a dopant. In Table 2.3, the dopants for CdTe material and binding energies are detailed.

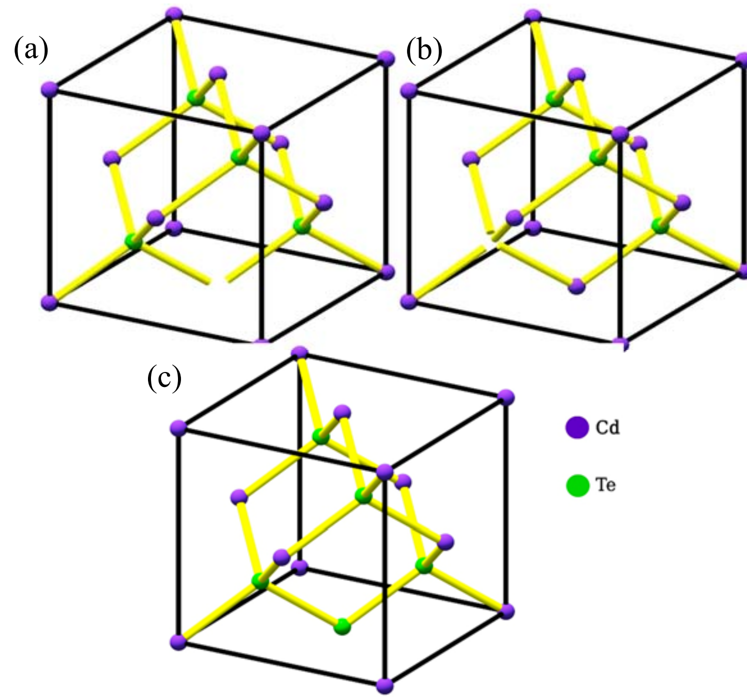

Figure 2.31. Some of defects in zincblende structure of CdTe (a) Cation vacancy (V_{Cd}), (b) Anion vacancy (V_{Te}), (c) Tellurium antisite (Te_{Cd}).

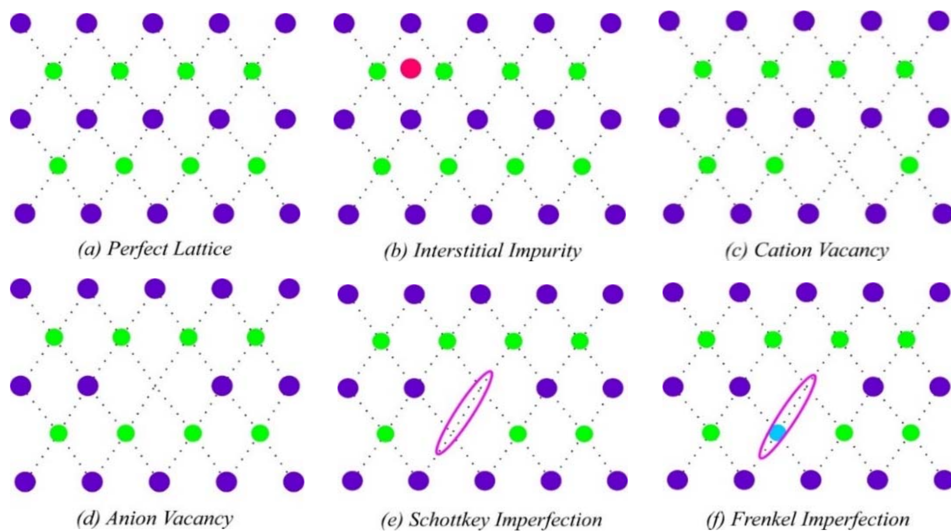

Figure 2.32. Schematic representation of comparasion of perfect lattice with some point defect types; (a) Perfect lattice (b) Interstitial impurity, (c) Cation vacancy (d) Anion Vacancy (e) Schottkey Imperfection (f) Frenkel Imperfection.

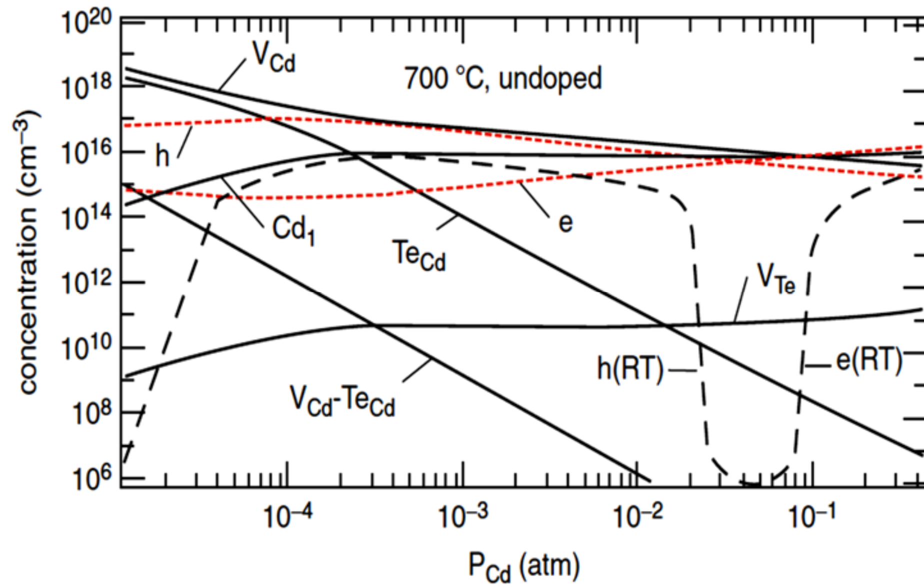

Figure 2.33. Point defect densities as a function of Cd partial pressure. h and e are holes and electrons, and RT refers room temperature [82].

Table 2.5. Ionization energies of point defects in CdTe.

Point Defect Type	Thermal Ionization Energies (eV)	Refecences
V_{Cd}	E_v+0.2, 0.8	[128]
Te_{Cd}	E_c-0.2, 0.4	[128]
Te_I	E_c-1.28, 1.48	[128]
Cd_I	E_c-0.5	[122]
Te_{Cd}+ V_{Cd}	E_v+0.7, 0.79	[129]

2.3.2. Line Defects

The most important factor which directly affects the crystal quality of epitaxial grown films is lattice mismatch between the epitaxial layer and the substrate. For nearly lattice matched or small lattice mismatched surfaces (around 1%-9%), the initial growth will be strained to match the atomic spacings of the substrate. The homogenously strained states generally called as pseudomorphic growth. In pseudomorphic growth, no lattice relaxation occurs. Pseudomorphic growth is not valid for large lattice mismatched systems and it dominates when the epilayer thickness is small [130].

Assuming the lattice constant of the grown layer as a_L and lattice constant of the substrate a_s, the lattice mismatch or misfit f between the an epilayer and the substate can be calculated by the following equation;

$$f = \frac{a_L - a_S}{a_S} \tag{2.73}$$

For CdTe layer grown on GaAs substrate, lattice mismatch at 300 K becomes approximately;

$$f_{CdTe/GaAs} = \frac{a_{CdTe} - a_{GaAs}}{a_{GaAs}} \approx \frac{6.48 - 5.65}{5.65} \approx 14.6\% \tag{2.74}$$

For large and small lattice mismatched surfaces as the thickness of the growing layer increases, strain energy in the layer also increases. At some epilayer thickness known as the critical thickness, it becomes energetically favorable to diminish strain energy and relax the some of the strain by introduction of misfit dislocations. The critical thickness (d_c) can be briefly explained as the thickness at which the first misfit dislocation introduced and it is approximately given by eq. 2.75 where it can be deduced that the critical thickness is directly proportional to substrate lattice constant and the misfit strain ($\in$) [131]. Misfit dislocations lie parallel to the substrate-layer interface and expected to be present in partially relaxed layers. On the other hand, threading dislocations are inclined to the substrate-layer interface and introduce during the relaxation process [132].

$$d_c \approx \frac{a_S}{2|\in|} \tag{2.75}$$

If the film is strained due to lattice mismatch between the substrate and growing film, the misfit strain can be defined by;

$$\in = \frac{a_L^{str} - a_L}{a_S} \tag{2.76}$$

where a_L^{str} is strained lattice constant of grown layer. If both strain and dislocation exist, the misfit can be given be [130];

$$f = \in + \gamma \tag{2.77}$$

where γ is lattice relaxation. For the case of a positive value of f; some atomic planes in the epilayer will be missing and the misfit strain is compressive type and for a negative value; misfit strain is tensile type and extra atomic planes will lie in the epilayer [133].

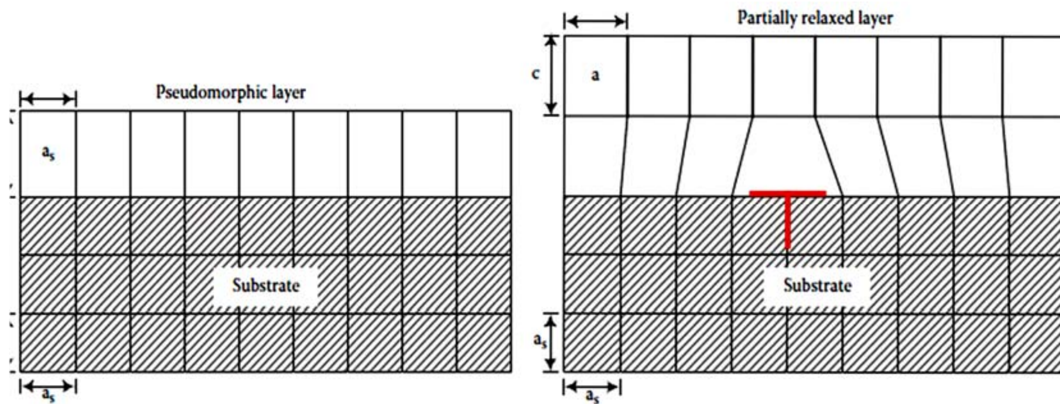

Figure 2.34. Growth of heteroepitaxial layer on a lattice mismatched substrate. (a) Strained layer below the critical thickness, (b) Partially relaxed layer above the critical thickness by forming misfit dislocations which it is shown in red color.

Dislocation types can be basicly classified as the edge dislocation and the screw dislocation. Edge dislocation is formed when extra atomic planes lie in the epilayer and the Burger vector is perpendicular to dislocation line (Figure 2.35 (a) and (b)). In screw dislocation, the defect line movement is perpendicular to atom displacement and the Burger's vector is parallel to dislocation line (Figure 2.35 (c) and (d)). The motion of a screw dislocation is also a result of shear stress and more difficult to visualize than edge

dislocation. A stress arises when the applied force acts perpendicular to the area of interest and a shear stress arises when the force acts in a direction parallel to the area of interest. In Figure 2.35, Burger's vector is denoted by '**b**' describing the magnitude and direction of the lattice distortion of dislocation in a crystal lattice [134].

The introduction of dislocations due to lattice mismatch between the substrate and the film and other defects such as point defects or surface defects degrades the performance of devices build on these material and affects the operation of detectors.

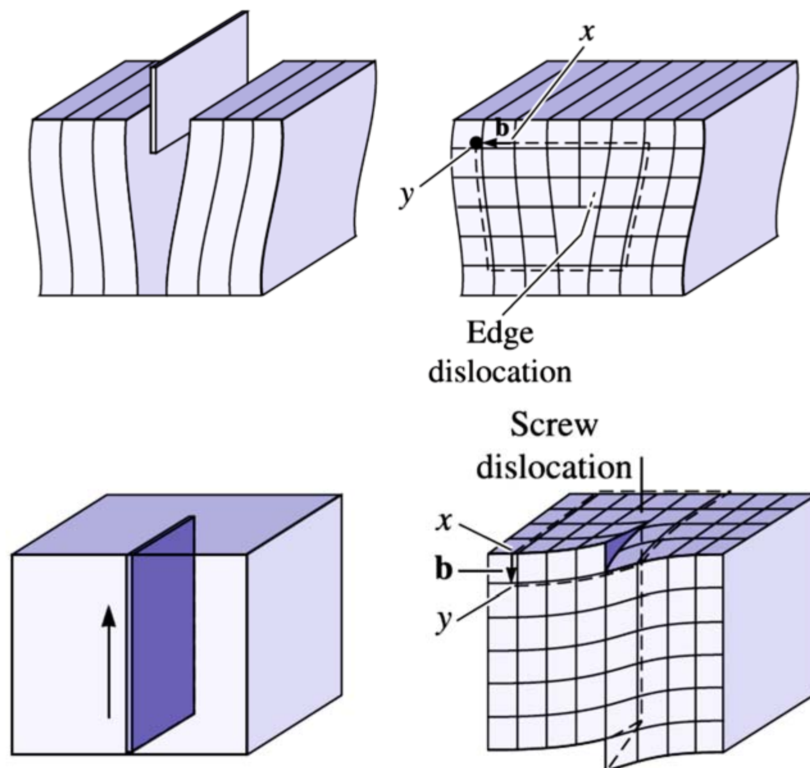

Figure 2.35. The perfect crystal is cut and an extra half plane of atoms is inserted in (a) and forms extra half plane is an edge dislocation in (b) where Burger's vector **b** is perpendicular to dislocation line. In (c) the perfect crystal is cut and sheared one atom spacing, and formed screw dislocation in (d) where Burger's vector **b** is parallel to dislocation line [135].

2.3.3. Surface Defects

Areal defects or sometimes referred as planar defects are 2-dimensional imperfections arise from a change in the atomic sequence which separate regions with two different orientations in a crystal. Surface defects can be grouped into four classes as stacking faults, twin boundaries, grain boundaries and tilt boundaries.

Stacking fault is observed when a change occur in the stacking sequence of a close-packed structure over a few atomic spacings. Stacking fault can be divided as intrinsic and extrinsic stacking faults. In the case of intrinsic stacking fault a close-packed plane of atoms are removed and in extrinsic stacking fault case, there is an extra plane. In Figure 2.37, examples of both two types of stacking faults for a Close-spaced sublimation (CSS) grown CdTe/CdS thin film are shown. In Figure 2.36, examples of stacking sequences of close-packed planes for the HCP and FCC structures are illustrated. There are four nonparallel close-packed planes in the FCC lattice with (111), $(11\bar{1})$, $(1\bar{1}1)$ and $(\bar{1}11)$ and forms ABCABCABC arrangement. Missing C planes in FCC structure forms stacking faults and the arrangement becomes ABCABCAB_ABC. Apart from FCC lattice, HCP structure has two close-packed planes as (0001) and (0002) and forms ABABABAB sequence. If the sequence of HCP lattice change by an extra plane of C, ABABABCAB arrangement formed and stacking fault occurs.

However, if a stacking fault is repeated with perfect periodicity it is not a fault, it creates a new crystal structure. For example, when CdTe films grown on GaAs substrate, it creates mixture of two FCC arrangement as AaBbCcAaBbCc. Twin boundary also can be called as a stacking fault, but separates two arragement of crystal that are mirror images of one another. For example, atomic sequence in FCC lattice becomes ABCAB$|C|$BACBA, plane marked C is a twin boundary and behaves like a mirror. In Figure 2.38, shematic illustration of a formation of twin and twin boundaries are given.

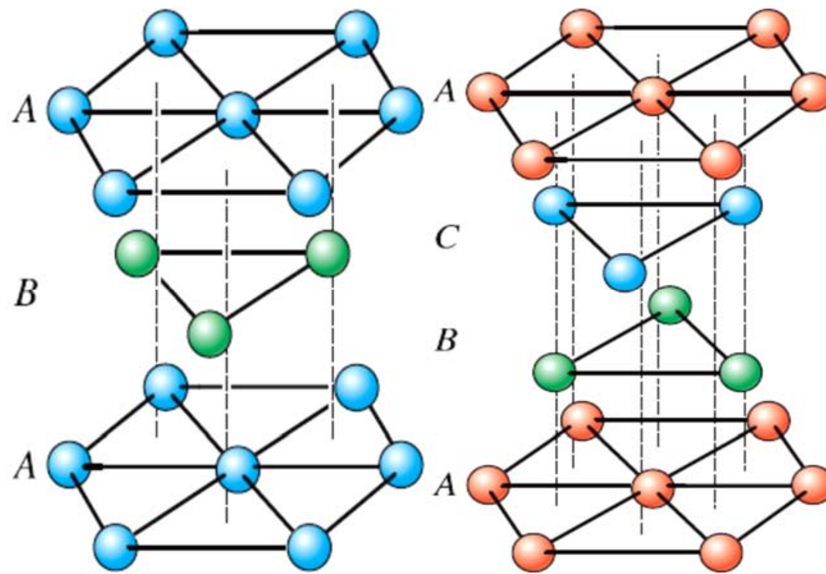

Figure 2.36. On the left the ABABAB stacking sequence of close-packed planes of the HCP structure and on the right the ABCABCABC stacking sequence of close-packed planes of the FCC structure [135]

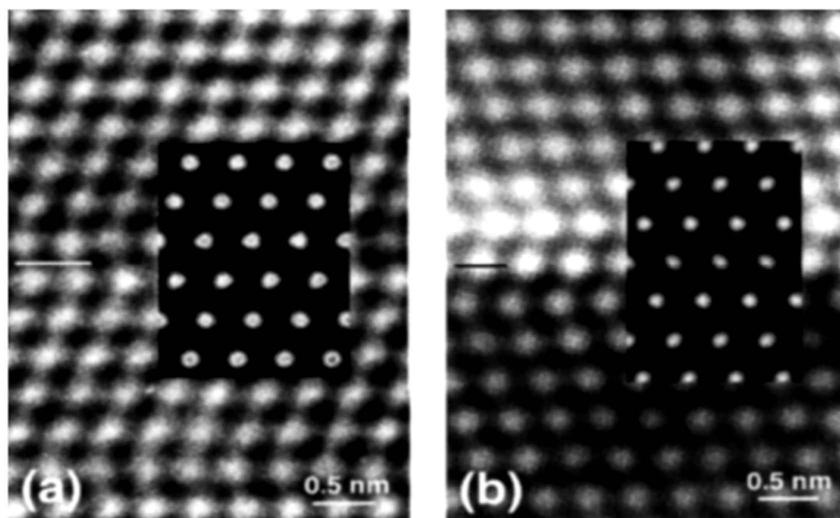

Figure 2.37. Examples of intrinsic and extrinsic stacking faults in close-spaced sublimation (CSS) grown polycrystalline CdTe/CdS film of [110] zone axis HRTEM images of an (a) intrinsic stacking fault and (b) extrinsic stacking fault. The insets are simulations of faults [136].

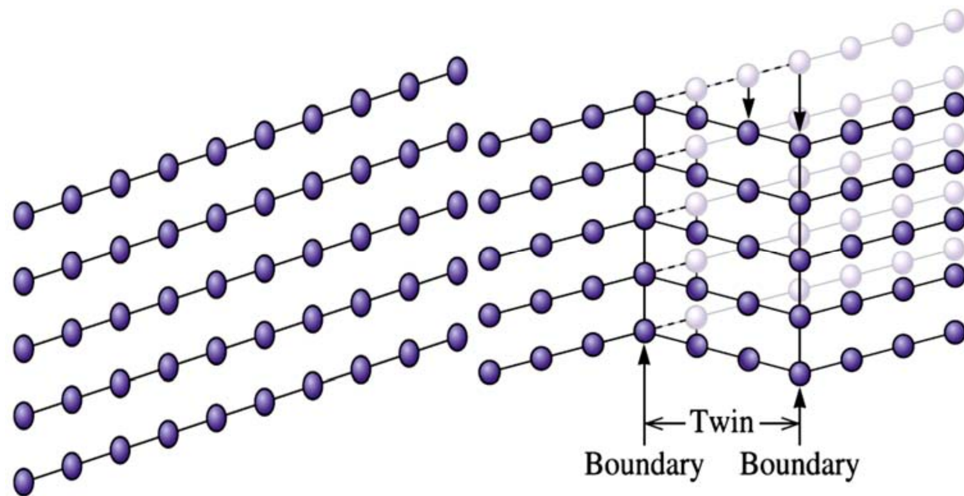

Figure 2.38. (a) Perfect cystal and (b) Formation of twin and twin boundaries [135]

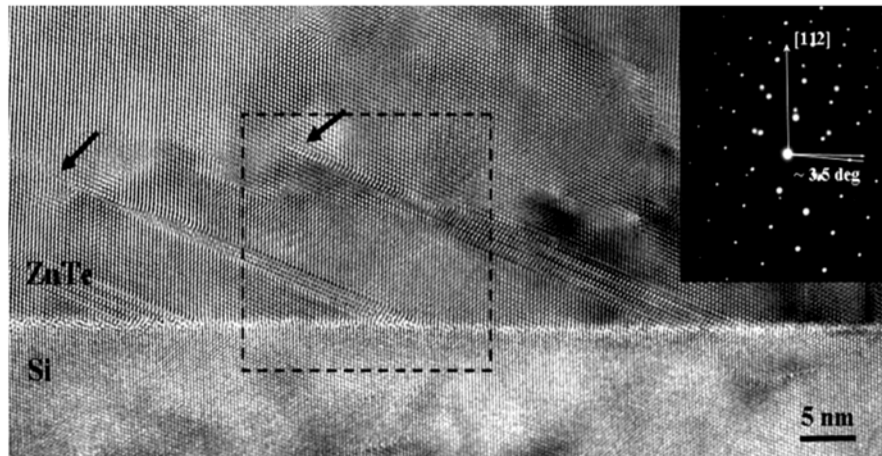

Figure 2.39. Cross-sectional electron micrograph of CdTe(211)B/ZnTe/Si(211) interface where (111)-type stacking faults and twinning defects originating at the Si substrate surface. Inset shows electron diffraction pattern where approximately 3.5° rotation between CdTe/Si crystal lattices [137].

Grains are a group of atoms having the same orientation and spacing. Grain boundaries are transition regions between grains where crystals of different orientations meet. Grain boundaries tend to decrease the electrical and thermal conductivity of the material. Grain boundaries can be divided as low angle and high angle grain boundaries

depending on the orientation differences between two neighbouring crystals. If the orientation difference between two neighbouring crystals θ is less then 10°, it is called low angle grain boundary and if higher than 10°, it is called high angle grain boundary. In Figure 2.40, a representation of a regular grain boundary and low angle grain boundary is shown. When low angle grain boundaries are formed by edge dislocations, they are called tilt boundaries and when they are caused by screw dislocations, they are called twist boundaries. In the condition for tilt boundary, tilt angle can be calculated by [138];

$$\theta = \frac{b}{D} \tag{2.78}$$

where b is the magnitude of the Burger vector and D is average vertical distance between dislocations.

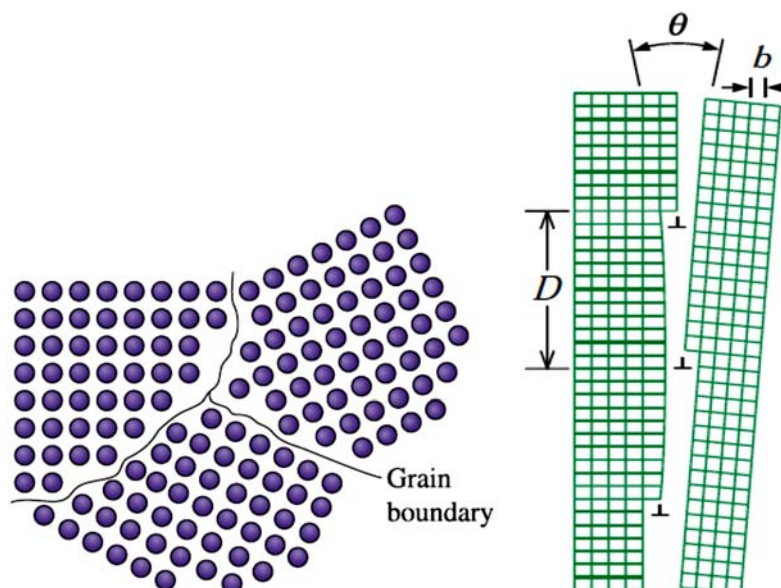

Figure 2.40. (a) Three grains with different orientations and spacing seperated by grain goundary (b) Low angle grain boundary [135].

2.3.4. Volumetric Defects

Volume defects or bulk defects are three dimensional defects and they include voids, cracks, precipitates and inclusions. Volume imperfections generally have the dimension of the order of 20 nm [138]. Voids are the areas formed by missing atoms in

the lattice structures and causes vacancies and dislocations in a crystalline structure. Cracks generally formed during heating up and cooling down processes. Inclusions occur as a result of imputity atom incorporations. Impurity atoms can form clusters with different phase from the regular atoms and generates precipitates.

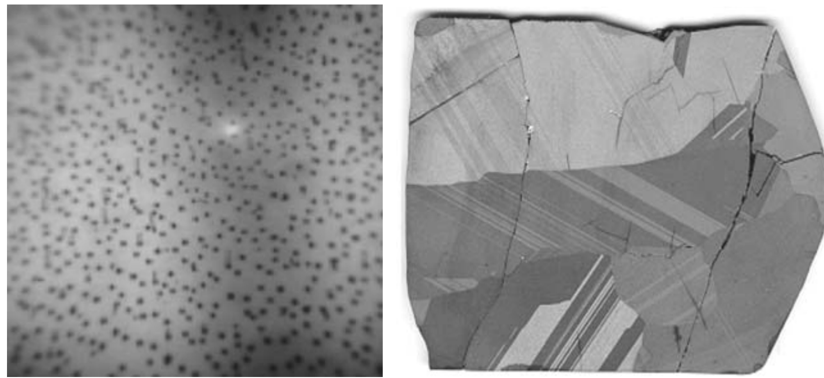

Figure 2.41. High-Pressure Bridgman (HPB) grown CdZnTe (a) Infrared micrograph of Te inclusions (b) Image of macroscopic cracks [139].

CHAPTER 3

EXPERIMENTAL TECHNIQUES AND PROCEDURES

Optical and structural characterization techniques are of fundamental importance in the determination of the properties of semiconductor structures such as CdTe thin films and their epilayers which are the main focus of this thesis. Fourier Transform (FT), and Raman Spectroscopies, along with Nomarski Microscopy are such optical techniques employed in our works, while, structural and morphological characterization techniques such as Atomic Force Microscopy, Secondary Electron Microscopy and X-ray Diffraction are also utilized. Below we give a brief description of the experimental techniques and procedures along with some associated theory needed for this work.

3.1. MBE System Configuration

Iztech Gen-20MZ MBE system consists of three chambers. They are; load-lock, storage, and growth (or main) chambers. The load lock chamber allows storage of wafers prior to the growth and removal of deposited thin films after the growth. In Figure 3.1, the load lock chamber is labelled as number 12. This chamber includes an elevator controlled casette holder, which can accommodate up to eight wafers at one time and can be moved up or down by load lock casette elevator. After the wafers are stored in the load lock chamber, they are transferred to the preparation chamber (labelled 10) by the X-axis transfer rod (labelled 4) where wafers are outgassed to remove any residual water vapor or contaminants before the transfer to the growth chamber. After outgassing in the preparation chamber, the wafers are transferred to growth chamber (labelled by 2) by the Y-axis transfer rod (labelled 7) and mounted on to the substrate holder by the Z-axis manipulator (labelled 16). Z-axis manipulator enables the wafers to rotate and heat for homogenous thicknesses and smooth surfaces during the growth of films. Many MBE sytems include an additional *preparation chamber*. Since, Iztech Gen-20MZ MBE system does not include a preparation chamber, both oxide removal and growth procedures are

carried out in the main chamber. Gen-20MZ MBE system facility at Izmir Institute of Technology (Iztech) is shown in Figure 3.3.

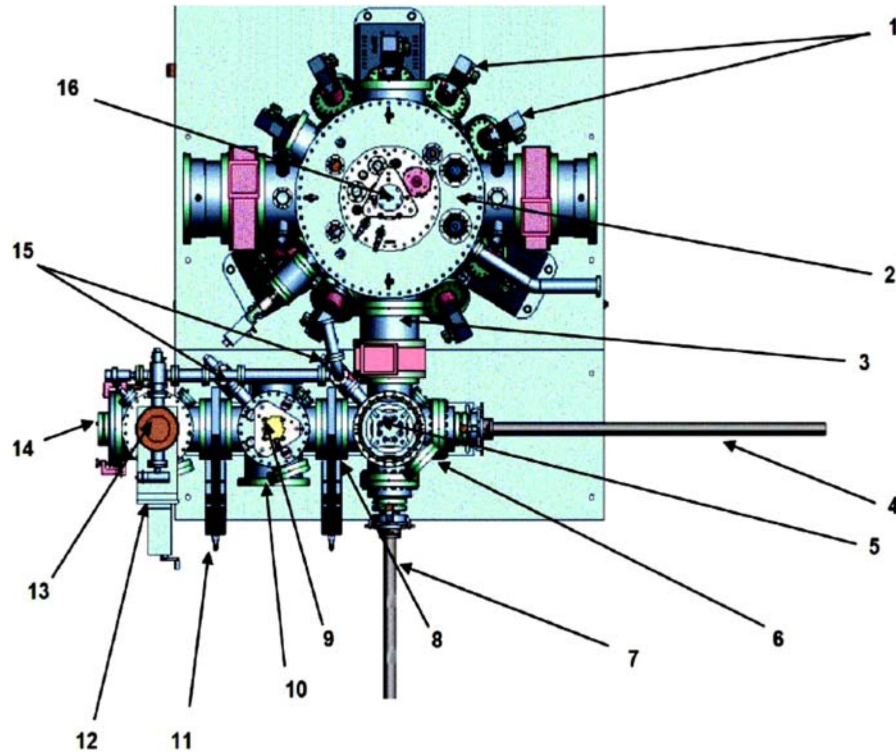

Figure 3.1. Functional Diagram of Gen-20MZ MBE system. 1. Effusion cells, 2. Growth module, 3. Storage module gate valve, 4. X-axis transfer rod, 5. Storage module elevator, 6. Storage module, 7. Y-axis transfer rod, 8. Storage module gate valve, 9. Heated station for substrate outgassing, 10. Preparation module, 11. Preperation module gate valve, 12. Load lock module, 13. Load lock casette elevator, 14. Load lock door, 15. Venting/roughing manifold, 16. Z-axis manipulator [140].

The growth chamber of our MBE system consists of ion vacuum gauges, effusion cells with shutters (12 ports for sources), cryopanel, a RHEED fluorescent screen, which allows in-situ characterization of the film surface during the growth, a residual gas analyzer (RGA), a band-edge thermometer, pyrometer, and a beam flux monitor (BFM). The residual gas analyzer (RGA) or sometimes called a quadrupole mass spectrometer is used for measuring the species of mass-to-charge (m/z) ratio and also for leakeage tests. The pyrometer is used for measuring the substrate temperature. Effusion cell flux is viewed by a beam flux monitor (BFM).

The main component of an MBE is the effusion cell or sometimes called a Knudsen cell. Effusion cells in a MBE system are the sources of molecular beams which are generated by thermal evaporation or sublimation. A source material is heated by irradiation from filaments while its temperature is controlled by proportional-integral-derivative (PID) controllers and a thermocouple feedback [141]. As shown in Figure 3.2 (a), the source of an effusion cell is placed within a crucible which can be of cylindrical, conical, or SUMO type, depending on the source material.

Crucibles are generally made of Pyrolytic Boron Nitride (PBN), Tantalum (Ta), Graphite, or Quartz. Each cell has a tantalum shutter to control the deposition of materials during a growth. SUMO crucibles, compared to cylindrical and conical crucibles, provide excellent charge material capacity, superior uniformity, the longest-term flux stability, and minimal shutter-related flux transients. Cylindrical crucibles, on the other hand, provide a high charge material holding capacity and excellent long-term flux stability, but, their large shutter flux transients with decreasing charge material causes poor film uniformities. Conical crucibles also provide excellent uniformity, but have poor long-term flux stability, decreasing charge material capacity, and large shutter flux transients. In addition to effusion cells, some materials of sources, such as arsenic and phosphorus, are utilized by a valved cracking cell due to their higher vapor pressures and low sticking coefficients. Crucibles of this type of sources are generally made of graphite [142].

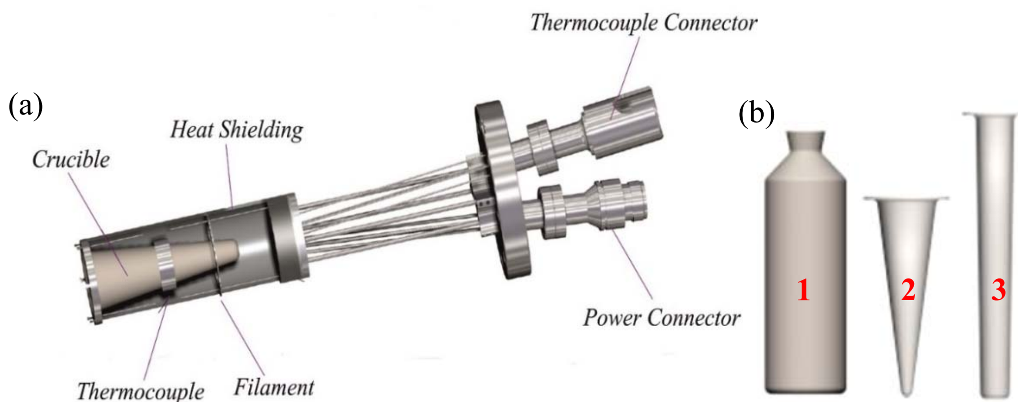

Figure 3.2. (a) A typical effusion cell image (b) Different crucible types where number 1 is SUMO, 2 is conical and 3 is cylindrical crucible [143].

Thickness uniformity and composition of the films vary depending on uniformities of the molecular beam fluxes and geometrical relations between the sources and the substrate material. The flux (*f*) during a growth can be calculated from [144];

$$f = \frac{Pa}{\pi L^2 \sqrt{2\pi m k_B T}} \frac{1}{s.cm^2} \tag{3.1}$$

where T is the source temperature (K), P; the equilibrium vapor pressure in the cell, a; the area of the cell aperture, L; the distance between the source and the substrate, k_B; Boltzmann's constant, and m; the mass of the effusing species. Source material molecular beam fluxes can be calculated from the beam equivalent pressure (BEP) which can be measured by an ion gauge mounted in front of the substrate. BEP can be expressed using the ideal-gas law as [145];

$$BEP = I k_B T_R n \tag{3.2}$$

where I is relative ionization cross section, T_R; the room temperature, and n; molecular density.

Figure 3.3. Gen-20MZ MBE system facility in the department of physics at Iztech.

3.2. CHARACTERIZATION TECHNIQUES

3.2.1. OPTICAL CHARACTERIZATION TECHNIQUES

Optical characterization techniques utilize the measurement of light coming from a material medium. There exist two different class of spectroscopic techniques, namely; 1. Emission spectroscopies and 2. Absorption spectroscopies. 1. In the case of emission spectroscopy, light emitted from the excited entites (atoms, molecules, etc.) of medium are collected and analyzed as the medium entities go back to their natural states loosing energy in the form of light. Raman and Luminescence spectroscipies are typical examples. 2. In absorption spectroscopy, generaly, some incident broad band of a light beam is incident upon the entities of a medium. As the beam traverses the medium, the photons with resonant frequencies between the internal energy levels of the medium atoms will be absorbed exciting the atoms to higher energy levels. Thus any absorbed photon will contribute to a reduction in the intensity of the traveling light beam at the corresponding resonant frequency compared with the incident beam as it travels through the medium. All these transitions are associated mostly with an electrical dipole and hence require charge separation. The absorbtion spectrum thus display all the possible excitations of the medium entities by the incident light photons with varying probabilities seen as a peak with some height in the absorption spectrum at each possible resonant frequency position.

3.2.1.1. Raman Spectroscopy

When a beam of light travels through a material medium, various processes can occur depending on the thickness and the density of the medium atoms. If the medium is thick and dense enough, the incident photons will interact with the medium atoms and will be scattered in a direction usually different from the incident beam direction. During a scattering process, usually a photon is absorbed by a medium entity (atom, molecule, etc.) which is then excited to a higher enery level. Such excited entity will lose its energy by either emitting a new photon or by some other thermal relaxation mechanism such as collisions etc. In the case of a photon emission, most probably the photon will have the

same energy (frequency) as the incident (exciting) photon. This is the case of *elastic* scattering. Such a scattering is also called ‘Rayleigh scattering’. If, on the other hand, the scattered photon has a different energy than that of the incoming photon, the scattering is called *inelastic*. Raman scattering is an inelastic scattering of light from the medium entities. If the scattered photon has a higher (lower) energy than that of the incident one, the scattering is called Stokes (Anti-Stokes) scattering. Thus, Stokes (anti-Stokes) scattered photons will be observed at energies that are lower (higher) than the incident photon energy (Rayleigh line) by the amount equal to the energy difference between the initial and final energy states of the scattering medium entity. Since at ordinary temperatures, most scattering medium atoms are in their ground states, Stokes shifted Raman lines have higher intensities than those of Anti-Stokes lines Anti-stokes lines require medium atoms being already in excited states which are far less populated than the ground state at room temperature and below. Thus, the intensity of Stokes lines will decrease with increasing temperature while that of anti-Stokes lines will increase. For historical reasons scattering of photons from pressure waves (acoustic phonons) is called Brillouin Scattering. Raman scattering was discovered by Chandrasekhara Venkata Raman and published his study with title of ‘*A New Radiation*’ in 1928 [146].

Figure 3.4 illustrates schematically some possible quantum mechanical energy transitions during a scattering of a photon from a medium entity (here it is vibrations of a molecule) whose internal energy levels are indicated. In all cases, a medium entity at an intial state is excited to a virtual state at an energy higher than the initial state by the incident photon energy. Rayleigh, Stokes and anti-Stokes scattering process are all shown in the figure. The ratio of the intensities of the Stokes and anti-Stokes scattering can be calculated from the Boltzmann equation [147];

$$\frac{N_n}{N_m} = \frac{g_n}{g_m} exp\left[\frac{-\left(E_n - E_m\right)}{kT}\right] \tag{3.3}$$

where N_n and N_m are the number of entities in the excited level (n) and in the ground energy level (m), respectively. g_i represents the degeneracy of a level i (n or m), E_n-E_m is the difference in energy between the energy levels, and k is Boltzmann’s constant.

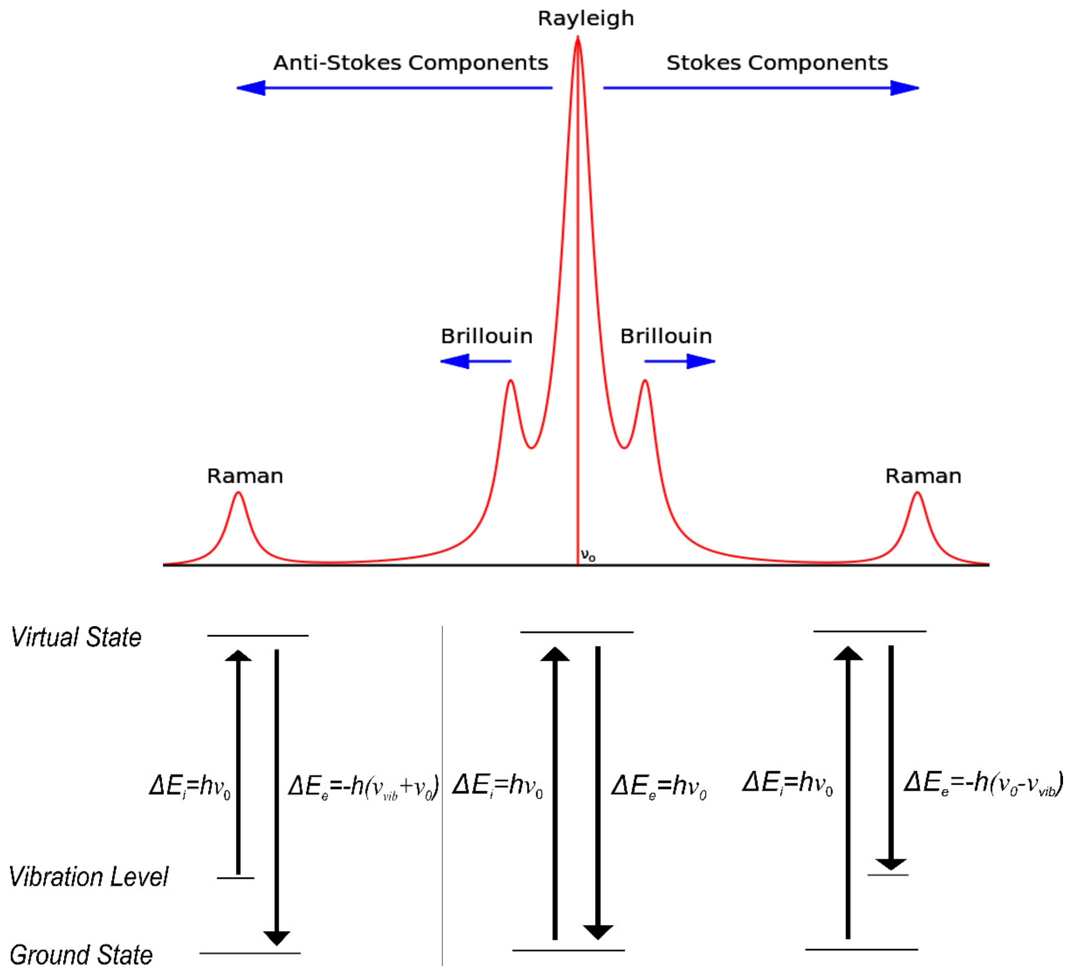

Figure 3.4. Top: A typical spectrum for Anti-Stokes, Rayleigh, and Stokes scattered photons ordered from left to right respectively. Bottom: Quantum excitations and de-excitations of the vibrational levels for the corresponding peaks.

Raman scattering technique thus provides information about the internal energy level separations which yield information about the nature of the material medium entities. Raman spectroscopy requires a minimum sample preparation and provides a non-destructive analysis of solid liquid and gaseous samples. Since a typical Raman scattering probability is about 10^5 or more times smaller than that of a Rayleigh, usualy lasers are employed as monochromatic and intense light sources. If too much laser power is focused on a sample for long enough durations, the effective power on the sample can reach thousands of watts at the point where light is incident. Such laser powers will usually destroy the molecular bonding at that point especially if the sample is thin, organic, or not in a good thermal contact with it's surrounding. Thus, care must be taken for such

samples by reducing the incident light intensity or changing the incident ligh frequency, etc.

A rigorious theoretical treatment of inelastic light scattering requires the proper use of quantum mechanics. However, we can gain a fundamental understanding of the phenomenon employing the classical scattering theory. In the classical picture, one can observe that light, incident upon a medium, induces polarization. The polarized entities of the medium will have their own resonant frequencies usually different from the incident photon frequency. However, the emitted light photon from such a polarized and oscillating entity will be either at the same energy (Rayleigh) or at a lower energy by the amount of internal resonant energy (Stokes) or at a higher energy by an internal resonant energy (anti-Stokes).

As an example let us consider the scattering of light from internal vibrations of molecules. Interaction of incident radiation whose electric field is given as

$$\vec{E} = \vec{E}_0 \cos\left(2\pi\nu_0\right) \tag{3.4}$$

will induce a polarization vector (total dipole moment avaraged over some volume devided by that volume) proportional to this field:

$$\vec{P} = \alpha\vec{E} = \alpha\vec{E_0}\, cos\left(2\pi\nu_0 t\right) \tag{3.5}$$

where α is the polarizability tensor, $\vec{E}_0$ is the vibrational amplitude of the electric field, at frequency ν_0 and t is time. The amplitude q of the vibrating dipoles of molecules with a natural frequency ν and amplitude q_0 is given by ;

$$q = q_0\, cos\left(2\pi\nu t\right) \tag{3.6}$$

One can expand the polarizability tensor into Taylor series interms of displacement about some equilibrium value (usually $q = 0$ for equilibrium, for an initially unpolarized medium) as;

$$\alpha = \alpha_0 + \left(\frac{\partial\alpha}{\partial q}\right)_0 q_0 + \ldots \tag{3.7}$$

where the subscript "*0*" represents the equilibrium values. For small displacements q, one can ignore the higher order terms in (3.7) and keep only the first two terms (linear regime

for polarization). Using (3.7) in (3.5) and after some simplifications one obtains the polarization as

$$\vec{P} = \alpha_0 \overrightarrow{E_0} \cos(2\pi\nu_0 t) + \frac{1}{2}\left(\frac{\partial \alpha}{\partial q}\right)_0 q_0 \overrightarrow{E_0} \left[\cos\{2\pi(\nu_0 - \nu)t\} + \cos\{2\pi(\nu_0 + \nu)t\}\right] \quad (3.8)$$

As is well known from the classical theory of electromagneric radiation, any oscillating dipole with a particular frequency will emit electromagnetic radiation at that frequency. Since the polarization represents the collective behavior of all dipoles in a medium, we conclude that any medium with a polarization as in (3.8) will emit electromagnetic radiation at three distinct frequencies; ν_0 (Rayleigh), $(\nu_0 - \nu)$ (Stokes), and $(\nu_0 + \nu)$ (anti-Stokes) represented by the first, second and third terms in (3.8), respectively.

If there exist strong polarization in a medium due to strong field-medium coupling (either due to strong external field, or strong polarizability, or both) one can no longer ignore the higher order terms in the Taylor expansion of the polarizibility tensor. Thus so called second or higher order terms will also appear in the Polarization vector give rise to corresponding higher order Raman lines in the scattered light.

The intensity (*I*) of the Raman scattered light is given as proportional to the exciting light power (l)on the power of the laser used to excite (*l*), the square of the polarizability of the electrons in molecule (α) , and the fourth power of the frequency of the incident radiation (ω);

$$I = Kl\alpha^2\omega^4 \quad (3.9)$$

where *l* is the incident light power, ω is the (angular) frequency and *K* is a constant [147]. Dependence of *I* to the fourth power of the frequency is easily varified by the strong scattering of blue light in sky compared to the red during a day.

In Raman spectroscopy after collecting the scattered light from a medium, one usually filters the Rayleigh light using appropriate band-pass or band edge filters or uses appropriate scattering angle of a grating spectromter to avoid the Rayleigh line being detected by a proper detector. Raman side bands, seen as shifted lines from the Rayleigh line, thus can easily be detected by an appropriate detector after going through a spectral separation as in a grating spectrometer or it can be obtained from the Fourier Transformed Interferogram in the case of interferometric spectrographs. The spectrum is then recorded

as the intensity of scattered light as a function of photon enery or frequency. Usually one only needs the spectrum recorded at the relative frequencies with respect to the Rayleigh line which corresponds to the internal excitations of a scattering medium. This is optained by simply subtracting the observed spectrum frequencies from the Rayleigh frequency). Thus, usual Raman spectra are recorded as 'Raman shifts' (Usually Stokes, but sometimes anti-Stokes shifted).

In this thesis, Raman measurements were performed by the Iztech Raman system. It is a S&I MonoVista Raman system which includes a 700 mm focal length Princiton Instruments grating spectrometer with a selectable choice of a set of three gratings of 150 grooves(gr)/mm, 600gr/mm, and 1800 gr/mm which are holographic, sensitive from the near IR to near UV region. An Melles-Griot Ar-Ion laser is used for sample excitation. It gives a maximum radiation power at 120 mW for 514 nm and 488 nm wavelengths. A second laser, He-Ne laser, operating at 633 nm is also a part of the system. A motorized rotating mirror on the pathway of the lasers selects one of them. Light coming from a laser is first filtered from the plasma lines and directed to a beamsplitter after passing through a set of neutral density (ND) filters. The beam splitter (BS) diverts some part of the light on to an Olympus BX51 optical microscope from top to bottom. Passing down through a proper objective (5x, 10x, 50x, or 100x) laser light is focused onto the sample surface. (The minimum spot size on a flat sample surface is about 1 micron for 100x objective). The scattered light from the sample which is mounted on an XYZ stage with a full computer and hand control in all directions, is collected in the back-scattering geometry by the same microscope objective. Then, scattered light follows the same optical path back up to the beam splitter where a portion of it is transmitted through the BS and will be directed to the entryway of the monochramator via mirrors. Between the BS and the entrance slit of the monochromator, there exist a rotating set of three Rayleigh rejection notch filters with wavelengths of 633 nm, 514 nm and 488 nm to be selected by the computer to block the particular excitation wavelength. After reaching the monochromator, the light is detected on an array CCD detector (ProEM-EMCCDs Detector) with 1600x200 pixels which has a highest pixel resolution of 0.3 cm^{-1} wavenumber. The data signal collected by the CCD is then sent to the controlling computer for analysis.

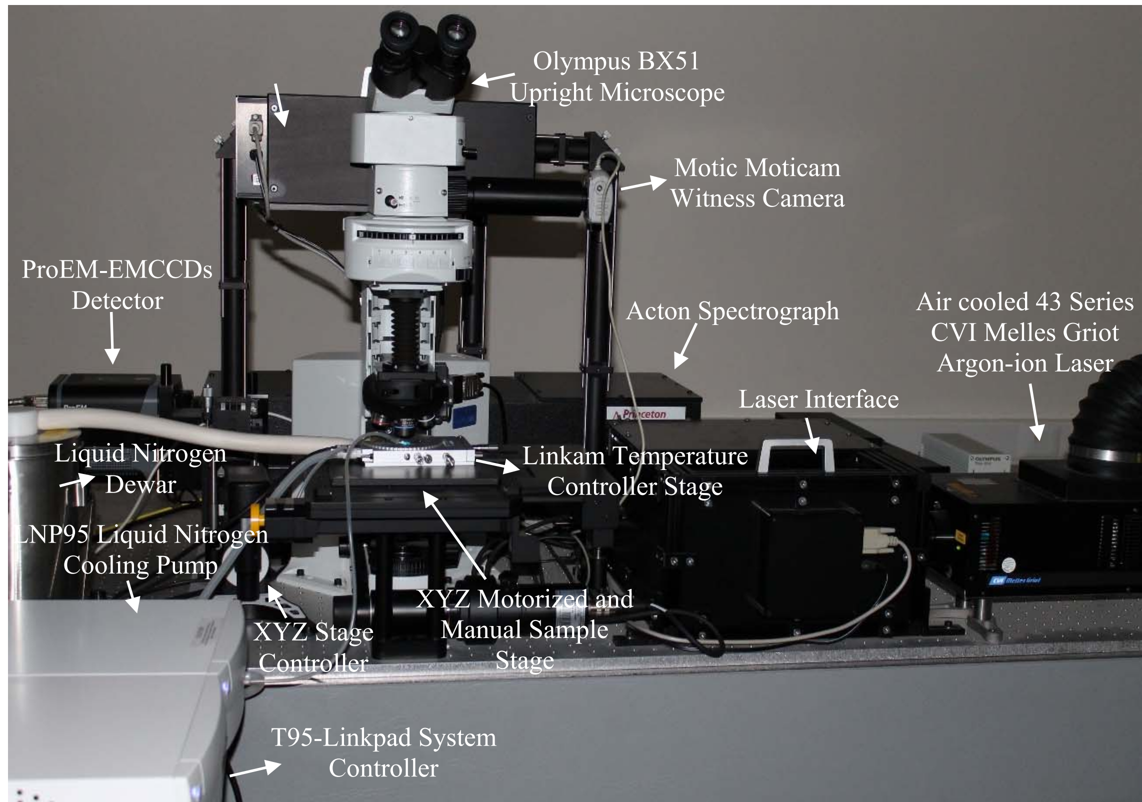

Figure 3.5. MonoVista Raman system components in the department of physics at Iztech.

3.2.1.1.1. Raman Scattering in Zincblende Structures of CdTe and GaAs

Both the II-VI semiconductor CdTe and the III-V semiconductor GaAs have the cubic zincblende (sphalerite) crystal structure with T_d^2 symmetry. The reciprocal lattice is body centered cubic whose first Brillouin zone is given in Figure 2.2 with important symmetry points. Electronic bandstructure and other main properties of CdTe are given in Chapter 2, briefly. Like CdTe, GaAs is also a direct bandgap semiconductor whose valence band maximum and conduction band minimum are at the centre of the Brillouin zone (Γ symmetry point). Electronic band structure of GaAs is given in Figure 3.6. The conduction band minimum is separated by an energy E_0 from the valence band which is four-fold degenerate (Γ_8 symmery). The valence band is separated into three sub-bands namely; heavy hall (*hh*), light hole (*lh*), and a split-off (*so*) bands. The split-off band is doubly degenerate (Γ_7 symmetry) and separated by an energy Δ_0 from the hh and lh bands. The bandgap energy of GaAs (E_0) is about 1.42 eV at room temperature (300 K) and 1.517 eV at zero Kelvin [148]. The spin-orbit splitting value at the zone center (Δ_0) and

in the <111> directions (Δ_1) is given as 0.341 eV and 0.220 eV at zero Kelvin, respectively [149].

Phonon dispersion curves gives phonon energies (E_{phonon}) as a function of phonon wavevector ($\vec{k}_{phonon}$). Direct measurements of the phonon energies and momentums in crystals are provided by either neutron or x-ray scattering experiments. Phonon dispersion curves in GaAs and CdTe along some high symmetry axes are shown in Figure 3.7 and Figure 3.8. In the zincblende type lattices such as GaAs and CdTe, there exist two atoms per primitive unit cell giving rise to six phonon branches with three acoustic phonon and three optical phonon branches. Along high symmetry points, the acoustic and optical phonons can be classified as transverse or longitudinal depending on their displacement directions with respect to the wave vector.

Figure 3.6. Calculated electronic band structure of GaAs [5].

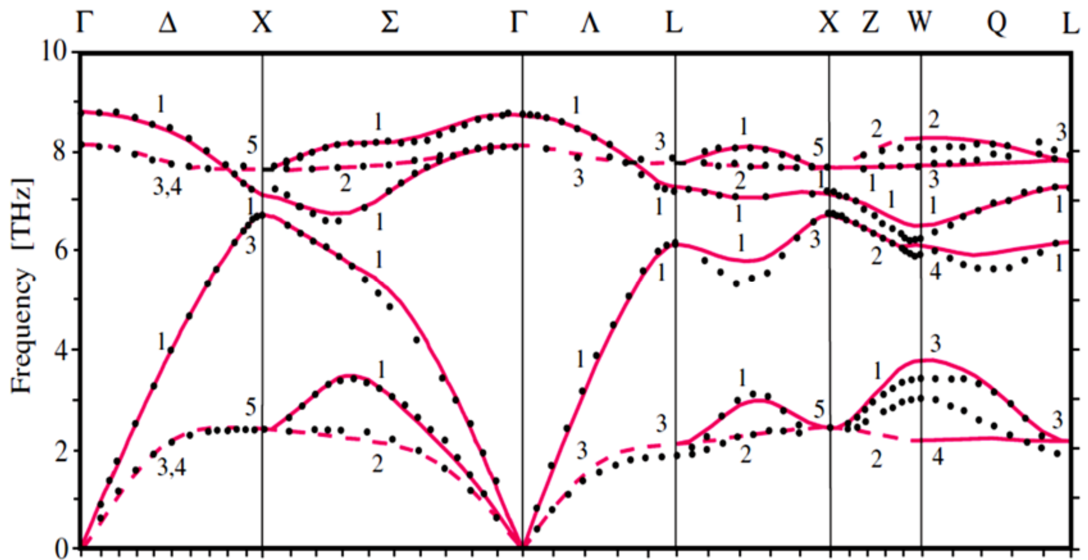

Figure 3.7. Phonon dispersion curves in GaAs. Experimental data shown as points were measured at 12 K by neutron scattering and continuous lines were calculated with a 15-parameter rigid-ion model [150].

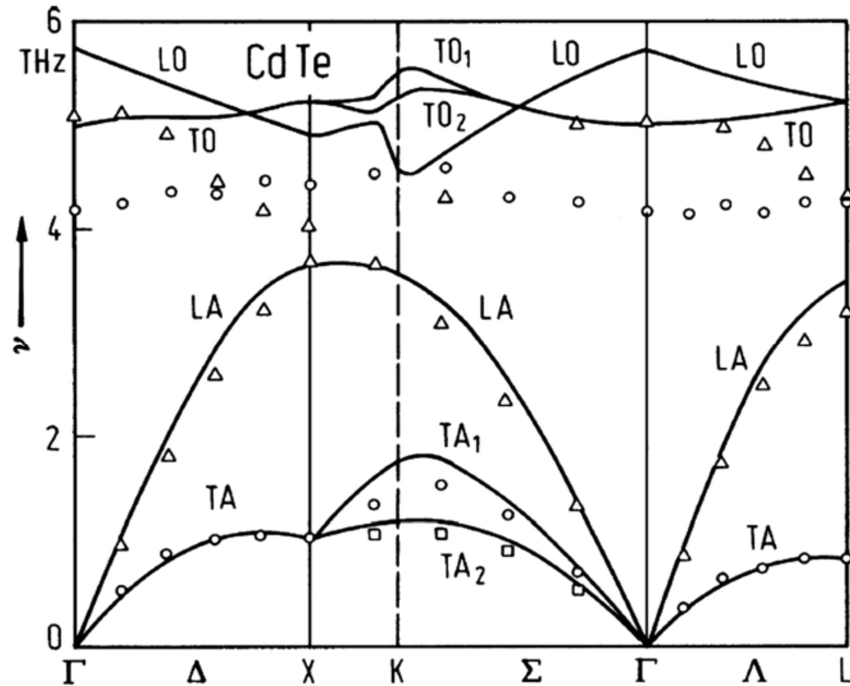

Figure 3.8. Phonon dispersion curves in CdTe where solid lines were calculated from a first principles binding force model in comparison with neutron scattering data [151].

In order to understand Raman scattering process in both CdTe and GaAs semiconductors, the intensity of scattered radiation (I_s) can be written in terms of polarizations of incident radiation (e_i)and scattered radiation (e_s) as [5];

$$I_s \alpha \omega_s^4 . \left| e_i . \left(\frac{\partial \chi}{\partial Q} \right)_0 Q(\omega_0) . e_s^2 \right| . E_i^2 \tag{3.10}$$

where e_i and e_S are the polarizations of incident and scattered radiation, respectively, Q; phonon amplitude, χ; the electric susceptibility, and E_i; the electric field of the incident radiation. If we assume Q is the vector displacement of a given atom induced by the phonon, Raman tensor is given by;

$$\Gamma = \left| \left(\frac{\partial \chi}{\partial Q} \right)_0 \hat{Q}(\omega_0) \right| \tag{3.11}$$

where $\hat{Q}$ is unit vector parallel to phonon displacement. The symmetry of the Raman tensor and hence the symmetry of the corresponding Raman-active phonons can be found using the dependence of the scattered intensity on the incident and scattered polarizations. Raman tensors for the symmetries of vibrational modes in zincblende structure were given by Loudon [152];

$$\begin{array}{ll} \Gamma_1 : \begin{pmatrix} a & 0 & 0 \\ 0 & a & 0 \\ 0 & 0 & a \end{pmatrix} & \Gamma_{15}(x) : \begin{pmatrix} 0 & 0 & 0 \\ 0 & 0 & d \\ 0 & d & 0 \end{pmatrix} \\ \Gamma_{12} : \begin{pmatrix} b & 0 & 0 \\ 0 & b & 0 \\ 0 & 0 & -2b \end{pmatrix} & \Gamma_{15}(y) : \begin{pmatrix} 0 & 0 & d \\ 0 & 0 & 0 \\ d & 0 & 0 \end{pmatrix} \\ \Gamma_{12} : \begin{pmatrix} -\sqrt{3b} & 0 & 0 \\ 0 & -\sqrt{3b} & 0 \\ 0 & 0 & 0 \end{pmatrix} & \Gamma_{15}(z) : \begin{pmatrix} 0 & d & 0 \\ d & 0 & 0 \\ 0 & 0 & 0 \end{pmatrix} \end{array} \tag{3.12}$$

where triply degenerate representation of Γ_{15} is given by polarized optical phonons in x,y and z axes while a, b and d equals to third rank tensor; $(\partial \chi / \partial Q)$. For CdTe and GaAs zincblende structures, both acoustic and optic modes have symmetry species Γ_{15} and triply degenerate at the zone center according to the group theory. Also, for surfaces of

both CdTe and GaAs, macroscopic electric field associated with the longitudinal optical optical mode (LO) gives higher energies than transverse optical phonon (TO) due to ionic nature of the bonding in zincblende crystals. Thus, LO phonon frequency in GaAs and CdTe are higher than the TO phonon frequencies. There exist a simple expression between TO and LO frequencies near the Brillouin zone centre which is known as Lyddane-Sachs-Teller equation [153];

$$\frac{\omega_{LO}^2}{\omega_{TO}^2} = \frac{\varepsilon_0}{\varepsilon_\infty} \tag{3.13}$$

where ε_0 and ε_∞ are static (long wavelength limit) and optical (high wavelength limit) dielectric constants, respectively. The first and second order Raman selection rules were determined by Poulet and Birman, respectively [154, 155]. According to Poulet's definition of the first order Raman scattering; the scattering intensity matrices for the (100) and (110) crystal orientations are given by;

$$\begin{aligned} \theta_{LO}(100) = E_i^2 \begin{pmatrix} 0 & \frac{1}{2} & 0 \\ \frac{1}{2} & 0 & \frac{1}{2} \\ 0 & \frac{1}{2} & 0 \end{pmatrix} \quad & \theta_{TO}(100) = E_i^2 \begin{pmatrix} 0 & \frac{1}{2} & 1 \\ \frac{1}{2} & 0 & \frac{1}{2} \\ 1 & \frac{1}{2} & 0 \end{pmatrix} \\ \theta_{LO}(110) = E_i^2 \begin{pmatrix} 0 & \frac{1}{2} & 0 \\ \frac{1}{2} & 0 & \frac{1}{2} \\ 0 & \frac{1}{2} & 0 \end{pmatrix} \quad & \theta_{TO}(110) = E_i^2 \begin{pmatrix} 1 & \frac{1}{2} & 0 \\ \frac{1}{2} & 0 & \frac{1}{2} \\ 0 & \frac{1}{2} & 1 \end{pmatrix} \end{aligned} \tag{3.14}$$

The second order Raman scattering involves two phonon processes most of which taking place near the first Brillouin zone boundary. Raman spectrum of the two phonon processes can be obtained for the critical points on the Brillouin zone boundary. For zincblende structures, critical points on the Brillouin zone boundary occur at Γ(0, 0, 0), X(1, 0, 0), L(1/2, 1/2, 1/2) and W(1, 1/2, 0) [156]. However, when compared to other critical points in zincblende structure, Γ(0, 0, 0) has low density of states. Birman found that all two phonon processes are Raman active in zincblende crystals. The selection rules for the zincblende structure are given in Table 3.1 where ⊗ symbol defines the overtone

of the phonon modes. The optical phonons at those critical points consist of two degenerate TO modes and one LO mode. At the exact zone center, the TO and LO phonons in the zincblende cystals are degenerate due to the cubic symmetry.

Table 3.1. The selection rules for the zincblende structure according to Birman.

Critical Point	Irreducible Representation	Polarization	Sums and overtones	Raman Activity
L	L_3	TA(L)	LA⊗LO	$\Gamma_1+\Gamma_{15}$
	L_1	LA(L)	LA⊗LO= TA⊗TO	$\Gamma_{12}+\Gamma_{15}$
	L_3	TO(L)	TA⊗LA= TO⊗LO	$\Gamma_{12}+\Gamma_{15}$
	L_1	LO(L)	TA⊗TO	$\Gamma_1+\Gamma_{12}+\Gamma_{15}$
			2LA=2LO	$\Gamma_1+\Gamma_{15}$
			2TA=2TO	$\Gamma_1+\Gamma_{12}+2\Gamma_{15}$
W	W_1		$W_1\otimes W_2= W_3\otimes W_4$	$\Gamma_{12}+\Gamma_{15}$
	$2W_2$		$W_1\otimes W_3= W_1\otimes W_4$	Γ_{15}
	$2W_3$		$W_2\otimes W_3= W_2\otimes W_4$	Γ_{15}
	W_4		$W_2\otimes W_2= W_3\otimes W_3$	$\Gamma_1+\Gamma_{12}$
			$2W_1=2W_2$	$\Gamma_1+\Gamma_{12}$
			$2W_3=2W_4$	$\Gamma_1+\Gamma_{12}$
X	X_5	TA(X)	LA⊗LO	Γ_{15}
	X_1	LA(X)	TA⊗LA= LA⊗TO	Γ_{15}
	X_5	TO(X)	TA⊗LO= TO⊗LO	Γ_{15}
	X_3	LO(X)	TA⊗TO	$\Gamma_1+2\Gamma_{12}+\Gamma_{15}$
			2LA=2LO	$\Gamma_1+\Gamma_{12}$
			2TA=2TO	$\Gamma_1+2\Gamma_{12}+\Gamma_{15}$
Γ	Γ_{15}	LO(Γ)	LO	Γ_{15}
	Γ_{15}	TO(Γ)	TO	Γ_{15}

Raman studies show that the Raman active modes in undoped-GaAs are TO and LO phonon modes. At the zone center (Γ(0, 0, 0)), TO and LO phonon modes of GaAs are at 268.2 cm^{-1} and 291.5 cm^{-1}, respectively [5] at zero Kelvin. Γ_1 and Γ_{15} components of the second-order Raman spectrum of GaAs is shown in Figure 3.9 in which first order scattering is observed only in Γ_{15} symmetry including the peaks at TO(Γ) and LO(Γ) phonon modes. Additionally, the surface-optical (SO) phonon mode can be observed at 279.0 cm^{-1} according to numerical calculations of dispersion relation of SO phonons for a GaAs film by A. M. Alencar *et al.* [157]. Generally, the SO phonon mode appears as a shoulder of LO phonon mode forming a broad linewidth which makes it hard to

distinguish. Due to being close to LO phonon mode, it is hard to distinguish. The existence of SO phonon mode feature is important especially for GaAs nanowires to determine the quality of the samples in which the size dependent shift of SO phonon mode gives information about the diameter of the nanowires [158].

Figure 3.9. Γ_1 and Γ_{15} components of the second-order Raman spectrum of GaAs with an excitation photon energy of 2.81 eV [159].

Observed phonon features in a doped-GaAs crystal is similar to those in an undoped-GaAs with a difference. The LO phonon observed in the undoped-GaAs couples with free carriers (Frohlich interaction) giving rise to two so called LO phonon--plasmon coupled modes (LOPC); L_- and L_+ instead whose frequencies change with the free carrier concentration [160]. On the other hand, there are four atoms per unit cell in the wurtzite GaAs which give rise to nine optical phonon modes which are; an A_1 mode polarized in the z direction, an E_1 mode polarized in the xy plane, two E_2 branches low (l) and high (h), referred as E_2^l and E_2^h, and two B_1 modes. A_1 and E_1 modes split into transverse and longitudinal optical components that are A_1(TO) and E_1(TO) observed at 267 cm^{-1}, and A_1(LO) and E_1(LO) modes at 291 cm^{-1} [161]. In addition, impurities and defect centers can give rise to additional vibrational modes or they can activate some of the inactive vibrational modes due to symmetry breaking. If the impurities replace heavier the host

atoms, their vibrational frequencies lie above the phonon frequency range and giving the localized vibrational modes (LVM's) observed as sharper peaks in their spectra. For example, intersititial oxygen, vacancy oxygen complexes, carbon impurities, carbon-hydrogen complexes, $(C_{As})_2H$ complexes in GaAs:C and SiO_2 complexes in oxygen implanted GaAs:Si leads to LVM spectra in GaAs [162]. Another important feature in the spectra of GaAs is a broad band observed between 180 and 260 cm^{-1} which is assigned to As precipitate formation by segregation of excess arsenic [163].

As in the zincblende GaAs, two main Raman active phonon modes in zincblende CdTe are TO and LO phonon modes. The TO and LO phonon modes of CdTe occur approximately at 140 and 175 cm^{-1}, respectively [164]. In addition to TO and LO phonon modes, the peaks at 120 cm^{-1} and 147 cm^{-1} are the phonon with A_1 and E symmetry modes of tellurium which shows Te precipitates in CdTe [165]. It has been reported that as the density of Te precipitates increases, the Raman intensity of A_1 and E symmetry modes of Te will also increase [166]. Additional modes observed near 92 and 103 cm^{-1} show the presence of Te on the surface of CdTe [167]. All Raman active mode frequencies shift to higher values with decreasing temperature. For example, in CdTe, TO mode frequency (wavenumber) shifts from 141 cm^{-1} at RT to 144 cm^{-1} at 100K while LO mode shifts from 168 cm^{-1} at RT to 170 cm^{-1} at 1.2K [168, 169]. In addition, infrared absorption studies reveal the transverse acoustic (TA) and the longitudional acoustic (LA) phonon modes with frequencies at 35 cm^{-1} and 97 cm^{-1} at room temperature, respectively [170]. Combined phonon mode frequencies in wave numbers (cm^{-1}) are listed in Table 3.2 for CdTe. In a doped CdTe, Raman intensities of phonon modes are reduced compared to the those of a pure CdTe [171]. Introducing Zn into CdTe with a fraction of x while reducing the Cd fraction by the same amount from 1 in pure CdTe to 1-x (which acturally requires addition of more Te duing the growth to maintain stoichiometry) produces a ternary compound; $Cd_{1-x}Zn_xTe$. Such a ternary will exhibit a band gap changing with the compositional fraction x which makes it suitable for 'band gap engineering'. Raman peaks of $Cd_{1-x}Zn_xTe$ also show a strong dependence on the compositional fraction x. In the Raman spectra, obtained from (100) surfaces of bulk $Cd_{1-x}Zn_xTe$, LO and TO frequencies change with the composition x as shown in Figure 3.10 where CdTe- and ZnTe-like LO and TO modes are denoted as LO_1, TO_1 and LO_2, TO_2, respectively.

Table 3.2. Combined phonon modes in CdTe and their frequencies in wave numbers (cm^{-1}) measured at 293 K using dispersive Fourier transform spectroscopy [172].

Combined Phonon Modes	Phonon wavenumber (cm^{-1})
TO(L)-LA(L)	40
2TA(L)	62.5
2TA(X)	69
TA(L)-TA(L)	73
TA(X)-TA(X)	91
LO(X)-TA(X)	102
TO(L)-TA(L)	112
TO(X)-TA(X)	116
LA(L)+TA(L)	134
LA(X)+TA(X)	160
LO(X)+TA(X)	171
TO(L)+TA(L)	173
TO(X)+TA(X)	184
2LA(L)	208

It can be seen that only LO phonons are allowed near the (100) surface of bulk $Cd_{1-x}Zn_xTe$. For fraction x equal to or greater than 0.01, the ZnTe and CdTe-like LO phonon modes are clearly resolved. For fractions of x smaller than 0.1, the second order LO phonons ($2LO_1$, LO_1+LO_2 and $2LO_2$) are observed between 310 and 380 cm^{-1}. TO (CdTe) and LO (CdTe) phonons in $Cd_{0.6}Zn_{0.4}Te$ occur approximately at 137 cm^{-1} and 163 cm^{-1}, respectively [173]. Second-order Raman scattering of CdTe and ZnTe involve A_1 and E symmetries. The peak at 120 cm^{-1} is due to the phonons with A_1 symmetry of Te precipitates in $Cd_{0.6}Zn_{0.4}Te$. In addition, it has been reported that the features at 122.5 cm^{-1} is associated with the E_1 symmetry of the phonon vibrations in the TeO structure[174].

LVMs generally introduce in doped CdTe with Se, H, Ti, Fe, Bi and Zn. Se and H doping leads to a LVM peak at 173 cm^{-1} and 1205 cm^{-1} at room temperatures, respectively [175, 176]. Ti isotopes (^{50}Ti, ^{49}Ti, ^{48}Ti, ^{47}Ti and ^{46}Ti) give five distinct LVM peaks around 225 cm^{-1} in Ti doped CdTe [177]. Thus one can study the isotopic

composition of the dopand atoms from their LVM signatures. It has been reported that Bi-doped CdTe samples show a Raman peak at 96 cm^{-1} [178]. In addition, Fe and Zn occupations of cadmium lattice sites give rise to LVMs at 196 cm^{-1} and 73 cm^{-1}, respectively [179].

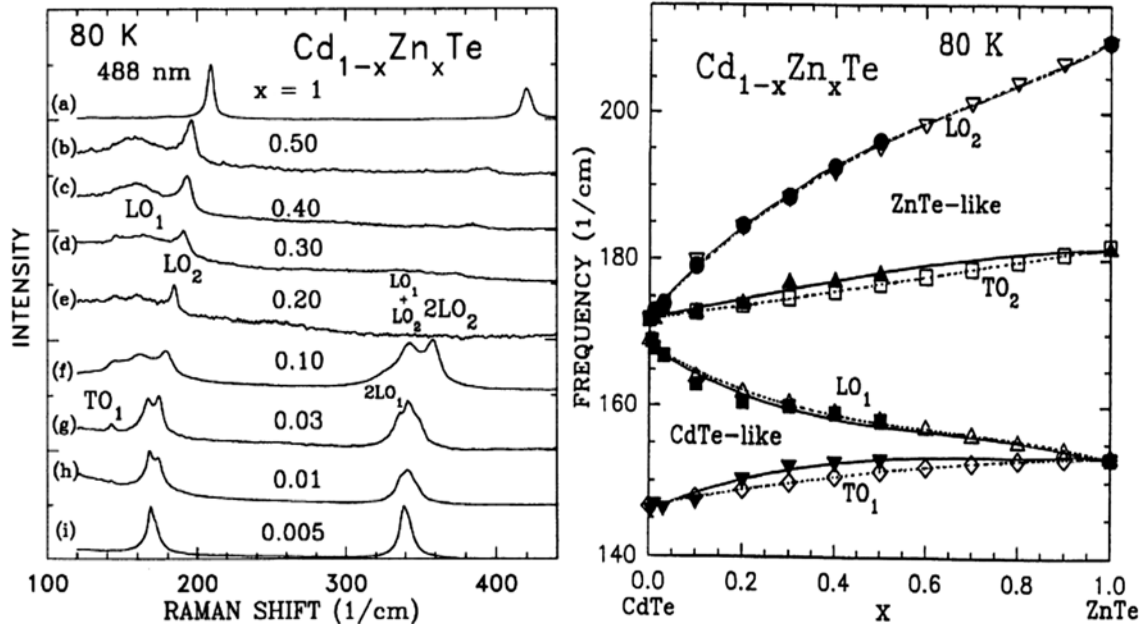

Figure 3.10. (a) Raman spectrum of bulk $Cd_{1-x}Zn_xTe$ at 80K with composition x of (a) 1, (b) 0.5, (c) 0.40, (d) 0.30, (e) 0.20, (f) 0.10, (g) 0.03, (h) 0.01, (i) 0.005 and (b) Variation of LO and TO frequencies in $Cd_{1-x}Zn_xTe$ as a function of composition x [180].

3.2.1.2. Fourier Transform Spectroscopy (FTRs)

Fourier Transform Spectroscopy (FTRs) is a non-destructive technique providing a very effective, fast, and high quality measurement of transmission, reflection and absorption spectra of thin films, bulk samples, liquids, and gases. It is also a very powerfull technique for emission spectroscopies especialy for near and far IR regions. It yields a broad range of information related to electronic, vibrational, and rotational excitations in samples. Additionally, it can provide geometric information for solid samples such as thickness for thin films and diameter for nano dots.

FTRs is based on an interferometric spectrometer whose data (interferogram) is Fourier Transformed, to yield the spectrum, and analized by a controlling host computer.

An ordinary FT spectrometer is composed of a range of broad band sources for abosorption studies (reflectance and transmittance) or some exciting high power single frequency sources, such as lasers, for emission spectroscopies (PL, Raman, etc..). In the emission spectroscopies, sample is first excited by a high power single frequency light then the radiation from the sample is analized. Thus, sample itself acts like a broad band source. Any broad band light coming from a source in an FT system goes through an interferometer (such as a Michelson Interferometer as seen in the Figure 3.11, A. A. Michelson in 1891 [181]. In the (Michelson) interferometer, light from a source, first collimated by a proper set of optics, is incident on a beam splitter (BS). The BS partially reflects the light and partially transmits with no significant absorption. The reflected and transmitted beams are recombined again at the BS after being reflected from a fixed and a moving mirror which are always positioned at 90 degrees with respect to each other with a zero degree angle of incidence as seen in the Figure 3.11. Thus recombined beam exhibiting the same polarization yields an intensity variation depending on the optical path difference, δ, between the two beams coming from the mirrors. Thus, the interferogram, the recombined beam intensity, is then recorded by a detector, placed on the optical path, in terms of digitized electrical signals and sent to the controlling computer. The detector can either be a single channel detector, such as a photomultiplier tube (PMT), or a multichannel detector, such as a CCD camera (more common recently). Thus, the digitized interferogram is Fourier Transformed from x-space (δ, the mirror separation distance or optical path difference (OPD)) to frequency space, usually using a Fast Fourier Transform algorithm (originally due to Cooley and Tukey, [182]) to yield the spectrum in the controlling computer. For absorption studies, sample is usually positioned between the interferogram and the detector as opposed to the emission case where sample must be positioned before the interferogram. In Figure 3.11, the OPD is seen to be

$$\delta = 2\left(\overline{OM} - \overline{OF}\right) \tag{3.15}$$

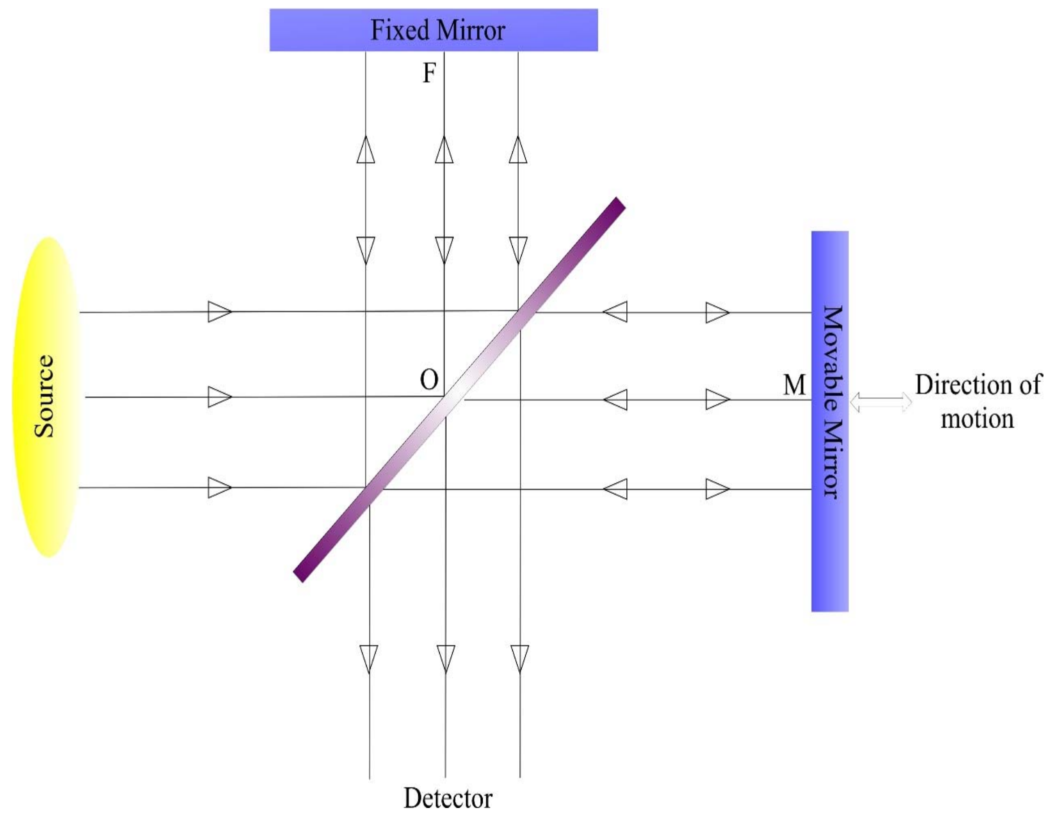

Figure 3.11. Michelson Interferometer

Note that sometimes a quarter wave plate is positioned on one of the beam arms to account for additional reflectivity at the beamsplitter. When fixed and movable mirrors are at the same distance from the beamsplitter, *zero path difference* (ZPD) occurs and two beams are perfectly in phase for all frequencies yielding a constructive interference. For a broad band source such constructive interference condition is lost at large optical path differences and usually intensites goes to zero.

Figure 3.12 shows interferogram obtained from low pressure air showing water vapor excitation lines in a specific region of spectrum.

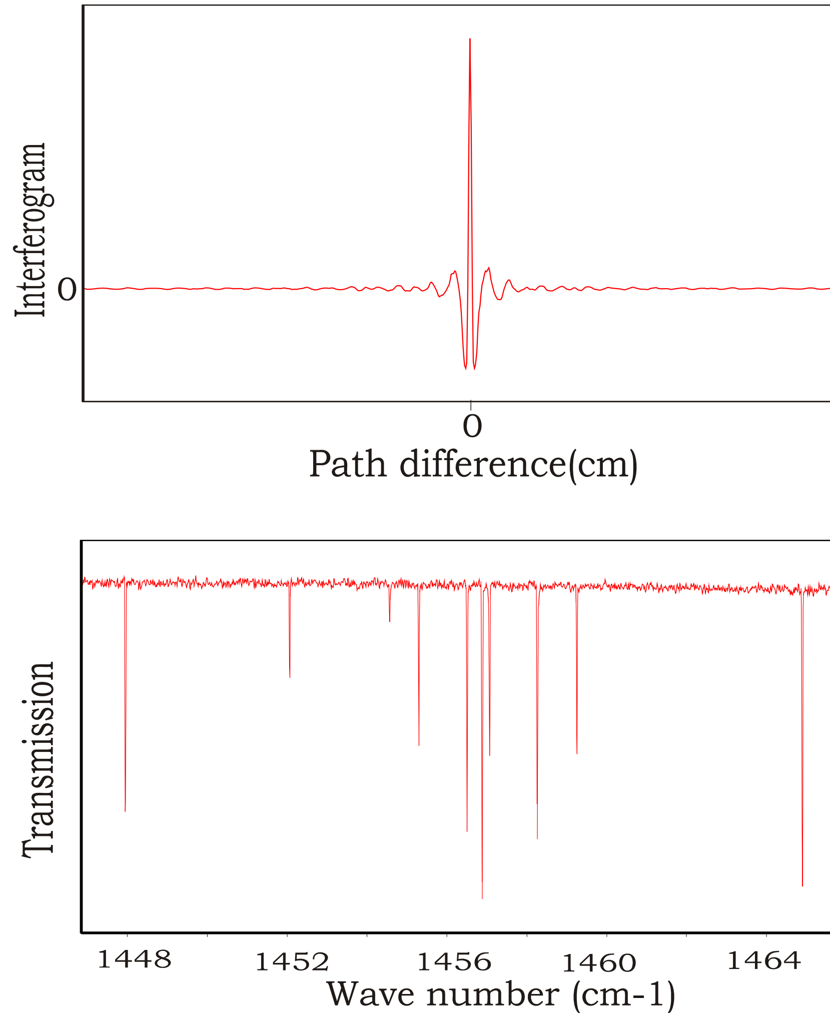

Figure 3.12. Interferogram (top) and spectrum (bottom) of water vapor in air.

3.2.1.2.1. Basic Theory of FT Spectroscopy

Let us consider a monochoromatic light beam incident on a beamsplitter from a laser. Its electric field at an angular frequency $\omega = 2\pi\nu$, ν being frequency, in complex notation, is given as

$$\vec{E}_{in} = \vec{E}_0 \, e^{-i(\vec{k}\vec{x}_0 - \omega t)} \tag{3.16}$$

where $\vec{E}_0$ is the maximum amplitude, $\vec{k}$; the wave vector, $\vec{x}_0$; the position of the field, and t ; time. After reaching BS, two beams emerge moving towards fixed and moving mirrors with fields given as

$$\vec{E}_1 = \vec{E}_{01} e^{-i(\vec{k}\vec{x}_{01} - \omega t)} \tag{3.17}$$

$$\vec{E}_2 = \vec{E}_{02} e^{-i(\vec{k}\vec{x}_{02} - \omega t)} \tag{3.18}$$

The final amplitude at the detector can be written as the superposition of the two beams;

$$\vec{E} = \vec{E}_1 + \vec{E}_2 \tag{3.19}$$

The intensity is proportional to $\vec{E}^* . \vec{E}$ and resultant intensity can be calculated as;

$$I \propto \left(\vec{E}\right)^* \cdot \vec{E} =$$

$$= \left(\vec{E}_{01} e^{i(\vec{k}\vec{x}_{01} - \omega t)} + \vec{E}_{02} e^{i(\vec{k}\vec{x}_{02} - \omega t)}\right) . \left(\vec{E}_{01} e^{-i(\vec{k}\vec{x}_{01} - \omega t)} + \vec{E}_{02} e^{-i(\vec{k}\vec{x}_{02} - \omega t)}\right)$$

$$= E_{01}^{\ 2} + E_{01}.E_{02} e^{i(\vec{k}\vec{x}_{01} - \omega t)} e^{-i(\vec{k}\vec{x}_{02} - \omega t)} + E_{02}^{\ 2} + E_{02}.E_{01} e^{i(\vec{k}\vec{x}_{02} - \omega t)} e^{-i(\vec{k}\vec{x}_{01} - \omega t)}$$

$$= E_{01}^{\ 2} + E_{02}^{\ 2} + E_{01}.E_{02} e^{i\vec{k}(\vec{x}_{01} - \vec{x}_{02})} + E_{02}.E_{01} e^{i\vec{k}(\vec{x}_{02} - \vec{x}_{01})}$$

$$= E_{01}^{\ 2} + E_{02}^{\ 2} + E_{01}.E_{02}\left(e^{i\vec{k}(\vec{x}_{01} - \vec{x}_{02})} + e^{i\vec{k}(\vec{x}_{02} - \vec{x}_{01})}\right) \tag{3.20}$$

where the last term in paranthesis can be written using the Euler's formula;

$$\cos\theta = \frac{e^{i\theta} + e^{-i\theta}}{2} \tag{3.21}$$

and eq. 3.21 becomes;

$$= E_{01}^{\ 2} + E_{02}^{\ 2} + 2E_{01}E_{02}\cos\left(\vec{k}.\vec{\delta}\right) \tag{3.22}$$

where $\vec{\delta} = \vec{x}_{02} - \vec{x}_{01}$ and $\vec{k}.\vec{\delta} = 2\pi\delta / \lambda$, $\vec{k}$ is the wave vector. Beamsplitter splits light beam into two equal amplitudes as;

$$E_{01} = E_{02} = E_0 \quad (3.23)$$

Then, eq. 3.23 becomes;

$$= 2E_0^{\,2}\left(1 + \cos\left(\frac{2\pi\delta}{\lambda}\right)\right) \quad (3.24)$$

In terms of *wave number,* $\sigma = 1/\lambda$

$$\left(\vec{E}\right)^{*} \cdot \vec{E} = 2{E_0}^{2}\{1 + \cos(2\pi\sigma_0\delta)\} \quad (3.25)$$

The intensity at the detector will now be

$$I(\delta) = B(\sigma_0)\{1 + \cos(2\pi\sigma_0\delta)\} \quad (3.26)$$

where $B(\sigma_0) \propto {E_0}^2$ is the individual beam intensity from each mirror. At ZPD, $\delta = 0$

$$I(0) = B(\sigma_0)\{1 + \cos(0)\} = 2B(\sigma_0) \rightarrow B(\sigma_0) = \tfrac{1}{2}I(0) \quad (3.27)$$

Thus,

$$I(\delta) = \tfrac{1}{2}I(0)\{1 + \cos(2\pi\sigma_0\delta)\} \quad (3.28)$$

or

$$I(\delta) - \tfrac{1}{2}I(0) = \tfrac{I(0)}{2}\cos(2\pi\sigma_0\delta) \quad (3.29)$$

which can also be expressed as

$$F(\delta) = I(\delta) - \tfrac{1}{2}I(0) = B(0)\cos(2\pi\sigma_0\delta) \quad (3.30)$$

Thus, it is clear that the observed intensity $I(\delta)$, which is the interferogram, has a clear sinusoidal dependence on the beam path separation δ. The new intensity function $F(\delta)$ now, can easily be used for Fourier cosine transform of equation (3.30) to yield the intensity $B(\sigma)$ for all wavenumbers σ in the region of interest yielding the spectrum:

$$B(\sigma) = (constant)\int_{-\infty}^{\infty} F(\delta)\cos(2\pi\sigma\delta)\, d\delta \tag{3.31}$$

where the choice dependent ($constant$) before the integral is usually set to 1 for convenience. For a monochromatic light beam, using (3.30) in (3.31) and carrying out the integration, one obtains;

$$B(\sigma) = \frac{1}{2}[\delta_{dirac}(\sigma - \sigma_0) + \delta_{dirac}(\sigma + \sigma_0)] \tag{3.32}$$

This result produces two very sharp peaks of zero width (delta functions) at wavenumbers $-\sigma_0$ and $+\sigma_0$. But physically only $+\sigma_0$ is real. Hence any sinusoidal interferogram of a definite frequency in the real space will produce a delta function with that frequency in the frequency space which corresponds to the contribution of the sinusoidal component at that particular frequency. A real interferogram will consist of many sinusoidal components superposed on top of each other, thus producing a central sharp peak at the ZPD where they always interfere constructively and making oscillatory exponential decays with δ going to infinity as seen in the Figure 3.13. Generally, one obtains $F(\delta)$, the interferogram function, (the real interferogram is $I(\delta)$) from the measurement and uses it in the Equation (3.30) for all frequencies (here wavenumbers σ) to obtain the final spectrum.

In the Equation (3.31), the integral is carried out for all mirror separations from $-\infty$ to $+\infty$. However, that requires an infinitely long mirror arm movement (at least in one way, so the other way will be symmetrically equal). In practice that is impossible and the maximum mirror displacments are finite, say, from $-L$ to $+L$. Thus, the real Fourier transform equation of any interferogram functioin $F(\delta)$ will now be:

$$B(\sigma) = (constant)\int_{-L}^{L} F(\delta)\cos(2\pi\sigma\delta)\, d\delta \tag{3.33}$$

Now we can ask; what happenes to the monochromatic light incident on the interferometer? For that, again using (3.32) in (3.33) and carrying out integration, one finds the spectrum as;

$$B(\sigma) = 2L\left\{\frac{sin[2\pi(\sigma+\sigma_0)L]}{2\pi(\sigma+\sigma_0)L} + \frac{sin[2\pi(\sigma-\sigma_0)L]}{2\pi(\sigma-\sigma_0)L}\right\} \tag{3.34}$$

The first term, again gives a peak at $-\sigma_0$ while the second one is peaked at $+\sigma_0$. Ignoring the physically impossible first term, the solution now becomes;

$$B(\sigma) = 2L\frac{sin[2\pi(\sigma-\sigma_0)L]}{2\pi(\sigma-\sigma_0)L} = 2Lsinc[2\pi(\sigma-\sigma_0)L] \qquad (3.35)$$

Now the result is no longer a delta functioin peaked at $+\sigma_0$ but a sinc function which has a strong central maximum where its argument is zero but dying down oscillatorily when its argument goes to positive or negative infinity as seen in the figure below for $z = 2\pi(\sigma-\sigma_0)L$.

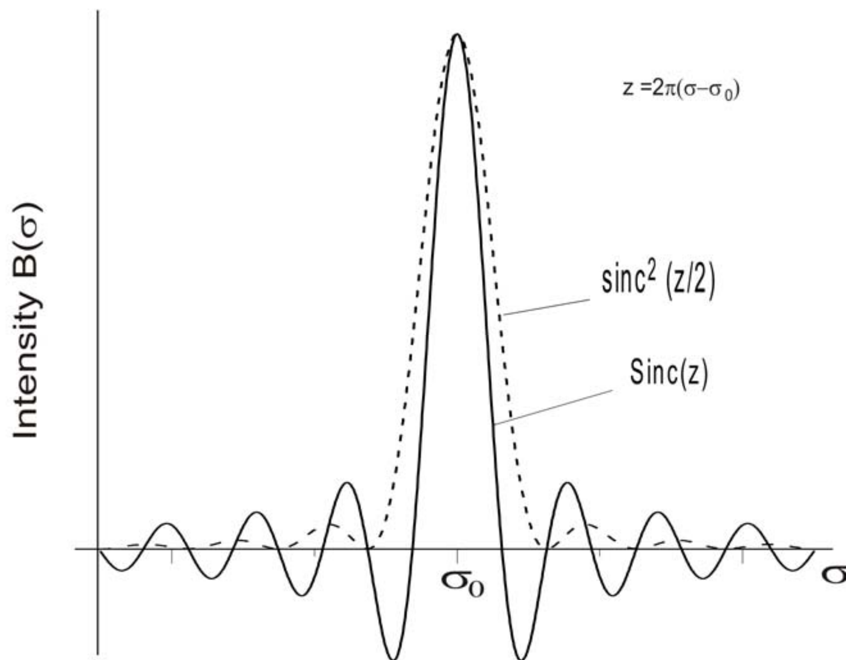

Figure 3.13. Spectrum of a monochoromatic line with a wavenumber $\boldsymbol{\sigma_0}$. Instrumental effect leads to a $\boldsymbol{sinc(z)}$ function. With a proper apodization $\boldsymbol{sinc^2(z)}$ function is obtained [183].

Thus, the effect of a finite maximum mirror displacement is a line broadening at σ_0 as well as some side lobes (peaks) near the major peak as seen in the Figure 3.13 in the *sinc* function. One reduces the effect of such secondary maxima (side lobes) by multiplying the interferogram with an 'apodization function' before carrying out the Fourier transform. We can for example employ $(1-|\delta|/L)$ as our apodizatioin function. Thus the result becomes $B(\sigma) = constant \times sinc^2(z)$ function which is also shown in

the same figure. Notice that side lobes are substantially reduced. Also no negative intensity effect is observed. However, the resolution which is measured as the full width of the central peak at its maximum height (FWMH) is now worse due to broadening.

Any Frourier transform spectrometer has two major advantages over a grating spectrometer working under similar conditions. Theser are; the *Jacquinot* or *throughput* advantage and the *Fellgett* or *multiplex* advantage. First one is due to the fact that the beam of light analized in a FT system will not suffer from an intensity reduction which is the case for grating spectrometers where only a small fraction of the total intensity is collected at a time due to dispersion. The second case is due to the ability of a FT system collecting all the frequencies at the same time in a wide spectral band while a grating spectrometer collects only a single frequency at a time as the average of a very narrow band of frequencies. The net effect of these two advantages is a reduction in the noise level increasing the signal to noise level (S/N). The radio of S/N levels for the two systems can be given as

$$\frac{(S/N)_{FT}}{(S/N)_{G}} = \sqrt{M} \tag{3.36}$$

where the index FT is for Fourier transform and the index G is four grating. M depicts the number of data points in the spectral range of interest [184]. Thus, for 10000 data points, for example, a FT system produces 100 times better S/N for a comparably set grating system. In the infrared, most of the noise is due to detectors and (3.36) is valid. In the visible, however, detectors are much more sensitive and source noise is dominant which will be the same for both techniques and Fellgett advantage of FT systems is lost.

An additional practical advantage of an FT system is that it is self-calibrating requiring no user manipulation which is known as the *Connes advantage*. [185, 186]. This has to do with the fact that the ZPD is self detected by the FT system and each and every mirror position is precisely calculated via internal electronics, mechanism, and optics.

3.2.1.3. Nomarski Interference Microscopy (NIM)

Nomarski Interference Microscopy (NIM) or sometimes referred as Differential Interference Contrast (DIC) Microscopy was first introduced by G. Nomarski and patented in 1960 [187]. NIM can be used to examine the surface morphology of

epitaxially grown structures in detail using phase variations due to surfaces in the two light beams of the interferometer.

A Nomarski Microscope uses a Wollaston prism and a set of polarizing filters. Wollaston prism is a beamspliting polarizer prism which has two calcite right-angle prisms. Its prism splits light beam into an *ordinary-ray (O-ray*) whose electric field oscillates along the optic axis and an *extraordinary-ray (E-ray)* whose field oscillates in the perpendicular direction to the optic axis (Which is a symmetry axis with respect to the form of a crystal and to its arrangement of atoms in an anisotropic crystal whose properties change with direction. Rays travelling parallel to the optic axis does not split, O-rays and E-rays oscillate in mutually perpendicular planes. When light is incident on the Wollaston prism, first calcite right-angle prism does not split the incident beam into two but the O-ray is delayed with respect to the E-ray. Nomarski microscope has a modified Wollaston prism where optic axis of first calcite right-angle prism is kept at 45° with respect to the polarizers, in other words, it is bended resulting an interference plane [188]. A design of Wollastron prism and its modified type in a Nomarski Interference Microscope is shown in Figure 3.14 where working principles are also indicated.

As seen in Figure 3.14 (b), in a Nomarski Microscope, light from a source is first linearly polarized by a set of linear polarizer and it is incident on a Wollaston prism where it is separated into two beams along the separation or *shear axis* (the axis of beam splitting and recombination of a DIC prism). Passing through a condenser lens and a transparent or a semitransparent sample, the two rays are focused by an objective onto the second Wollaston prism where they recombine to yield an interference effect which is defined by the phase variations between the two beams due to the sample. These phase variations arises from the optical path difference between the O and E rays and also from the variation in the sample's refractive index along the shear. Finally, an analyzer (polarizer) detects phase shifts producing coloured images of the material as a result of phase offset between rays and local changes in refractive index. However, NIM does not provide spatial resolution below the diffraction limit (λ/2) and structure dimensions can be observed larger than their actual dimensions.

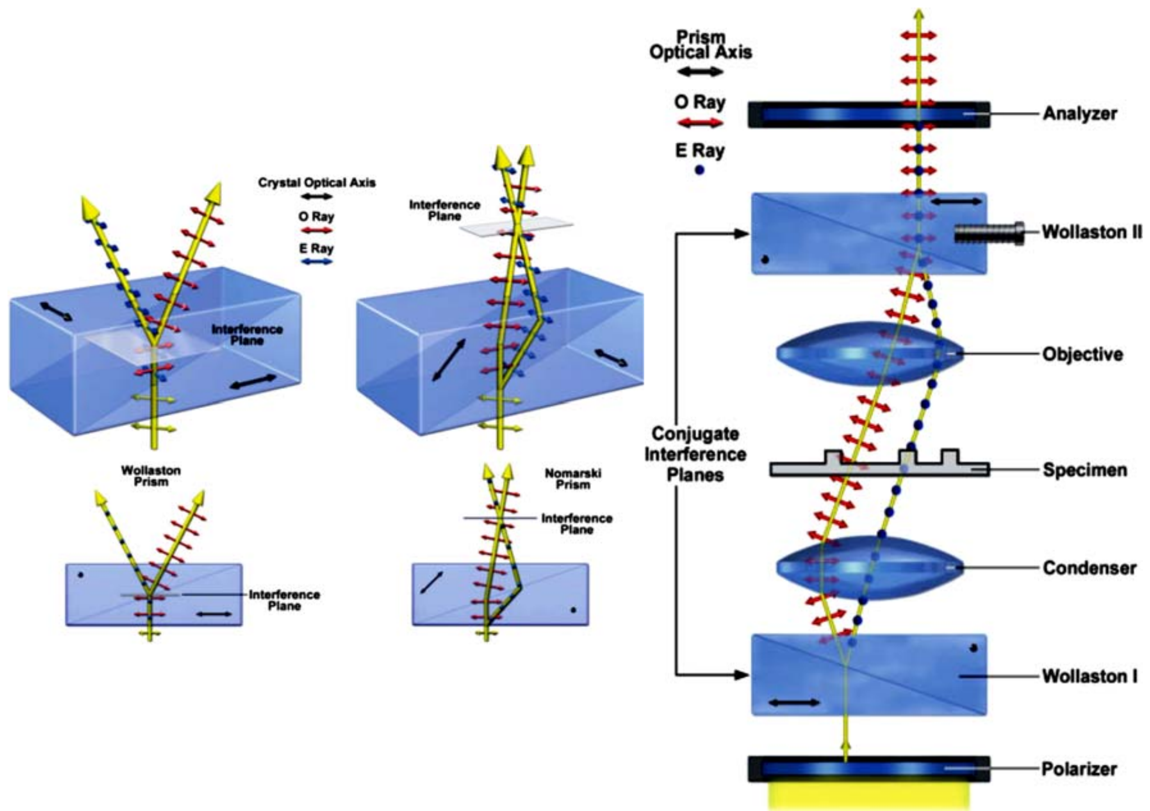

Figure 3.14. (a) Design of Wollastron and Nomarski prisms, (b) Working princible of Nomarski Interference Microscope [188].

Depending on the phase offset between O and E rays, destructive interference forms dark spots in the image. The image produced by DIC microscope can be expressed by measured intensity in cartesian coordinates [189];

$$I(x,y)=A(x,y)\left\{1+cos\left[\phi(x+s,y)-\phi(x,y)+\psi\right]\right\} \tag{3.37}$$

where I is the measured intensity, Ø is the phase gradient, and Ψ is a phase offset that can be adjusted by changing the bias setting of the second Nomarski prism, and by the term A which is amplitude and s is seperation distance between the O and E rays in the x direction. If the shear s is small compared to the microscope resolution, the measured intensity can be given by;

$$I(x,y)=A(x,y)\left\{1+cos\left[\Phi(x,y)+\psi\right]\right\} \tag{3.38}$$

where Φ is in terms of shear and phase gradient, is;

$$\Phi(x,y) = s\frac{\partial\phi(x,y)}{\partial x} \tag{3.39}$$

The ray bias in terms of wavenumber *k*, shear *s* and *Φ* can be given by;

$$sin\theta_x = \left[\frac{\Phi(x,y)}{k.s}\right] \tag{3.40}$$

In this thesis, the surface morphologies of (211)B CdTe/(211)B GaAs epilayers were examined by Nomarski microscopy using an A13.1013 DIC Metallurgical Microscope. The main components of a DIC misroscope are shown in Figure 3.15. The Nomarski sytem has a 24V/100 W halogen bulb, a NA0.9/0.25 condenser and a set of blue, green, yellow, frost and ND25 and ND6 filters. ND25 and ND6 filters are used to adjust the brightness of the light with %25 and 6% transmittance, respectively.

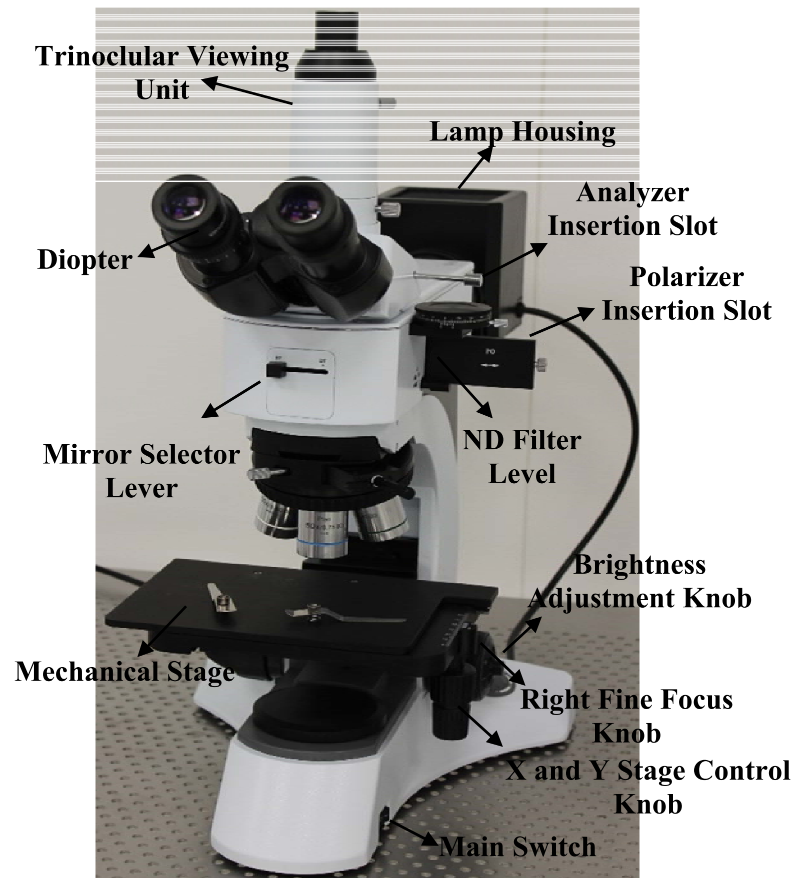

Figure 3.15. Main components of the A13.1013 DIC Metallurgical Microscope at Iztech.

3.2.2. STRUCTURAL CHARACTERIZATION TECHNIQUES

3.2.2.1. Atomic Force Microscopy (AFM)

After the invention of the Scanning Probe Microscope (SPM) and Scanning Tunneling Microscope (STM) in 1982, Atomic Force Microscopy (AFM) was invented by Greg Binning, Calvin F. Quate and Christopher Herber in 1986 [190]. SPM uses the basic principle of scanning a surface with a sharp probe to image and measure the properties of a sample. Depending on the tip interactions with the sample surface, an SPM is can be used as an AFM or a STM. The main components of AFM are a probe, a cantilever, a piezoelectric scanner, a laser, a data processor, and a photodetector. Probes are generally made from silicon nitride (Si_3N_4) or silicon (Si). There can also be coated probes depending on the sample properties and application. The probe of an AFM system consists of a cantilever and a tip which scans the sample surface during the measurement. The movements of the tip or sample is controlled by a piezoelectric scanner in x, y, and z directions.

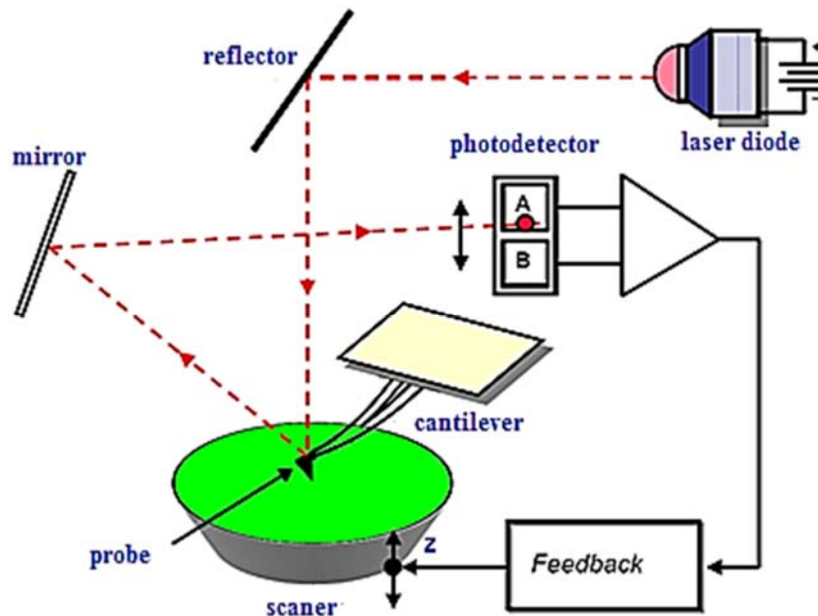

Figure 3.16. Main components of AFM [191].

There are three operating modes in an AFM. They are; a *contact mode*, an *intermittent-contact (tapping) mode,* and a *non-contact mode*. In the *contact mode*, the tip remains in contact, with the sample surface, defined by a constant contact force. In order to maintain the constant contact force between tip and the sample, the piezoelectric scanner moves in z direction. Contact mode, while works fine with hard samples, is not the proper mode of operation for soft samples whose surface might be demaged easily. Hence, the *intermittent-contact mode* is more commonly used for such samples. In the *intermittent-contact mode*, the cantilever oscillates at a certain frequency so that the tip also vibrates with a certain amplitude in the z direction while keeping the sample in the xy plane. Finally, in the *non-contact mode*, the tip does not contact the sample surface but oscillates during scanning as in the intermittent-contact mode, but, a much smaller contact force is applied onto the sample surface. Thus, surface topograpy can be measured from the change of amplitude z due to the attractive force between the tip and the sample. If cantilever is assumed to be an elastic spring, the magnitude of the force between the tip and a sample can be given by Hookes' law; $F = -k.x$ where k is the spring constant and x is the cantilever deflection.

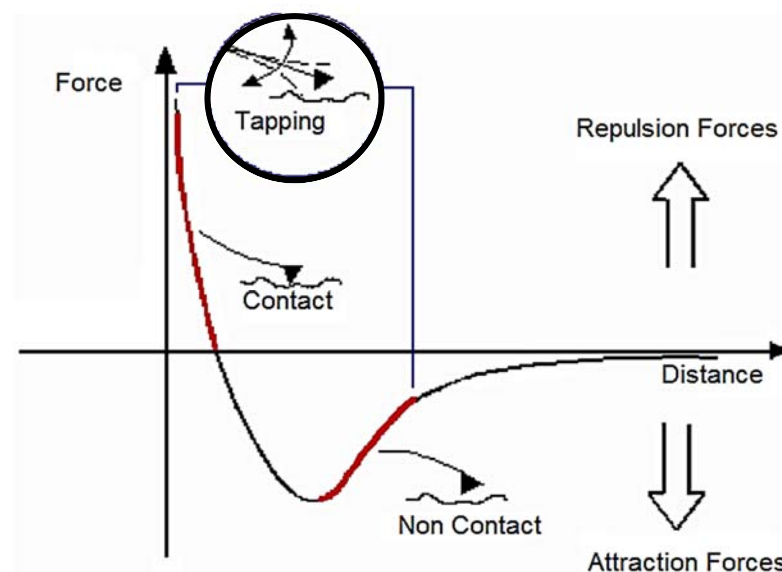

Figure 3.17. The force of interaction between the tip and a sample as a function of the tip-sample distance where proper modes of operation are also indicated [191].

AFM is generally used to image the surface topography and to measure the interacting forces between the tip and the sample. The force between atoms at the tip and

the sample can be measured when the tip is located as close as 0.1-100 nm [192]. As seen in Figure 3.17, as the tip-sample distance becomes smaller, the tip experiences a growing attractive force mainly first due to classical and, after some minimum distance, to quantum mechanical Coulombic interactions between the tip and the sample charges (both electrons and neclei). As the distance gets smaller, the repulsive force contributions from electron-electron repulsion (both classical and Quantum mechanical (Pauili repulsion)) and from core-core repulsion becomes larger and after some minimum distance is reached, the net force becomes repulsive. Attractive forces can be listed as; van der Waals (vdW) interaction, electrostatic force, and chemical force (quantum mechanical bonding). The vdW interaction between the tip and the sample can be described by Hamaker's approach which is applicable for a sample and tip of approximately 10 nm scale [193]. For a spherical tip with radius R, the vdW force between the tip and the sample (F_{vdW}) is given by [194];

$$F_{vdW} = -\frac{A_H R}{6z^2} \tag{3.41}$$

where z is the distance between the tip and the sample and A_H is the Hamaker constant. In addition, the electrostatic force as an attractive force can be generated between a charged or conductive tip and sample with a potential difference U. For the condition of distance between the tip and the sample z is smaller than the tip radius R, the electrostatic force F_{el} is given by the function of z [195];

$$F_{el}(z) = -\frac{\pi \varepsilon_0 R U^2}{z} \tag{3.42}$$

where ε_0 is the dielectic constant of empty space. The 'chemical force' takes effect when two or more atoms come together to form a molecule (quamtum mechanical bonding). The chemical bonding energy is described by the Morse potaential V_{Morse} [193];

$$V_{Morse} = -E_{bond}\left(2e^{-\kappa(z-\sigma)} - e^{-2\kappa(z-\sigma)}\right) \tag{3.43}$$

where E_{bond} is bonding energy, σ is equilibrium distance and $1/\kappa$ is decay length.

The repulsive force between the tip and the sample can be described by the Pauli exclusion or ionic repulsion. As an atom approaches another atom, their electronic wave function will be overlapped, a short range and strong repulsion. The electrostatic potential, at close distances, between the tip and the sample can be expressed in terms of an empirical potential, called the 'Lennard-Jones potential', as;

$$V = -4\varepsilon\left(\frac{\sigma^6}{z^6} - \frac{\sigma^{12}}{z^{12}}\right) \tag{3.44}$$

and by differentiating eq.(3.42) with respect to the distance, repulsive force between the tip and the sample can be given by;

$$\vec{F}\left(\hat{z}\right) = \frac{48\varepsilon}{z^2}\left[\left(\frac{\sigma}{z}\right)^{12} - \frac{1}{2}\left(\frac{\sigma}{z}\right)^{6}\right]\hat{z} \tag{3.45}$$

where ε governs strength of the interaction, σ is the distance at which the force is zero. At large z's, the second term is dominant creating a net attractive force while the first term in (3.44) becomes the dominant term at smaller z's and net force turns positive. The net force will be equal to zero when $\sigma = z$. The minimum of the net force corresponds to the maximum attraction, which can be obtained from the zero of the first derivative of (3.45) with respect to z.

Surface measurement by AFM generally includes surface shape and surface roughness. In the present work, surface topography and surface roughness were studied to evaluate the quality of GaAs(211)B wafers and CdTe(211)B epitaxial films. The roughness of samples can be characterized by height and spacing parameters. The roughness average (R_a) of a sample can be described by [196];

$$R_a = \frac{1}{L}\int_0^L \left|Z\left(x\right)\right| dx \tag{3.46}$$

where $Z(x)$ describes the surface profile analyzed in terms of the height Z and the position x of a sample and L is the evaluation length. A more sensitive method is the root mean square roughness (R_q) method which measures the mean squared absolute values of surface roughness profile [196];

$$R_a = \sqrt{\frac{1}{L}\int_0^L \left|Z^2\left(x\right)\right| dx} \tag{3.47}$$

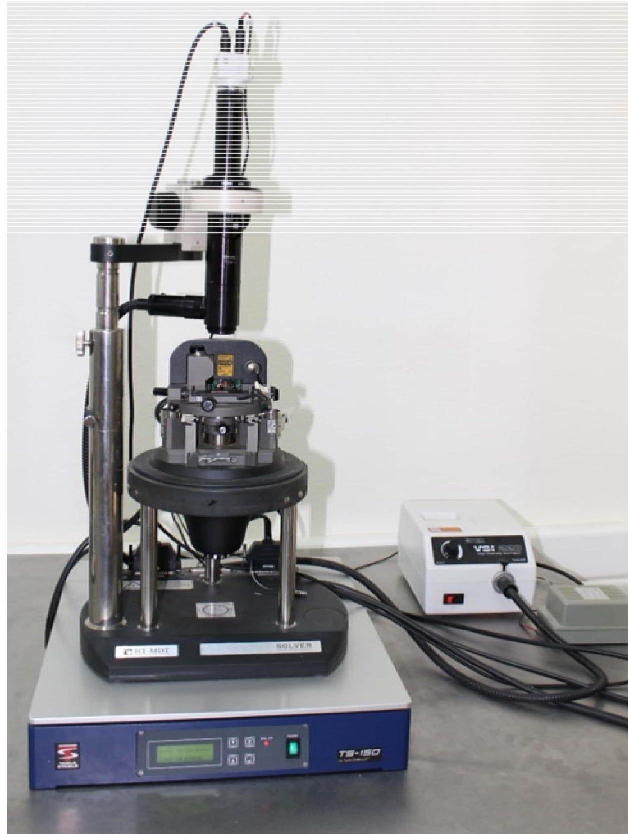

Figure 3.18. Scanning Probe Microscopy instrument (Solver Pro 7 from NT-MDT, Russia).

In this thesis, the AFM topographical images of GaAs(211)B wafers and CdTe(211)B epitaxial films were obtained in the intermittent-contact mode using a commercial Scanning Probe Microscopy instrument (Solver Pro 7 from NT-MDT, Russia) (Figure 3.18). During our AFM measurements, HA_NC silicon tips with cantilever thickness 1.75 µm and force constant 3.5 and 12 N/m were used.

3.2.2.2. Scanning Electron Microscopy (SEM) And Energy Dispersive X-Ray Spectroscopy (EDX)

Since the invention of scanning electron microscope (SEM) in 1935 by Knoll, this techique has been widely used to characterize the inner structure of matter [197]. SEM is a non-destructive technique giving information about surface morphology by magnification imaging. Unlike optical microscopy, SEM uses focused beam of electrons

which provide better resolution than optical microscopy (due to the short de-Broglie wavelengths associated with the focused electrons). In this technique, an electron beam, produced by an electron gun, strikes the surface of a sample. The primary electron beam creates different types of electron interactions with the sample. Secondary electrons (SE), back scattering electrons (BSE), transmitted electrons (TE), and characteristic X-rays are four important interactions for analyzing the sample.

Secondary electrons have low energies (<50 eV) interacting only with the sample surface. They are collected by secondary electron detectors to produce a detailed image of the sample surface., Characteristic X-rays, produced during the primary beam electrons-sample atoms interaction, on the other hand, play an important role in the 'Energy-dispersive X-ray Spectroscopy' (EDX) to determine the elemental composition of a sample. The energies (frequencies) and intensities of these X-rays give information about the weight and atomic elemental ratios in a sample.

In this thesis, a Quanta 250 FEG sytem was used for analyzing the surface of wet-chemically etched GaAs(211)B wafers and CdTe(211)B thin films. To carry out the measurements, GaAs(211)B wafers and CdTe(211)B thin films were mounted on an aluminum stub which was coated with a double sided conductive tape. In this system, Energy Dispersive X-ray (EDX) analysis was also used for the determination of the elemental composition of GaAs(211)B wafers after wet-chemical etch processes.

3.2.2.3. X-Ray Diffractometer (XRD)

X-ray diffraction is a powerful and non-destructive technique to characterize the structural properties, such as, lattice constants, strain relaxation, epitaxial tilting, and defect properties, of semiconductors. The history of X-ray diffraction dates back to accidental discovery of X-rays by Wilhelm Conrad Röntgen in 1895 [198]. X-rays are a form of electromagnetic radiation with photon energies in the range of 100 eV to 100 keV. Only short wavelength x-rays, in the range of a few angstroms, which corresponds to inter-atomic distances in crystalline solids, are used in XRD measurements. X-rays are generally produced by x-ray tubes or by synchrotron radiation. X-ray tubes contain a rotating anode, a filament cathode, a high voltage generator, all of which are located in a glass envelope under high vacuum. In an X-ray tube, electrons, emitted from a filament cathode, accelerate, under a high potential difference (a few kV, produced by a voltage

generator between the anode and the cathode) towards the anode which is usually made of a rotating tungsten or copper plate. After colliding with the anode at a few keV energies, electrons slow down to give up energy as continuous spectrum of x-rays (called as Bremsstrahlung radiation).

Diffraction of X-rays in crystals was first discovered by Max von Laue in 1912. In the following year, Bragg derived an equation to explain the interference patterns of X-rays scattered by crystals. According to Bragg's law, a parallel incident X-ray beam will be scattered by electrons of the regularly spaced atoms in the crystal producing a diffraction pattern. Interference can be destructive or constructive depending on the spacing between the regularly spaced parallel planes of atoms separated by a distance d and the wavelength of the incident radiation. The condition for diffraction will then be;

$$n\lambda = 2d_{hkl}\sin\theta \tag{3.48}$$

where n is the order of diffraction, λ; the wavelength of incident radiation (in the range 0.7-2 Å for X-rays), d_{hkl} ; the distance between crystal planes (interplanar spacing) and θ; the angle of incidence. Constructive interference will occur only when all scattered waves are in phase. In that case, the path length difference will be equal to an integer multiple of the wavelength. The lattice parameter (a) and the distance between lattice planes for a cubic lattice is given, in terms of miller indices (h, k, l), as;

$$d_{hkl} = \frac{a}{\left(h^2 + k^2 + l^2\right)} \tag{3.49}$$

In this thesis, X-ray triple axis rocking curve measurements were obtained to examine the crystalline quality of epitaxial CdTe films. Measurements were carried out using a Philips X'Pert Pro MRD X-Ray Diffraction system (Figure 3.21) located at Iztech physics department. In an X-ray rocking curve measurement, also referred as omega (ω) scan, the directions of the incident X-rays and the position of the detector is fixed while the sample is moved about its ω axis. From triple axis rocking curve measurements, full width at half maximum (FWHM) of a diffraction peak is obtained which is a very important indication of the crystalline quality of a sample. Rocking curves can only be obtained when the sample and detector are at some exact positions for constructive interference. The FWHM of a rocking curve is the width of a peak measured at the half of the maximum height of the peak. The crystal quality increases with decreasing FWHM.

The FWHM of a peak, thus, depends on the defects present in the crystal. Shematic representation of a typical FWHM of a triple axis rocking curve peak is illustrated in Figure 3.20. The broadening of a triple axis rocking curve peak can be traced to the instrumental errors, strain, dislocations, or stacking faults in a crystal.

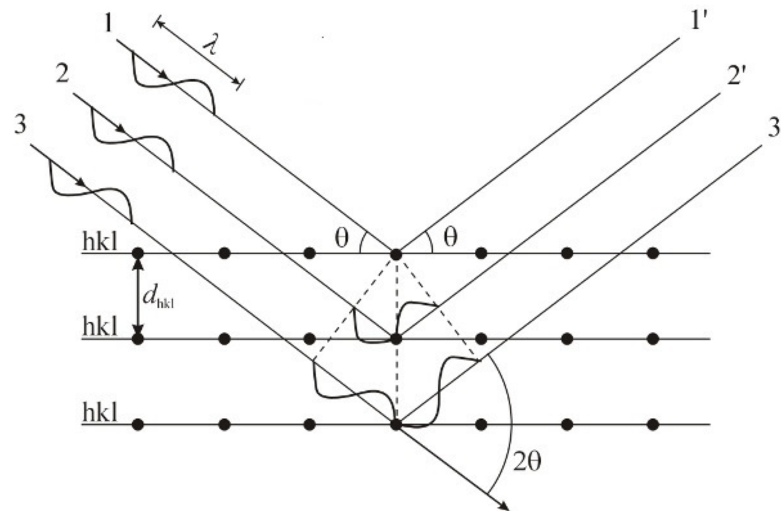

Figure 3.19. Schematic representation of Bragg reflection from crystal planes where d_{hkl} is the distance between a set of parallel crystal planes (interplanar spacing) and θ is the angle of incidence.

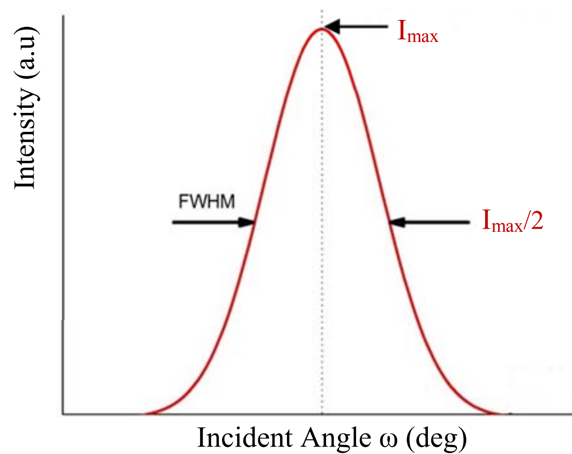

Figure 3.20. Schematic illustration of a typical X-ray triple axis rocking curve peak.

Another important factor is some tilt or misorientation of thin film and bulk crystal layers occurring during the growth. Such a tilt between the crystal planes leads to broadening of triple axis rocking curve peaks as well. A tilt may occur between the two arrangements (*a* and *b*) of atoms. For example, a tilt occuring between the substrate and a film layer can be given as;

$$\begin{aligned} \delta\theta_a &= \frac{\delta d}{d} \tan\theta - \delta\phi \\ \delta\theta_b &= \frac{\delta d}{d} \tan\theta + \delta\phi \end{aligned} \tag{3.50}$$

where $\delta\phi$ is the tilt between the substrate and the layer, θ is the Bragg angle, d is the interplanar spacing, $\delta\theta_a$ and $\delta\theta_b$ are peak splittings.

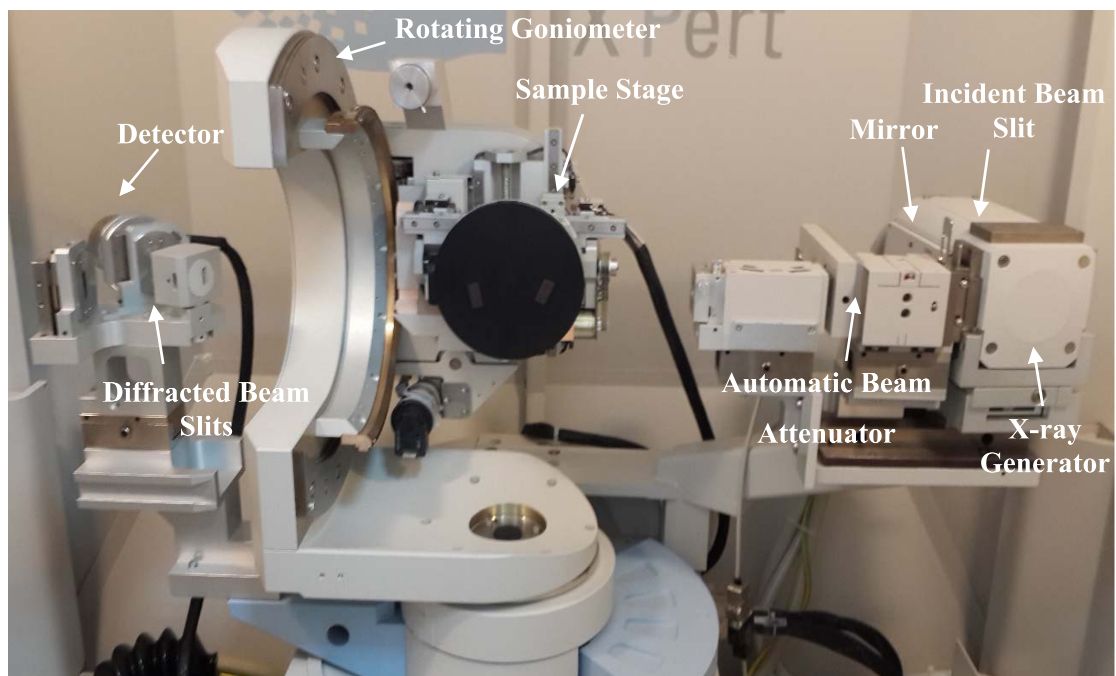

Figure 3.21. Thin Film Philips X'Pert Pro MRD System components in High Resolution X-ray diffraction configuration in the department of physics at Iztech.

CHAPTER 4

SURFACE PREPARATION PRIOR TO MOLECULAR BEAM EPITAXIAL GROWTH

4.1. Ex-situ Surface Preparation

It is very important to know the properties of a substrate surface to be able to reduce the growth related defects. A high performance infrared devices, for example, can be obtained only with a well prepared substrate surface. Today, it is not too difficult to find 'epiready' wafers as substrates (such as GaAs(211)B wafers which are the main focus of our investigation) in which an oxide layer protects the surface and no preparation is necessary before a growth. Despite having a protective oxide layer, the substrate surfaces have defects and contaminants occurring during their fabrications. Defects and contaminants on GaAs wafers have deleterious effects on CdTe growth on them. To overcome such problems, various chemical processes should be performed before a growth.

One must also notice that GaAs wafers can easily be oxidized over time even if they have protective oxide layers. GaAs surfaces, interacting easily with the atmospheric oxygen, form a thick or thin layer of native oxygen atoms on the surfaces. Thus, to protect oxidation of the GaAs wafers and to remove the native oxides from the GaAs surface, the choice of a cleaning process is important. Chemical treatment on GaAs wafers changes the stoichiometry of the surface depending on the particular acid or base employed. GaAs surface may either be Ga-rich, As-rich, or nearly stoichiometric. The Treatment of a GaAs wafer with acidic solutions tends to leave an As-rich surface due to their reactions with Ga. On the other hand, treatment of GaAs wafers with basic solutions dissolve As [199]. Oxide bulk of GaAs wafers is generally composed of a mixture of Ga_2O_3 and As_2O_3 in equal concentrations, but not homogeneously distributed on the surface. Initial oxidation of a fresh GaAs wafer forms Ga_2O_3 and As_2O_3 compounds through the following reactions;

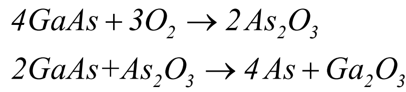

$$4GaAs + 3O_2 \rightarrow 2As_2O_3$$
$$2GaAs + As_2O_3 \rightarrow 4As + Ga_2O_3$$

Generally, a wafer-cleaning process includes dry and wet cleaning techniques. Wet chemical etching of III-V semiconductors, several solution are used such as; Br_2/metanol [200], $H_2O_2/NH_4OH/H_2O$ [201], $H_2SO_4/H_2O_2/H_2O$ [202] and $H_2SO_4/H_2O_2/HCl$ [203] some of which oxidize the wafer surface or etch the oxide. In addition, the removal of the protective and native oxide layer from the GaAs surface includes diluted acidic and basic solutions such as $HF:H_2O$, $HCl:H_2O$ and $NH_4OH:H_2O$ [199]. However, due to oxidative nature of H_2O_2, this acidic etchant is not recommended in the literature for the removal of the native oxides from GaAs surface. The performed cleaning or oxidation procedures can also lead to the formation of other oxides on the surface of GaAs wafers some of which are given in the following equations;

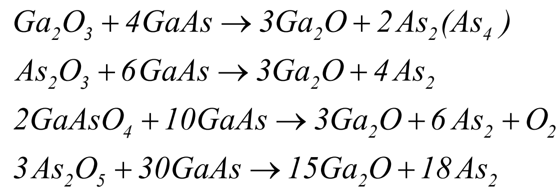

$$Ga_2O_3 + 4GaAs \rightarrow 3Ga_2O + 2As_2(As_4)$$
$$As_2O_3 + 6GaAs \rightarrow 3Ga_2O + 4As_2$$
$$2GaAsO_4 + 10GaAs \rightarrow 3Ga_2O + 6As_2 + O_2$$
$$3As_2O_5 + 30GaAs \rightarrow 15Ga_2O + 18As_2$$

4.1.1. Wet-Chemical Etching and Chemically Oxide Removal Processes of GaAs(211)B Wafers

In this thesis, in order to understand the effect of a wet cleaning procedure on the chemical composition of epiready GaAs wafers, wet-chemical etching and oxide removal processes was performed on undoped DS polished 625±25 µm thick GaAs(211)B wafers. After wafers were cut into pieces, by a dicer, of dimension of 1x1 cm^2, a wet-chemical etching process was performed. The wet chemical etching of GaAs included degreasing, chemical treatment, and drying steps. The degreasing was done with acetone (C_3H_6O) and methanol (CH_3OH) following the chemical treatment of surfaces with the piranha solution ($H_2SO_4:H_2O_2:H_2O$) with varying ratios and implementation times. Degreasing was achieved with boiling GaAs(211)B wafers for 3 minutes in acetone, followed by rinsing in de-ionized water and 3 minute boiling in methanol. After degreasing and rinsing in de-ionized water, samples were etched in $H_2SO_4:H_2O_2:H_2O$ with varying ratios. The

strength of hydrogen peroxide (H_2O_2) and sulfuric acid (H_2SO_4) was 30% and 95%, respectively.

Table 4.1. Wet-chemically etched samples with sample IDs, degreasing processes, H_2SO_4:H_2O_2:H_2O volume ratios, implementation times, drying processes.

Sample ID	Degreasing	H_2SO_4:H_2O_2:H_2O		Drying
		Volume Ratios	**Implementation Times (s)**	
G1C1-A1	✓	3:1:1	30	N_2
G1C1-A2			120	
G1C1-A3			15	
G1C1-B1		2:1:1	120	
G1C1-B2			60	
G1C1-B3			30	
G1C1-C1		3:1:1	60	Spin Dryer (4600 rpm)
G1C1-C2			120	
G1C1-C3			30	
G1C1-E1		3:0.75:1	120	
G1C1-E2			60	
G1C1-E3			30	
G1C1-F1		-	-	
G1C1-F2	-	3:1:2	60	
G1C1-G1	✓	3:1:2	30	
G1C1-G2			60	
G1C1-G3			120	

To obtain piranha solution, firstly H_2SO_4:H_2O mixture was prepared in a beaker and was boiled at 60 ^{o}C for 2 minutes. After H_2SO_4:H_2O mixture was cooled, hydrogen peroxide added and etching processes with various volume ratios and implemented times were performed. Finally, samples were rinsed again in de-ionized water and some of them dried with N_2 blower and the others were dried with a spin dryer. Table 4.1 shows the

performed degreasing processes, piranha solution volume ratios, implementation times, and drying processes with the sample IDs.

Table 4.2. Oxide removal processes of GaAs wafers with sample IDs, volume ratios and implementation time.

Sample ID	**HF:H_2O**	
	Volume Ratios	**Implementation Time (s)**
G2W24A	1:8	60
G2W25A	1:5	

To understand the change of reactions with acetone, methanol and piranha solution with GaAs wafers degreasing step was not performed for G1C1-F2 and etching with piranha solution was not performed for G1C1-F1. In addition, to evaluate the quality of epiready GaAs(211)B wafers, hydrofluoric acid (HF) was used to remove the protective oxide layer. HF:H_2O mixture was performed for 60 seconds with two different ratios which are given in Table 4.2. Before and after wet-chemical etching and oxide removal processes, the surface morphologies of GaAs(211)B samples were studied via Optical Microscopy, Scanning Electron Microscopy (SEM) and Atomic Force Microscopy (AFM) techniques. Energy Dispersive X-ray Spectroscopy (EDX) was used to assess the chemical composition of the surface. After wet-etching processes; the vibrational modes were observed and two-dimensional (x, y) maps were recorded by a Raman Spectroscopy.

4.1.2. Results

4.1.2.1. AFM and SEM Resuts

Root mean square roughnesses (RMS) of GaAs(211)B wafers, after a wet-chemical etching procedure and oxide removal processes, were obtained from ex situ AFM measurements carried out in the intermittent-contact mode.

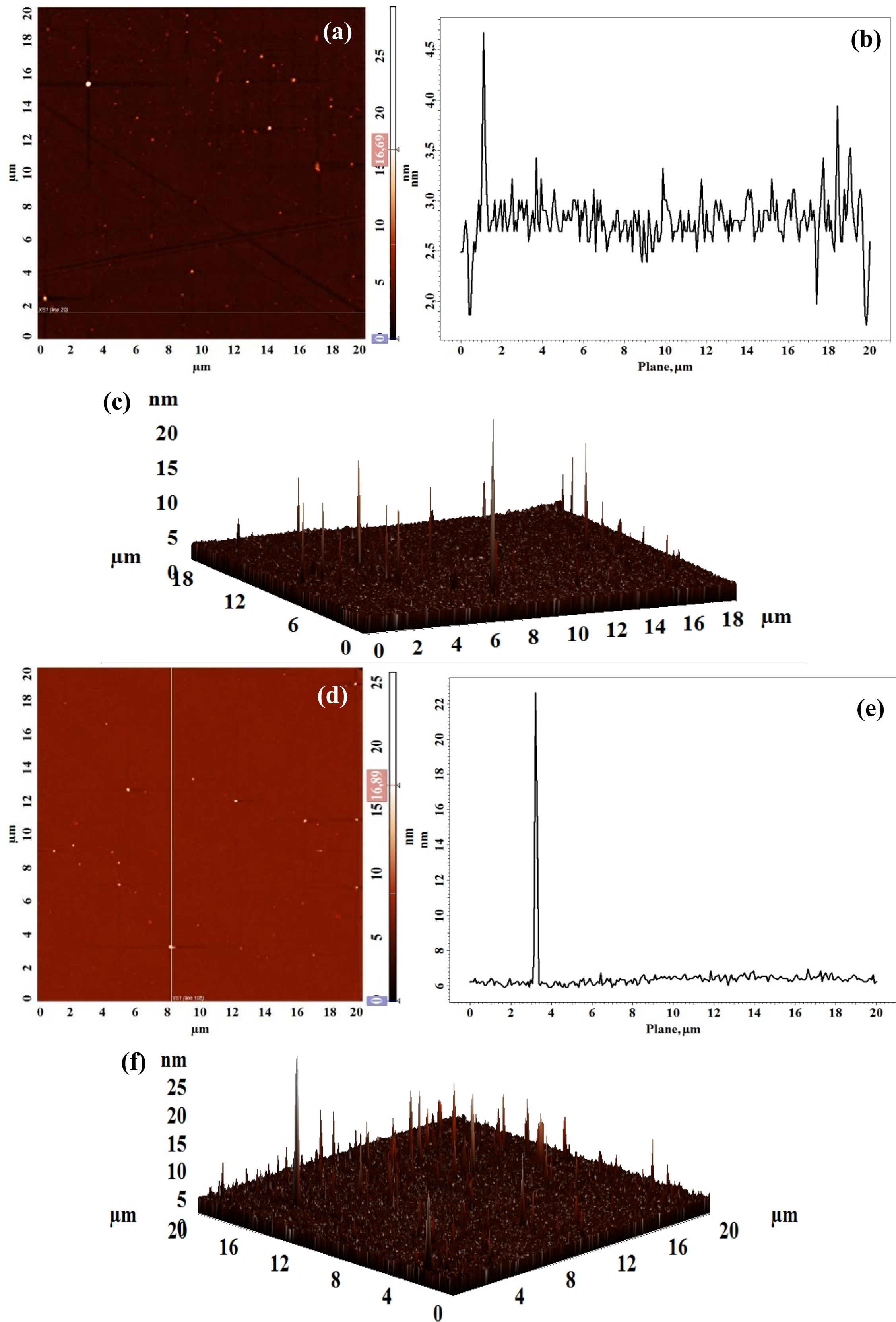

Figure 4.1. (a) and (c) are AFM 2D topographic images, (c) and (f) are AFM 3D topographic images of not chemically-etched GaAs wafer, (b) Profile line analysis of (a), and (e) Profile line analysis of (d).

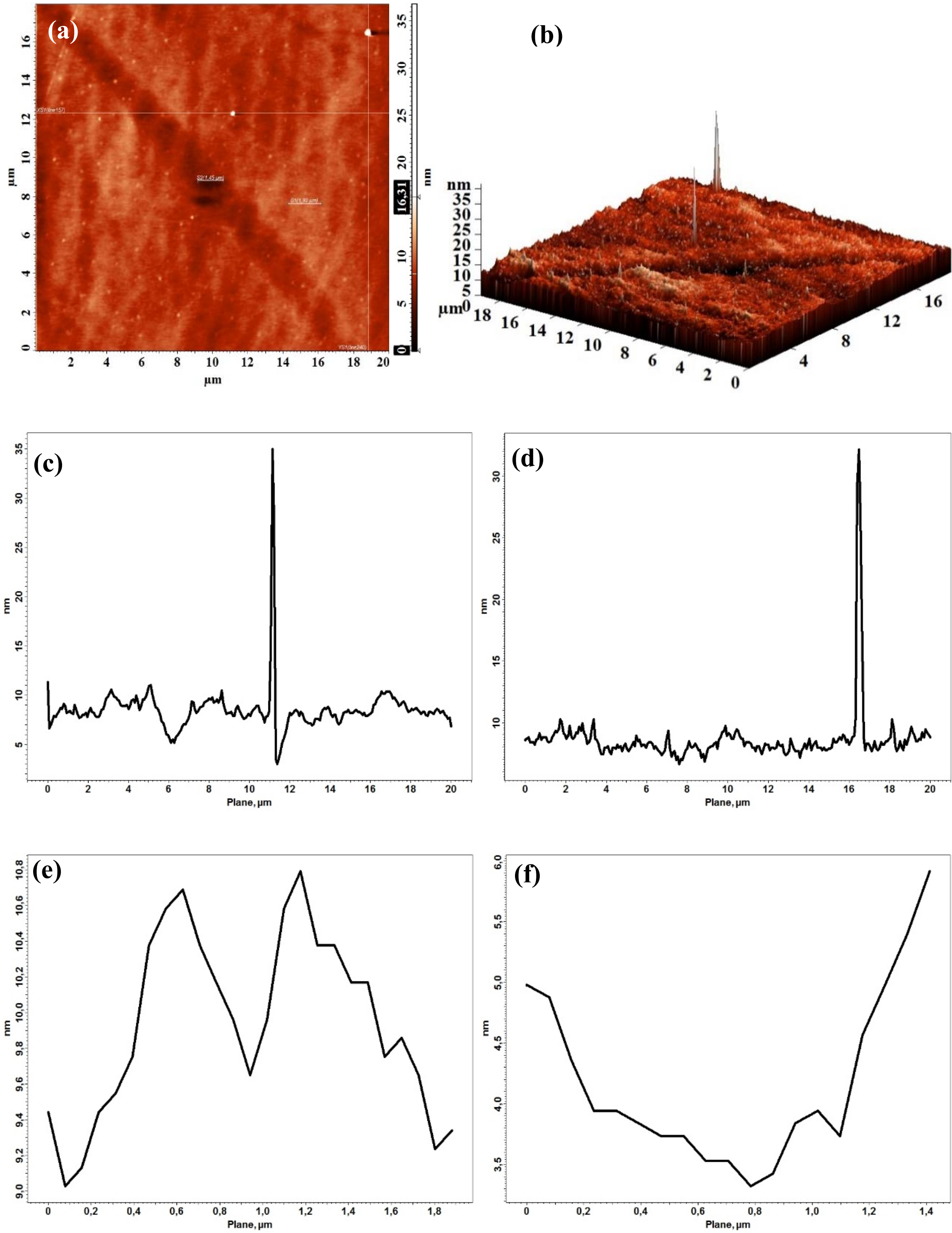

Figure 4.2. (a) AFM 2D Topographic image and (b) AFM 3D Topographic image of sample G1C1-A1 and profile line analysis of (c) XS1 (line 157), (d) XS2 (line 240), (e) S1 line of 1.92 µm width and (f) S2 line of 1.45 µm width.

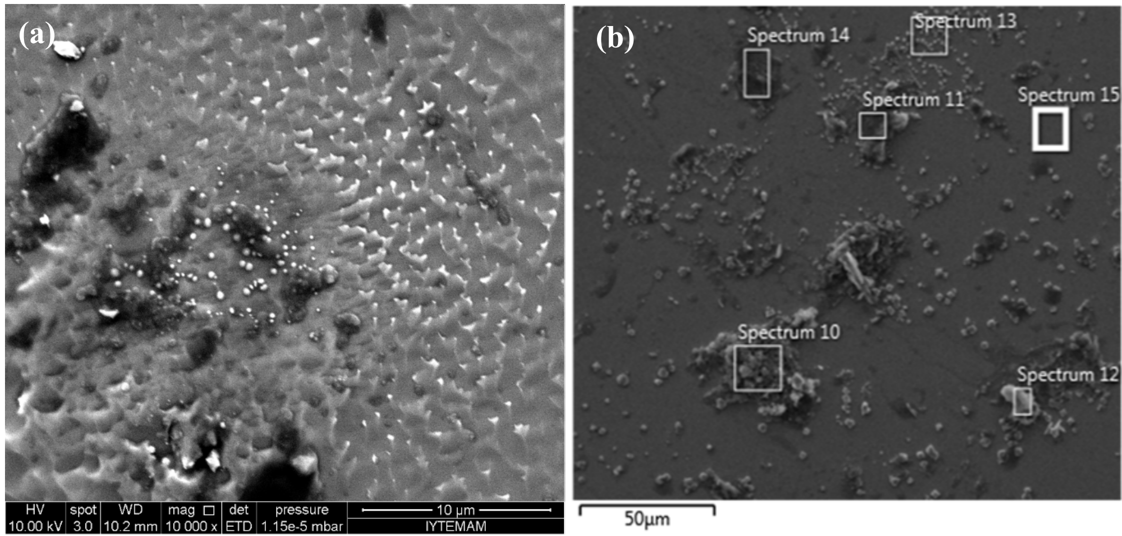

Element	Weight %	Atomic %
Spectrum 13		
Ga	40.04	33.88
As	53.44	42.08
O	6.52	24.05
Spectrum 15		
Ga	48.60	50.40
As	51.40	49.60

Figure 4.3. (a) and (b) are SEM micrographs of sample G1C1-A1 with 10 000 and 50 000 magnifications where spectra show the regions that EDX analysis were performed in SEM image (b) and the table shows the percentage of distributions of Ga, As and O in spectrum 13 and 15.

The change in the RMS values of wet-chemically etched GaAs(211)B wafers of various samples with differing mixture volumes and implemented times were compared. All topographic images of wet-chemically etched samples were obtained from a 20x20 μm^2 scan area. In addition, SEM micrographs and EDX analyses were performed after etching procedures. In Figure 4.1, AFM 2D and 3D topographic images and profile analyses on topographic images for not chemically-etched GaAs sample are shown. The average RMS roughness obtained from five scanned regions of a sample is found as 0.45 nm. Profile analyses showed that the maximum height of surface particules reach up to 29.26 nm before a wet-chemical etch process.

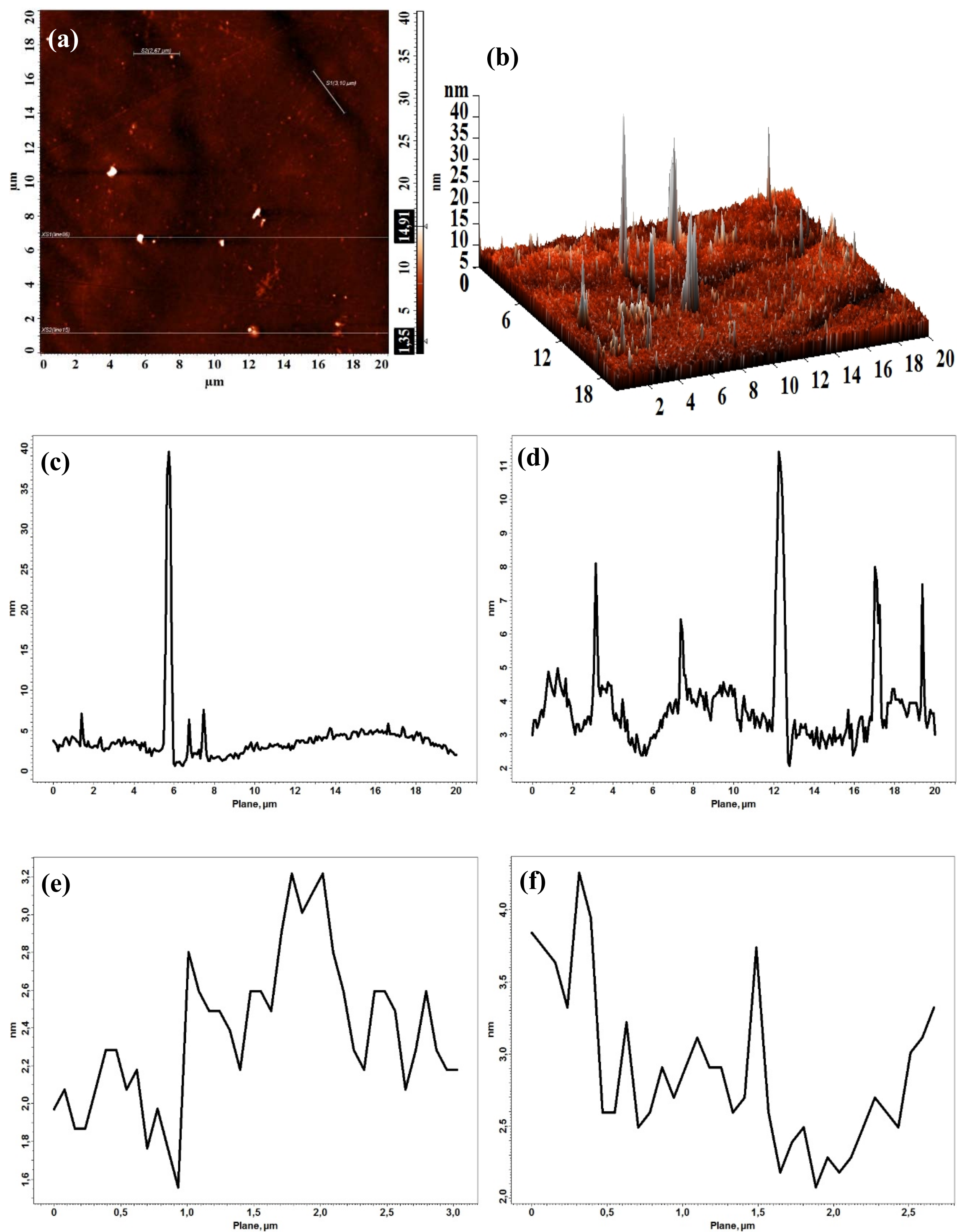

Figure 4.4. (a) AFM 2D Topographic image and (b) AFM 3D Topographic image of sample G1C1-A2 and profile line analysis of (c) XS1(line 86), (d) XS2 (line 15), (e) S1 line of 3,10 µm width and (f) S2 line of 2,67 µm width.

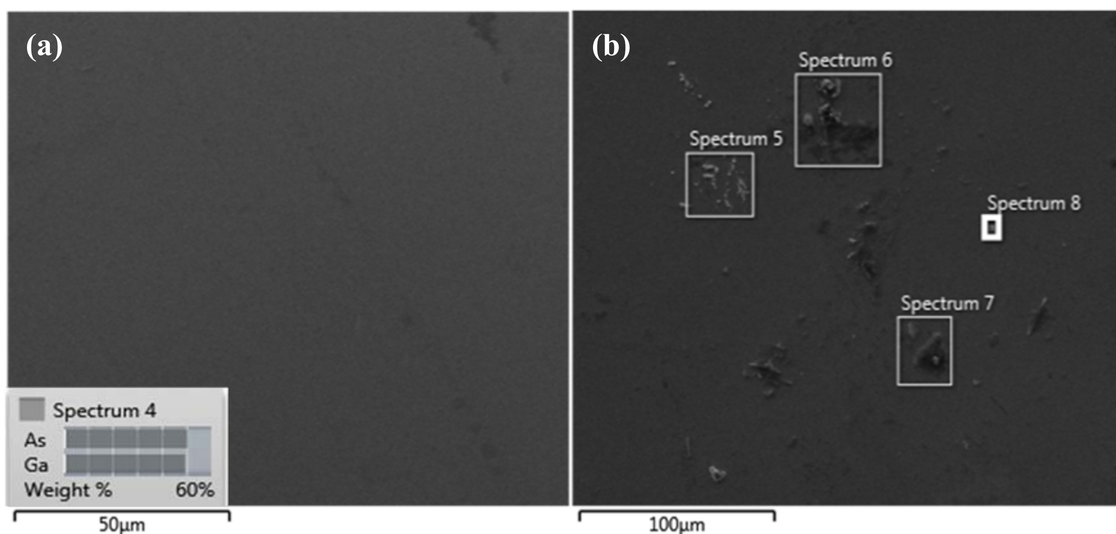

Element	Weight %	Atomic %
Spectrum 5		
Ga	47.94	37.91
As	45.90	33.78
C	6.16	28.31
Spectrum 8		
Ga	49.72	51.52
As	50.28	48.48

Figure 4.5. (a) and (b) are SEM micrographs of sample G1C1-A2 with 50 000 and 100 000 magnifications where spectra show the regions that EDX analysis were performed in SEM images and the table shows the percentage of distributions of Ga, As and C in spectrum 5 and 8.

AFM 2D and 3D topographic images and profile analyses on topographic images for the G1C1-A1 sample are shown in Figure 4.2. The average RMS roughness over the three scanned areas for this sample is found as 0.86 nm. Profile analyses showed that the maximum height of particules achieve up to 36.731 nm after etching sample with $3H_2SO_4$:$1H_2O_2$:$1H_2O$ mixture for 30 seconds. Also, profile analyses results showed that the mixture diffusively penetrated the surface, generating approximately 3 nm deep pits on the surface of GaAs(211)B sample. The SEM micrographs and EDX results are shown in Figure 4.3 for G1C1-A1. As seen from SEM images with 10 000 and 50 000 magnifications, the sample surface was damaged as a result of the high ratio of H_2SO_4 in the prepared piranha solution. Atomic percentages of the elements for scanned areas

showed that O contaminant appeared in the EDX spectra of sample G1C1-A1 which were located more damaged areas on the sample surface.

AFM 2D and 3D topographic images and profile line analysis of sample G1C1-A2 are shown in Figure 4.4. The average RMS roughness over scanned three area for this sample was found 1.38 nm. When compared to G1C1-A1, the average RMS roughness value is increased depending on the increasing implementation time to 120 seconds. Profile analyses showed that the maximum height of particules achieve up to 40.16 nm and the sample surface was damaged producing deep pits up to approximately 1.5 nm.

SEM micrographs of sample G1C1-A2 with 50 000 and 100 000 magnifications are given in Figure 4.5. As seen from SEM images, the sample surface was damaged as a result of high ratio of H_2SO_4 in the prepared piranha solution and longer-lasting piranha etching which is consistent with AFM topographic images. EDX analysis of G1C1-A2 sample showed that, the sample could not homogenously etched that some parts of the sample became Ga-rich and some parts were As rich after etching process. Also, atomic percentages of the elements for scanned areas showed that C contaminant appeared in the EDX spectra of sample G1C1-A2 which can be as a result of air exposure of sample, degreasing step of etching process with acetone and methanol or drying with N_2 blower.

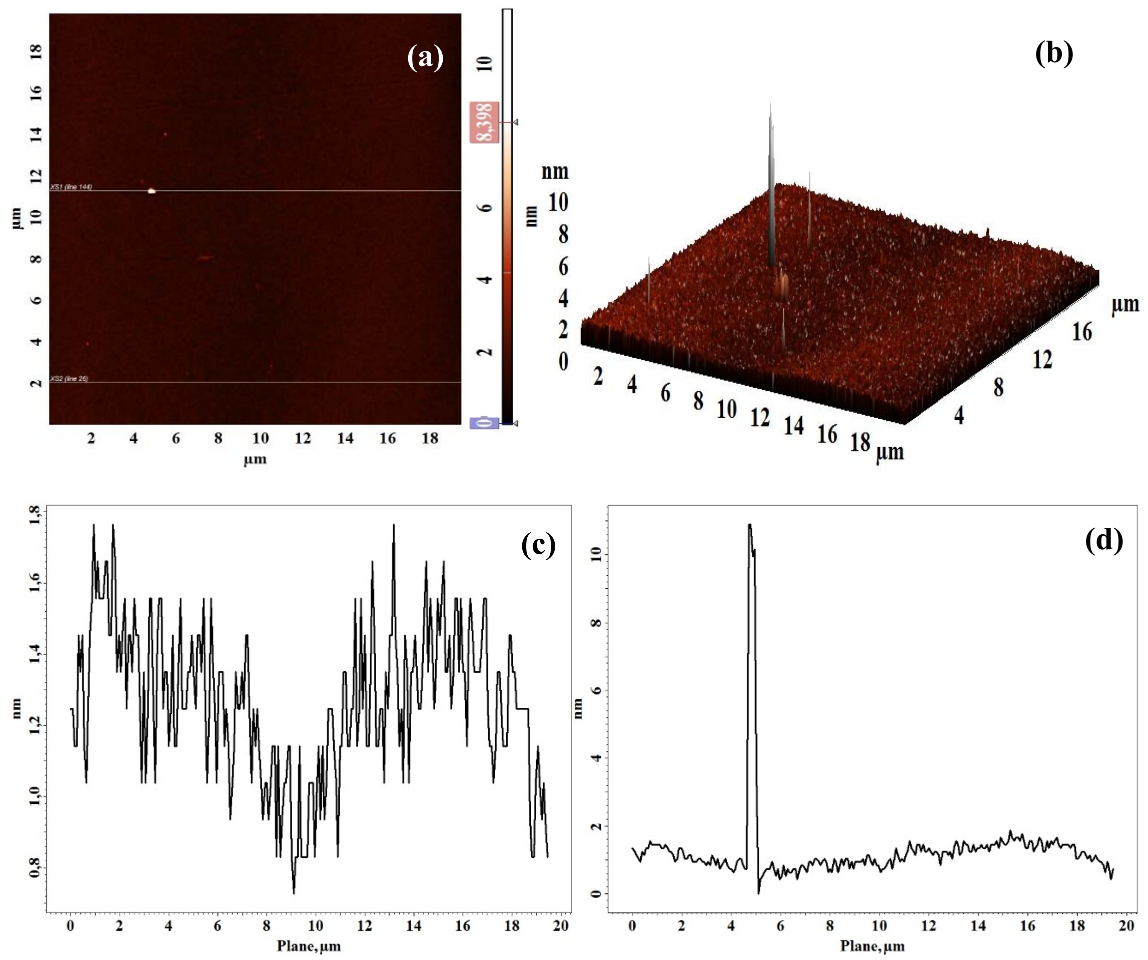

Figure 4.6. (a) AFM 2D and (b) AFM 3D Topographic images of sample G1C1-A3 and profile line analysis of (c) X2(line 26), (d) XS2 (line 144).

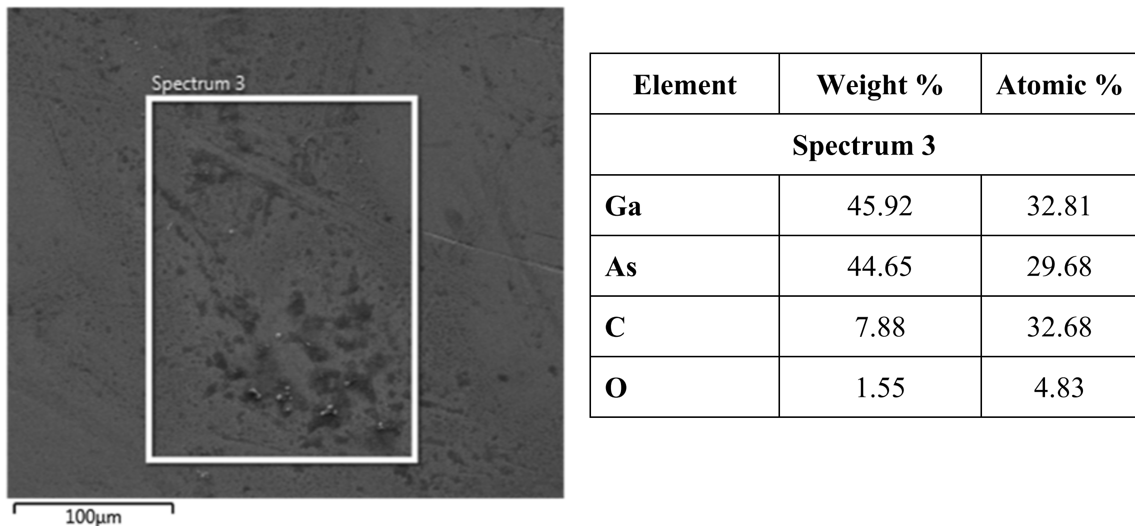

Element	Weight %	Atomic %
Spectrum 3		
Ga	45.92	32.81
As	44.65	29.68
C	7.88	32.68
O	1.55	4.83

Figure 4.7. Left side of the figure is SEM micrograph of sample G1C1-A3 with 100 000 magnification where spectra show the region that EDX analysis were performed in SEM image and the table shows the percentage of distributions of Ga, As, C and O in spectrum 3.

AFM topographic images and profile analyses for etching the sample with $3H_2SO_4:1H_2O_2:1H_2O$ mixture for 15 seconds (G1C1-A3) are shown in Figure 4.6. The average RMS roughness over scanned three area for this sample was found as 0.74 nm. When compared to G1C1-A2, the average RMS roughness value is decreased due to the decrease in the implementation time to 15 seconds. Profile analyses showed that the maximum height of particules reached 15,67 nm. The sample surface was damaged producing deep pits with depths up to 0.8 nm. In comparison to G1C1-A1 and G1C1-A2, maximum height of particules and depth of deep pits were decreased when GaAs(211)B sample etched for 15 seconds. The SEM micrograph of the sample G1C1-A3 with 100 000 magnification is shown in Figure 4.7. As seen in the figure, the sample surface had damaged areas. EDX analysis of G1C1-A3 sample showed that the sample had C and O contaminations. The O contaminants could be due to oxidative feature of H_2O_2 or protective oxide layer of GaAs(211)B sample.

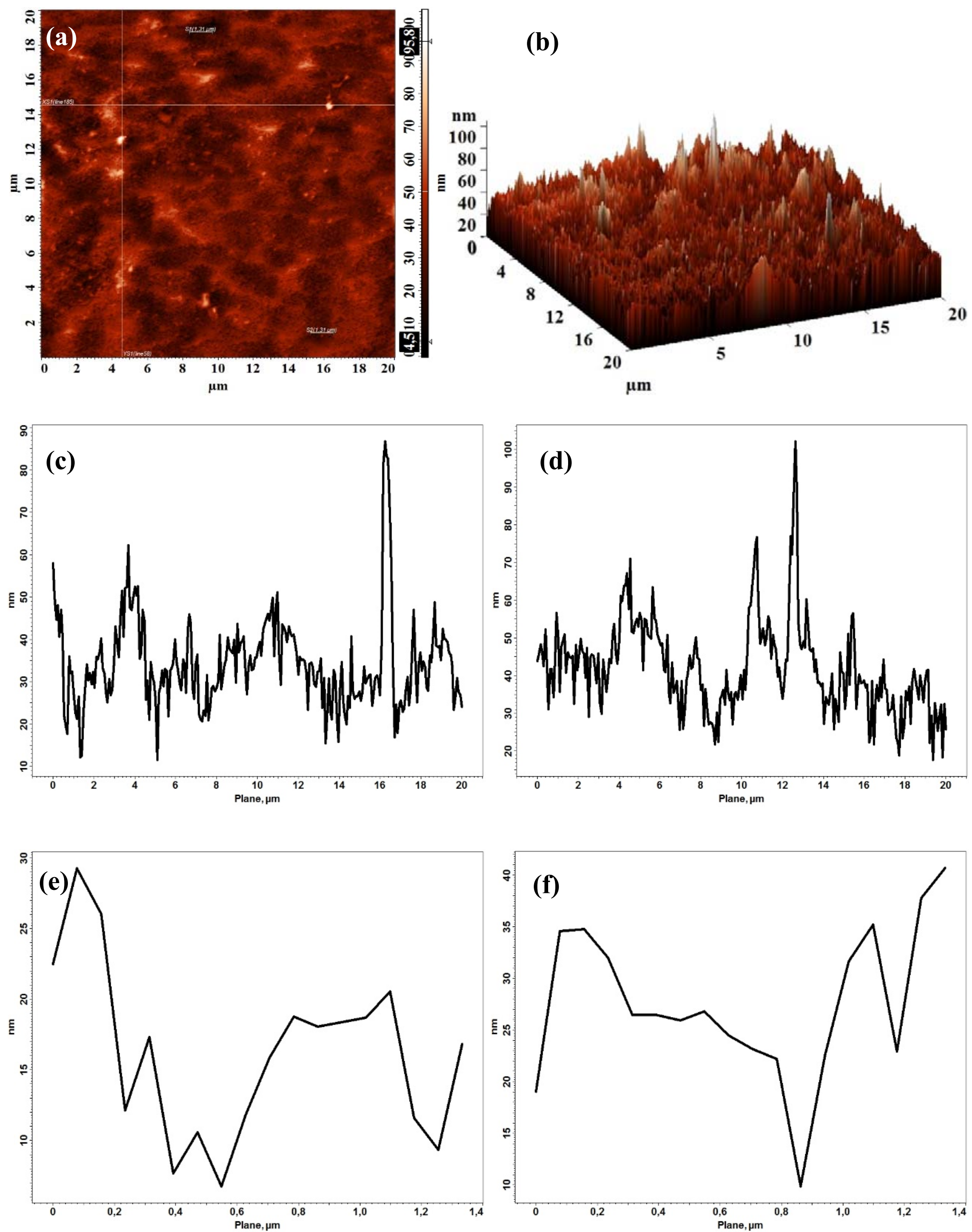

Figure 4.8. (a) AFM 2D Topographic image and (b) AFM 3D Topographic image of sample G1C1-B1 and profile line analysis of (c) XS1(line 185), (d) YS1 (line 58), (e) S1 and (f) S2 line of 1.3 µm width.

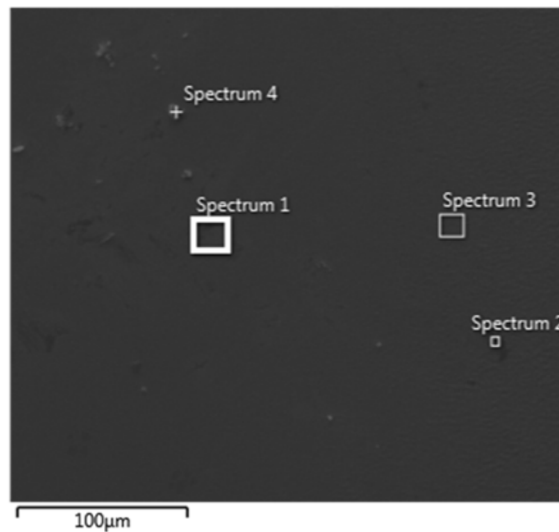

Element	Weight %	Atomic %
Spectrum 1		
Ga	33.52	14.41
As	28.43	11.37
C	4.75	11.85
O	33.29	62.37

Element	Weight %	Atomic %
Spectrum 3		
Ga	36.31	17.56
As	32.25	14.51
C	2.35	6.60
O	29.09	61.33

Figure 4.9. The figure is SEM micrograph of sample G1C1-B1 with 100 000 magnification where spectra show the region that EDX analysis were performed in SEM image and the table shows the percentage of distributions of Ga, As, C and O in spectrum 1 and 3.

2D and 3D topographic AFM images and the line profile analyses of the sample G1C1-B1 are shown in Figure 4.8. The average RMS roughness over the five scanned areas for this sample was found to be 8.36 nm. The Profile analyses showed that the maximum height of the particules had risen up to 141.72 nm and the damaged sample surface had pits up to 10 nm depths. Unlike G1C1-A series, the average RMS roughness of the sample G1C1-B1was considerably increased with the decreasing volume ratio of H_2SO_4. SEM micrograph of the sample G1C1-B1 with 100 000 magnification is shown in Figure 4.9. EDX analysis of the G1C1-A3 sample showed that both C and O contaminations exists on the sample surface. When compared to G1C1-A series atomic percentage of O was increased rapidly.

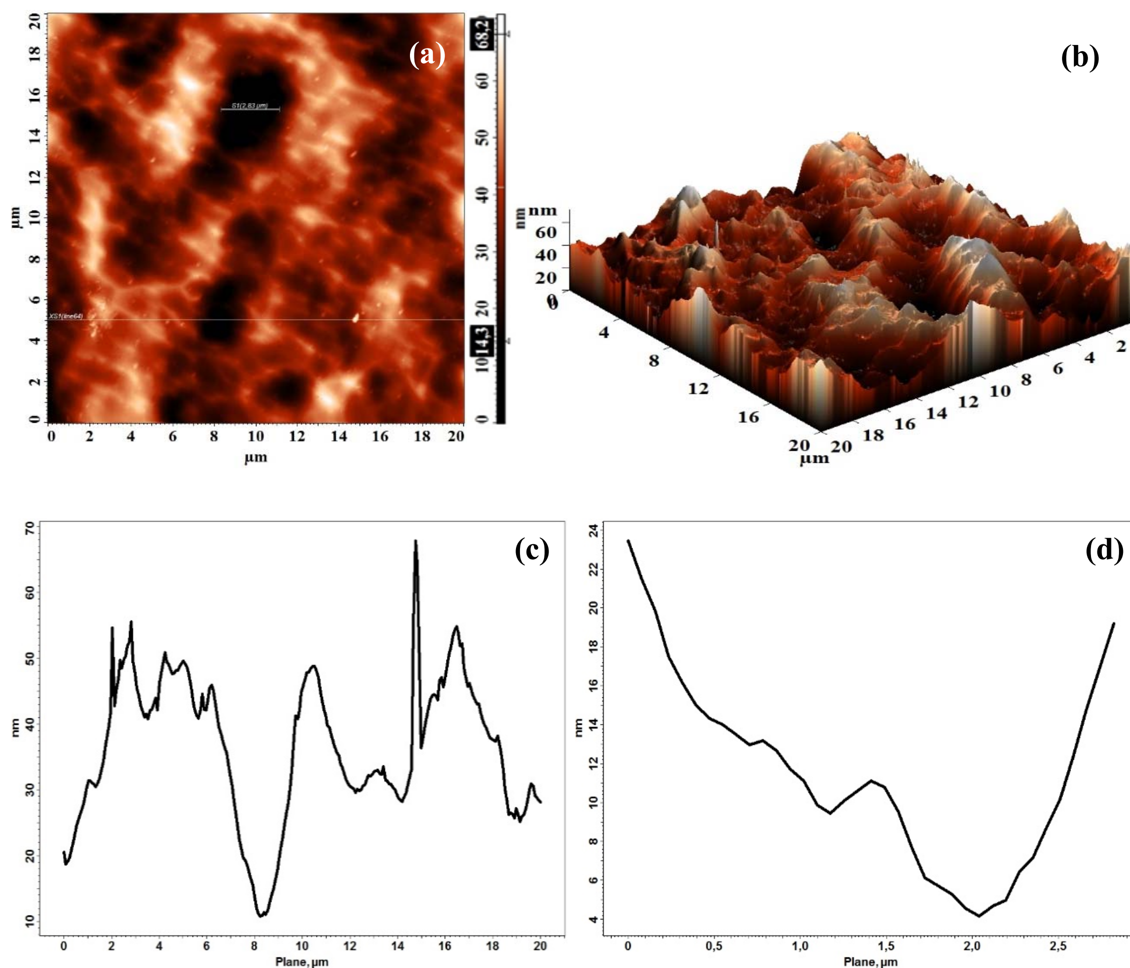

Figure 4.10. (a) AFM 2D Topographic image and (b) AFM 3D Topographic image of sample G1C1-B2 and profile line analysis of (c) XS1(line 64) and (d) S1 line of 2.83 µm width

In Figure 4.10 and Figure 4.11, 2D and 3D topographic AFM images and SEM images for sample G1C1-B2 are given. The average RMS roughness over the scanned three areas for this sample was found to be 6.92 nm which was decreased due to the reduced implementation time of 60 seconds. Profile analyses showed that the maximum height of particules goes up to 71.49 nm and the sample surface was etched up by approximately 4 nm. The AFM topographic image consistent with the SEM image with 10 000 magnification which shows the sample surface shows porous structure. The EDX elemental analyses showed that the surface has O, C and also less than one atomic percentage of S contamination. S contaminant can be formed as a result of implementation of the surface with H_2SO_4 mixture.

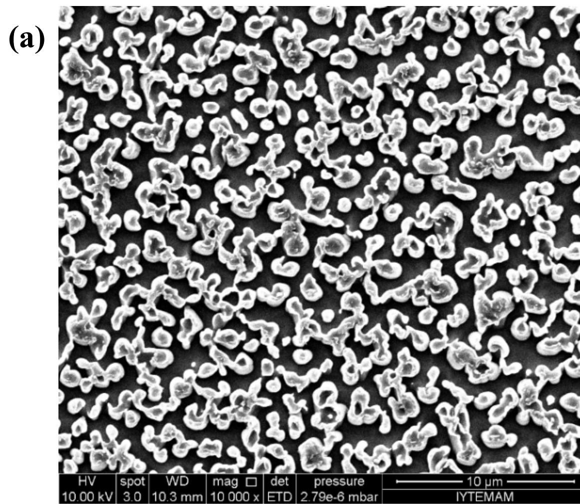

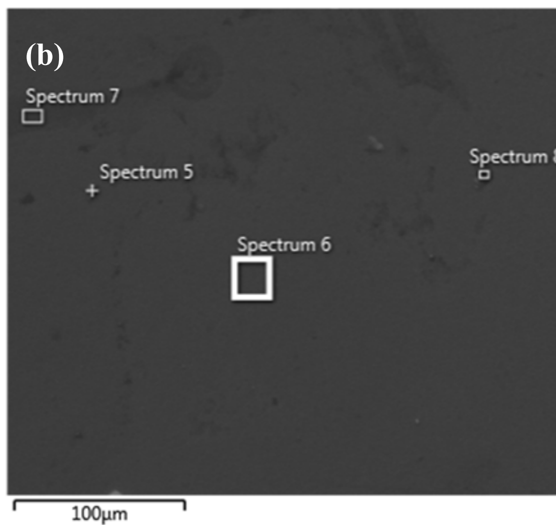

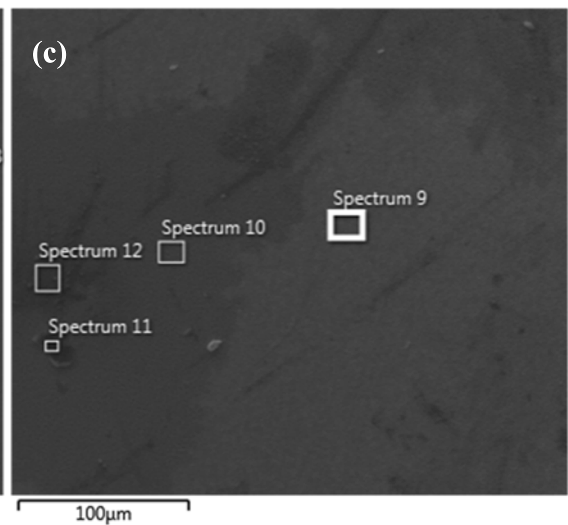

Element	Weight %	Atomic %
Spectrum 6		
Ga	47.72	42.01
As	48.75	39.94
C	3.53	18.05
Spectrum 7		
Ga	45.51	31.30
As	44.05	28.20
C	9.25	36.93
O	1.19	3.57

Element	Weight %	Atomic %
Spectrum 9		
Ga	47.33	40.19
As	48.28	38.16
C	4.39	21.65
Spectrum 11		
Ga	21.27	5.31
As	15.73	3.65
C	62.81	90.94
S	0.19	0.10

Figure 4.11. (a), (b) and (c) are SEM micrographs of sample G1C1-B2 with 10 000 and 100 000 magnifications where spectra show the regions that EDX analysis were performed in SEM image (a) and (b), the table shows the percentage of distributions of elements in spectrum 6, 7, 9 and 11.

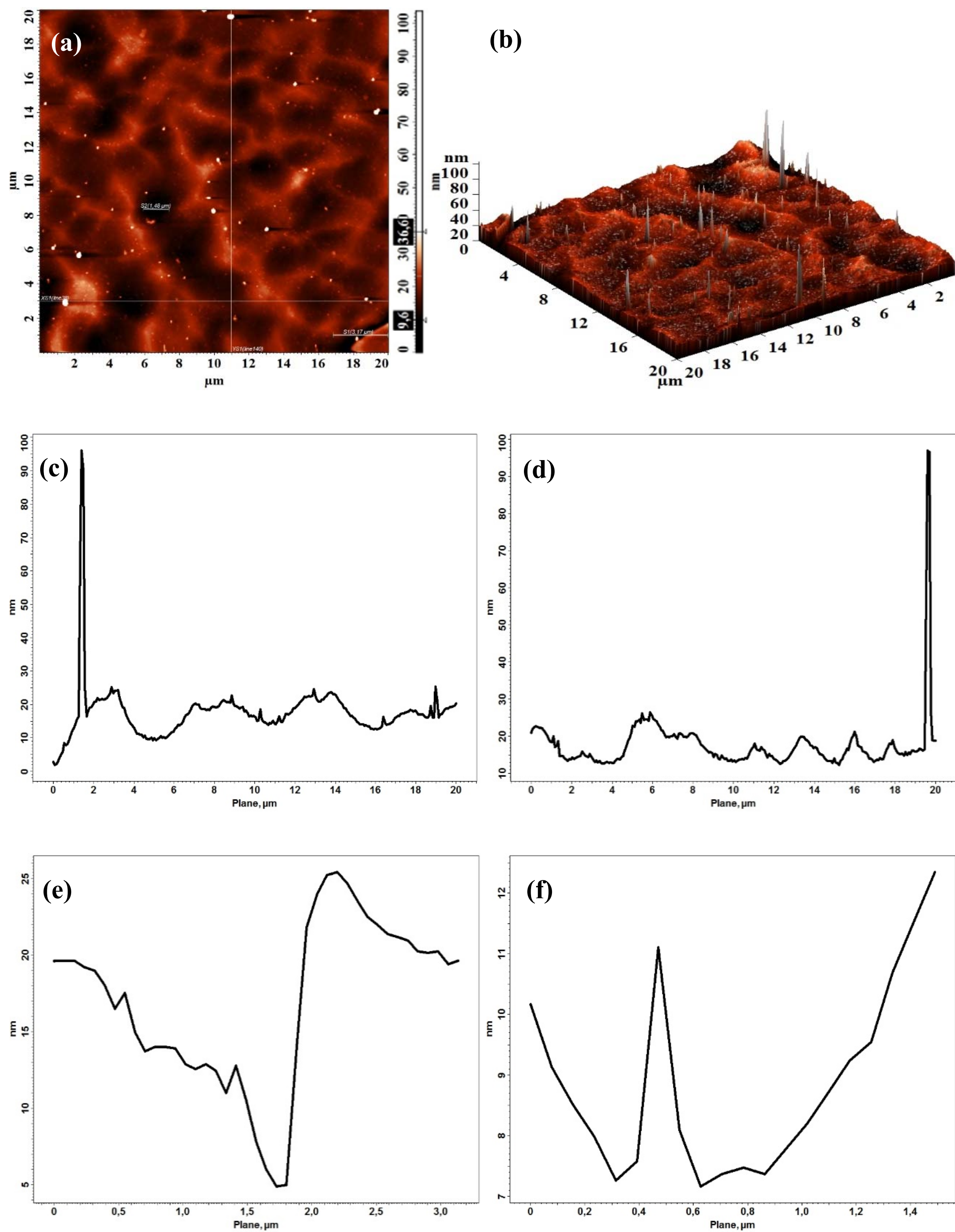

Figure 4.12. (a) AFM 2D Topographic image and (b) AFM 3D Topographic image of sample G1C1-B3 and profile line analysis of (c) XS1(line 38), (d) YS1 (line 140), (e) S1 line of 3.17 µm width and (f) S2 line of 1.48 µm width.

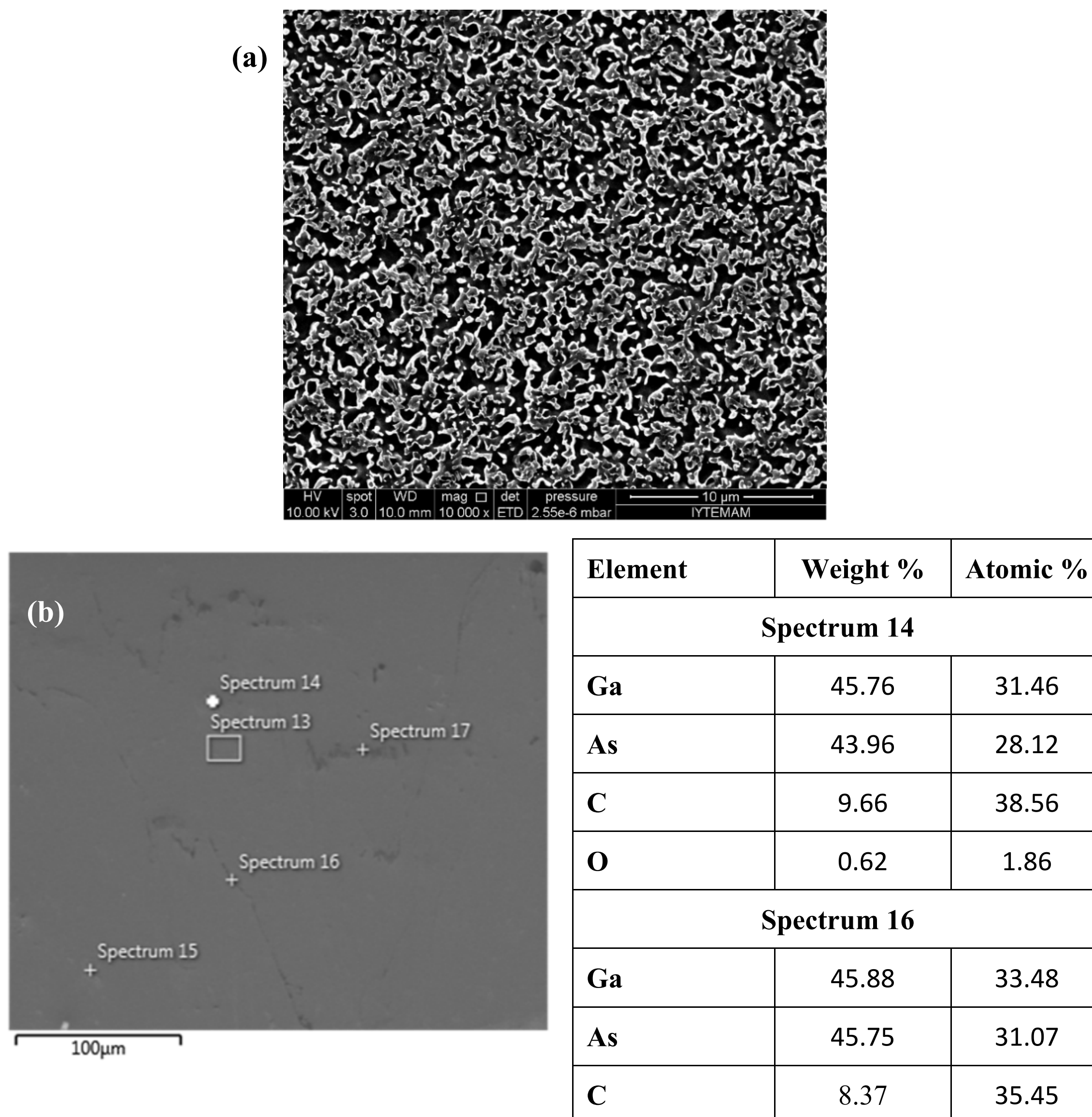

Element	Weight %	Atomic %
Spectrum 14		
Ga	45.76	31.46
As	43.96	28.12
C	9.66	38.56
O	0.62	1.86
Spectrum 16		
Ga	45.88	33.48
As	45.75	31.07
C	8.37	35.45

Figure 4.13. (a), (b) are SEM micrographs of sample G1C1-B3 with 10 000 and 100 000 magnifications where spectra show the regions that EDX analysis were performed in SEM image (b), the table shows the percentage of distributions of elements in spectrum 14 and 16.

2D and 3D topographic AFM images and SEM images for the sample G1C1-B3 are given in Figure 4.12 and Figure 4.13. The average RMS roughness over the scanned three areas for this sample was found as 2.30 nm, which is much decreased from the above values due to the reduced exposure times down to 30 seconds using the piranha solution. Decreasing the implementation time of the mixture on the sample, the maximum particule height increased to 103.66 nm from the values of maximum particule heights for the sample G1C1-B2. However, for the sample G1C1-B1, the maximum height of particules could not be associated with the implementation time which has a higher value compared

to the other G1C1-B series. Profile analyses showed that the sample surface was etched by up to approximately 5 nm.

The AFM topographic image was consistent with the SEM image with 10 000 magnification which showed that the sample surface had a porous structure. As seen in the SEM image with 10 000 magnification, areas of deep pits are less than those of the G1C1-B2 sample which can be deduced from the SEM image shown in Figure 4.11. The EDX elemental analyses showed that the surface had O and C contaminations. Also, it was observed in the EDX spectra of this sample that some parts of the sample surface were nearly stoichiometric and some parts were Ga-rich.

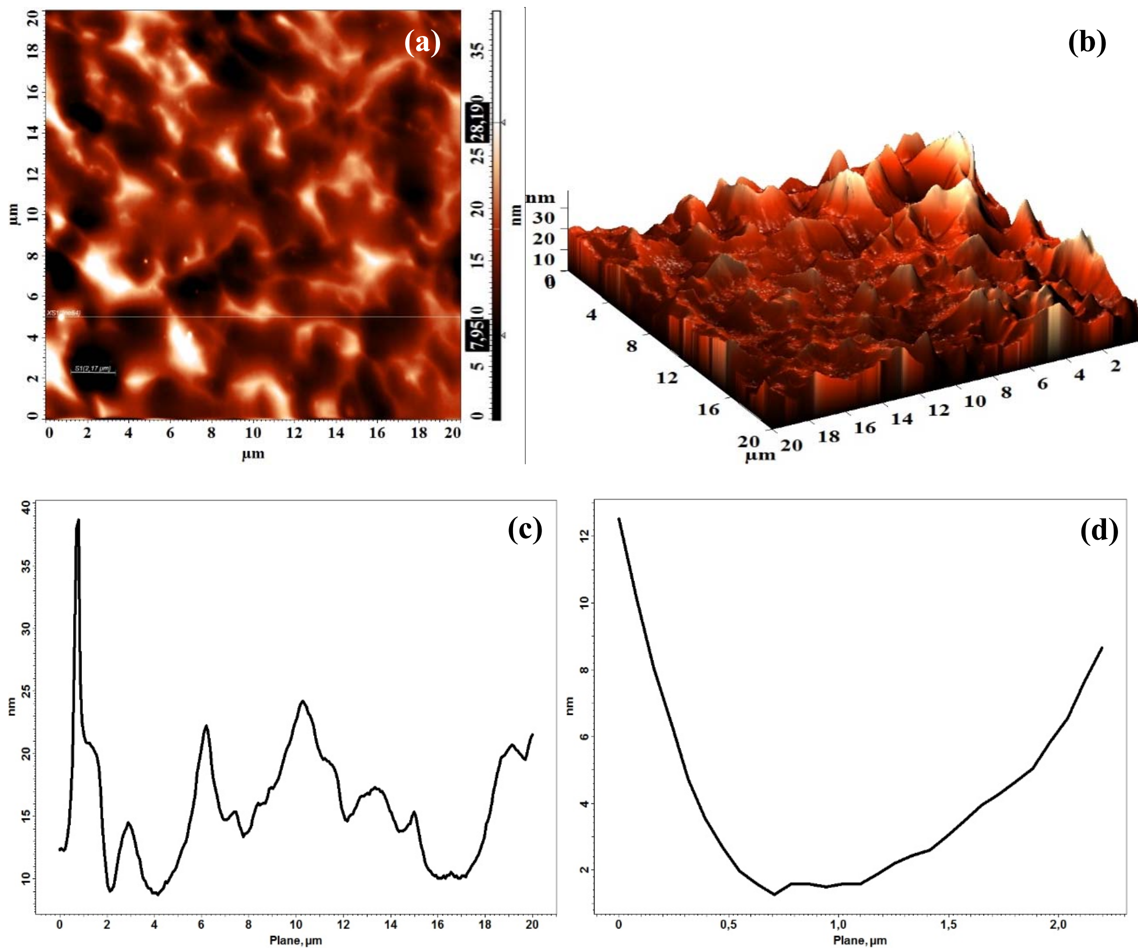

Figure 4.14. (a) AFM 2D Topographic image and (b) AFM 3D Topographic image of sample G1C1-C1 and profile line analysis of (c) XS1(line 64) and (d) S1 line of 2.17 µm width.

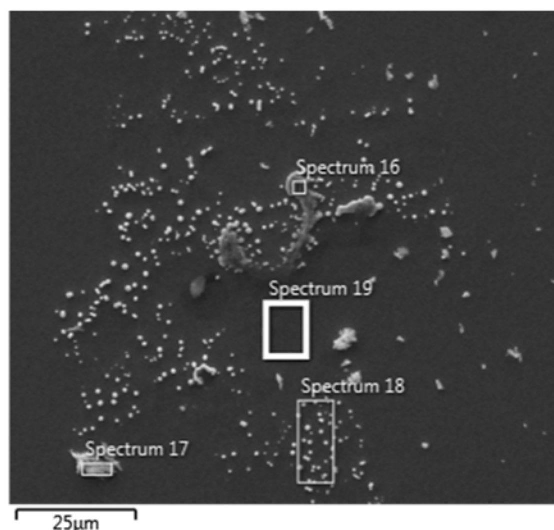

Element	Weight %	Atomic %
Spectrum 16		
Ga	48.42	50.21
As	51.58	49.79
Spectrum 17		
Ga	48.58	50.38
As	51.42	49.62

Element	Weight %	Atomic %
Spectrum 18		
Ga	50.06	51.86
As	49.94	48.14
Spectrum 19		
Ga	49.48	51.28
As	50.52	48.72

Figure 4.15. SEM micrograph of sample G1C1-C1 with 25 000 magnification where spectra show the region that EDX analysis were performed in SEM image and the tables show the percentage of distributions of Ga and As in spectrum 16, 17, 18 and 19.

AFM 2D and 3D topographic images and the line profile analyses of the sample G1C1-C1 are shown in Figure 4.14. The average RMS roughness found from the three scanned areas for this sample was found to be 3.26 nm. The line profile analyses showed that the maximum height of the particules reached up to 36.93 nm and the sample surface was etched up as much as 2 nm. As seen in the AFM topographic images of the sample G1C1-C1, sample surface, it has a porous structure similar to the surface of the G1C1-B series. The SEM micrograph of the sample G1C1-C1 with 25 000 magnification is shown in Figure 4.15. O and C contaminations were not observed from the EDX analysis of the G1C1-C1 sample. From the EDX analyses, it was seen that some parts of the sample surface were As-rich while some parts were Ga-rich or nearly stoichiometric.

.

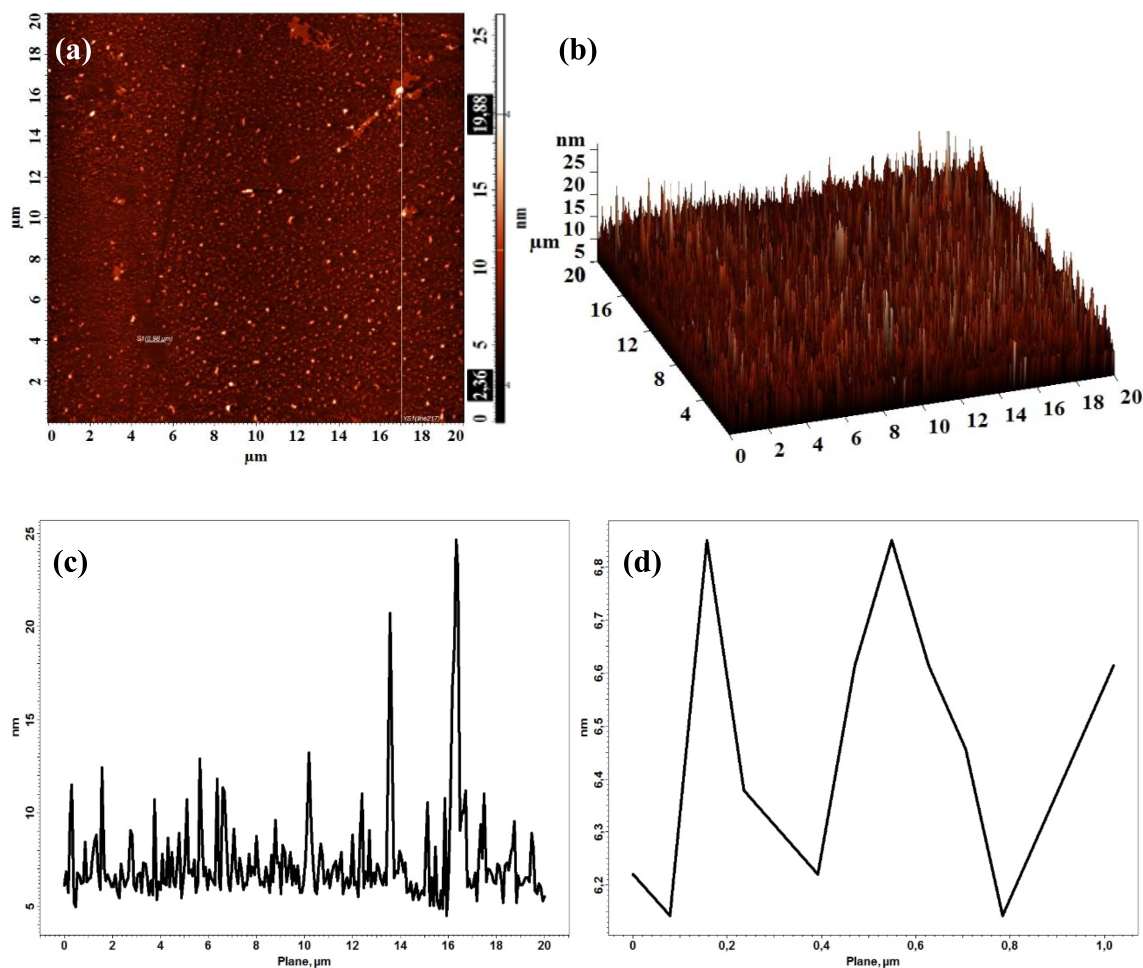

Figure 4.16. (a) AFM 2D Topographic image and (b) AFM 3D Topographic image of sample G1C1-C2 and profile line analysis of (c) YS1(line 217) and (d) S1 line of 0.98 µm width.

2D and 3D topographic AFM images and profile analyses for the sample G1C1-C2 are given in Figure 4.16. The average RMS roughness was found to be 3.43 nm which is smaller than the earlier values mentioned above due to the increased implementation time of 120 seconds with piranha solution. Also, increasing the implementation time of the mixture with sample the maximum height decreased to 24.96 nm when compared to sample G1C1-C1. The etching depth was about 6 nm. Unlike the G1C1-B series and G1C1-C1 sample, the porous structure could not be observed from AFM topographic images of G1C1-C2 sample.

The SEM micrograph with 50 000 magnification and the EDX analyses results are given in Figure 4.17 for sample G1C1-C2. As seen in the SEM image, the sample surface has some lightly damaged areas. O and C contamination were not observed in the lightly

damaged areas and in the dark areas from the EDX elemental analyses. Both lighter and darker areas are As-rich.

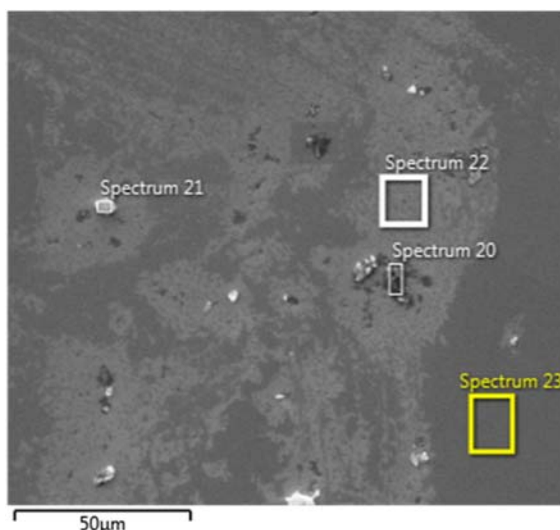

Element	Weight %	Atomic %
Spectrum 22		
Ga	48.45	50.25
As	51.55	49.75

Element	Weight %	Atomic %
Spectrum 23		
Ga	48.77	50.57
As	51.23	49.43

Figure 4.17. SEM micrograph of sample G1C1-C2 with 50 000 magnification where spectra show the region that EDX analysis were performed in SEM image and the tables show the percentage distributions of Ga and As in spectrum 22 and 23.

AFM images of the sample G1C1-C3 are given in Figure 4.16. The average roughness was found as 4.11 nm which is more than those for the G1C1-C1 and G1C1-C2 due to the reduced implementation time of 30 seconds of the piranha solution. The maximum height was also decreased to down to 36 nm from those for the G1C1-C1 and G1C1-C2 samples. The surface of the G1C1-C3 was etched up by 20 nm which is the most among all the G1C1-C series. This can be associated with reduced exposure time. Figure 4.19 shows the SEM images of the sample G1C1-C3 with 100 000 magnification. Both C and O contaminations could not be observed on lighter and darker areas on the sample surface from the EDX spectra like as other G1C1-C series. Both lighter and darker areas become As-rich after the etching the sample with $3H_2SO_4:1H_2O_2:1H_2O$ mixture for

30 seconds. When compared to the G1C1-A series, the C contamination couldn't be observed for G1C1-C series due to drying sample in a spin dryer at 4600 rpm.

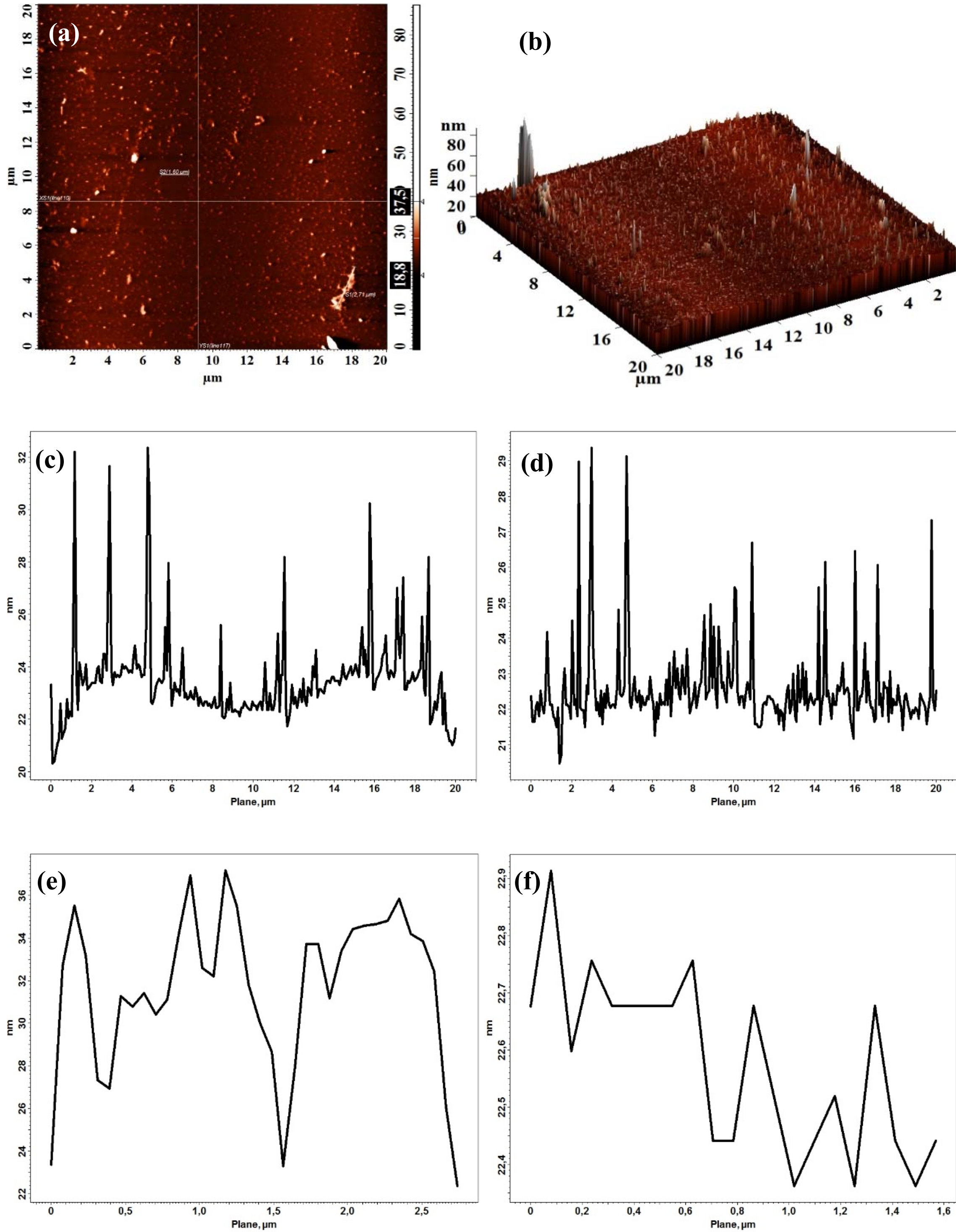

Figure 4.18. (a) AFM 2D Topographic image and (b) AFM 3D Topographic image of sample G1C1-C3 and profile line analysis of (c) XS1(line 110), (d) YS1 (line 117), (e) S1 line of 2.17 µm width and (f) S2 line of 1.60 µm width.

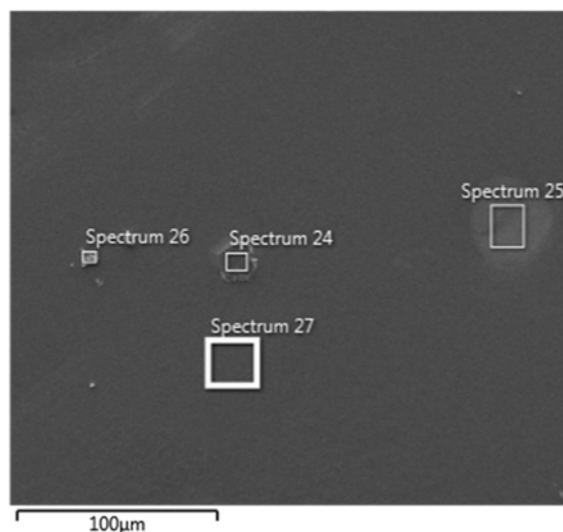

Element	Weight %	Atomic %
Spectrum 24		
Ga	48.80	50.60
As	51.20	49.40

Element	Weight %	Atomic %
Spectrum 27		
Ga	49.07	50.87
As	50.93	49.13

Figure 4.19. SEM micrograph of sample G1C1-C3 with 100 000 magnification where spectra show the region that EDX analysis were performed in SEM image and the tables show the percentage distributions of Ga and As in spectrum 24 and 27.

AFM images and EDX results for the G1C1-E1 obtained as before are given in Figure 4.20. The average RMS roughness was found as 1.48 nm. The maximum height of particules was about 12.80 nm and the sample surface was etched up to 3 nm. The AFM images show that the sample surface has a porous structure like as G1C1-B1 and G1C1-B2 but differs in the areas of deep pits which are smaller compared to G1C1-B1 and G1C1-B2.

The SEM images and EDX results of the sample G1C1-E1 are shown in Figure 4.21. Despite drying the sample with a spin dryer after the etching process, EDX spectra showed some C contamination on the sample surface which can be as a result of air exposure of sample or degreasing step of etching process with acetone and methanol.

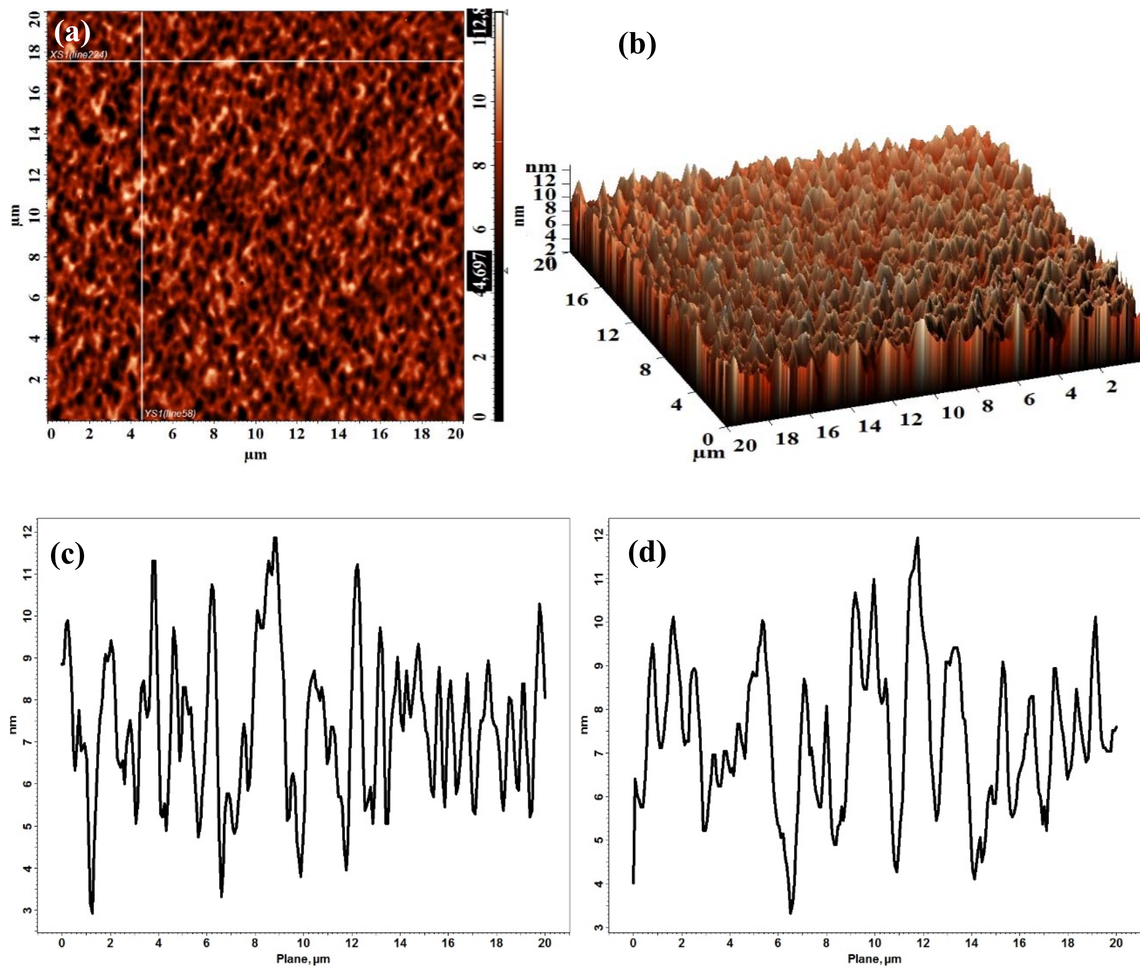

Figure 4.20. (a) AFM 2D Topographic image and (b) AFM 3D Topographic image of sample G1C1-E1 and profile line analysis of (c) XS1 (line 224) and (d) YS1 (line 58).

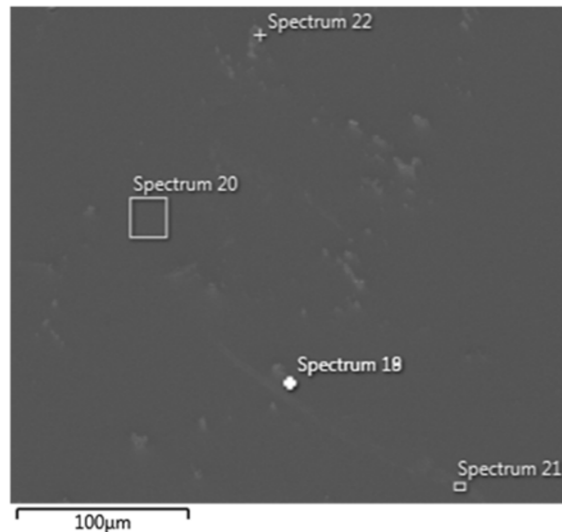

Element	Weight %	Atomic %
Spectrum 18		
Ga	47.36	40.61
As	48.48	38.68
C	4.16	20.71

Element	Weight %	Atomic %
Spectrum 20		
Ga	46.73	40.15
As	49.14	39.29
C	4.12	20.56

Figure 4.21. SEM micrograph of sample G1C1-E1 with 100 000 magnification where spectra show the region that EDX analysis were performed in SEM image and the tables show the percentage distributions of Ga, As and C in spectrum 18 and 20.

Similar results for G1C1-E2 are given in Figure 4.22. It has a roughness of 0.32 nm which with a maximum particule height of 5.5 nm obtained after 60 second implementation of the etchant. However, decreasing the implementation time could not correlated with the maximum height of particules. The SEM micrograph with 100 000 magnification and EDX analyses results for two scanned area of this sample are shown in Figure 4.23. Some C contamination was observed for both damaged and not damaged areas on the sample surface despite drying the sample with a spin dryer which can be observed as a result of air exposure of the sample after etching process or decreasing step. Inspite of decreasing H_2O_2 volume ratio with respect to other etched GaAs(211)B samples, O contamination was observed on lighter areas on the sample surface from the EDX spectra.

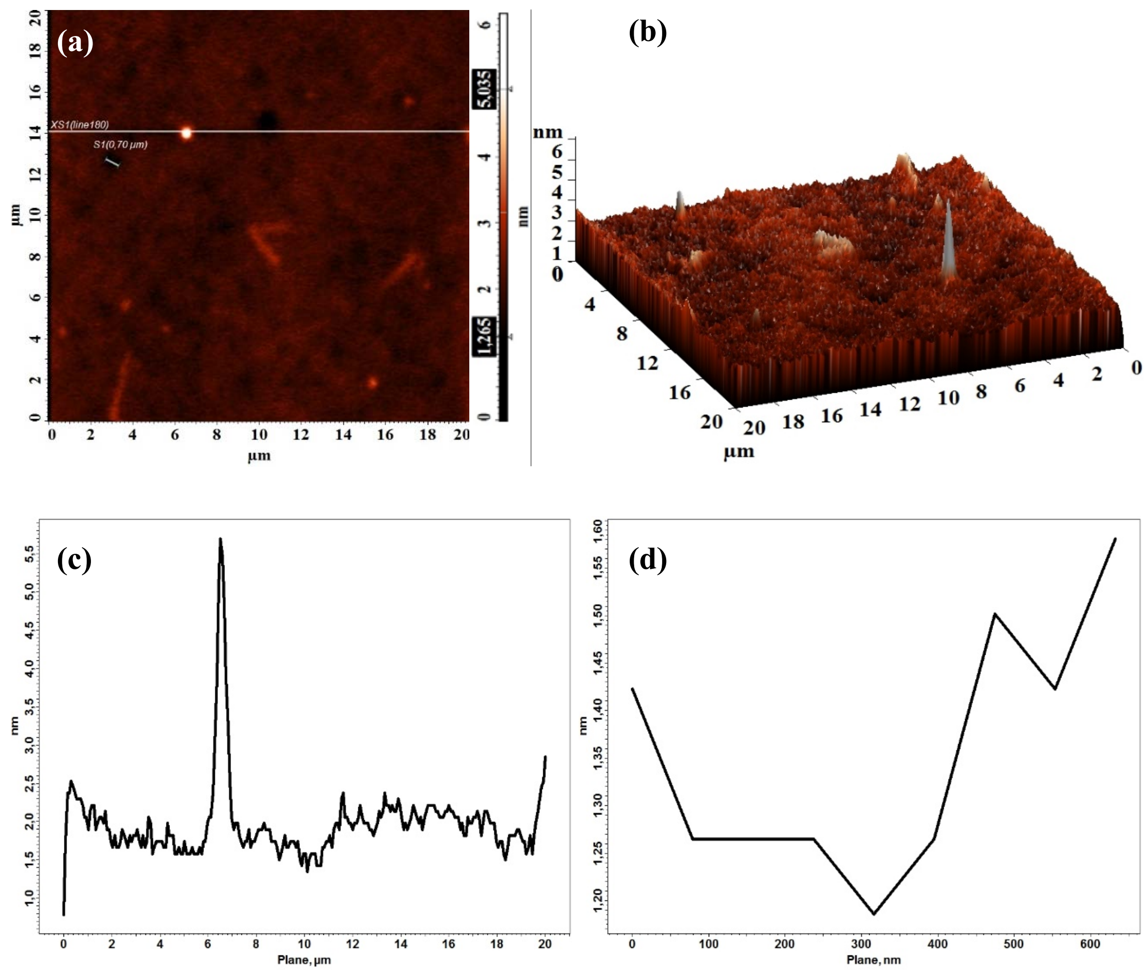

Figure 4.22. (a) AFM 2D Topographic image and (b) AFM 3D Topographic image of sample G1C1-E2 and profile line analysis of (c) XS1 (line 180) and (d) S1 line of 0,70 µm width.

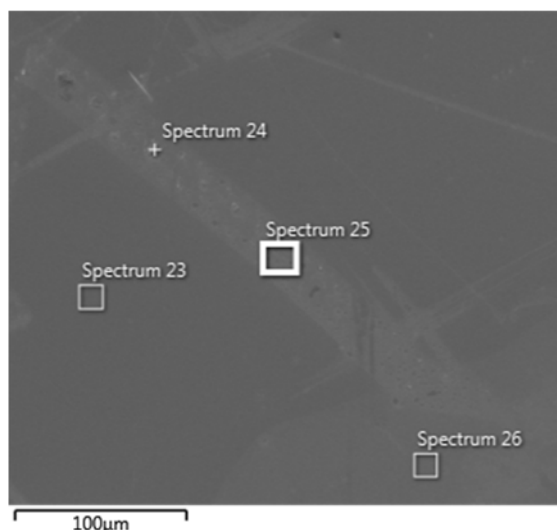

Element	Weight %	Atomic %
Spectrum 23		
Ga	47.45	41.75
As	49.00	40.12
C	3.55	18.13

Element	Weight %	Atomic %
Spectrum 25		
Ga	46.95	38.97
As	47.56	36.73
C	3.72	17.91
O	1.77	6.40

Figure 4.23. SEM micrograph of sample G1C1-E2 with 100 000 magnification where spectra show the region that EDX analysis were performed in SEM image and the tables show the percentage distributions of Ga, As, C and O in spectrum 23 and 25.

The results for G1C1-E3 are given in Figure 4.24. Its roughness was found as 0.14 nm which decreased with decreasing implementation time of 30 seconds when compared to other G1C1-E series. The height of the particules are as 3.56 nm which is less than those for the earlier samples mentioned due to the reduced exposure time of the piranha solution with the sample. The sample surface was etched up by approximately 0.5 nm. The SEM images and EDX analyses results are given in Figure 4.25. The sample surface became Ga-rich after chemical. Also some C contamination was observed on the lighter regions of the sample surface.

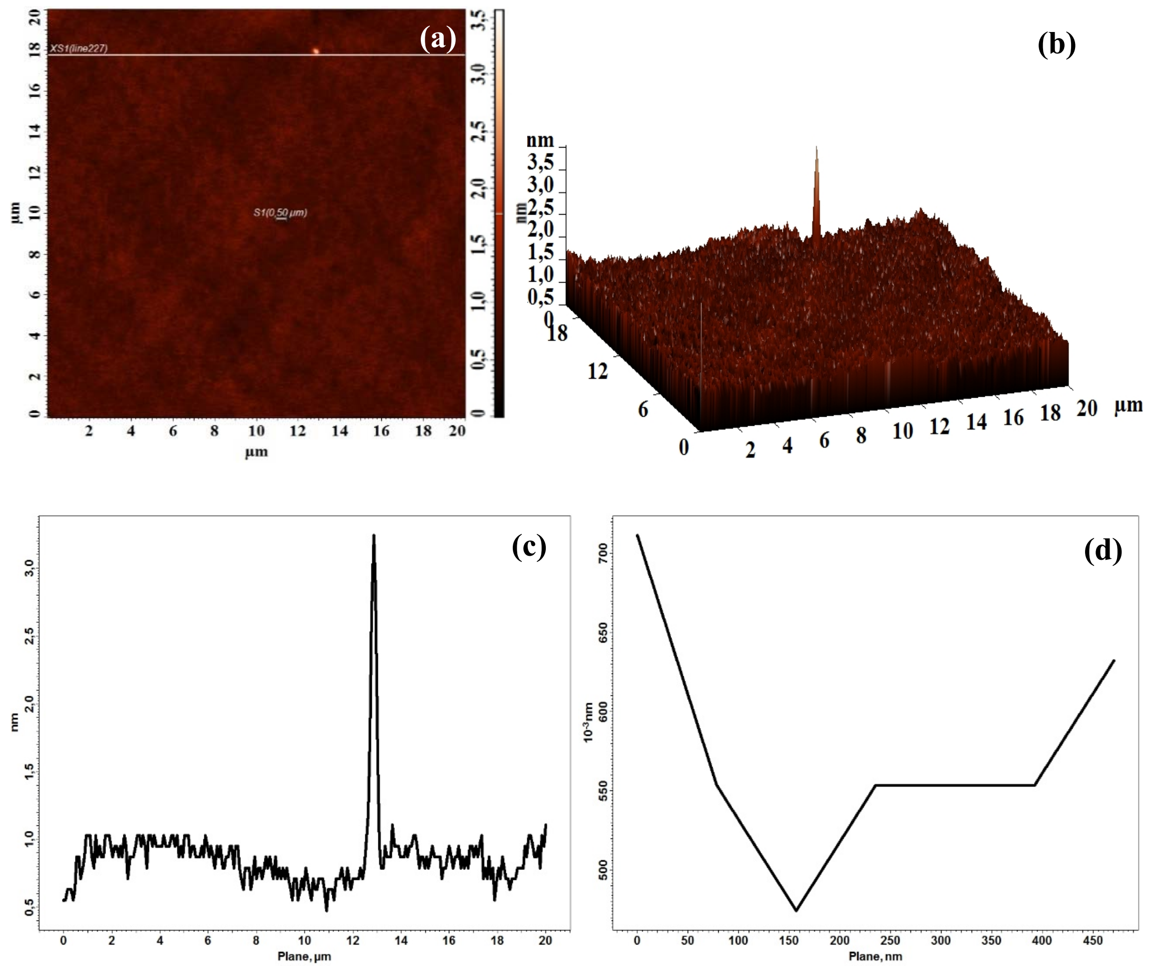

Figure 4.24. (a) AFM 2D Topographic image and (b) AFM 3D Topographic image of sample G1C1-E3 and profile line analysis of (c) XS1 (line 227) and (d) S1 line of 0,50 µm width

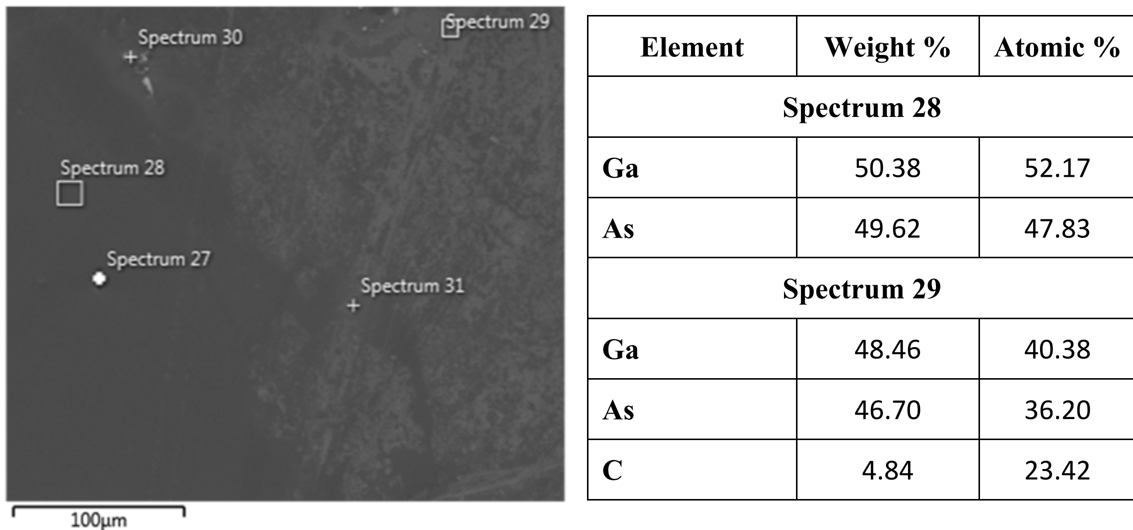

Element	Weight %	Atomic %
Spectrum 28		
Ga	50.38	52.17
As	49.62	47.83
Spectrum 29		
Ga	48.46	40.38
As	46.70	36.20
C	4.84	23.42

Figure 4.25. SEM micrograph of sample G1C1-E3 with 100 000 magnification where spectra show the region that EDX analysis were performed in SEM image and the tables show the percentage distributions of Ga, As and C in spectrum 28 and 29.

AFM 2D and 3D topographic images for only degreasing step performed sample is shown in Figure 4.26. The average RMS roughness over scanned three area for this sample was found as 0.75 nm which showed when only degreasing step was performed, the sample surface was damaged due to boiling in acetone and methanol. The maximum height of particules achieve up to 27.09 nm.

Figure 4.27 give the SEM and the EDX analyses results for two regions for the sample G1C1-F1, the sample is not damaged due to skipping the etching step. However, the sample surface was Ga-rich after performed acetone and methanol rinsing. Also, both C and O contaminations were observed that C contamination had a high percentage due to decreasing step.

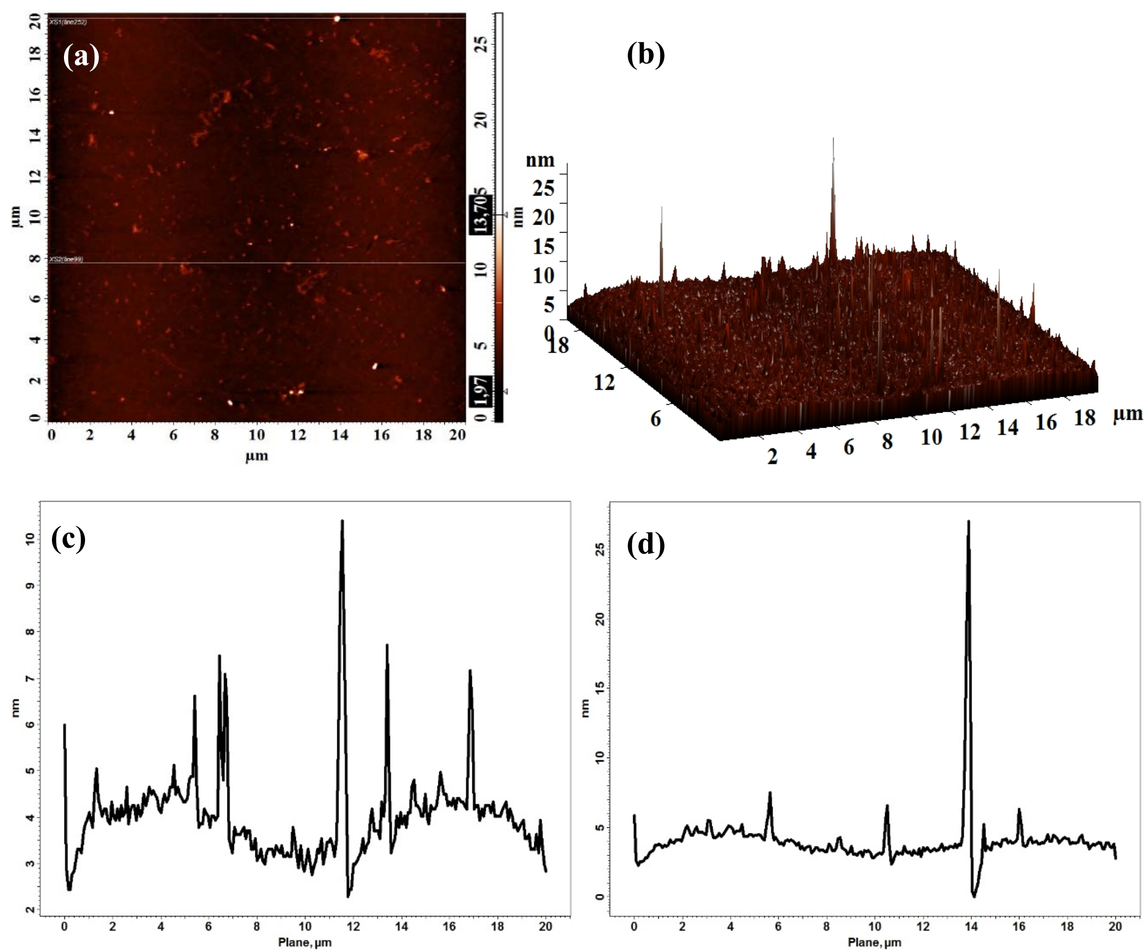

Figure 4.26. (a) AFM 2D Topographic image and (b) AFM 3D Topographic image of sample G1C1-F1 and profile line analysis of (c) XS2 (line 99) and (d) XS1 (line 252).

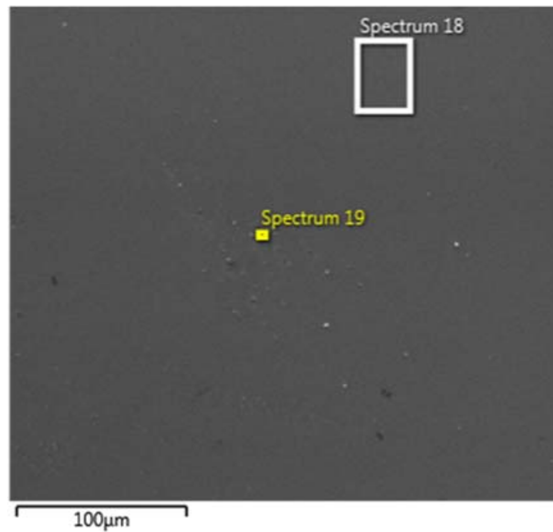

Element	Weight %	Atomic %
Spectrum 18		
Ga	47.54	40.52
As	48.00	37.95
C	4.08	20.11
O	0.38	1.42

Element	Weight %	Atomic %
Spectrum 19		
Ga	46.52	34.7
As	45.39	31.39
C	7.15	30.86
O	0.94	3.05

Figure 4.27. Left side of the figure is SEM micrograph of sample G1C1-F1 with 100 000 magnification where spectra show the region that EDX analysis were performed in SEM image and the table shows the percentage of distributions of Ga, As, C and O in spectrum 18 and 19.

AFM 2D and 3D topographic images for only etched sample with piranha solution are shown in Figure 4.28. The average RMS roughness over scanned three area for this sample was found 0.33 nm which is better result with respect to only degreasing step performed sample. The sample etched up to approximately 3.5 nm. The surface is smooth and the profile analyses showed that the maximum height of particules decreased to 9.21 nm when compared to other etched GaAs(211)B samples.

Similar SEM and EDX measurements of the G1C1-F2 sample for two regions are given in Figure 4.29. We see from the SEM picture of the sample G1C1-F2, the sample surface had lighter and darker areas as a result of etching. From the EDX spectra, the sample was seen to be Ga-rich. In addition, likely to G1C1-F1, both C and O contaminations were observed that C contamination had a high percentage.

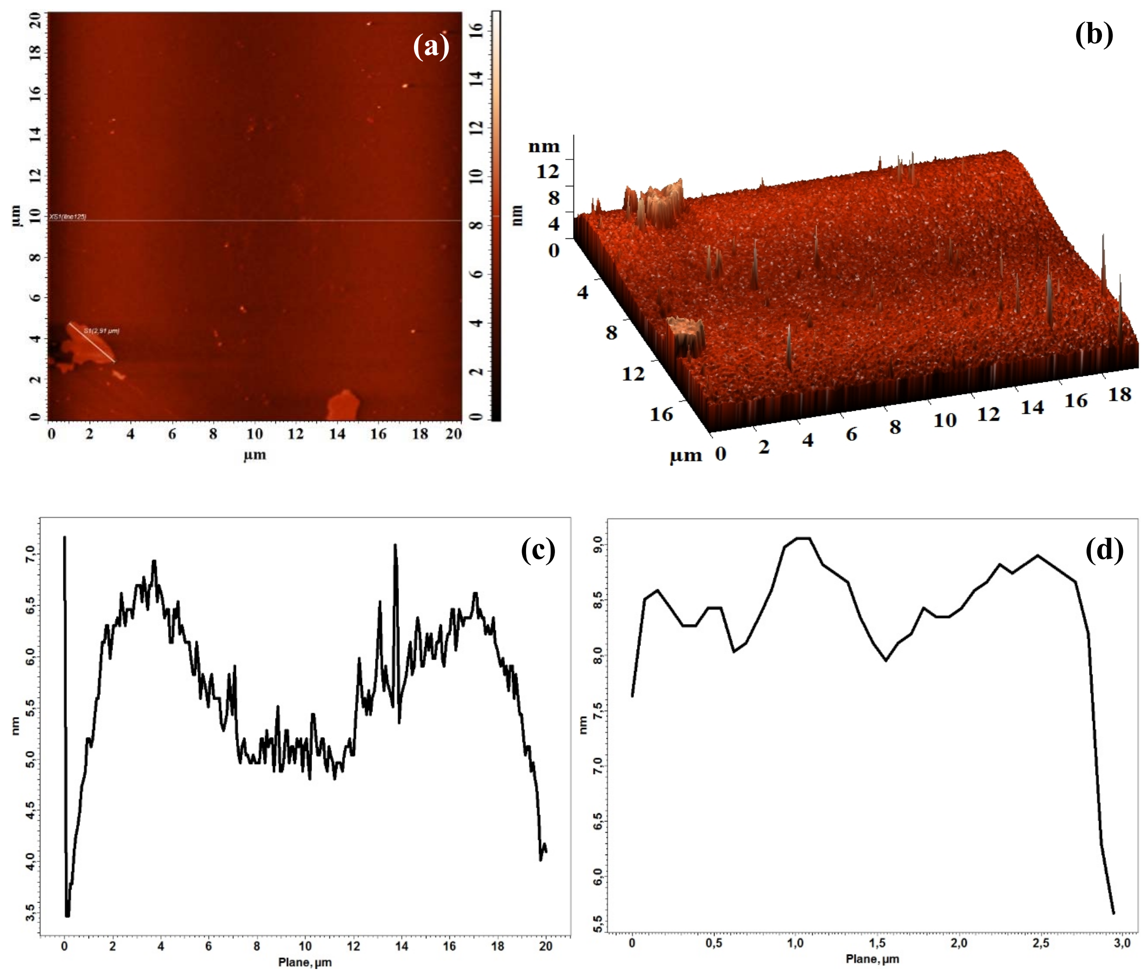

Figure 4.28. (a) AFM 2D Topographic image and (b) AFM 3D Topographic image of sample G1C1-F2 and profile line analysis of (c) XS2 (line 125) and (d) S1 line of 2,91 µm width.

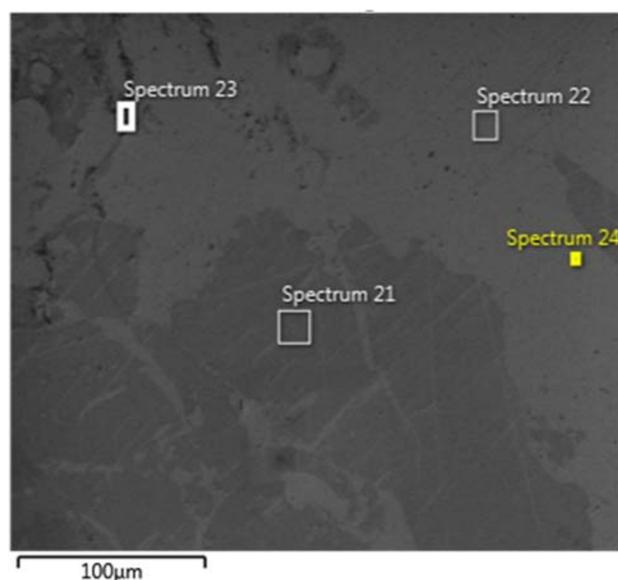

Element	Weight %	Atomic %
Spectrum 23		
Ga	41.55	21.53
As	38.03	18.29
C	18.98	56.93
O	1.44	3.25

Element	Weight %	Atomic %
Spectrum 24		
Ga	45.76	34.84
As	46.87	33.21
C	6.79	30.01
O	0.58	1.94

Figure 4.29. SEM micrograph of sample G1C1-F2 with 100 000 magnification where spectra show the region that EDX analysis were performed in SEM image and the tables show the percentage distributions of Ga, As, C and O in spectrum 23 and 24.

AFM 2D and 3D topographic images and profile analyses for sample G1C1-G1 are given in Figure 4.30. As seen in AFM topographic images and SEM micrographs with 100 000 magnification in Figure 4.31, the sample surface was damaged after the etching with $3H_2SO_4$:$1H_2O_2$:$2H_2O$ for 30 seconds. The average RMS roughness over scanned three area for this sample was found 0.73 nm and the maximum height of particules achieve up to 44.80 nm. The sample surface was etched up to approximately 3.5 nm. EDX analyses results for scanned two regions showed that the sample surface became Ga-rich after etching with piranha solution. According to the atomic percentages of the elements, C and O contaminations was observed on the lighter and darker regions of the sample surface.

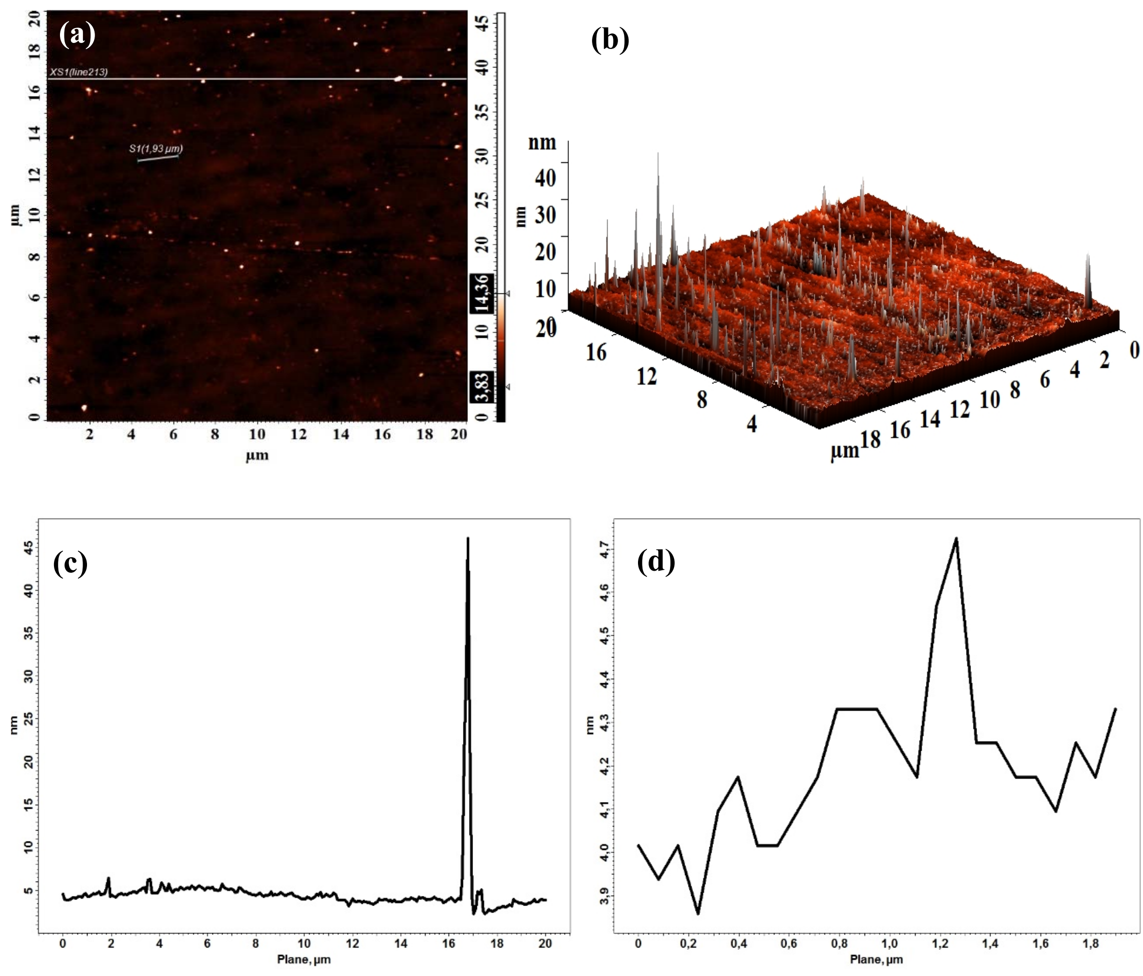

Figure 4.30. (a) AFM 2D Topographic image and (b) AFM 3D Topographic image of sample G1C1-G1 and profile line analysis of (c) XS1 (line 213) and (d) S1 line of 1,93 µm width.

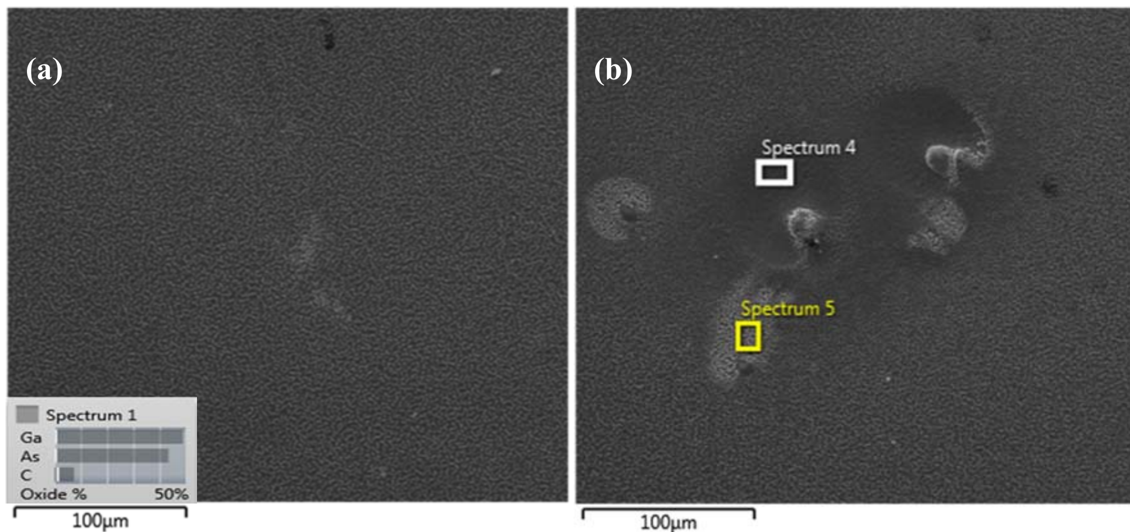

Element	Weight %	Atomic %
Spectrum 4		
Ga	49.00	43.24
As	47.51	39.02
C	3.38	17.33
O	0.11	0.41

Element	Weight %	Atomic %
Spectrum 5		
Ga	50.36	42.94
As	45.30	35.91
C	4.09	20.22
O	0.25	0.93

Figure 4.31. (a) and (b) are SEM micrographs of sample G1C1-G1 with 100 000 magnification where spectra show the region that EDX analysis were performed in SEM image (b) and the tables show the percentage distributions of Ga, As, C and O in spectrum 4 and 5.

In Figure 4.32, AFM 2D and 3D topographic images and the profile analysis for selected areas are shown for sample G1C1-G2. The average RMS roughness over scanned three area for this sample was found 0.71 nm and the maximum height of particules achieve up to 49.61 nm. It wasn't observed significantly change in the values of the average RMS roughness and the maximum height of particules, despite increasing the exposure time of mixture with the sample with respect to G1C1-G1. However, the sample surface was etched up to approximately 0.1 nm which is the highest value over the etched GaAs(211)B samples. SEM micrograph with 100 000 magnification and EDX analyses performed regions on the image are shown in Figure 4.33. According to EDX analyses, higher percentages of C and O contaminations were obtained on the darker and damaged areas.

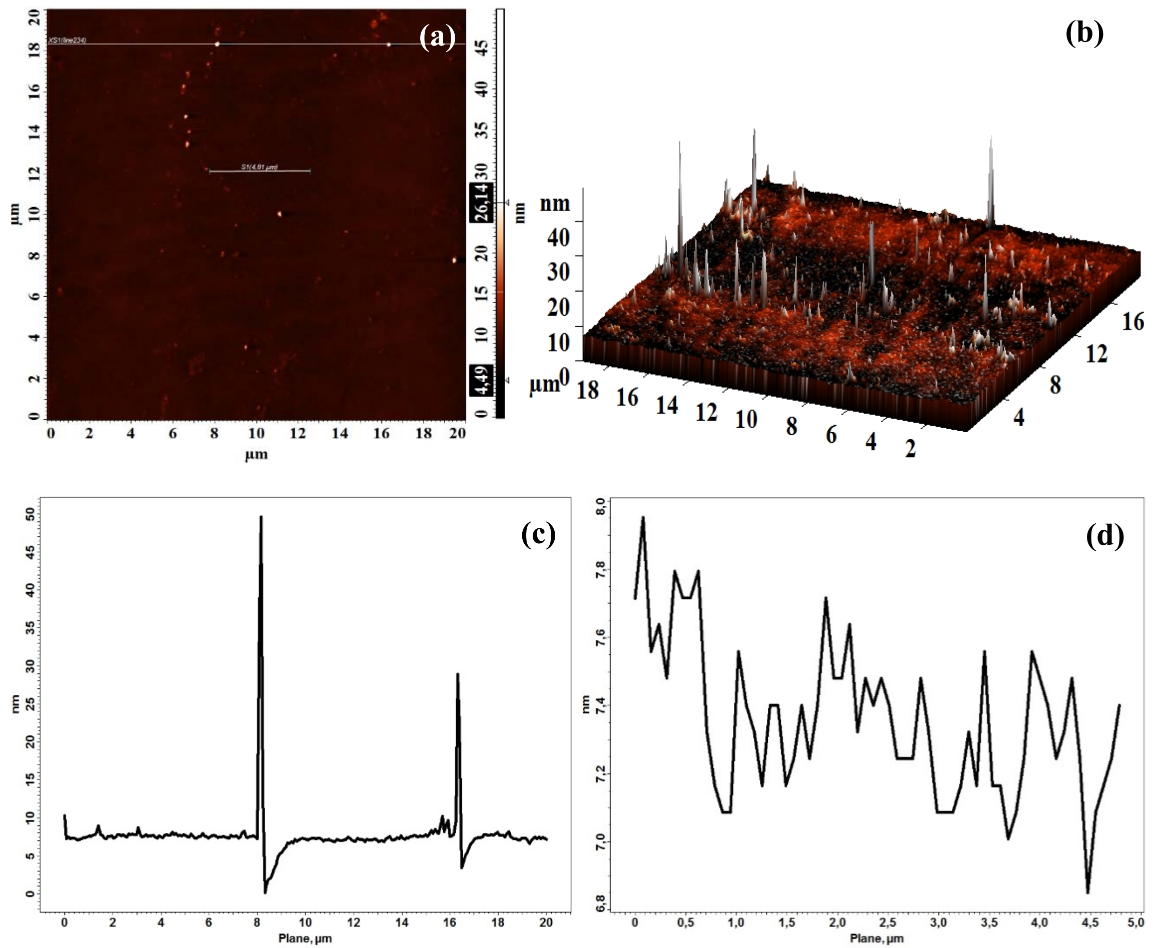

Figure 4.32. (a) AFM 2D Topographic image and (b) AFM 3D Topographic image of sample G1C1-G2 and profile line analysis of (c) XS1 (line 234) and (d) S1 line of 4,81 μm width.

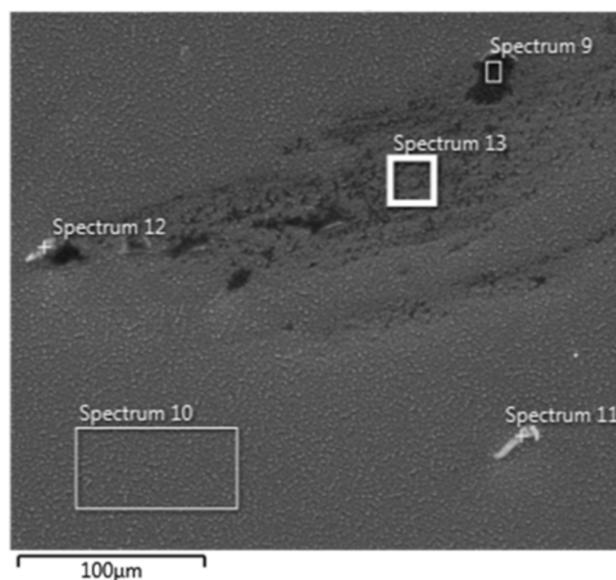

Element	Weight %	Atomic %
Spectrum 10		
Ga	47.29	41.46
As	49.00	39.97
C	3.49	17.77
O	0.21	0.80

Element	Weight %	Atomic %
Spectrum 13		
Ga	43.63	26.07
As	41.15	22.73
C	13.80	47.53
O	1.42	3.68

Figure 4.33. SEM micrograph of sample G1C1-G2 with 100 000 magnification where spectra show the region that EDX analysis were performed in SEM image and the tables show the percentage distributions of Ga, As, C and O in spectrum 10 and 13.

AFM 2D and 3D topographic images and profile analyses for sample G1C1-G3 are given in Figure 4.34. The average RMS roughness over scanned three area for this sample increased to 1.08 nm with respect to other G1C1-G series in which implementation time of the mixture was increased to 120 seconds. The maximum height of particules achieve up to 73.70 nm. However, it was expected that the maximum height of particules should be decreased with increasing the exposure time of the mixture with the sample surface. According to profile analyses, the sample was etched up to approximately 0.1 nm like as G1C1-G2 sample.

The SEM micrograph with 100 000 magnification and EDX analyses results for scanned two region are given in Figure 4.35. According the atomic percentages of the elements, it was observed that the sample surface became Ga-rich after chemical etching.

In addition, C and O contaminations was observed on both scanned regions in which atomic percentage of C contamination was increased damaged region on the sample surface.

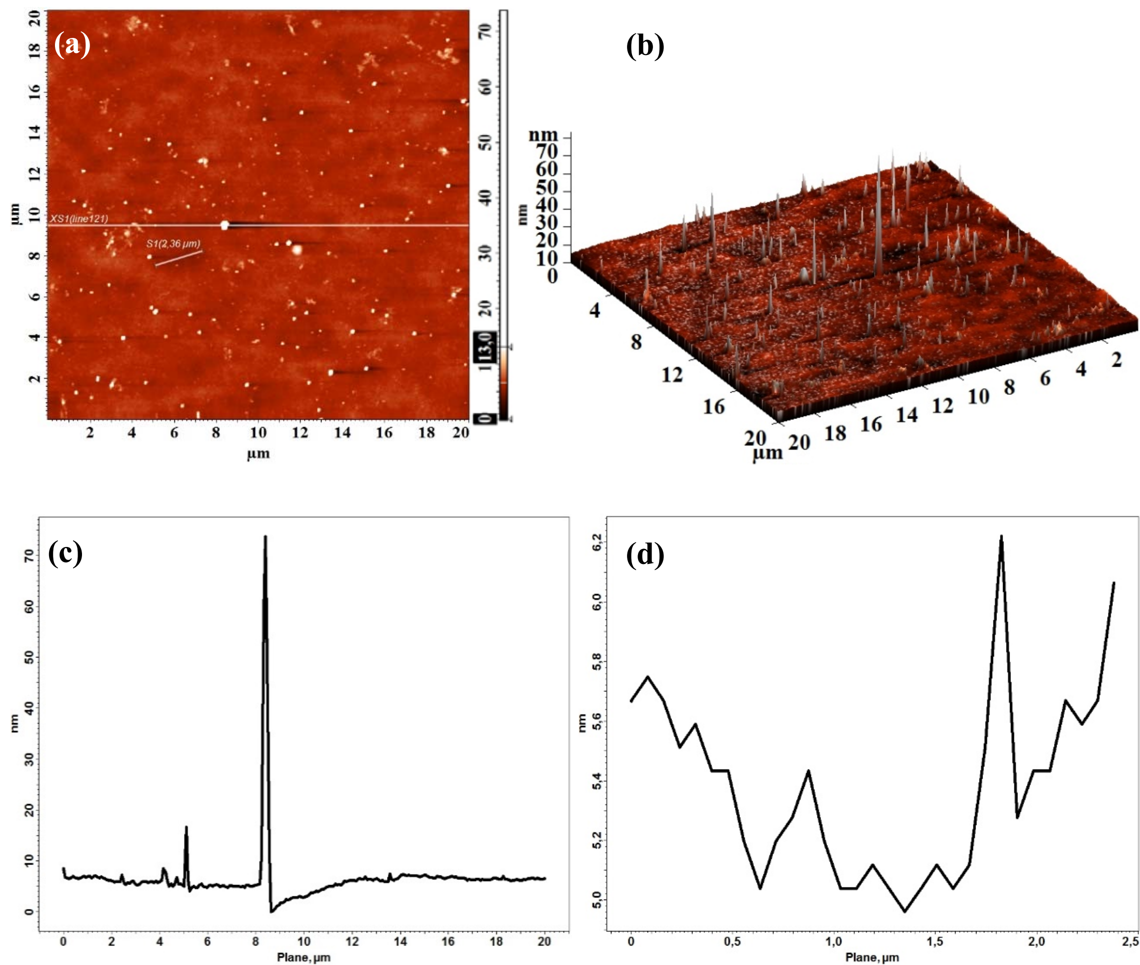

Figure 4.34. (a) AFM 2D Topographic image and (b) AFM 3D Topographic image of sample G1C1-G3 and profile line analysis of (c) XS1 (line 121) and (d) S1 line of 2,36 μm width.

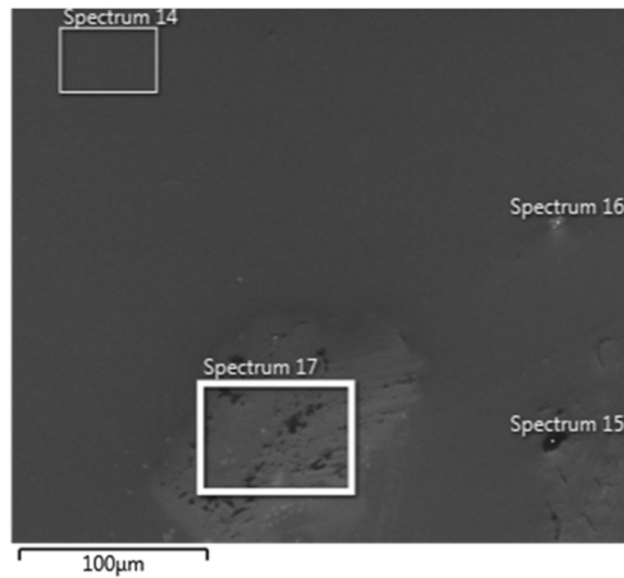

Element	Weight %	Atomic %
Spectrum 14		
Ga	47.64	41.09
As	48.19	38.54
C	3.85	19.20
O	0.31	1.16

Element	Weight %	Atomic %
Spectrum 17		
Ga	46.24	35.14
As	46.36	32.77
C	6.91	30.47
O	0.49	1.61

Figure 4.35. SEM micrograph of sample G1C1-G3 with 100 000 magnification where spectra show the region that EDX analysis were performed in SEM image and the tables show the percentage distributions of Ga, As, C and O in spectrum 14 and 17.

Surface morphologies of etched samples with piranha solution was obtained from the AFM topographic images, AFM profile analyses, and SEM micrographs. In addition; Ga, As, C, and O atomic percentage distributions were performed for selected areas on the sample surfaces. It was observed that average RMS roughness values change depending on the piranha mixture volume ratios and implementation times. Obtained average RMS roughness values, piranha mixture volume ratios and approximate etch depths are summarized in Table 4.3.

Table 4.3. The change of RMS roughness average depending on the mixture volume ratios and implementation times.

Sample ID	$H_2SO_4:H_2O_2:H_2O$		RMS Roughness Average (nm)
	Volume Ratios	Implementation Times (s)	
G1C1-A1	3:1:1	30	0.86
G1C1-A2		120	1.38
G1C1-A3		15	0.74
G1C1-B1	2:1:1	120	8.36
G1C1-B2		60	6.92
G1C1-B3		30	2.30
G1C1-C1	3:1:1	60	3.26
G1C1-C2		120	3.43
G1C1-C3		30	4.11
G1C1-E1	3:0.75:1	120	1.48
G1C1-E2		60	0.32
G1C1-E3		30	0.14
G1C1-F1	-	-	0.75
G1C1-F2	3:1:2	60	0.33
G1C1-G1	3:1:2	30	0.73
G1C1-G2		60	0.71
G1C1-G3		120	1.08

In addition to the etching with $H_2SO_4:H_2O_2:H_2O$ mixture, AFM topographic images and profile analyses were obtained for oxide removal process with $HF:H_2O$ mixture applied two GaAs(211)B samples; G2W24A and G2W25A. AFM 2D and 3D topographic images and profile analyses of these two samples before and after the etching process are shown in Figure 4.36 and Figure 4.37.

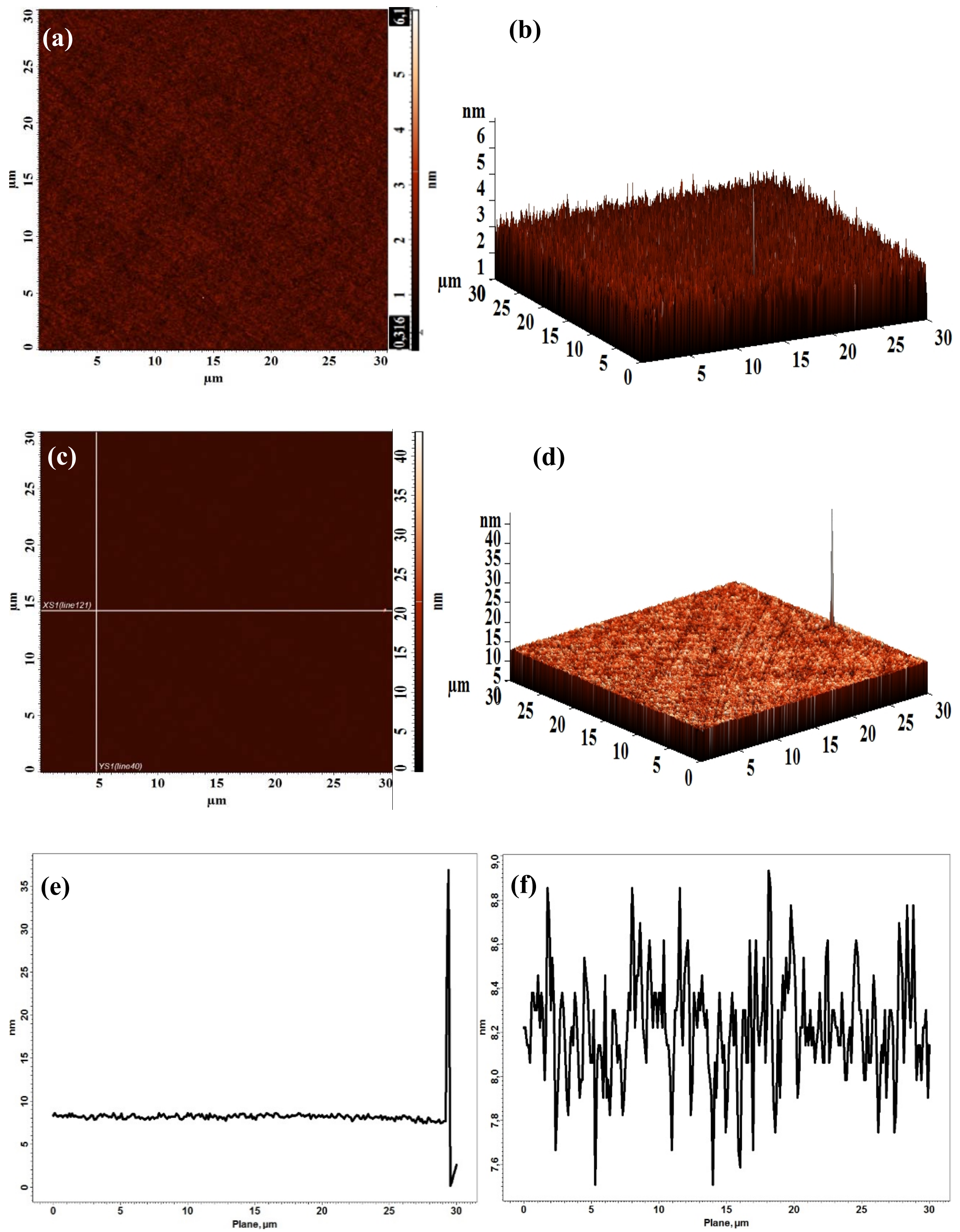

Figure 4.36. (a) and (b) are AFM 2D and 3D Topographic images before oxide removal, (c) and (d) are AFM 2D and 3D Topographic images and (d) and (e) are profile line analysis of XS1 (line 121) and (d) YS1 (line 40) of sample G2W24A after oxide removal process.

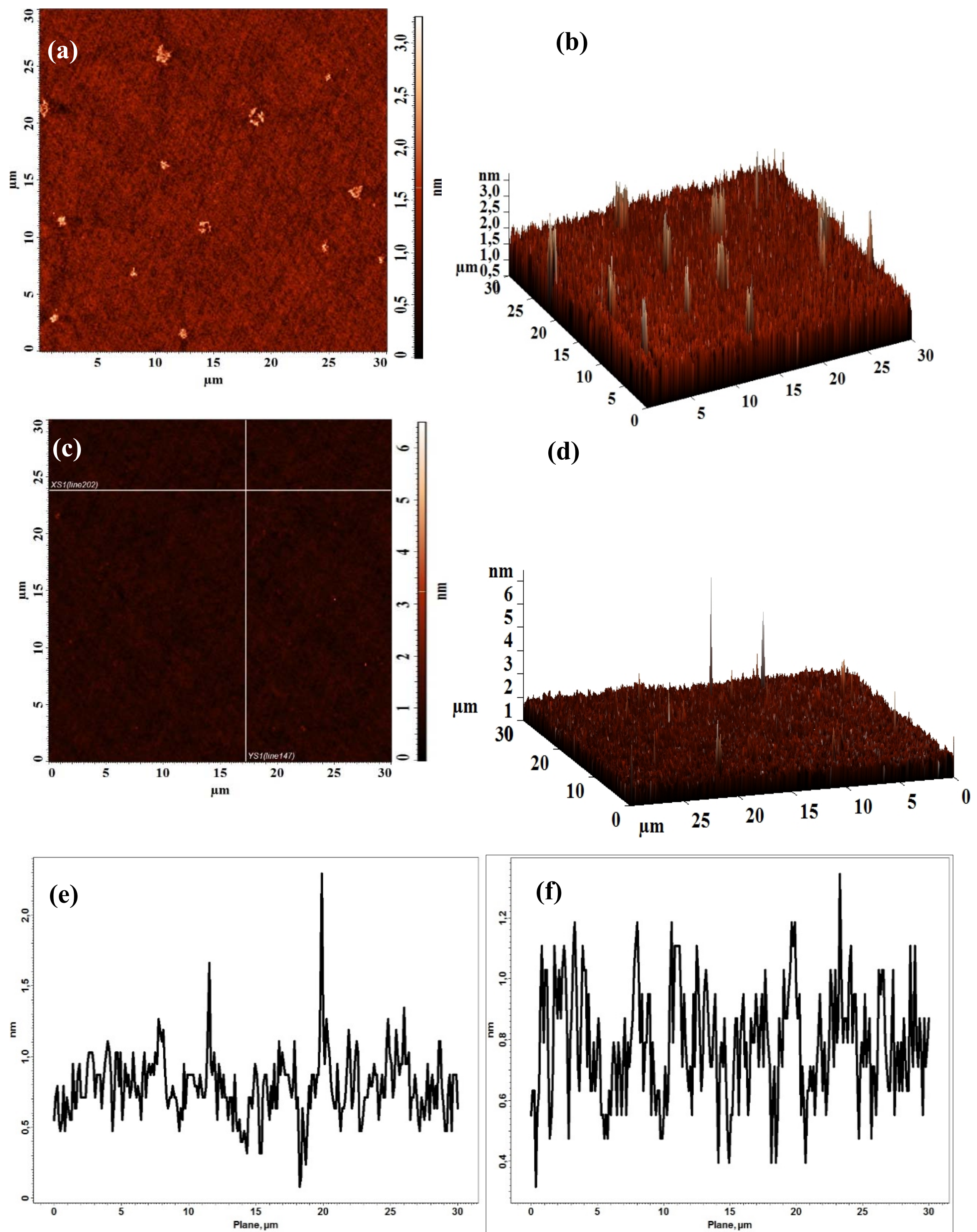

Figure 4.37. (a) and (b) are AFM 2D and 3D Topographic images before oxide removal, (c) and (d) are AFM 2D and 3D Topographic images and (d) and (e) are profile line analysis of XS1 (line 202) and (d) YS1 (line 147) of sample G2W25A after oxide removal process.

As seen in AFM 2D and 3D topographic images before and after oxide removal procedure, GaAs(211)B samples have a smooth surface. The average RMS roughness over scanned five area for G2W24A sample before etching with HF:H_2O mixture was found 0.78 nm and after etching, this value increased to 0.94 nm. The profile analyses after etching showed that the maximum height of particules was 33.35 nm and the etch depth was approximately 0 nm. For G2W25A sample, the average RMS roughness over scanned five area decreased from 1.09 nm to 0.62 nm due to increasing volume ratio of HF in the solution. The maximum height of particules was approximately 2 nm and the etch depth was approximately 0 nm for G2W25A. Average RMS values of etched samples by HF:H_2O are summarized in Figure 4.4.

Table 4.4. Average RMS roughness value change of before and after oxide removal.

Sample ID	HF:H_2O	
	Condition	Average RMS (nm)
G2W24A	Not-etched	0.78
	Etched with 1HF:8H_2O	0.94
G2W25A	Not-etched	1.09
	Etched with 1HF:5H_2O	0.62

4.1.2.2. Raman Spectroscopy Resuts

After wet chemical etching in piranha solution and oxide removal by HF:H_2O mixture, the quality of the surface and oxide structures of GaAs(211)B samples were studied with Raman scattering technique. The Raman active modes in the zincblende structure of undoped-GaAs were explained in detail in section 3.2.1.1.1. The two Raman active modes observed are TO and LO phonon modes which give peaks at 268.2 cm^{-1} and 291.5 cm^{-1} in the Raman spectrum of GaAs [5]. In addition, the SO phonon mode appears as a shoulder of LO phonon mode forming broad line width at 279.0 cm^{-1} [157].

GaAs wafers usually contain oxidized gallium in +3 charge state as Ga_2O_3 species. There also exists oxidized arsenic in +3 and +5 charge states as in As_2O_3 and As_2O_5 compounds, respectively. The Raman spectrum of As_2O_3 has sharp peaks at 85, 183, 268,

469, 414, 471, 560, and 781 cm^{-1}. Ga_2O_3 has very weak and distinct peaks at 201, 418 and 769 cm^{-1} [204]. *D. A. Allwood et al.* obtained the As_2O_3 peak at 260 cm^{-1} in GaAs in an oxygen rich ambient. transfer In such an environment, As_2O_3 gives away oxygens to Ga to form Ga_2O_3 species as the GaAs wafers age in the oxygen rich atmosphere [205]. In addition, due to cleaning and some oxidation processes, As_4 species can be produced as Ga_2O_3 reacts with GaAs. The spectra of As_4 species contains A_1, E and f_2 modes with reported vibrational wavenumbers at 200, 250 and 340 cm^{-1}, respectively. Also, A_1 mode of As_2 was reported at 421 cm^{-1} [206-208].

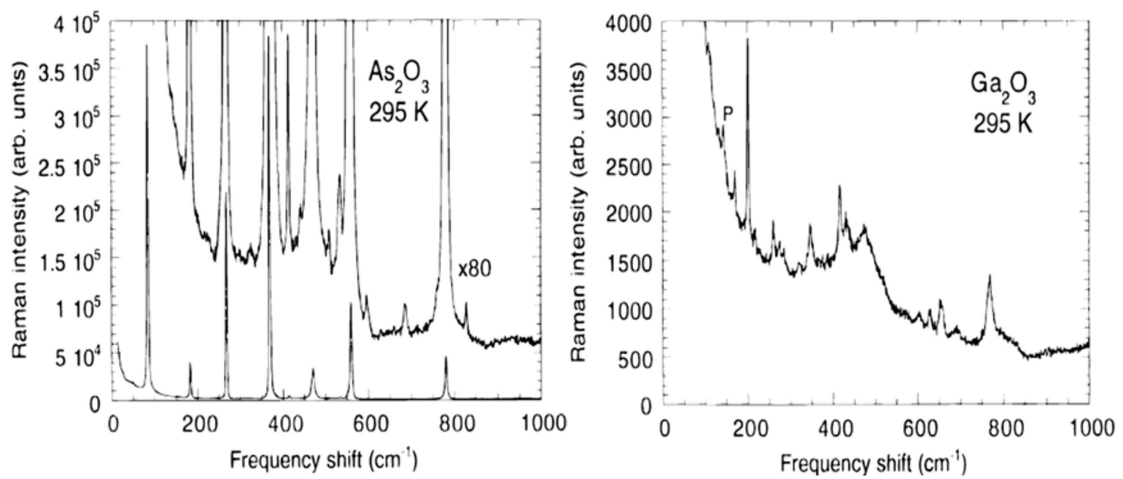

Figure 4.38. Room temperature Raman spectrum of powdered As_2O_3 and Ga_2O_3 [204].

After the wet-chemical etching and oxide removal processes, the Raman spectra of GaAs samples were measured using an $Ar^{(+)}$ laser with 488 nm and 514 nm emission lines at room temperature. The variations in the As_2O_3 vibrational Raman mode intensities on/near the sample surface were recorded during point by point two-dimensional (x, y) Raman mapping scans from some selected areas. Figure 4.40 (a) and (b) show the Raman spectra recorded before the wet-chemical etching of GaAs(211)B wafer. In Figure 4.40 (a), the first order TO and LO phonon modes are observed at 267.7 and 291.3 cm^{-1}, respectively.

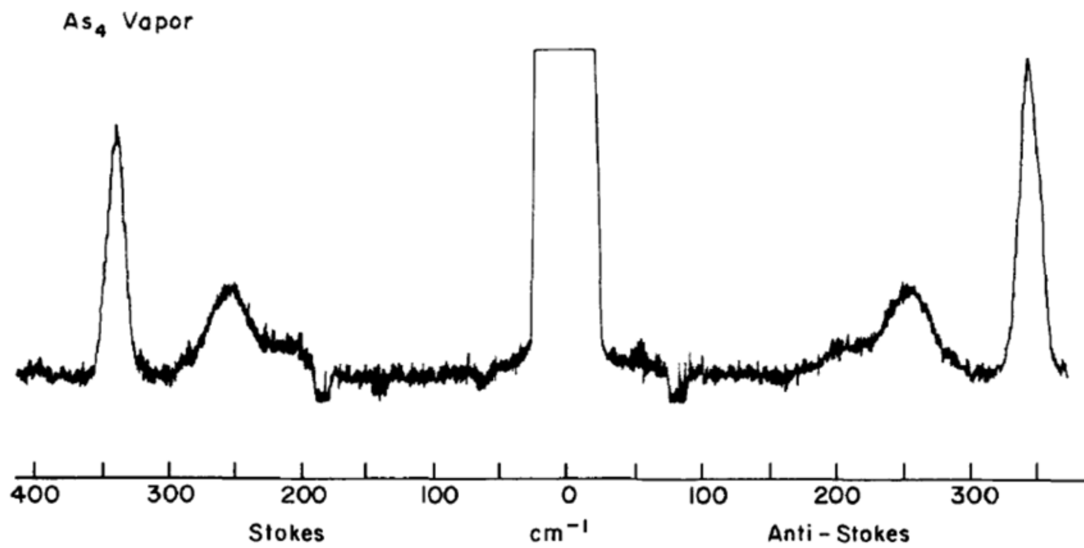

Figure 4.39. Raman spectra of As vapour at 610 ºC [207].

The FWHM of Lorentzians fitted to the TO and LO phonon modes had the values of 17.2 cm^{-1} and 13.2 cm^{-1}, respectively. The broad peak observed between 263.1 and 394.3 cm^{-1} had a maxium at 340.7 cm^{-1} which was regarded as the f_2 mode of As_4 and had a Lorentzian with fit a FWHM value of 65.97 cm^{-1}. In addition, broad peak between 109.3 and 211.62 cm^{-1} with Lorentzian fitted FWHM value of 65.96 cm^{-1} had a maximum at 158.6 cm^{-1} which was associated with As related defects (labelled as D_{As}) at the sample surface. The peak at 222.4 with 16.83 cm^{-1} FWHM value was attributed to the elemental As precipitates formed by the segregation of excess arsenic [163].

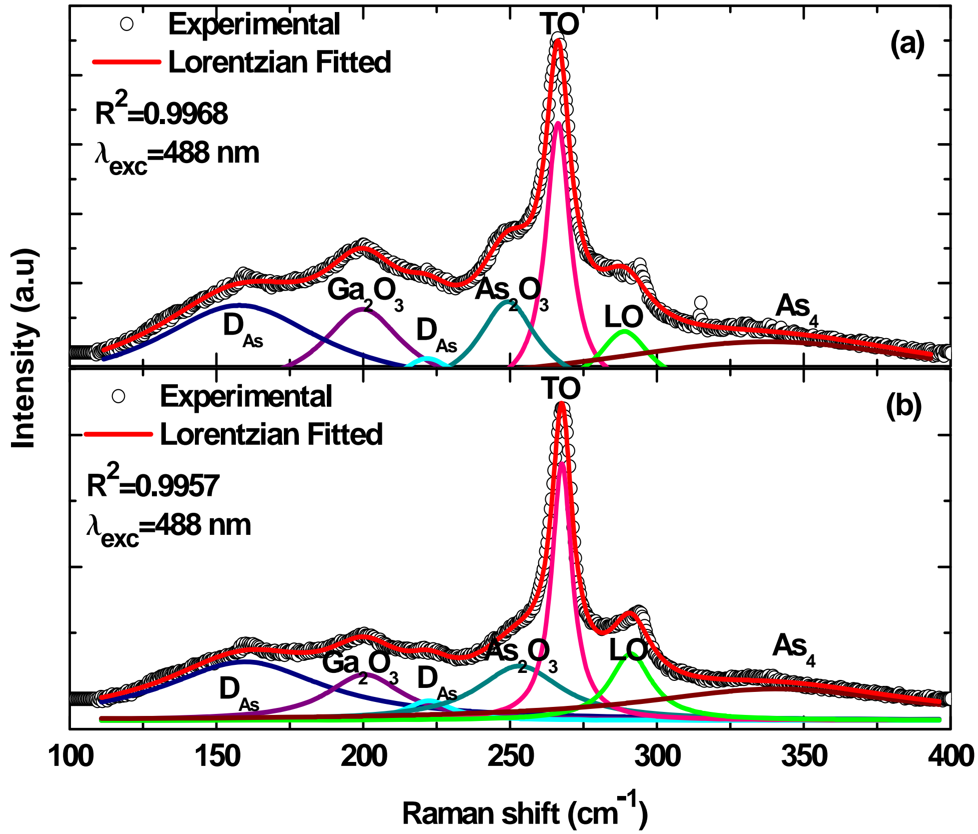

Figure 4.40. (a) and (b) are the Raman spectra under 488 nm excitation for the GaAs(211)B wafer before the wet-chemical etching

In addition to the Raman active modes of GaAs and the As-related defect phonon modes, Ga_2O_3 and As_2O_3 species obtained from GaAs(211)B wafers before wet-chemically etching, also show some Raman peaks. In Figure 4.40 (a), phonon modes belonging to GaO_3 and As_2O_3 species were observed at 200.5 and 253.2 cm^{-1} with 25.2 and 20.1 cm^{-1} FWHM values, respectively. Both phonon modes of GaO_3 and As_2O_3 species became broader with 28.2 and 29.3 FWHM values in the Raman spectrum of GaAs(211)B in Figure 4.40 (b). No significant changes were observed at the peak positions of the Raman spectra from GaAs(211)B wafers. In addition, the intensity ratio of LO and TO phonon modes (I_{LO}/I_{TO}) stayed constant at about 1.08.

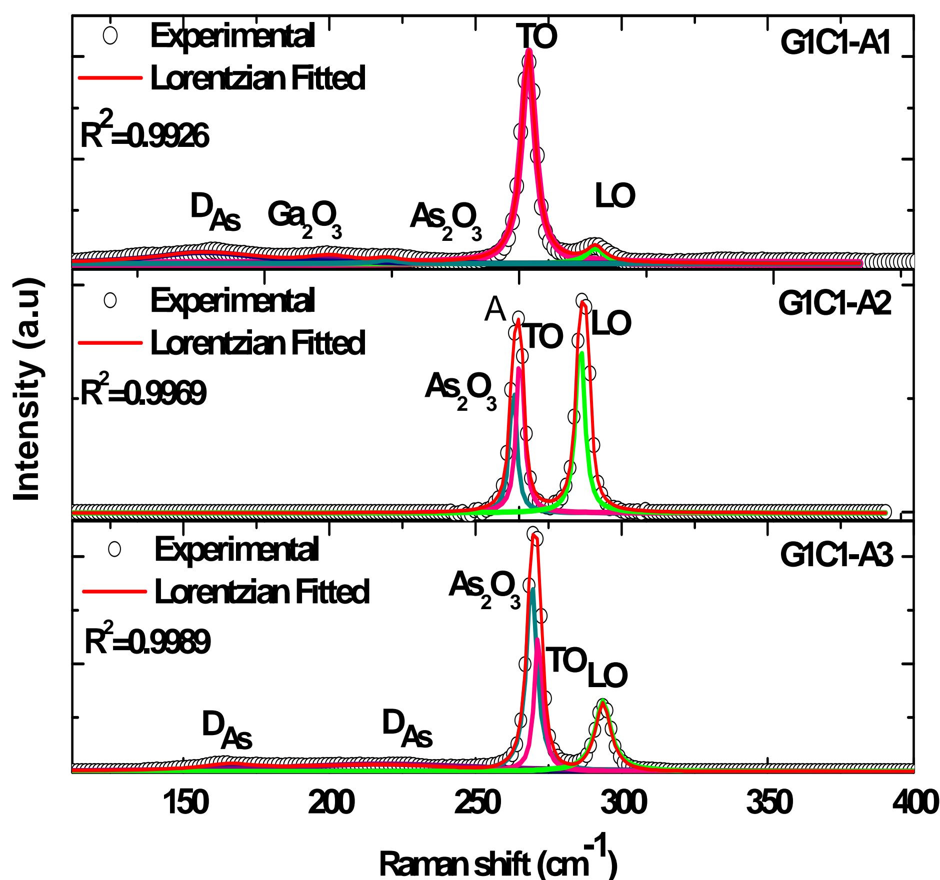

Figure 4.41. Experimentally obtained and Lorentzian fitted whole range Raman spectra of samples G1C1-A1, G1C1-A2 and G1C1-A3 under 488 nm excitation

Figure 4.41 shows the Raman spectra of G1C1-A1, G1C1-A2 and G1C1-A3. The first-order TO Raman active modes were observed at 268.1, 270.4 and 271.6 cm^{-1} for samples G1C1-A1, G1C1-A2 and G1C1-A3, respectively. LO Raman active modes were observed at 291.1, 291.6 and 293.6 cm^{-1} for G1C1-A1, G1C1-A2 and G1C1-A3 samples, respectively. The As-related defect modes were also observed in the spectra of both 30 and 15 second etched samples which is consistent with the SEM-EDX result that the G1C1-A1 sample had a higher atomic percentage of As than that of G1C1-A2 sample (Figure 4.3). Intensities of these modes are very low when compared to Raman active modes. However, As-related modes were not observed in the Raman spectrum of G1C1-A2 which was etched for 120 seconds. As-related modes due to elemental As precipitates, were observed near 157.4 cm^{-1} with 21.8 cm^{-1} FWHM value. For G1C1-A3, the peak position of the As-related defect mode was shifted to 165.8 cm^{-1} with a narrower FWHM of 10.7 cm^{-1}. In addition, at 218.2 cm^{-1}, a second As feature was observed with a much broader FWHM of 41.3 cm^{-1}. The vibrational modes of As_2O_3 species were observed in

the Raman spectra of three different samples with different intensities in which the highest was observed as the peak at 269.2 cm^{-1} with a narrow FWHM of 2.2 cm^{-1} for the sample G1C1-A3. As_2O_3 phonon mode was shifted to lower frequencies by 29.7 and 1.38 cm^{-1} and their FWHM were decreased to 1.1 and 1.4 cm^{-1} for G1C1-A1 and G1C1-A2 samples, respectively. The 239.5 peak was regarded as As_2O_3 phonon mode peak which was confirmed by X-ray reflectivity and X-ray Photoelectron Spectroscopy (XPS) measurements. The As_2O_3 vibrational mode was seen as a shoulder near the TO Raman mode, for both G1C1-A2 and G1C1-A3 samples which coupled with TO phonon modes and gave rise to higher intensities. Despite having higher As atomic percentages, the Raman active vibrational mode of Ga_2O_3 species were observed only in the spectrum of G1C1-A1 sample in A series at 203.2 cm^{-1} with a 12.8 cm^{-1} FWHM.

Figure 4.42 shows the Raman spectra and the proper Lorentzian fits for the G1C1-B series samples. The first-order TO Raman active modes were observed at 268.7, 265.8 and 267.2 cm^{-1} for samples G1C1-B1, G1C1-B2 and G1C1-B3, respectively. LO Raman active modes were observed at 291.5, 289.2 and 290.9 cm^{-1} for G1C1-B1, G1C1-B2 and G1C1-B3 samples, respectively. As-related defect modes were observed at 164.0, 161.8 and 158.1 cm^{-1} for all G1C1-B series; G1C1-B1, G1C1-B2 and G1C1-B3, respectively, in which was shifted to lower frequencies with a decrease in their FWHM with increasing exposure times of the piranha solution. In addition, compound of Ga_2O_3 observed for three samples that Ga_2O_3 vibrational mode became more intense as increasing implementation time of the mixture with samples. Ga_2O_3 vibrational mode was observed at 210.2 cm^{-1} for sample G1C1-B1 and shifted to lower frequencies by 6.1 and 10.2 cm^{-1} for the samples G1C1-B2 and G1C1-B3, respectively. The FWHM value of Ga_2O_3 vibrational mode peak of sample G1C1-B1 and G1C1-B2 were measured as 29.3 cm^{-1} and 41.1 cm^{-1}, respectively. For the sample G1C1-B3, As_2O_3 vibrational modes were observed for both G1C1-B1 and G1C1-B3 which appear as a shoulders near the TO phonon mode peak at 266.2 and 255.12 cm^{-1}, respectively. As_2O_3 vibrational mode peaks exhibit very small FWHM; 2.4 and 4.4 cm^{-1} for samples G1C1-B1 and G1C1-B3, respectively. In addition, the broad peak for samples G1C1-B2 and G1C1-B3 at point 341.9 cm^{-1} (FWHM; 37.7 cm^{-1}) and 337.9 cm^{-1} (FWHM; 45.3 cm^{-1}) were regarded as F_2 mode of As_4, respectively.

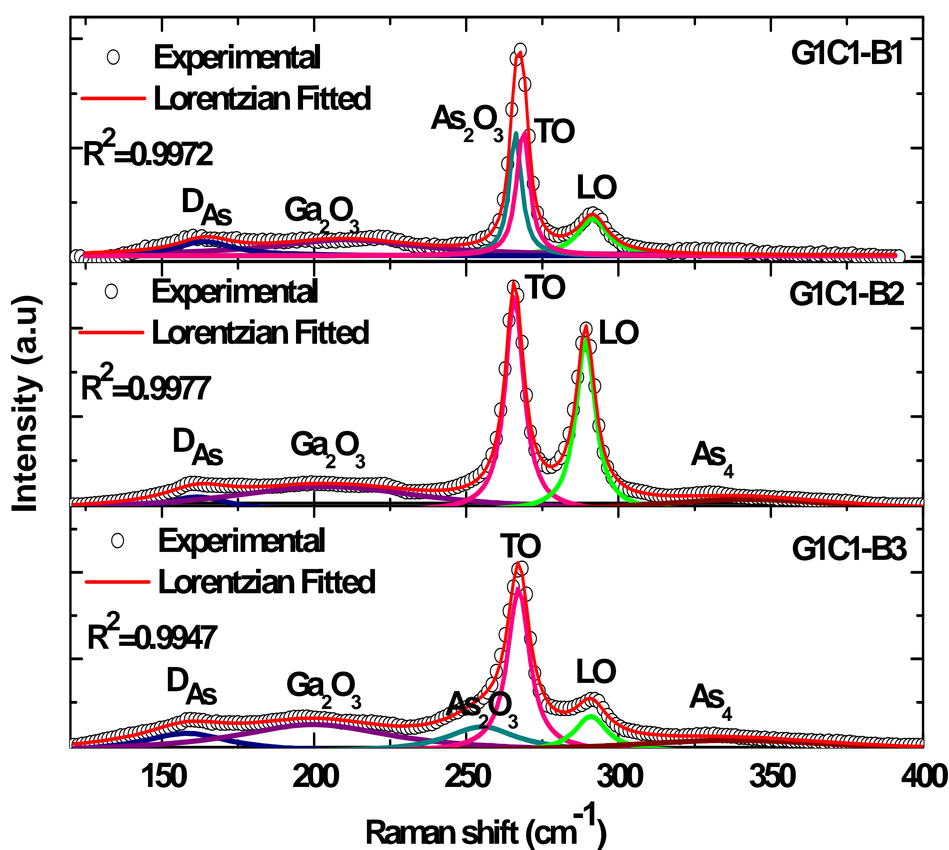

Figure 4.42. Experimentally obtained and Lorentzian fitted whole range Raman spectra of samples G1C1-B1, G1C1-B2 and G1C1-B3 under 488 nm excitation

Figure 4.43 shows the whole range of Raman spectra of G1C1-C1, G1C1-C2 and G1C1-C3 samples. The first-order TO Raman active modes were observed at 268.4 cm^{-1} for three samples. LO Raman active modes were observed at 292.7, 291.9 and 292.5 cm^{-1} for G1C1-C1, G1C1-C2 and G1C1-C3 samples, respectively. As-related defect mode was observed at 159.4 cm^{-1} for sample G1C1-C1 sample and it shifted to lower frequencies by 0.4 and 0.2 cm^{-1} for G1C1-C2 and G1C1-C3, respectively. FWHM of As-related mode peak for sample G1C1-C2 decreased to 19.5 cm^{-1} when compared to G1C1-C1 (FWHM; 29.6 cm^{-1}) and G1C1-C3 (FWHM; 26.1 cm^{-1}). In addition, compound of Ga_2O_3 phonon mode peak was observed for only G1C1-C2 and G1C1-C3, it observed at 206.6 $cm^{-1}$for sample G1C1-C2 and it shifted to lower frequency by 8.2 cm^{-1} and became sharper with FWHM value of 13.7 cm^{-1} for sample G1C1-C3. As_2O_3 vibrational mode was observed for all samples and appeared as a shoulder of TO phonon mode at 253.1 cm^{-1} for only sample G1C1-C2. As_2O_3 vibrational modes were observed at 222.9 and 225.3 cm^{-1} and became broader but more intense for samples with 26.2 and 21.7 cm^{-1}

FWHMs for samples G1C1-C1 and G1C1-C3, respectively. Broad peak for G1C1-C1, G1C1-C2 and G1C1-C3 samples at point 328.3 (FWHM; 54.7 cm^{-1}), 336.7 (FWHM; 47.4 cm^{-1}) and 335.6 cm^{-1} (FWHM; 49.7 cm^{-1}) regarded as f_2 mode of As_4, respectively.

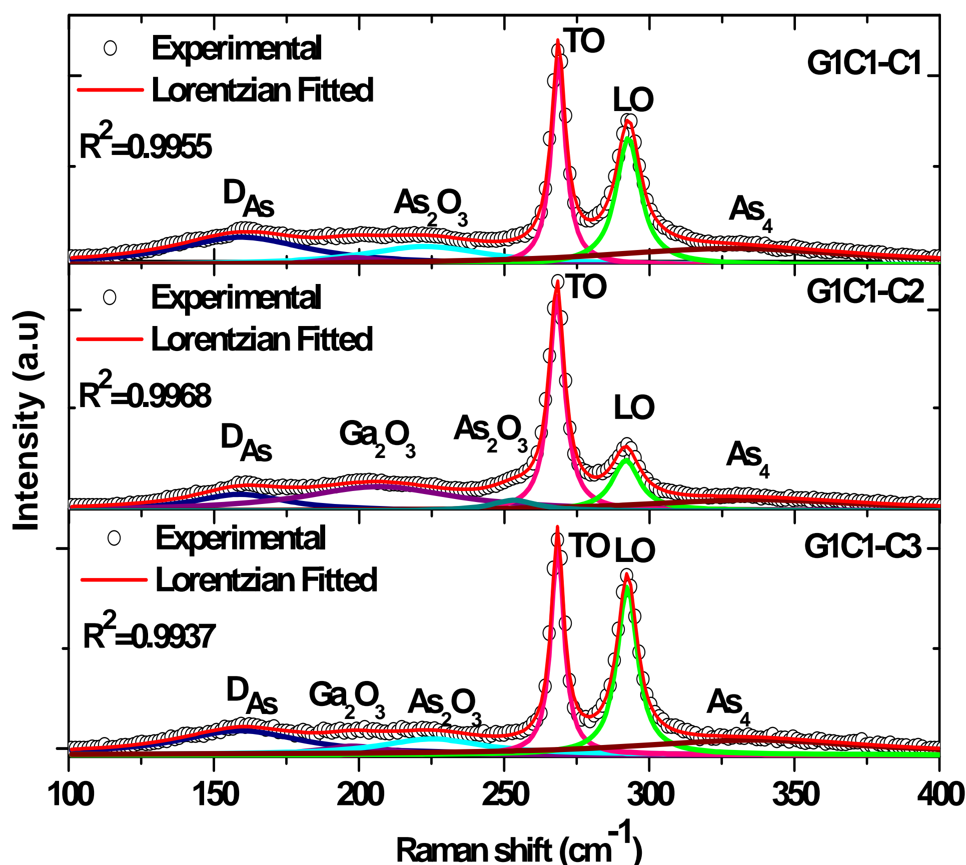

Figure 4.43. Experimentally obtained and Lorentzian fitted whole range Raman spectra of samples G1C1-C1, G1C1-C2 and G1C1-C3 under 488 nm excitation

The whole range of Raman spectra of G1C1-E series is shown in Figure 4.44. The first-order TO Raman active modes were observed nearly at 270 cm^{-1} and LO Raman active modes were observed at 293.9 cm^{-1} for three samples. The oxide compounds of As and Ga were not observed for three samples despite appearing oxygen contamination at EDX spectra of sample G1C1-E2. Broad As-related modes were observed for G1C1-E1 and G1C1-E3 samples at 166.6 cm^{-1} (FWHM; 72.0 cm^{-1}) and, at 151.1 (FWHM; 114.5 cm^{-1}) and 216.4 cm^{-1} (FWHM; 23.1 cm^{-1}), respectively. f_2 mode of As_4 was observed for

samples G1C1-E2 and G1C1-E3 and formed peaks at 337.6 and 318.6 cm^{-1} with 2.9 cm^{-1} and 53.8 FWHM values, respectively.

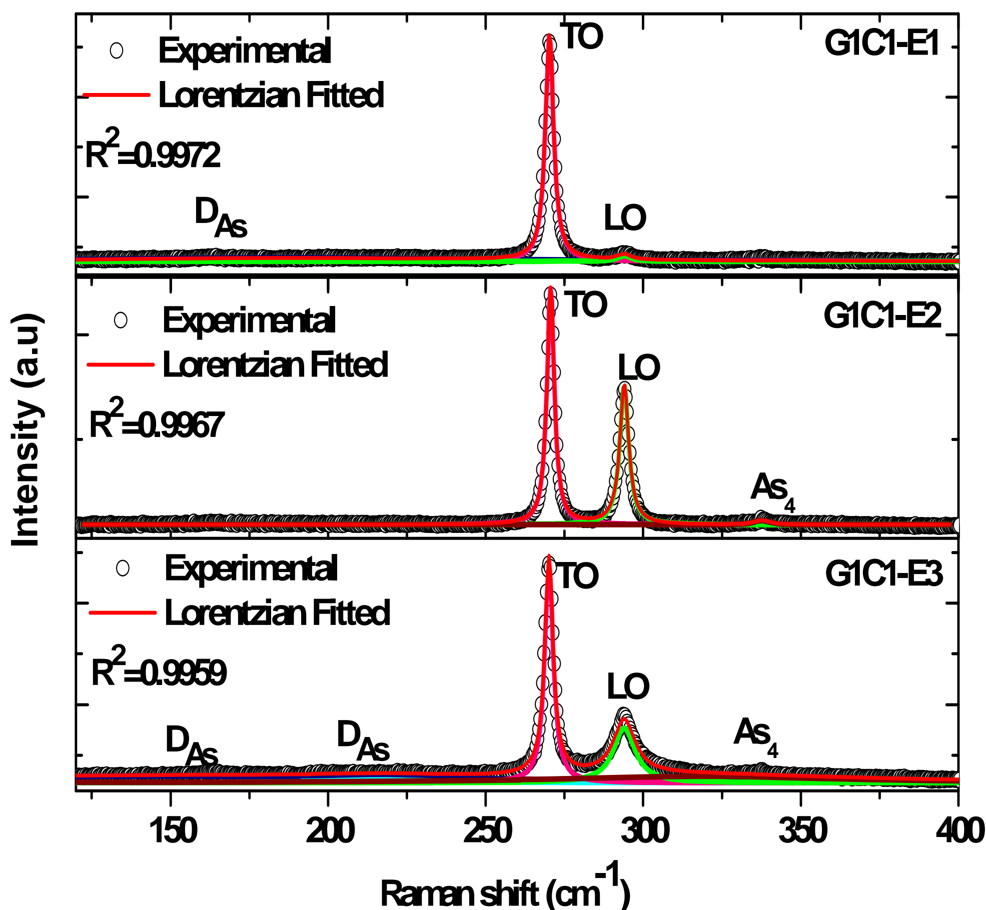

Figure 4.44. Experimentally obtained and Lorentzian fitted whole range Raman spectra of samples G1C1-E1, G1C1-E2 and G1C1-E3 under 488 nm excitation.

Unlikely to G1C1-E series, Ga_2O_3 vibrational mode was observed due to increasing volume ratio of H_2O_2 in the piranha solution for all G1C1-G1, G1C1-G2 and G1C1-G3 samples. Ga_2O_3 appeared at 210.7 cm^{-1} and 210.4 cm^{-1} for samples G1C1-G1 and G1C1-G3, and shifted to higher frequency by approximately 3 cm^{-1} for sample G1C1-G2. In addition, As-related defect mode was also observed as a broad peak for all three samples which was narrow for samples G1C1-G1 and G1C1-G3 samples with FWHM values of 6.2 cm^{-1} and 3.2 cm^{-1}, respectively and was a broad peak for G1C1-G1 sample with 20.8 cm^{-1} FWHM value when compared to other G series. D_{As} mode was appeared

at 161.9 cm^{-1} for sample G1C1-G1 and it shifted to lower frequencies for samples G1C1-G2 and G1C1-G3. As_2O_3 phonon mode was observed only for sample G1C1-G1 as a shoulder of Raman active TO phonon mode at 268.0 cm^{-1}.

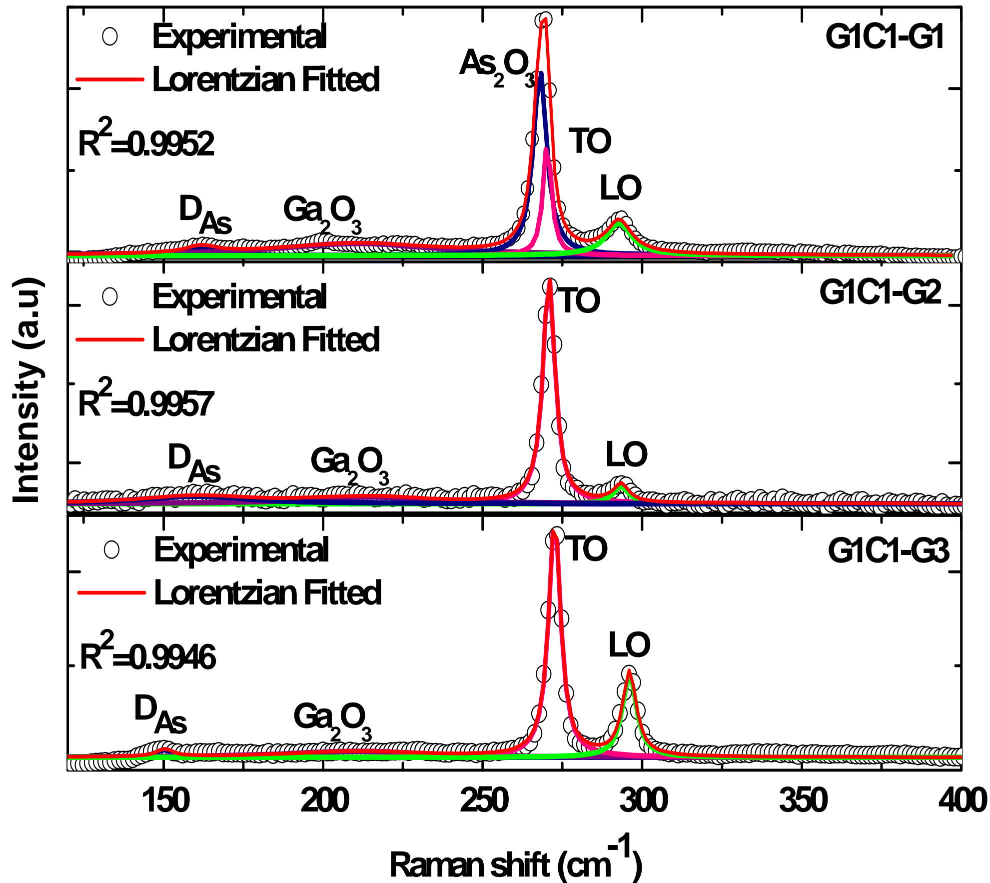

Figure 4.45. Experimentally obtained and Lorentzian fitted whole range Raman spectra of samples G1C1-G1, G1C1-G2 and G1C1-G3 under 488 nm excitation.

Before and after oxide removal by HF:H_2O mixture experimentally obtained and Lorentzian fitted whole range Raman spectra of G2W24A and G2W25A is shown in Figure 4.46 and Figure 4.47. Before oxide removal procedure of sample G2W24A, in addition to first order Raman active modes of GaAs, As-related defect and Ga_2O_3 phonon modes were observed at 165.1 and 209.7 cm^{-1}, respectively. Intensities of these two modes were too low and broader compared to TO and LO phonon modes in which As-related defect mode had FWHM value of 14.6 cm^{-1} and Ga_2O_3 had FWHM value of 17.5

whereas first order TO and LO phonon modes had 2.3 and 2.5 cm^{-1} FWHM values, respectively. For sample G2W25A, both common oxide compounds of Ga and As observed; Ga_2O_3 and As_2O_3. Broad peak of Ga_2O_3 was observed at 200.8 cm^{-1} (FWHM; 45.5 cm^{-1}) and As_2O_3 was appeared as a shoulder of TO phonon mode at 267.9 cm^{-1} (FWHM; 1.7 cm^{-1}).

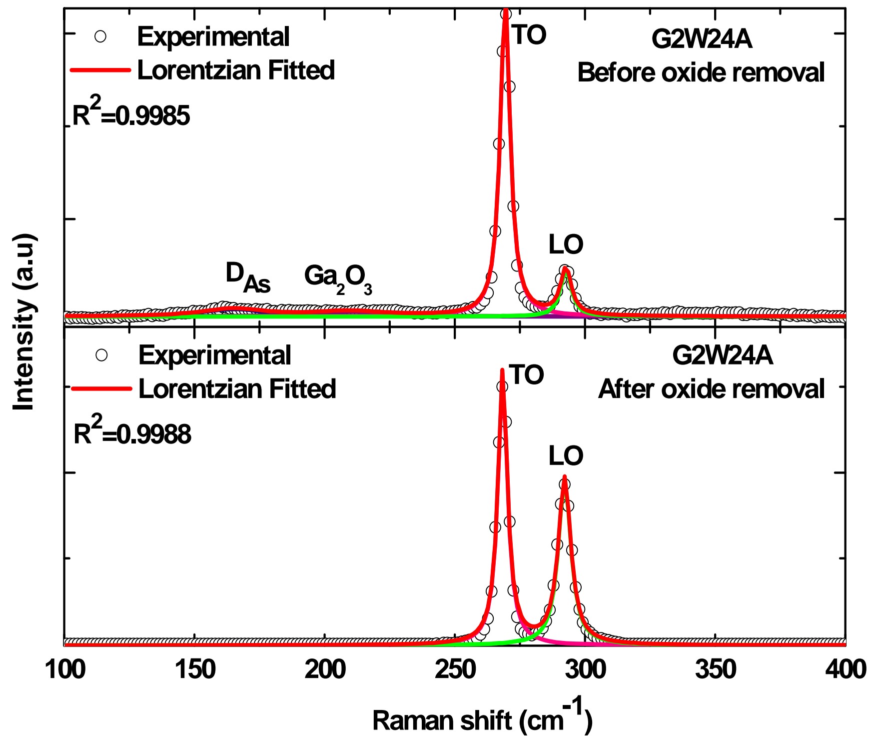

Figure 4.46. Experimentally obtained and Lorentzian fitted whole range Raman spectra of sample G2W24A before and after oxide removal procedure under 488 nm excitation.

After the oxide removal, As-related defect mode and any oxide compounds of Ga and As were not observed for both G2W24A and G2W25A samples. Raman active LO phonon mode was appeared narrower, its width at half-height decreased approximately one-third.

As we see in Raman spectra of the piranha etched GaAs(211)B samples, the peak positions and intensities of Ga_2O_3 and As_2O_3 species varies. As_2O_3 compounds mostly appeared as shoulder of TO phonon mode which made a contribution to increase TO phonon mode Raman intensity. Also, we observed As-related defect modes which was hard to identify in Raman spectra. However, after the oxide removal by two different

volume ratio of HF:H_2O, Ga_2O_3-As_2O_3 species and also As-related defect modes could not observed. They were completely removed after oxide removal procedure which was also supported by X-ray reflectivity and XPS measurements. The observed mode positions with FWHM values depending on the applied process of samples are summarized in Table 4.5 and Table 4.6.

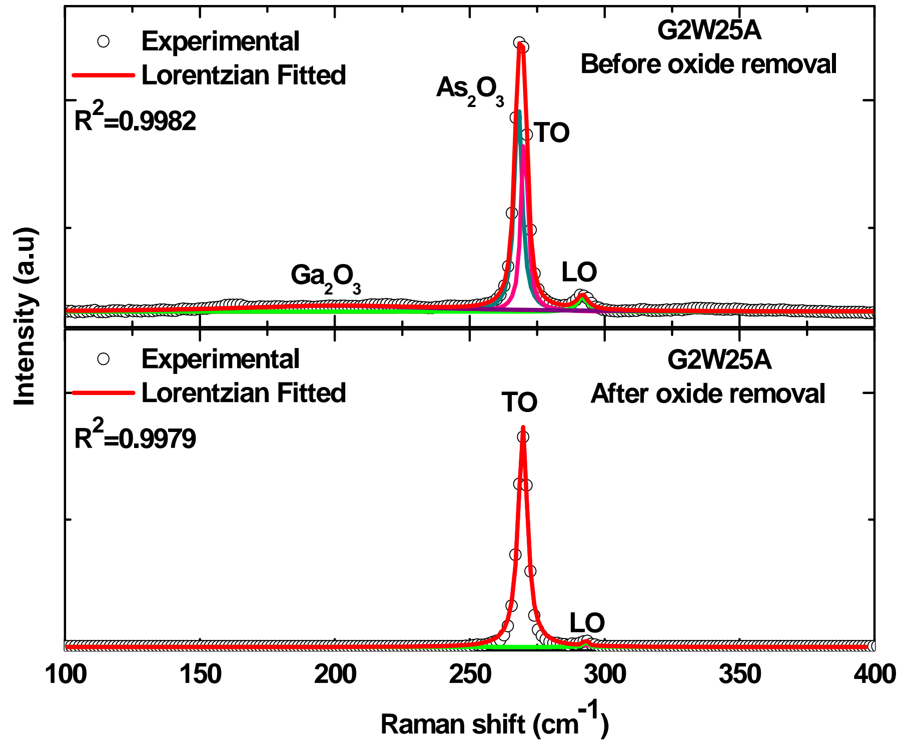

Figure 4.47. Experimentally obtained and Lorentzian fitted whole range Raman spectra of sample G2W25A before and after oxide removal procedure under 488 nm excitation

To investigate the distribution of vibrational modes of As_2O_3 and As_4 along with the LO phonon mode on the sample surface, the xy-Raman mapping technique was used for the piranha etched samples. The optical microscope images of scanned sample surfaces and the Raman intensity distributions of these modes over some selected sample areas are given in Figure 4.48, Figure 4.49, Figure 4.50, Figure 4.51, Figure 4.52, and Figure 4.53.

Table 4.5. Behavior of the Raman peaks depending on the wet-chemical etching by piranha solution.

Sample ID	Observed Raman Peaks	Wavenumbers (cm^{-1})	FWHM (cm^{-1})
G1C1-A1	D_{As}	157.4	21.8
	Ga_2O_3	203.2	12.8
	As_2O_3	239.5	1.1
	TO	268.1	2.8
	LO	291.1	3.6
G1C1-A2	As_2O_3	267.8	1.4
	TO	270.4	1.5
	LO	291.6	1.8
G1C1-A3	D_{As}	165.8-218.2	10.7-41.3
	As_2O_3	269.2	2.2
	TO	271.6	1.6
	LO	293.6	23.8
G1C1-B1	D_{As}	164.0	11.3
	Ga_2O_3	210.2	29.3
	As_2O_3	266.2	2.4
	TO	268.7	2.5
	LO	291.5	5.9
G1C1-B2	D_{As}	161.8	13.1
	Ga_2O_3	204.2	41.1
	TO	265.8	3.7
	LO	289.2	3.8
	As_4	341.9	37.7
G1C1-B3	D_{As}	158.1	17.7
	Ga_2O_3	199.8	31.9
	As_2O_3	255.2	14.3
	TO	267.2	4.4
	LO	290.9	6.5
	As_4	337.9	45.3
G1C1-C1	D_{As}	159.4	29.6
	As_2O_3	222.9	26.2
	TO	268.4	2.9
	LO	292.7	5.1
	As_4	328.3	54.7
G1C1-C2	D_{As}	158.9	19.5
	Ga_2O_3	206.6	32.1
	As_2O_3	253.1	9.7
	TO	268.4	3.3
	LO	291.9	5.7
	As_4	336.7	47.4

(cont. on next page)

Table 4.5. (Cont.)

G1C1-C3	D_{As}	159.2	26.1
	Ga_2O_3	198.4	13.7
	As_2O_3	225.3	21.7
	TO	268.4	2.7
	LO	292.5	4.2
	As_4	335.6	49.7
G1C1-E1	As	166.6	72.0
	TO	270.3	1.6
	LO	293.9	2.5
G1C1-E2	TO	270.1	1.4
	LO	293.9	1.7
	As_4	337.6	2.9
G1C1-E3	D_{As}	151.1-216.4	114.1-46.1
	TO	270.1	1.6
	LO	293.9	4.2
	As_4	318.6	53.8
G1C1-G1	D_{As}	161.9	6.2
	Ga_2O_3	210.7	31.3
	As_2O_3	268.0	2.5
	TO	270.3	1.5
	LO	292.7	4.8
G1C1-G2	D_{As}	160.3	20.8
	Ga_2O_3	213.9	23.1
	TO	270.8	2.3
	LO	293.4	2.9
G1C1-G3	D_{As}	150.3	3.2
	Ga_2O_3	210.4	26.4
	TO	272.6	2.3
	LO	296.0	2.6

Figure 4.48 shows (a) the 2x2 μm^2 scanned optical microscope image of the G1C1-A1 sample surface, (b) Raman intensity distribution of As_2O_3 vibration mode and (c) As_4 vibration mode are shown. Raman mapping technique was implemented on the examined area of the G1C1-A1 sample surface with a 0.105 µm step size in both x and y directions. We studied the defected areas carefully by etching, in this case, because the As_2O_3 vibration peak could not be observed for Raman measurements on non-defected areas. As seen from the Raman mapping results, intensities of As_2O_3 and As_4 vibration peaks are higher for darker regions in the optical image indicating larger amounts of defects on those areas.

Table 4.6. Behavior of the Raman peaks before and after oxide removal process.

Sample ID	Observed Raman Peaks	Wavenumbers (cm^{-1})	FWHM (cm^{-1})
G2W24A (Before Removal)	D_{As}	165.1	14.6
	Ga_2O_3	209.7	17.5
	TO	269.4	2.3
	LO	292.7	2.5
G2W24A (After Removal)	TO	268.4	2.2
	LO	292.2	2.9
G2W25A (Before Removal)	As_2O_3	267.9	1.7
	Ga_2O_3	200.8	45.5
	TO	270.4	1.4
	LO	291.8	2.5
G2W25A (After Removal)	TO	269.7	2.1
	LO	293.1	0.9

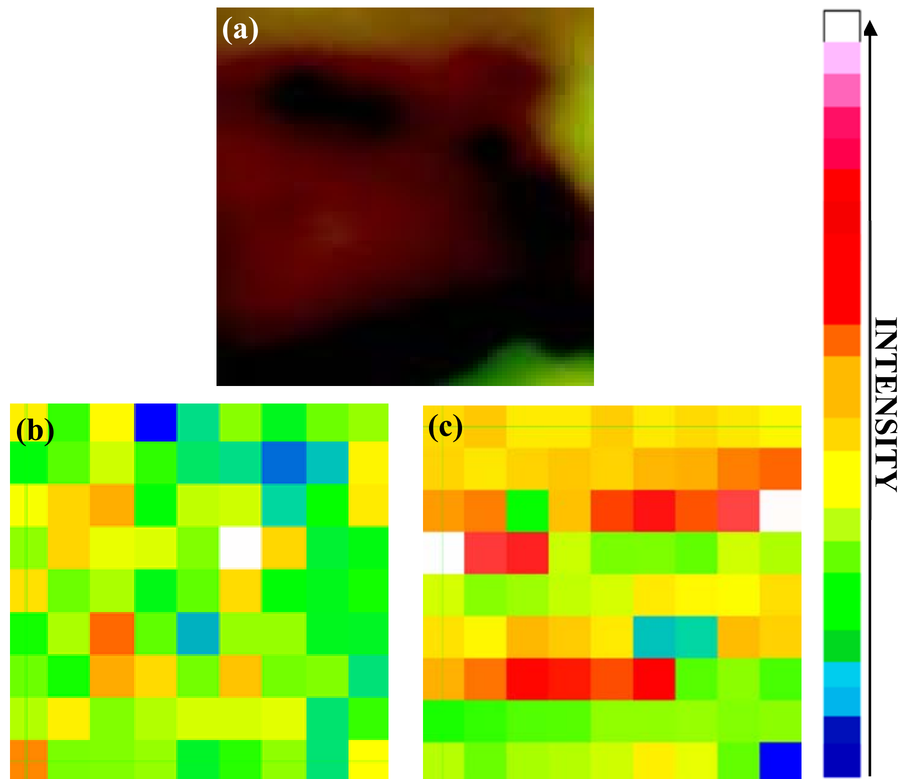

Figure 4.48. (a) Optical microscope image of 2x2 μm^2 scanned area on sample G1C1-A1, Raman intensity change of (b) As_2O_3 phonon mode and (c) As_4 phonon mode.

As_2O_3 vibration mode gave a shoulder peak near TO phonon mode peak in the Raman spectrum of G1C1-A2 sample. To observe the mass distribution of As_2O_3, a 20x20 μm^2 surface area was scanned with a stepsize of 0. 211 µm in both x and y directions. As seen in Figure 4.49, As_2O_3 phonon mode peak intensities vary with position although the scanned surface was not defected by etching. Besides, LO phonon mode intensities were distributed homogenously on the scanned area which had higher intensities than As_2O_3 and As_4 vibrational modes. Also, the As_4 vibrational mode have higher intensities on defected areas which produce darker areas on the optical image.

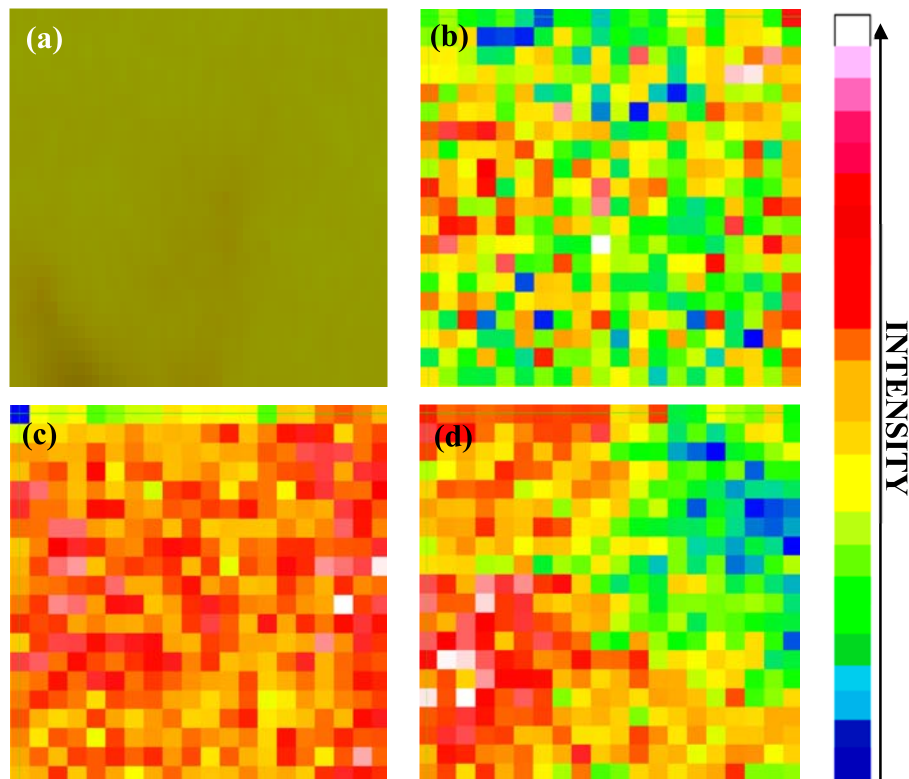

Figure 4.49. (a) Optical microscope image of 20x20 μm^2 scanned area on sample G1C1-A2, Raman intensity change of (b) As_2O_3 phonon mode, (c) LO phonon mode and (d) As_4 phonon mode

Figure 4.50 shows the optical image and the 0.211 µm step-size- xy Raman mapping of a 2x2 μm^2 area of the sample G1C1-A2. Raman intensity distribution of the As_2O_3 vibrational mode, LO phonon mode and As_4 vibrational mode of As are shown in the figure. The As_2O_3 vibrational mode and the LO phonon mode peak intensities increases at the defect positions where LO phonon mode intensity is higher on some parts. Unlike the F_2 phonon mode distribution seen in Figure 4.49, intensity distribution of the As_4 vibrational mode is independent of the defected area position on the sample.

For the samples G1C1-B1 and G1C1-B2 only the Raman intensity distribution of the As_2O_3 vibrational mode on some surface area was investigated which are shown in Figure 4.51 and Figure 4.52. G1C1-B1 and G1C1-B2 samples surfaces were scanned by 1.053 µm and 1 µm step sezes in x and y directions, respectively. It was found that the 10x10 μm^2 scanned area of G1C1-B1 sample was highly defected by the piranha etch solution. As can be seen, As_2O_3 vibrational peak was more intense for darker parts on the sample. The defected part on the scanned area of G1C1-B2 can also be seen in its Raman mapping result. Similar to G1C1-B1 case, As_2O_3 vibrational Raman peak is more intense on the darker part of the scanned surface area. Due to lower intensities on smoother surface parts of the sample G1C1-B2, we couldn't be observed As_2O_3 vibrational mode in Raman spectrum of the sample.

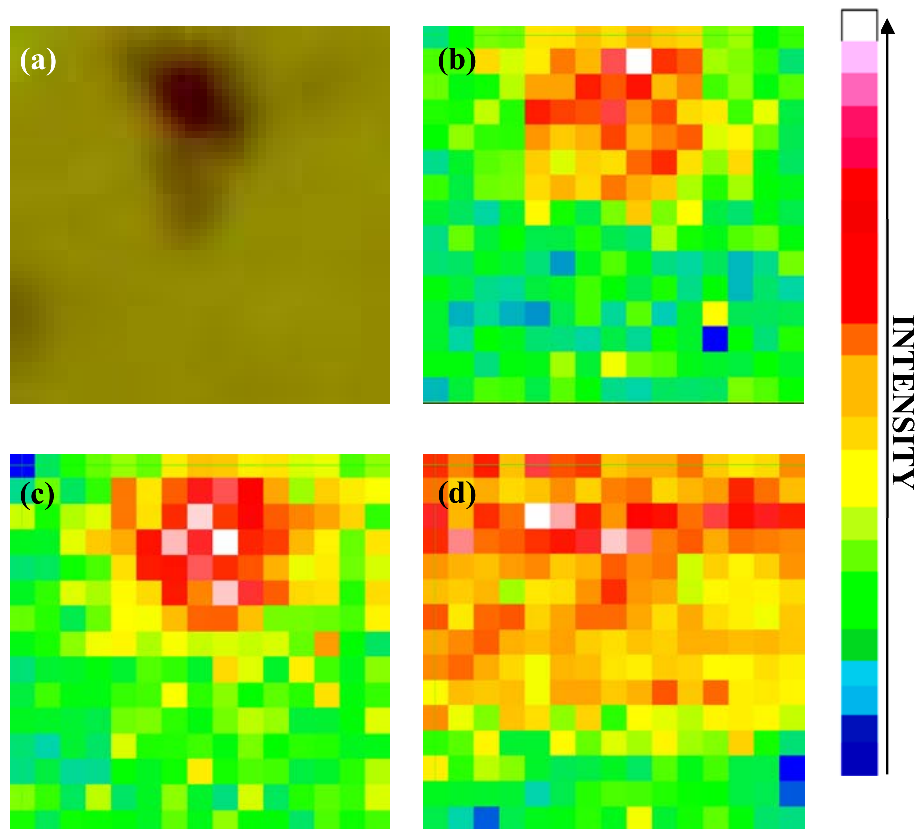

Figure 4.50. (a) Optical microscope image of 2x2 μm^2 scanned area on sample G1C1-A2, Raman intensity change of (b) As_2O_3 phonon mode, (c) LO phonon mode and (d) As_4 phonon mode.

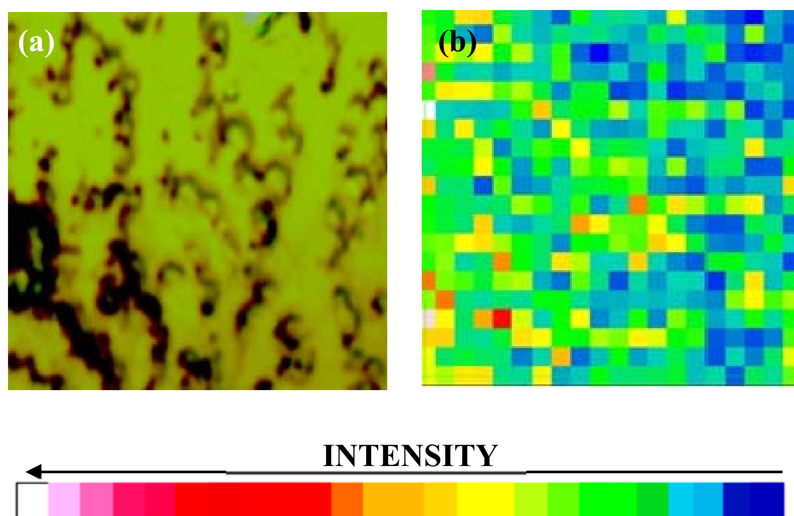

Figure 4.51. (a) Optical microscope image of 10x10 μm^2 scanned area on sample G1C1-B1 and (b) Raman intensity change of As_2O_3 phonon mode on scanned area.

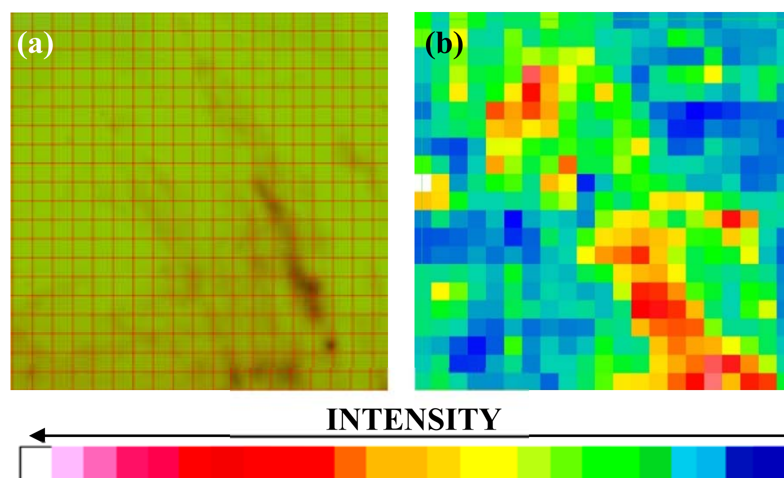

Figure 4.52. (a) Optical microscope image of 20x20 μm^2 scanned area on sample G1C1-B2 and (b) Raman intensity change of As_2O_3 phonon mode on scanned area.

Another scanned sample was G1C1-G1 by Raman mapping technique and its optical microscope image with Raman intensity distribution of As_2O_3 vibrational mode and LO phonon mode are given in Figure 4.53. The Raman mapping was obtained from a 10x10 μm^2 area with 1 μm step size on each direction. As_2O_3 species was not distributed homogenously on the surface in which some parts of the sample have high amounts of

As_2O_3 and some parts have low. The intensity of LO phonon mode also varies on the scanned area, but it remains mostly lower than those for the As_2O_3 vibrational mode.

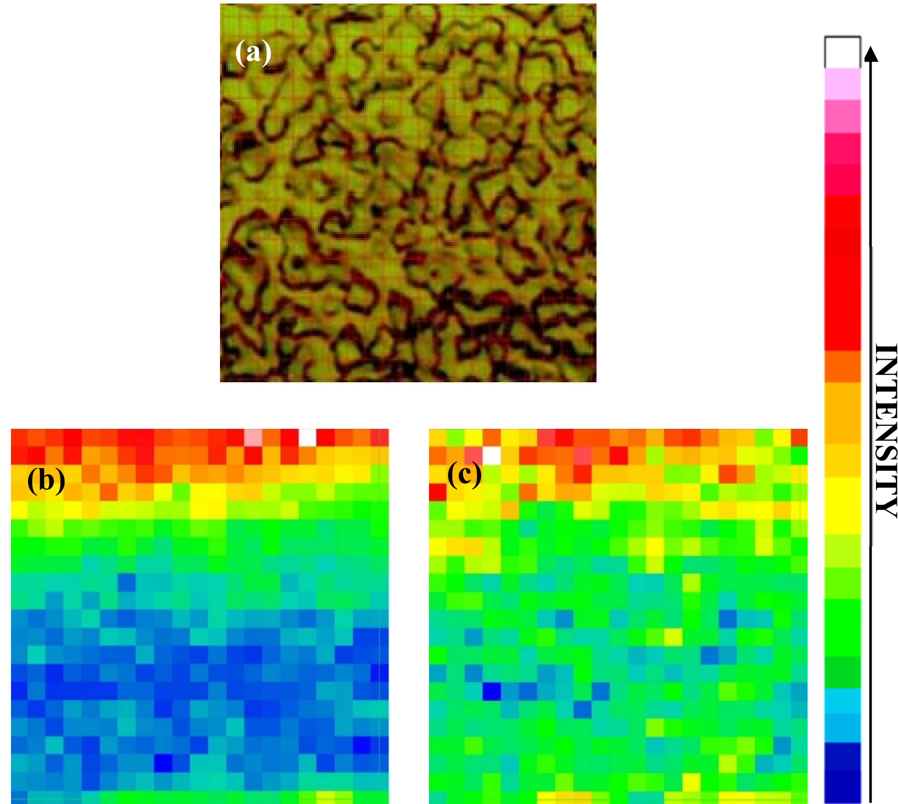

Figure 4.53. (a) Optical microscope image of 10x10 μm^2 scanned area on sample G1C1-G1, Raman intensity change of (b) As_2O_3 phonon mode on scanned area and (c) LO phonon mode.

4.2. In-situ Surface Preparation

4.2.1. Thermal Oxide Desorption

Protective and native oxides of GaAs can be removed by heating the wafers with minimal damage. Thus, prior to growing CdTe epitaxial layers on epiready GaAs(211)B wafers, the wafers were heated to remove protective oxide layer in the growth chamber of the MBE system. To prevent the arsenic loss at high temperatures from GaAs surface, the desorption of the oxide was performed under As_4 flux. Before heating the GaAs wafers to remove oxide layer, the As cracker cell bulk module was increased to 325 °C

and crack module increased to 600 °C to obtain As_4 flux. After the arsenic shutter was opened with 50, 100, 150, 200, 250, 300 mil valve positions, the change of pressure in growth chamber increased from 4.95x10^{-9} to 1.21x10^{-6} Torr. The change of BFM vacuum reading with As cracker cell valve position and time is illustrated in Figure 4.54.

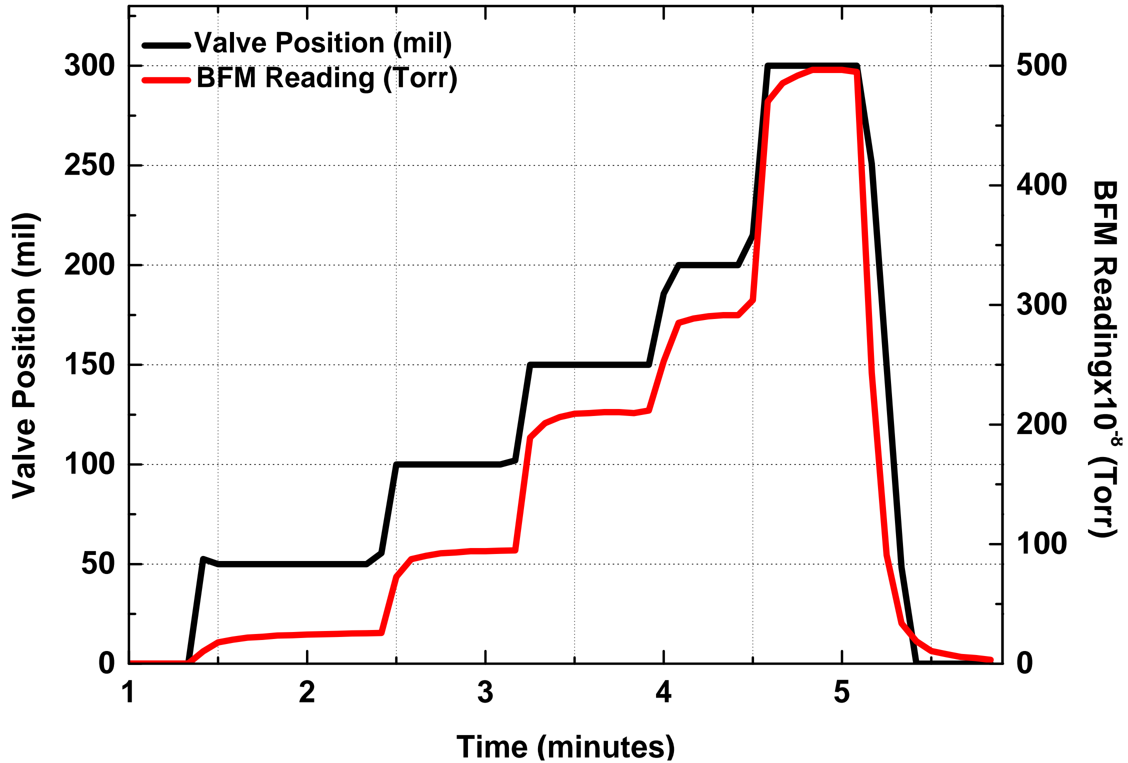

Figure 4.54. The change of BFM reading with As cracker cell valve position and time during flux calibration prior to oxide removal.

The change of pressure monitored by growth module ion gauge during oxide removal and nucleation of CdTe layer growth. Before the GaAs(211)B wafers were heated to oxide removal temperature, the As cracker cell shutter was opened with 100 mil valve position producing an As_4 beam flux. The temperature of the wafer set to 710 °C and ramped with a rate of 20 °C/min. The temperature of GaAs wafer was measured as 582 °C by the kSA Bandit using optical absorption edge of GaAs material. The measured GaAs wafer temperature by kSA Bandit and the change of background pressure in growth chamber is illustrated in Figure 4.55. As seen in Figure 4.55, the As_2O_3 and Ga_2O_3 desorption produced peaks at approximately 550-582 °C.

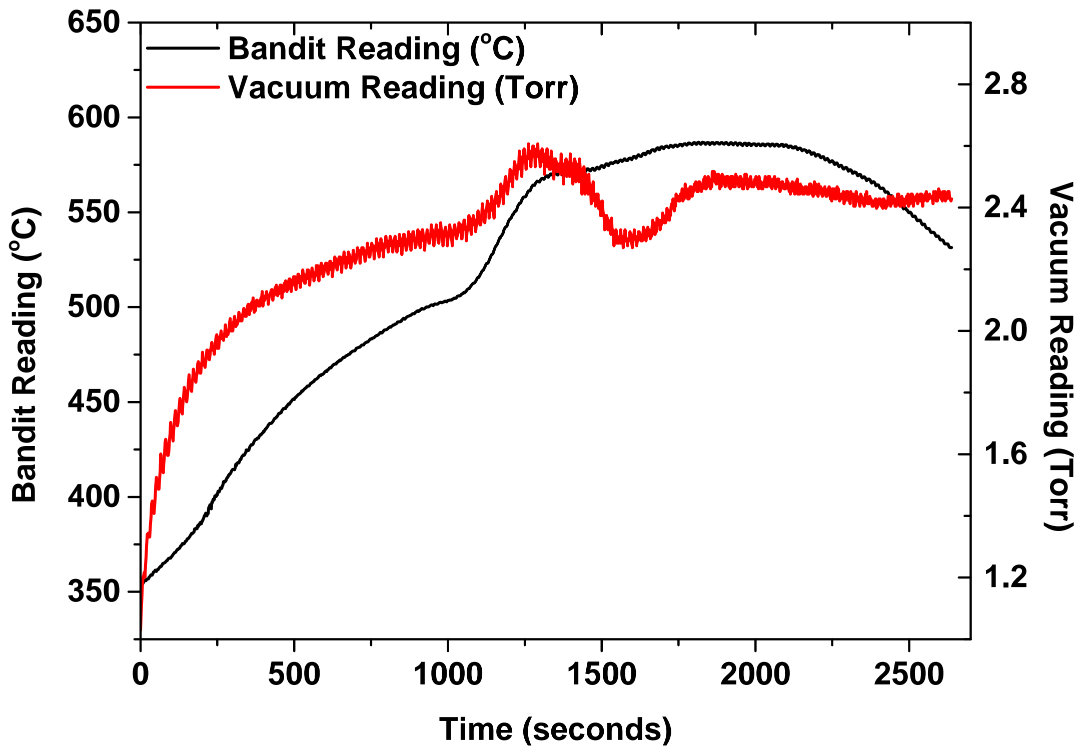

Figure 4.55. Obtained GaAs(211)B wafer temperature by kSA Bandit and vacuum reading during oxide removal process.

During oxide removal processes, the surface structure of GaAs wafers was monitored by in-situ Reflection High Energy Electron Diffraction (RHEED). RHEED patterns corresponding to the GaAs surfaces before and during oxide desorption is shown in Figure 4.56. As seen, spots on RHEED fluorescent screen forms streaky pattern during oxide desorption process.

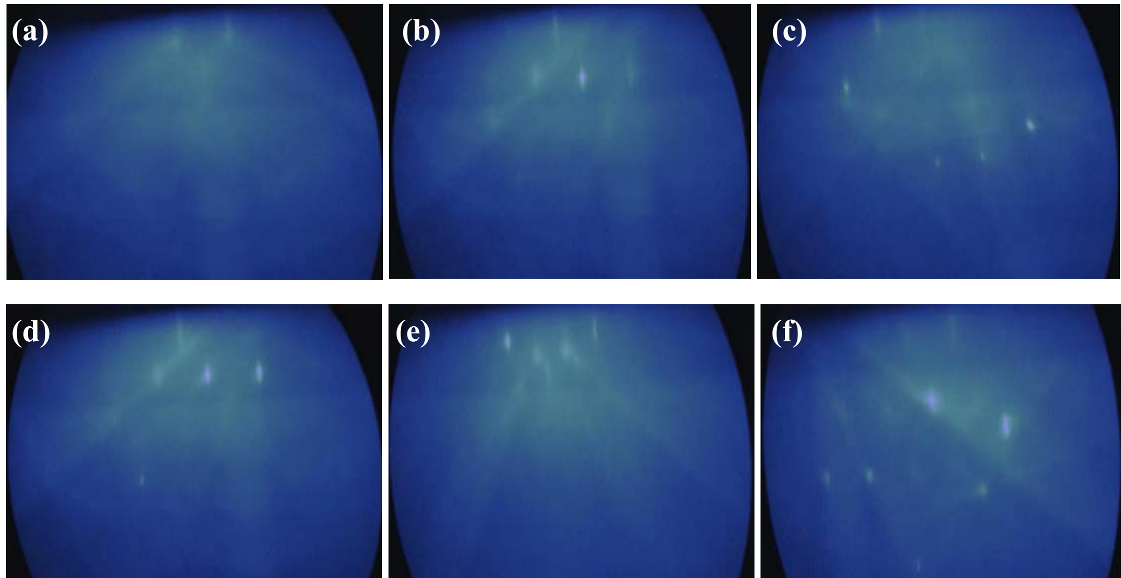

Figure 4.56. RHEED diffraction pattern of (a) and (b) before oxide desorption, (c), (d), (e) and (f) during oxide desorption at 582 ^{o}C of GaAs wafer.

CHAPTER 5

CHARACTERIZATION OF MBE-GROWN CDTE EPITAXIAL FILMS

5.1. Structural Characterizations

5.1.1. AFM and SEM Results

In order to evaluate the surface quality of MBE-grown CdTe thin films on GaAs(211)B wafers, the surface morphologies were observed via AFM and SEM techniques. Ex-situ AFM technique was performed in tapping mode to determine RMS roughness values and profile analyses of epitaxial CdTe films. All topographic images of CdTe films was obtained in 20x20 μm^2 scanned area. In addition, SEM-EDX and EDX-mapping techniques were performed to assess the chemical composition of the surface and the distribution of Cd, Te, Ga and As elements on the surface of films.

In Figure 5.1, AFM 2D and 3D topographic images and the profile analysis for selected areas are shown for sample CdTe18. The RMS roughness value from three 20x20 μm^2 scanned area found as 3.89 nm. As clearly seen in 2D and 3D topographic images and profile analyses of CdTe18 sample, the surface has growth-related defects that small pits formed on the surface with approximately 14 nm depths.

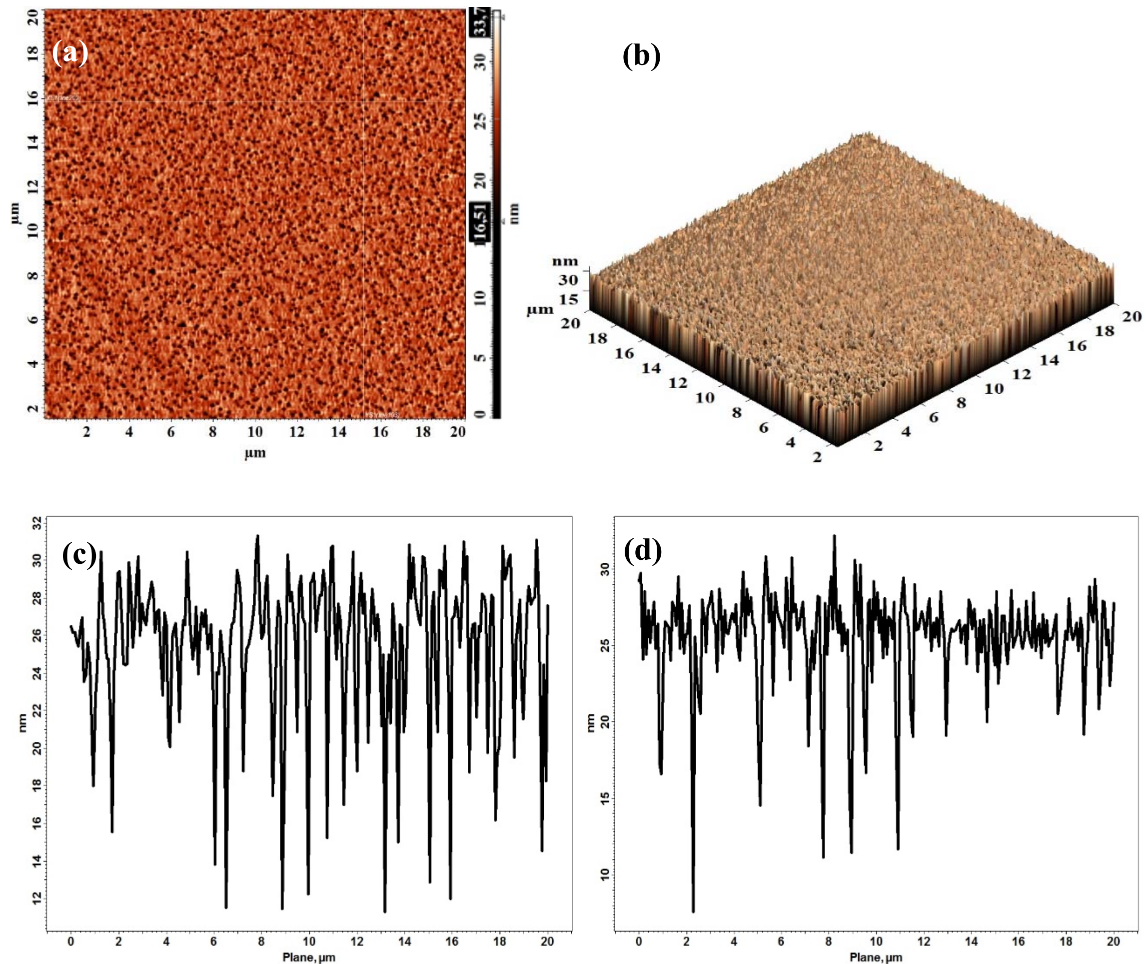

Figure 5.1. (a) AFM 2D Topographic image and (b) AFM 3D Topographic image of sample CdTe18 and profile line analysis of (c) YS1 (line 193) and (d) XS1 (line 202)

SEM micrographs and EDX-maps with percentage distributions of elements of CdTe18 sample are given in Figure 5.2. The growth-related defects on the surface of CdTe film could be observed in SEM micrographs with 50 000 magnifications. EDX analysis were performed for two areas and elemental distributions can be clearly seen in EDX-map analyses. EDX analyses showed that the atomic percentage of Cd was higher than Te. In addition, Ga contaminations, most probably Ga diffusing from substrate, observed in some parts of CdTe18 sample.

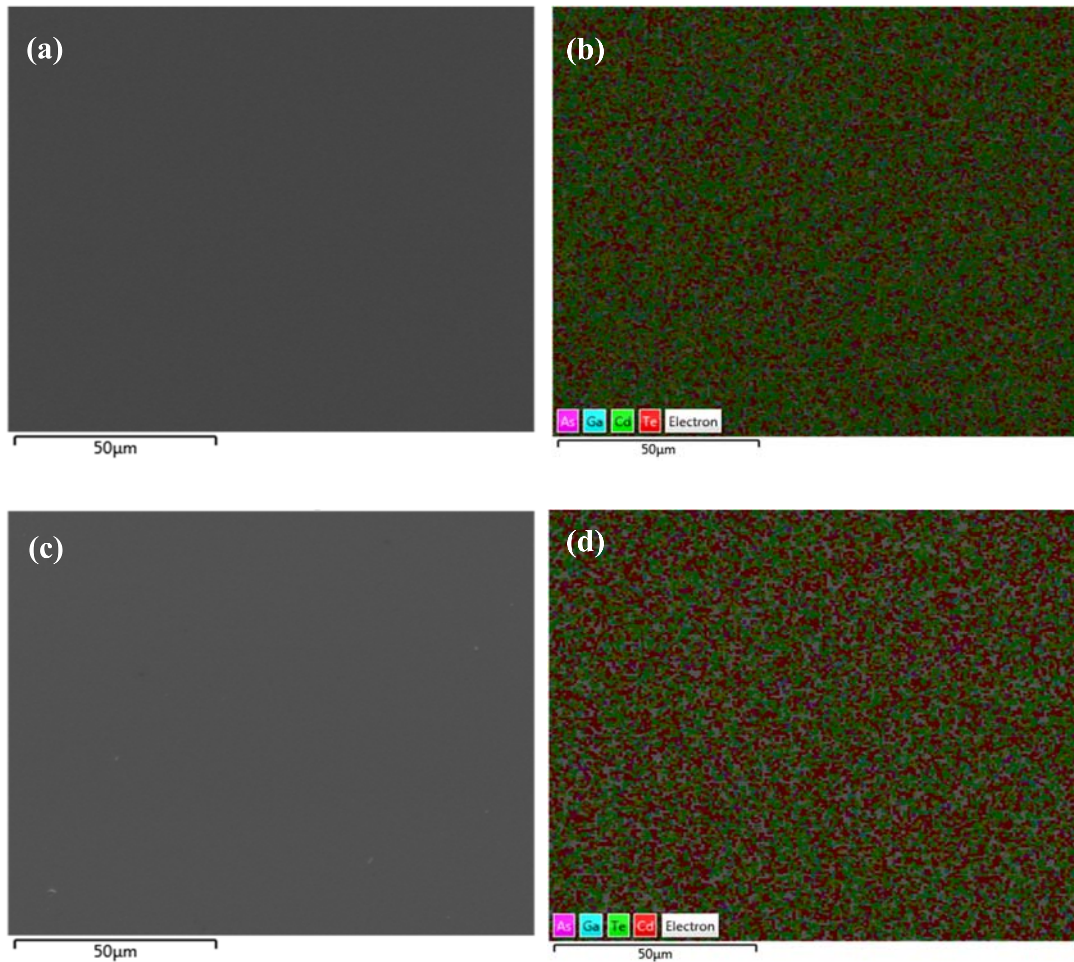

Element	Weight %	Atomic %
Cd	48.62	51.78
Te	51.33	48.15
Ga	0.00	0.00
As	0.05	0.07

Element	Weight %	Atomic %
Cd	48.21	51.31
Te	51.61	48.39
Ga	0.18	0.30
As	0.00	0.00

Figure 5.2. (a) and (c) are SEM micrographs of sample CdTe18 with 50 000 magnifications, (b) and (d) are EDX-map of SEM micrographs of (a) and (c), respectively and tables show the percentage distributions of Cd, Te, Ga and As in scanned area of (b) and (d), respectively.

AFM 2D and 3D topographic images and the profile analysis for selected areas are shown for sample CdTe23 are shown in Figure 5.3. The RMS roughness value of sample CdTe23 from three 20x20 μm^2 scanned area was 3.18 nm which is smaller than that of sample CdTe18. Likely to CdTe18 sample, the surface has growth-related defects, but as

seen pits with approximately 6 nm depths from AFM profile analysis. The number of growth-related pits counted manually and dislocation density of sample CdTe23 was calculated via AFM 2D topographic image within a 20x20 μm^2 scanned area. Surface defect density of CdTe23 sample was approximately 2.8 x 10^7 cm^{-2} which was lower than CdTe18 sample.

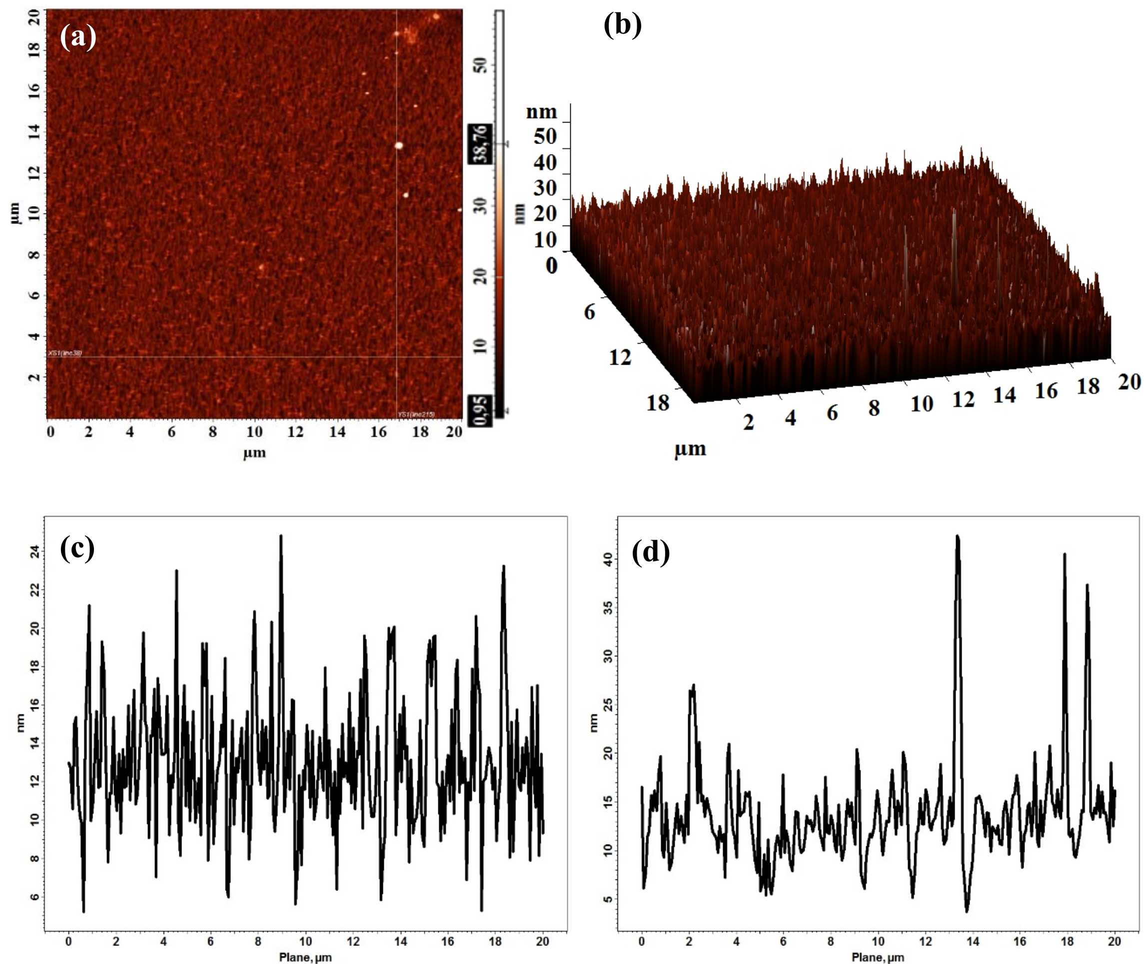

Figure 5.3. (a) AFM 2D Topographic image and (b) AFM 3D Topographic image of sample CdTe23 and profile line analysis of (c) XS1 (line 38) and (d) YS1 (line 215).

SEM micrographs and EDX-maps with atomic and weight percentage distributions for scanned two areas of sample CdTe23 are given in Figure 5.4. The elemental distributions are listed in tables. The growth-related defects on the surface of CdTe film couldn't observed in SEM micrographs with 50 000 magnifications.

Surprisingly, EDX analyses showed that the atomic percentage of Cd and Te are lower than Ga and As atoms. CdTe samples that thin film thickness of CdTe samples will be discussed in the following sections.

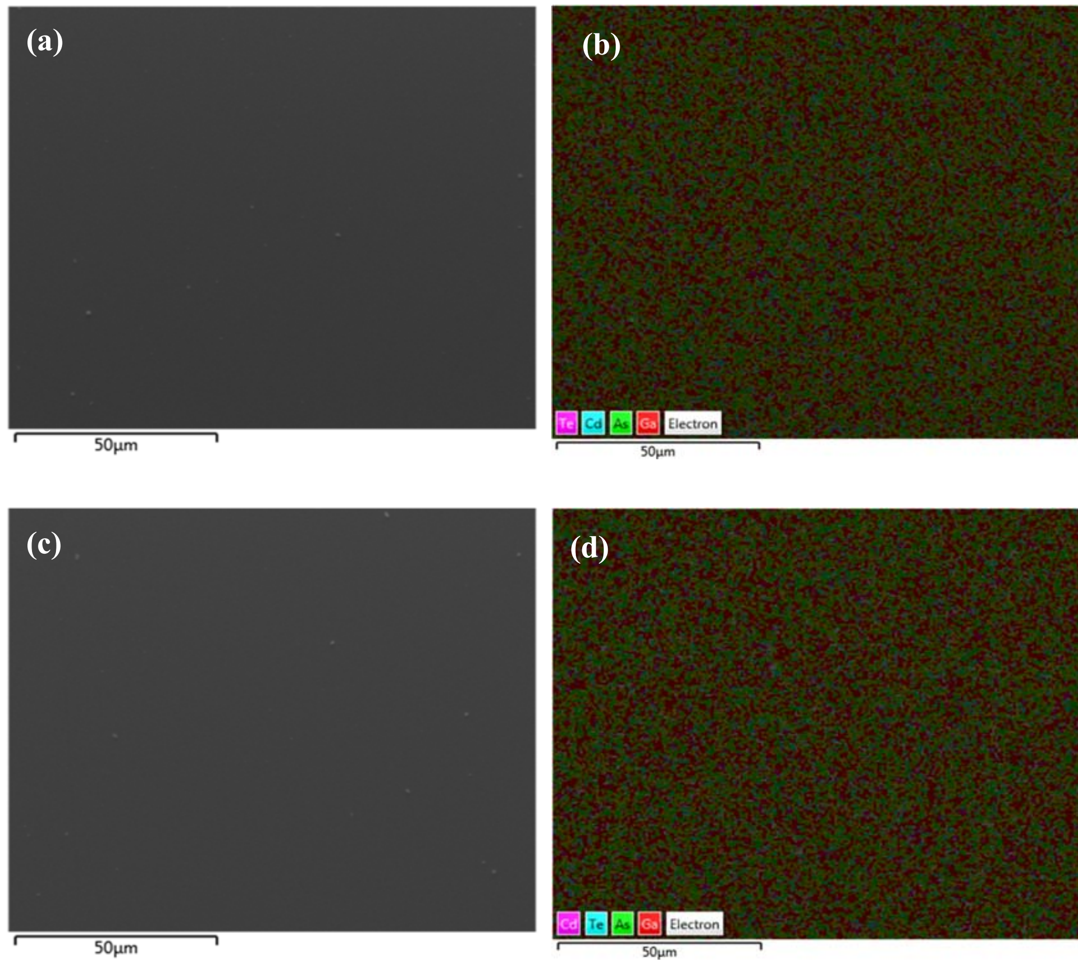

Element	Weight %	Atomic %
Cd	1.32	0.86
Te	1.72	0.99
Ga	47.48	49.83
As	49.48	48.32

Element	Weight %	Atomic %
Cd	1.84	1.20
Te	1.82	1.04
Ga	47.43	49.89
As	48.91	47.87

Figure 5.4. (a) and (c) are SEM micrographs of sample CdTe23 with 50 000 magnifications, (b) and (d) are EDX-map of SEM micrographs of (a) and (c), respectively and tables show the percentage distributions of Cd, Te, Ga and As in scanned area of (b) and (d), respectively.

AFM 2D and 3D topographic images of sample CdTe24 and the profile analyses for selected areas are shown in Figure 5.5. The average RMS roughness value of sample CdTe24 from three 20x20 μm^2 scanned area was 1.18 nm that the surface of CdTe24 sample exhibits smoother morphology compared to that of CdTe18 and CdTe23 samples. The surface of CdTe24 has low defect density with approximately 2 nm depths of pit. The grown-related defects could not counted manually for this sample that they are not clearly observable in AFM 2D topographic images and SEM micrographs. In addition to small pits, AFM profile analyses showed that the surface of CdTe24 sample have particules up to approximately 15 nm height. To reveal and to calculate the dislocation densities, Everson etch technique was performed for all three samples which will be discussed in detail in the following sections.

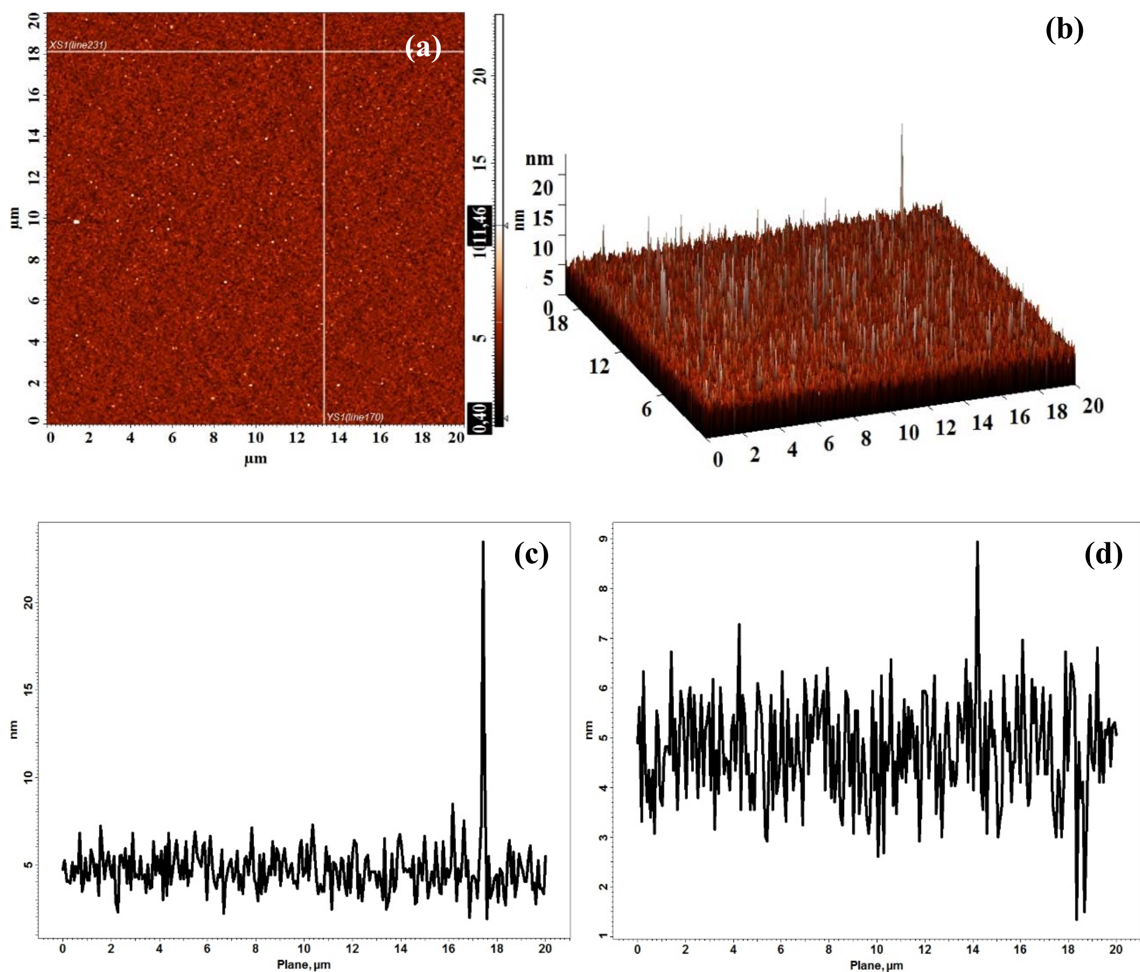

Figure 5.5. (a) AFM 2D Topographic image and (b) AFM 3D Topographic image of sample CdTe24 and profile line analysis of (c) XS1 (line 231) and (d) YS1 (line 170).

SEM micrographs and EDX-maps with percentage distributions of elements of CdTe24 sample are given in Figure 5.6. EDX analysis were performed for two scanned area and elemental distributions can be clearly seen in EDX-map analyses and the results are listed in tables. Likely to CdTe18 sample, EDX analyses showed that the atomic percentage of Cd was higher than Te which shows the some parts of CdTe24 sample surface terminated by cation (group II, Cd) atoms forming A polar surface. In addition, small amounts of Ga and As contaminations, most probably Ga and As diffusing from substrate, observed in some parts of CdTe18 sample.

In addition, SEM cross-sectional images were also taken in back-scattered electron (BSE) mode to estimate the CdTe film thicknesses of CdTe18, CdTe23 and CdTe24 samples. To obtain cross-sectional images, samples were placed cross-sectionally on the stubs after manually dicing with a scriber. Cross-sectional SEM micrographs of CdTe samples are shown in Figure 5.7. As clearly seen in SEM micrographs of CdTe18 and CdTe24 samples with 25 000 and 20 000 magnifications, the CdTe layer thicknesses were approximately 1 µm. Despite the lower atomic percentages of Cd and Te elements in sample CdTe23, the estimated CdTe layer thickness is approximately 2 µm according to SEM-BSE image. The defect lines in cross-sectional images inferred to cutting induced damages, it is hard to interpret growth-related defects from cross-sectional SEM micrographs.

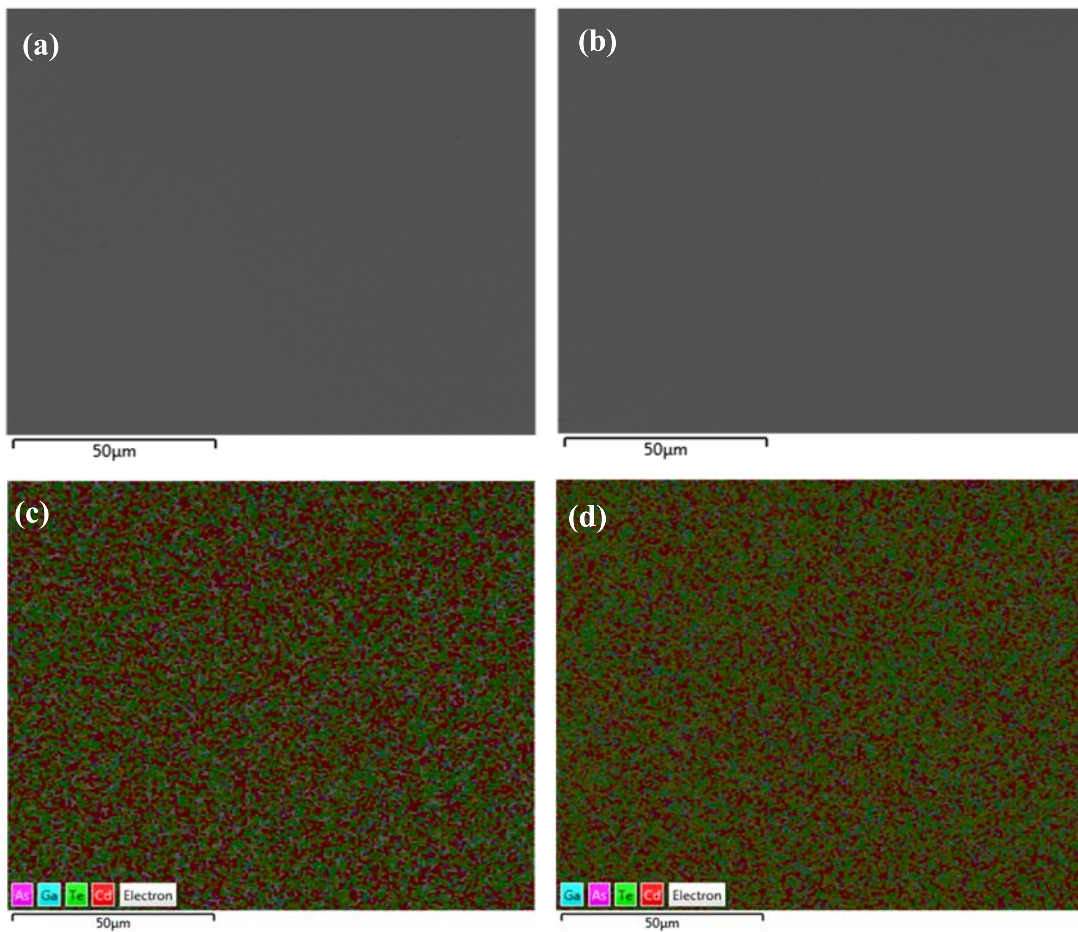

Element	Weight %	Atomic %
Cd	48.09	51.26
Te	51.91	48.74
Ga	0.00	0.00
As	0.00	0.00

Element	Weight %	Atomic %
Cd	48.06	51.22
Te	51.91	48.73
Ga	0.01	0.02
As	0.02	0.03

Figure 5.6. (a) and (b) are SEM micrographs of sample CdTe24 with 50 000 magnifications, (c) and (d) are EDX-map of SEM micrographs of (a) and (b), respectively and tables show the percentage distributions of Cd, Te, Ga and As in scanned area of (c) and (d), respectively.

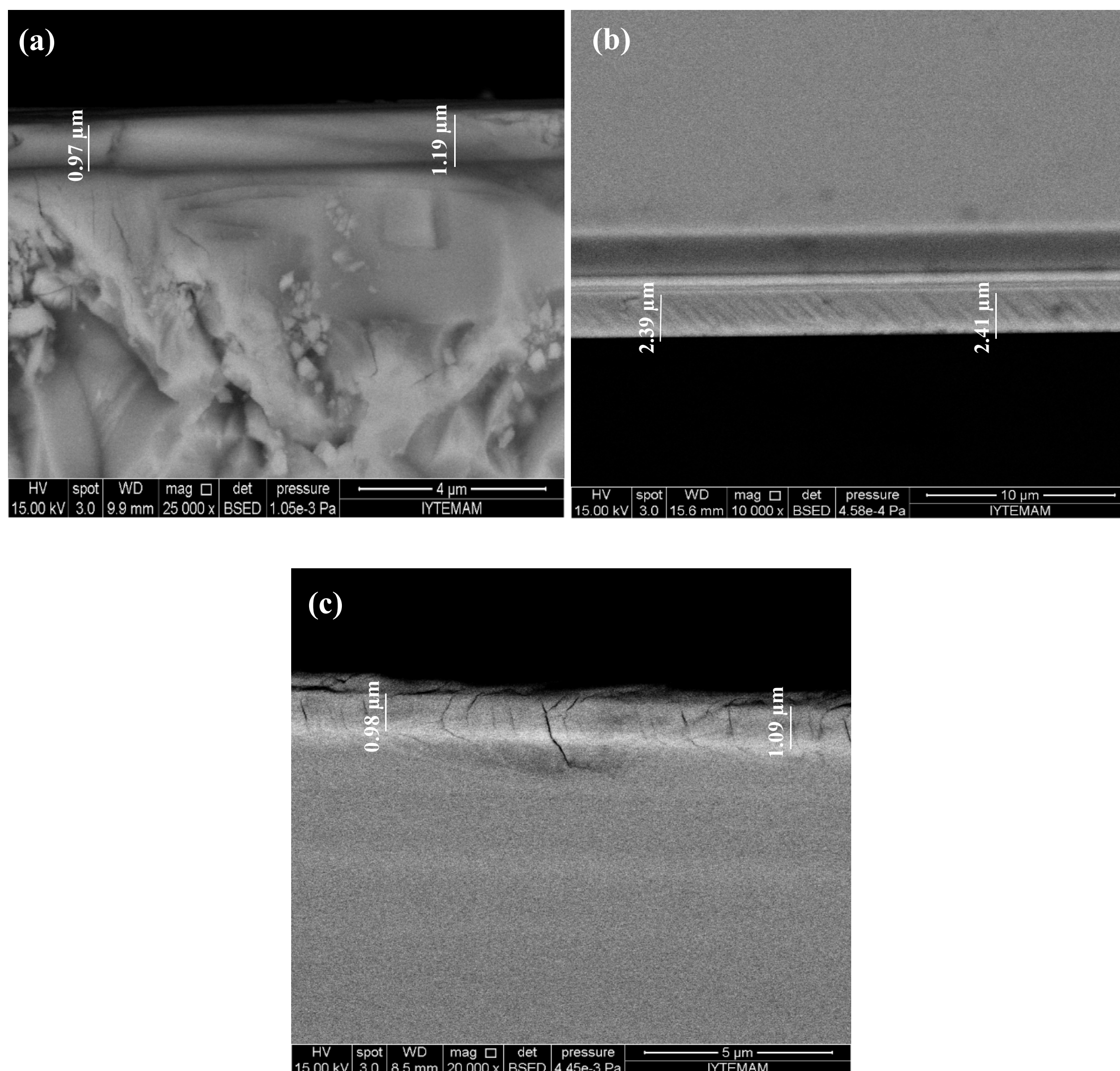

Figure 5.7. Cross-sectional SEM micrographs of (a) CdTe18, (b) CdTe23 and (c) CdTe24

5.1.2. XRD Results

X-ray triple axis rocking curve measurements performed to investigate the crystalline quality of of MBE grown CdTe(211)B epitaxial films. Full-width at half-maximum (FWHM) values were determined for selected samples of (211)B CdTe epitaxial films using Philips X'Pert Pro MRD X-Ray Diffraction system. In addition, X-ray Reflectivity (XRR) measurements were performed to determine thin-film parameters such as thickness, roughness, density and the layer structure. During XR-DCRC and X-ray Reflectivity (XRR) measurements, a Cu-Kα X-ray source with 1.5418 Å wavelength

was used. For all (211)B CdTe epitaxial films, (422) lattice plane was used to assess the growth orientation.

A typical XRD rocking curve of (422) peak of GaAs wafer which was used in our experiments as a substrate is given in Figure 5.8. The lattice parameter was calculated via Bragg reflection and found 5.6597 Å at position 41.858°. FWHM$_{\theta}$ of GaAs(211)B wafers were determined with the help of X-pert XRD data software and found 21 arcsec (0.00583°) for all wafers.

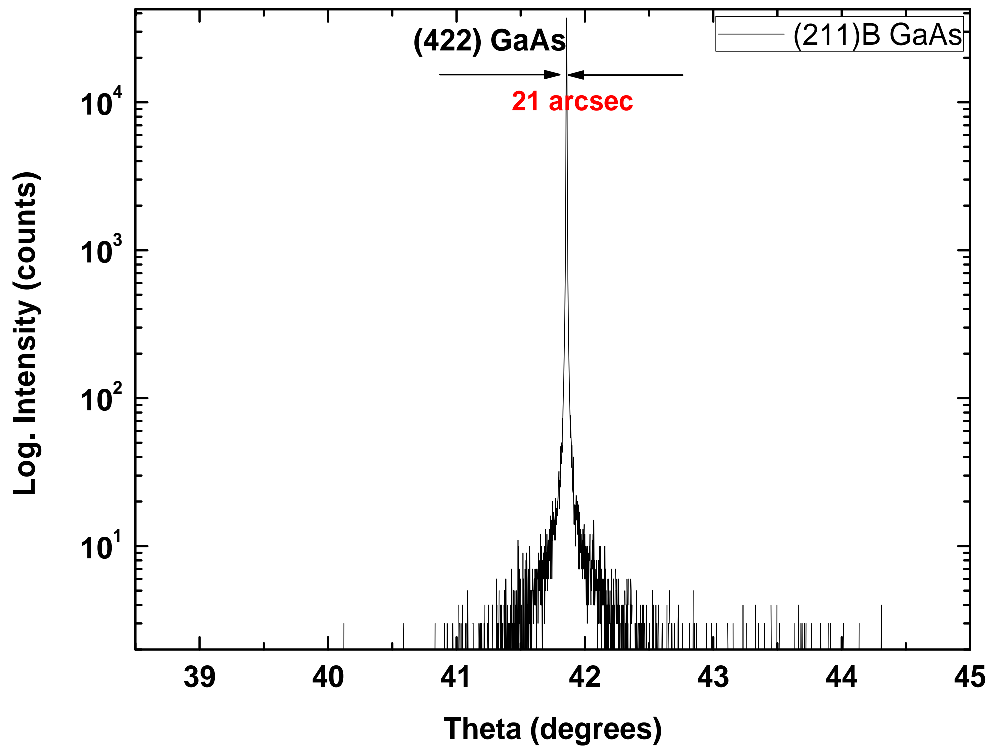

Figure 5.8. A typical (422) GaAs XRD rocking curve which was used as a substrate for epitaxially growth of CdTe(211)B films.

High resolution triple axis XRD rocking curve scan with CdTe (422) reflection of CdTe18 and CdTe24 samples in the θ-2θ geometry are shown in Figure 5.9 and Figure 5.10, respectively. FWHM$_{\theta}$ value for CdTe18 sample was found 269 arcsec (0.07472°) at position 35.6750° with 6.4758 Å. The best (211)B CdTe/(211)B GaAs films grown in this study was CdTe24 sample with a rocking curve with FWHM$_{\theta}$ of 190 arcsec (0.05278°) at position 33.9764°. The lattice parameter for CdTe24 sample calculated as 6.7578 Å using Bragg's law of reflection. Additional peaks were not observed during the scan which

indicates good (211) single-crystal quality of CdTe18 and CdTe24 films. However, XRD rocking curve couldn't achived with (422) reflection of CdTe23 sample which might be due to amorphous structure.

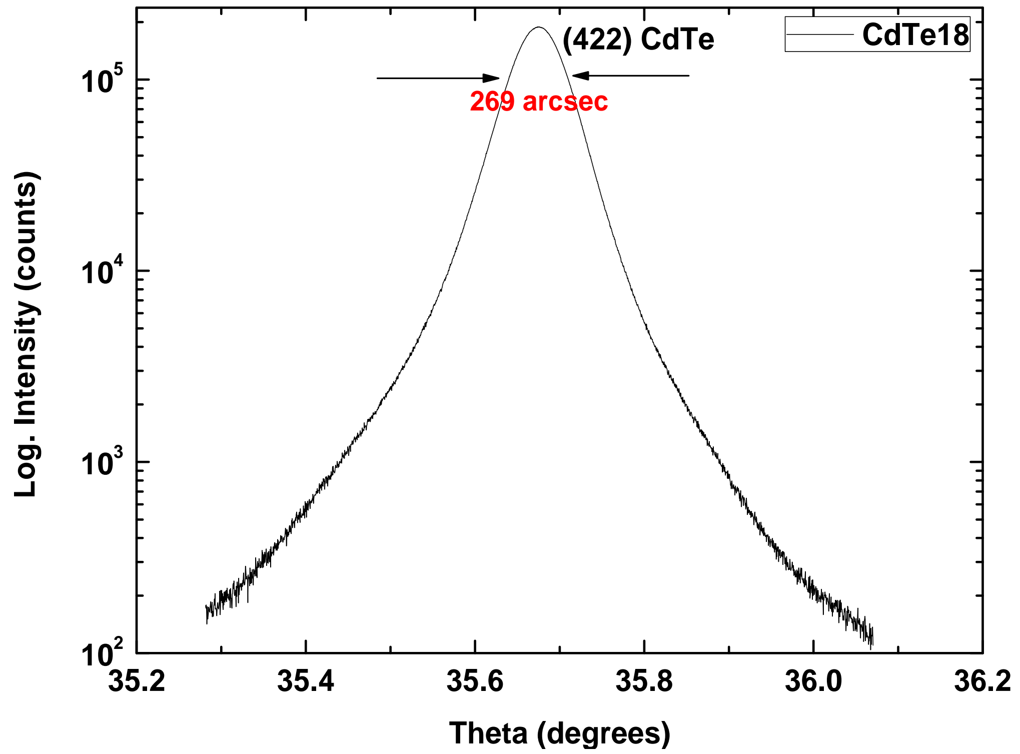

Figure 5.9. XRD rocking curve of (422) CdTe for CdTe18 sample.

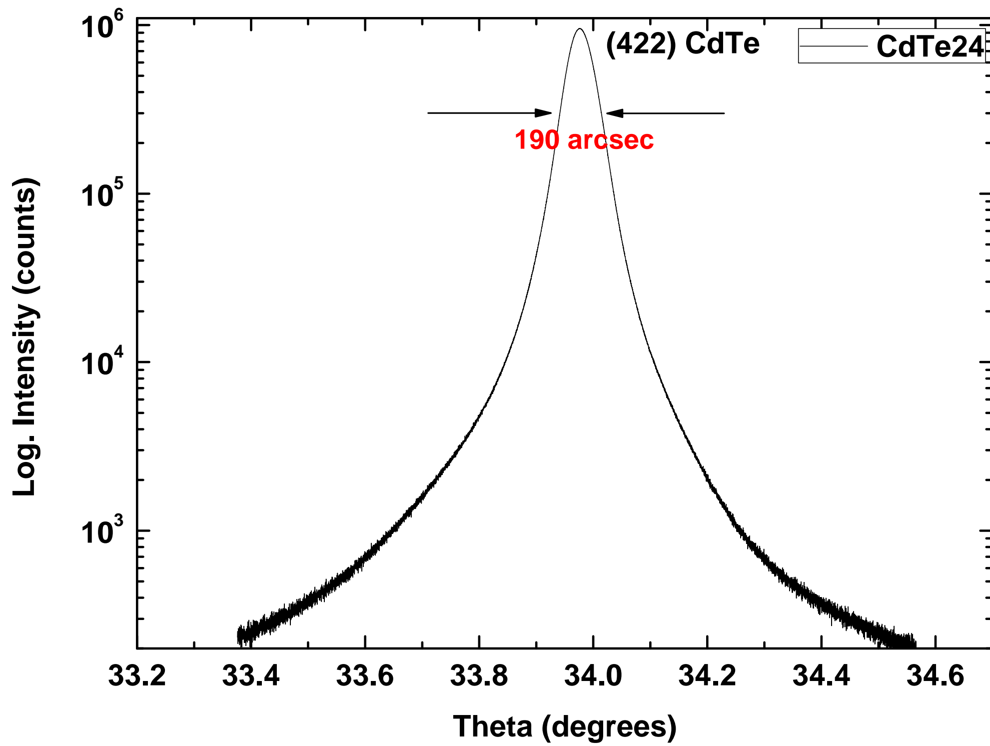

Figure 5.10. XRD rocking curve of (422) CdTe for CdTe24 sample.

XRR measurements performed for CdTe18 sample to determine the density, thickness and roughness values of GaAs substrate, grown CdTe film and possible oxide layers. As seen in Figure 5.11, most of the reflection occurs in the range of approximately 0.2^o to 0.7^o. The density, thickness and roughness of CdTe layer obtained from XRR curve fitting. Fitting estimates listed in Table 5.1, CdTe layer have 1.018 µm thickness and 2.801 nm roughness value. In addition, multilayer oxide structure obtained with a total oxide thickness of 0.005 µm with low density which might be due to exposure to atmosphere.

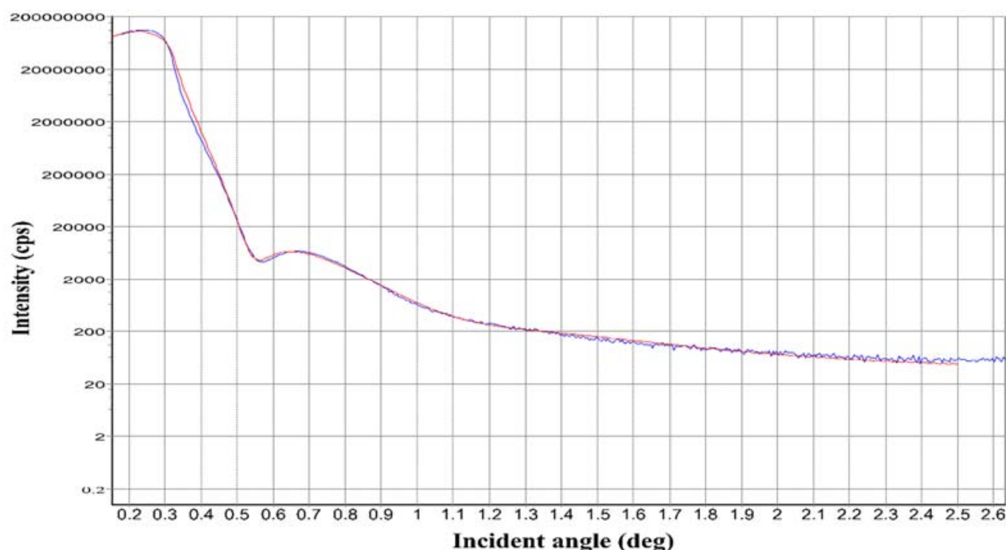

Figure 5.11. X-ray reflectivity curve of CdTe18 sample where blue line represents measured curve and red line represent fitted curve by X-pert XRD data sorftware.

Table 5.1. Obtained density, thickness and roughness of CdTe18 sample layers from XRR curve fitting

Layer	Density (g/cm^3)	Thickness (µm)	Roughness (nm)
GaAs	5.316	600	0.028
CdTe	5.850	1.018	2.801
Oxide	0.882	0.005	3.851

5.2. Optical Characterizations

5.2.1. Infrared Spectroscopy Results

FTIR spectrometry was used to measure the transmittance and calculate the thickness of MBE grown CdTe films. The transmittance of CdTe layers were measured at room temperature using a Bruker Vertex-80v spectrometer. The Vertex-80v system configuration equipped with a pyroelectric L-alanine doped triglycine sulfate (DLaTGS) detector with potassium bromide (KBr) window. DLaTGS detector covers a spectral

range from 12 000 to 250 cm^{-1} with a sensivity of $D^{*}>4x10^{8}$ $cm.Hz^{1/2}.W^{-1}$. During FTIR measurements a HeNe laser with a wavelength of 632.8 nm and a 5 mW power output was used. In Figure 5.12, FTIR transmittance spectra with 4 cm^{-1}resolution of CdTe18, CdTe23 and CdTe24 samples are given in the range of 700 to 7000 cm^{-1}.

The thicknesses of CdTe layers calculated from transmittance curves using the relation;

$$t_{CdTe} = \frac{1}{2n\left(\Delta k\right)_{avg}}$$

where t is the thickness of the CdTe layer, n is the index of refraction of CdTe and Δk is the distance wavenumber difference two oscillations. The thickness of CdTe layers estimated by taking the average of wavenumbers in interference fringes and index of refraction of CdTe was taken as 2.76 at 1.53 eV (at 300 K) which was obtained from ex-situ spectroscopic ellipsometry measurement. According to FTIR transmittance spectra, the thickness of CdTe layers were found to be 1.078 µm, 2.098 µm and 1.085 µm for CdTe18, CdTe23 and CdTe24 samples, respectively.

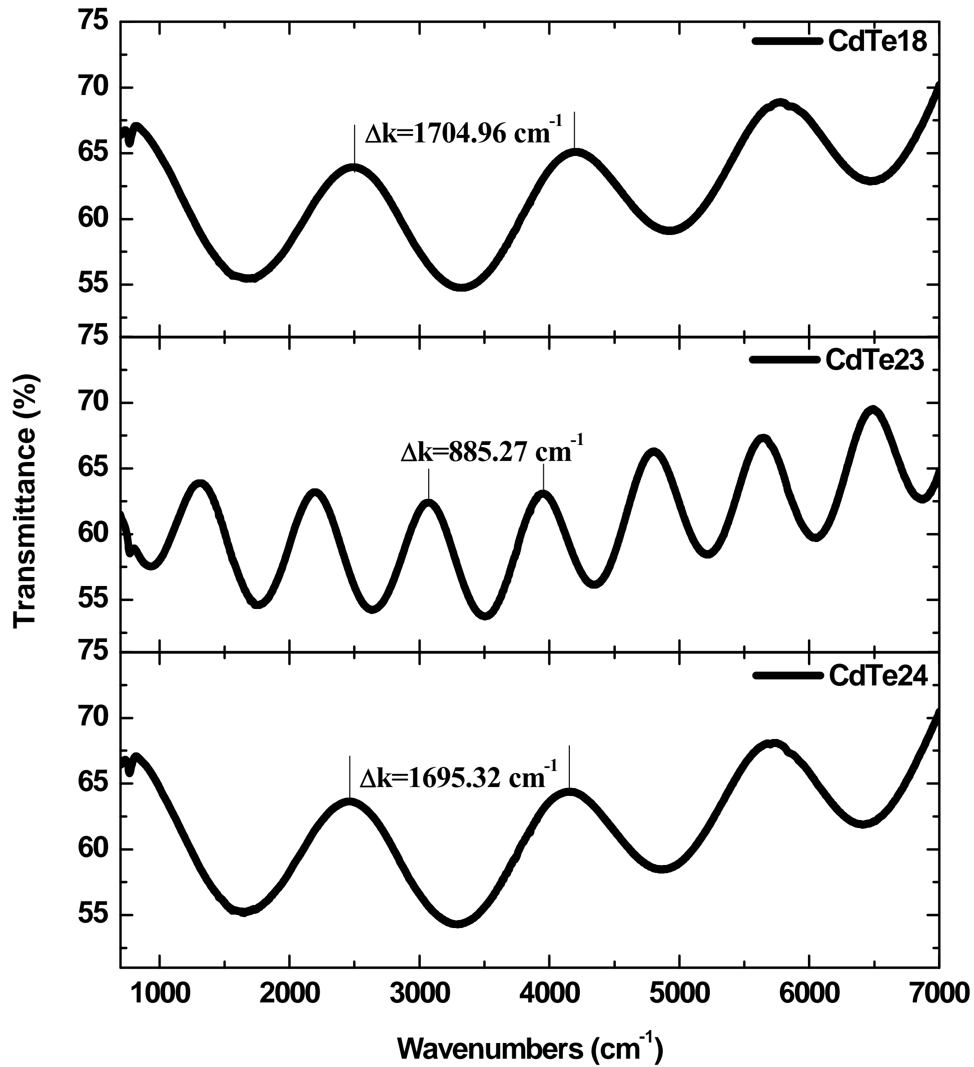

Figure 5.12. Room temperature IR transmission curves of MBE-grown CdTe epitaxial films.

The FTIR slightly transmittance curves of samples indicates that transmission of CdTe layers decreases with increasing film thickness. In addition, to investigate the cutoff wavelengths of the CdTe layers, PerkinElmer model Lambda 950 UV/VIS/NIR spectrometer was used and the transmittance curves of layers obtained in the range of 3800 to 13 000 cm^{-1} wavenumbers. The full range of transmittance spectra of CdTe samples are given in Figure 5.13. Cutoff wavelengths found 0.879 μm, 0.883 μm and 0.886 μm for CdTe18, CdTe23 and CdTe24 samples, respectively. However, due to close bandgaps of CdTe and GaAs, given cutoff wavelengts belongs to GaAs.

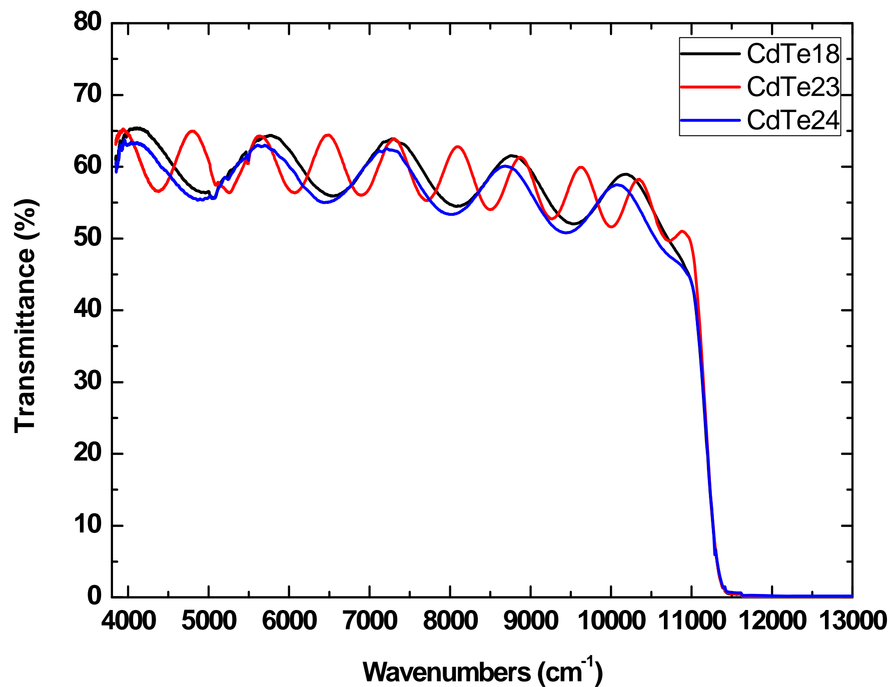

Figure 5.13. Room temperature transmittance curves of CdTe samples in the range of 3800 to 13 000 cm^{-1} taken with UV/VIS/NIR spectrometer.

5.2.2. Spectroscopic Ellipsometry Results

To obtain refractive index and extinction coefficient of CdTe epitaxial films as a function of wavelength ex-situ spectroscopic ellipsometry system was used in the range of 200 nm to 1000 nm. The change of refractive indexes and extinction coeffients depending on the wavelengths are shown in Figure 5.14.

Table 5.2. CdTe layer thicknesses obtained from spectroscopic ellipsometry (SE) and calculated using FTIR transmittance curves.

Sample ID	Layer Thickness (µm)	
	FTIR	SE
CdTe18	1.078	1074
CdTe23	2.098	0.002
CdTe24	1.085	1088

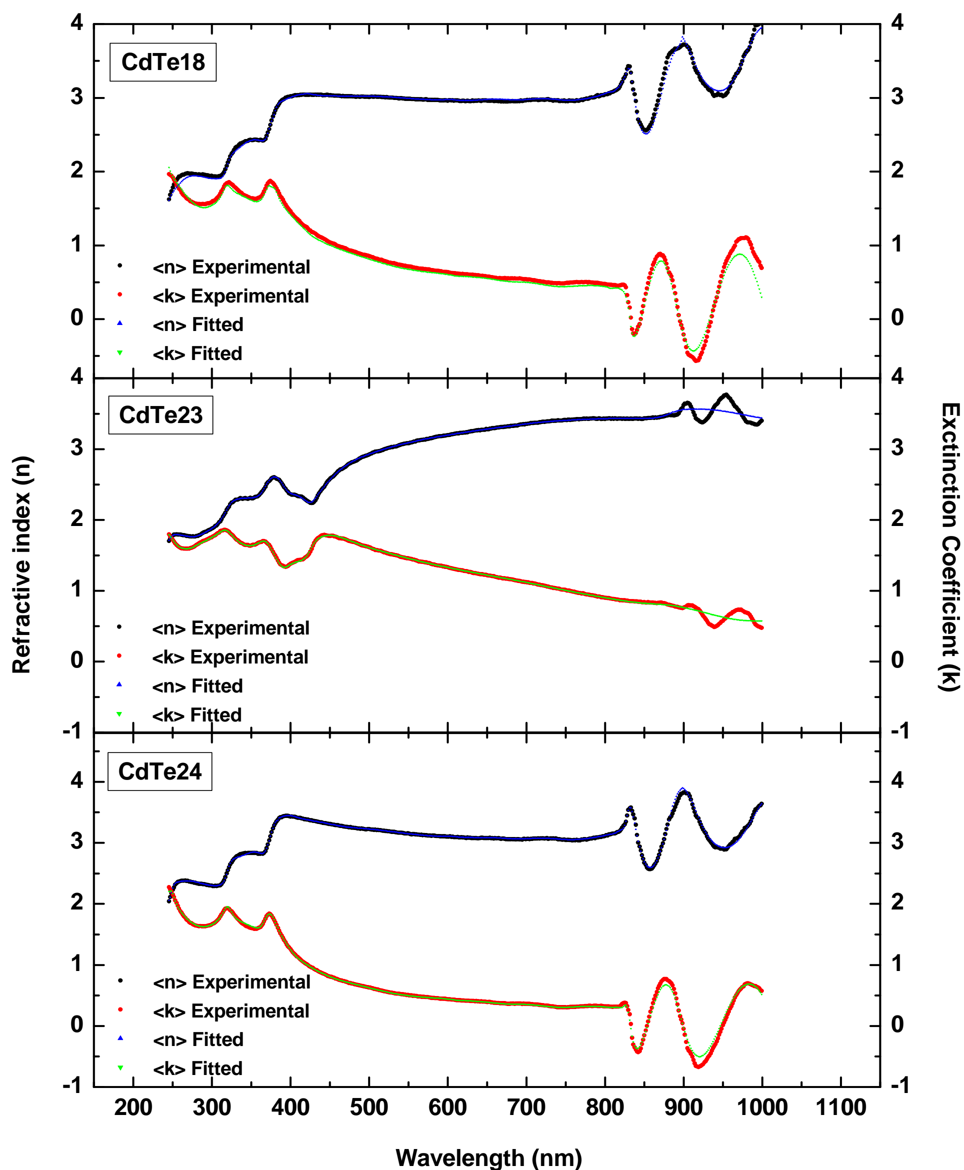

Figure 5.14. Ex-situ spectroscopic ellipsometry data of experimentally obtained and fitted using oscillator model refractive index and extinction coefficient of CdTe18, CdTe23 and CdTe24.

Curves fitted using oscillator models and thickness obtained from fitting are listed in Table 5.2 and compared with calculated layer thickness using FTIR transmittance curves. As listed in Table 5.2, CdTe layer thickness found only 19.14 nm via spectroscopic ellipsometry oscillator model that results could not fitted correctly. This might be due to amorphous nature of the film as was also indicated by XRD measurements.

5.2.3. Raman Spectroscopy Results

In order to characterize Te precipitates in CdTe and to investigate quality of MBE grown CdTe (211)B epitaxial films on GaAs (211)B wafers, temperature dependent Raman scattering experiments were performed. The samples were placed in a Linkam Temperature Controlled stage and excited with emission of an $Ar^{(+)}$ laser with 488 nm line. In addition to 488 nm, 514 nm laser line was also used in experiments, however spectral resolution of CdTe-like phonon modes was not high enough to observe at this wavelength. The detailed information about the Raman active modes in zincblende structure of CdTe was given in section 3.2.1.1.1.

In Figure 5.15, the full ranges Raman spectra of CdTe18 sample at various measurement temperatures are given. Figure 5.16 shows Raman spectra of CdTe18 sample at various temperatures which normalized to the first order LO phonon mode of CdTe. As seen from Figure 5.15 and Figure 5.16, Te-related modes and Raman active TO phonon mode of CdTe become more prominant at lower temperatures. At room temperature, first order Raman active TO and LO phonon modes of CdTe were observed at 149.54 cm^{-1} and 172.28 cm^{-1}, respectively. First order LO phonon mode shifted to 175.12 cm^{-1} at 250 K, 200 K and 150 K, and shifted to 176.54 cm^{-1} at 120 K and 100 K, respectively. At 80 K, LO phonon mode observed at 177.96 cm^{-1}. On the other hand, the position of first order TO phonon mode CdTe stayed constant up to 150 K that TO phonon mode shifted to 150.95 cm^{-1} at lower temperatures than 150 K. Also, second order scattering LO phonon mode observed at 337.06 cm^{-1} which shifted higher wavenumbers at lower temperatures. In addition to Raman active modes, peaks at 112.45 cm^{-1} and 132.43 cm^{-1} (at 300 K) indicated the presence excess Te and Te precipitates at CdTe layers. As clearly seen in Figure 5.18, E-symmetry mode of Te at 112.45 cm^{-1} at room temperature shifted to lower wavenumbers at 150 K and 250 K. On the other hand, A_1 symmetry mode of Te shifted to higher wavenumbers as the temperature decreases, except at 80 K.

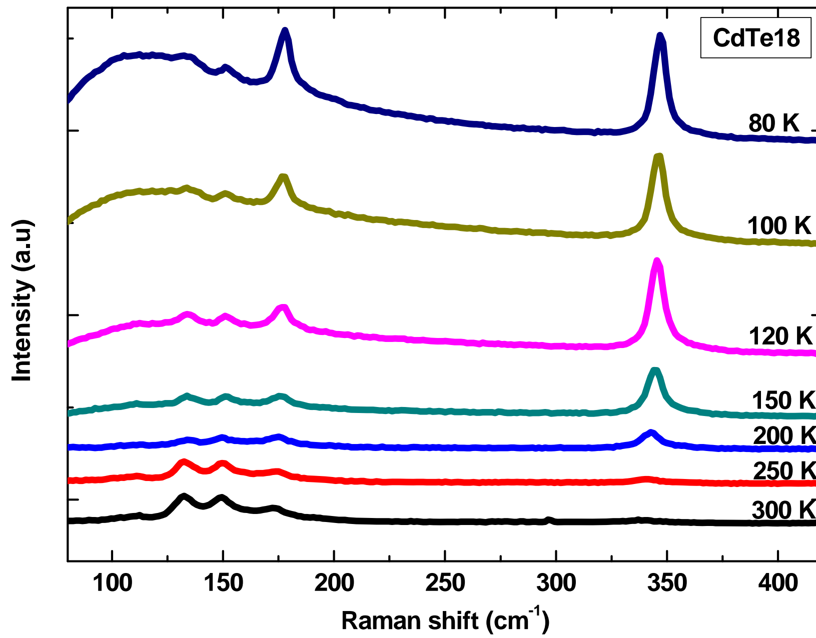

Figure 5.15. Temperature dependence Raman spectra of CdTe18 sample under 488 nm excitation.

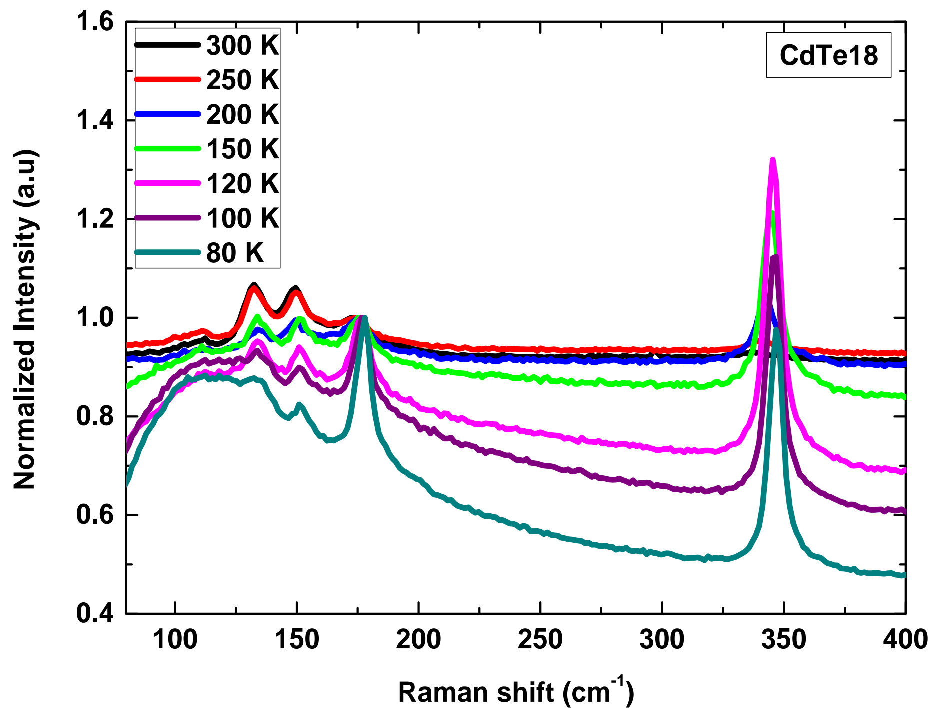

Figure 5.16. Raman scattering spectra of CdTe18 at various temperatures. The spectra were normalized to the first order TO phonon mode of CdTe.

The intensity ratio of 2LO and 1LO gives information about the quality of CdTe film. If the intensity ratio of second-order to first order LO Raman active mode is close to unity, CdTe layer has the perfect crystallity [52]. Both first and second order LO phonon mode intensities were increased as the measurement temperature was decreased.

In order to investigate the Raman active and Te-related phonon modes in more detail, the experimentally obtained Raman spectra of CdTe18 sample at different temperatures fitted with Lorentzian peaks. Figure 5.17 shows the whole range of Raman spectra of CdTe18 sample at 300 K and 250 K. The first-order TO Raman active modes obtained at 149.44 cm^{-1} (FWHM; 7.9 cm^{-1}) and 149.97 cm^{-1} (FWHM; 5.8 cm^{-1}) for measurement the features of 300 K and 250 K, respectively.

Second-order LO Raman active mode intensity increased with respect to that of at room temperature; 2LO/LO ratios were found 0.24 and 0.43 at 300 K and 250 K, respectively. 2LO phonon mode observed at 338.3 cm^{-1} with FWHM of 9.39 cm^{-1} shifted to higher frequencies by 2.49 cm^{-1} with FWHM of 6.22 cm^{-1} according to Lorentzian fitting. In addition to Raman active modes of CdTe, Te specific A_1 symmetry mode was observed at 132.43 cm^{-1} (FWHM; 5.68 cm^{-1}) and 132.85 cm^{-1} (FWHM; 4.73 cm^{-1}) for 300 K and 250 K measured temperatures, respectively, and E-symmetry mode of Te was observed at 109.39 cm^{-1} (FWHM; 2.88 cm^{-1}) and 109.97 cm^{-1} (FWHM; 3.33 cm^{-1}) at 300 K and 250 K, respectively.

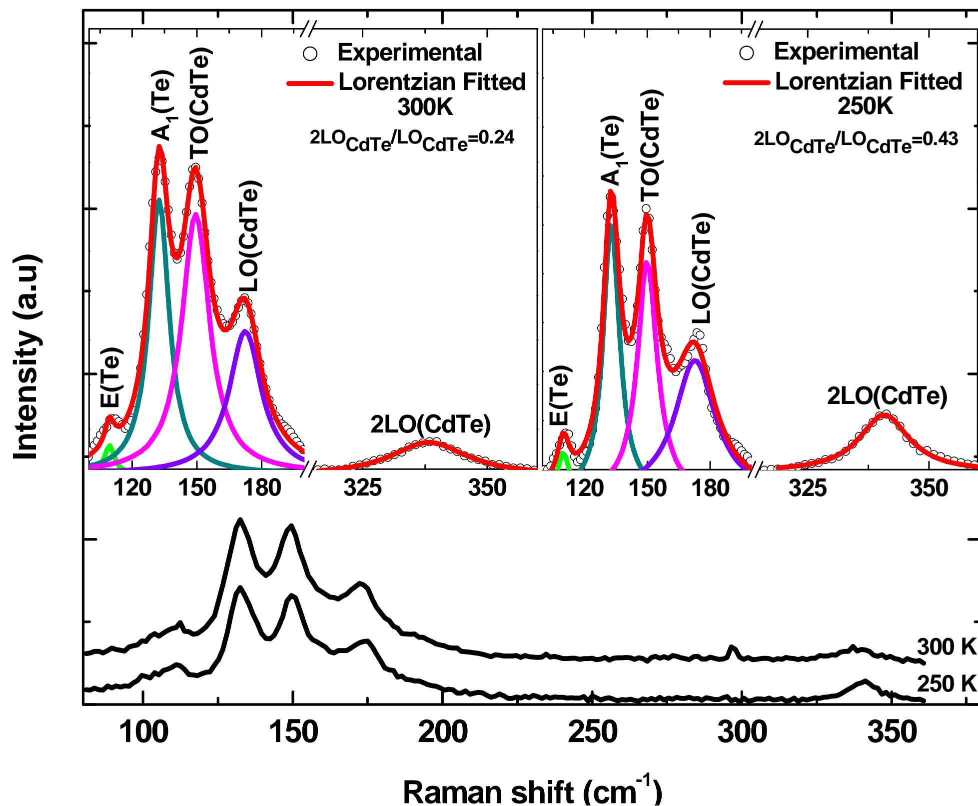

Figure 5.17. The whole range Raman spectra of CdTe18 at 300 K and 250 K. The insets show experimentally obtained and Lorentzian fitted Raman spectra at 300 K and 250 K.

The comparison of Raman spectra of CdTe18 sample at 200 K and 150 K are given in Figure 5.18. As seen from the Fig., the intensity of overtone of CdTe-like LO phonon mode increased at 150 K with respect to the measured temperature at 200K. The intensity ratio of 2LO and 1LO was found as 1.62 at 200 K and 3.27 at 150 K. Overtone of LO phonon mode observed at 342.86 cm^{-1} at 200 K and it shifted to higher frequencies by 1.83 cm^{-1} and became more sharper with a FWHM value of 5.71 cm^{-1} at 150 K. A_1 symmetry mode of Te was observed as a shoulder of CdTe-like first order TO phonon mode at 200 K which is splitted at 150 K. Raman active TO phonon mode of CdTe observed at 150.31 cm^{-1} with FWHM of 9.25 cm^{-1} for 200 K and it shifted to higher frequencies by 1.92 cm^{-1} with FWHM of 6.89 cm^{-1} for 150 K. Te specific E-symmetry mode observed at 110.76 cm^{-1} for 200 K and 109.0 cm^{-1} for 150 K measurements, respectively. The band at 132.96 cm^{-1} (200 K) and 133.84 cm^{-1} (150 K) attributed to the A_1 symmetry mode of Te.

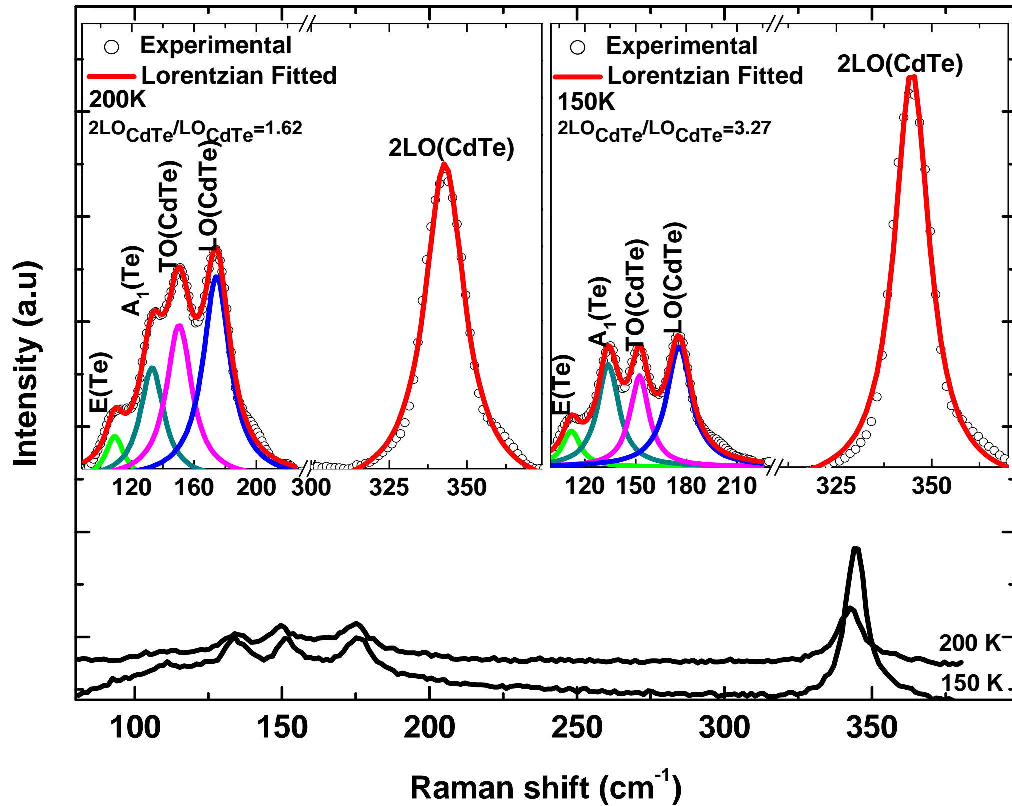

Figure 5.18. The whole range Raman spectra of CdTe18 at 200 K and 150 K. The insets show experimentally obtained and Lorentzian fitted Raman spectra at 200 K and 150 K.

Experimentally obtained and Lorentzian fitted Raman spectra of CdTe18 sample at 120 K and 100 K are shown in Figure 5.19. As seen from the Fig., overtone of LO phonon mode of CdTe18 sample become most intense at 100 K within all measured temperatures. The intensity ratio of 2LO and 1LO was found as 0.69 at 120 K and as 0.87 at 100 K. The band at 111.32 cm^{-1} (120 K) and 110.81 cm^{-1} (100 K) attributed to E-symmetry mode of Te and Te specific A_1-symmetry mode were observed at 133.66 cm^{-1} (120 K) and 133.67 cm^{-1} (100 K). A_1 mode became broader at 100 K with FWHM value of 30.66 cm^{-1} which is approximately doubled with respect to FWHM value at 120 K. Raman active TO phonon modes observed at 152.08 cm^{-1} (FWHM; 7.17 cm^{-1}) and at 152.89 cm^{-1} (FWHM; 5.98 cm^{-1}) at 120 K and 100 K, respectively. According to Lorentzian fitting, a small shift occurred for LO phonon mode of CdTe which is observed at 176.39 cm^{-1} (FWHM; 5.81 cm^{-1}) and at 176.94 cm^{-1} (FWHM; 4.17 cm^{-1}) for 120 K and 100 K, respectively.

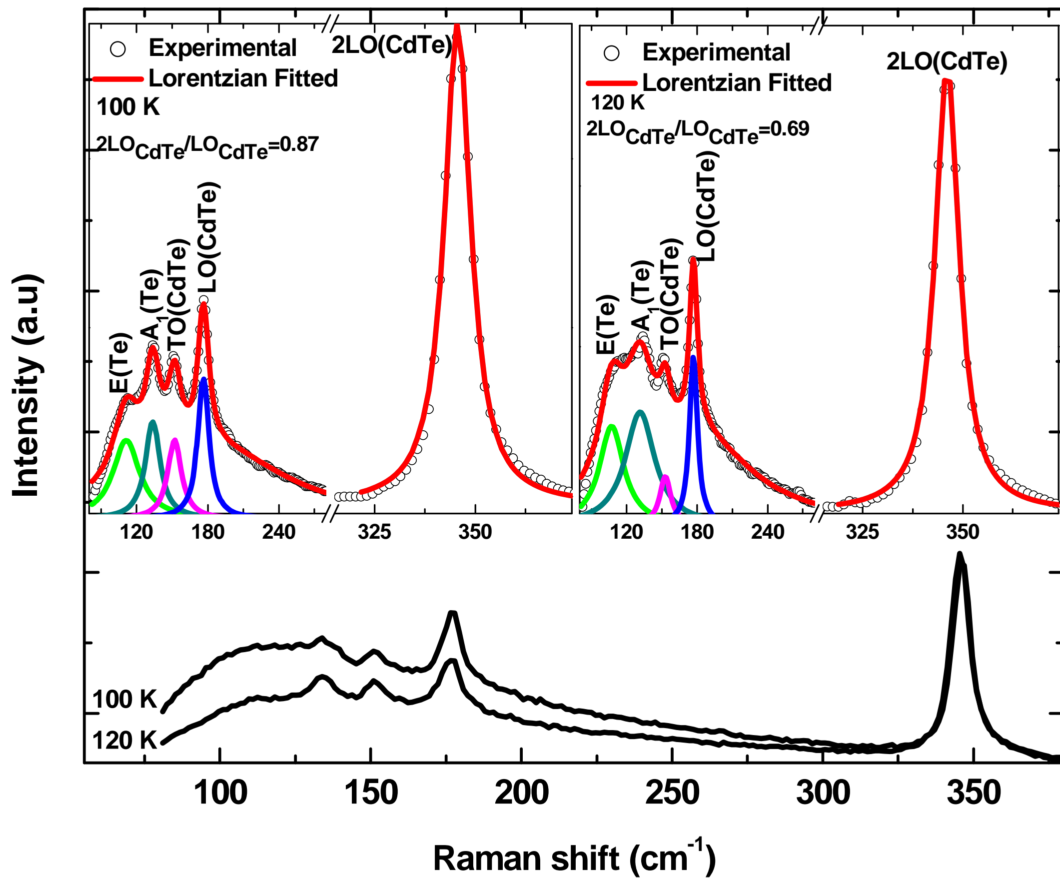

Figure 5.19. The whole range Raman spectra of CdTe18 at 120 K and 100 K. The insets show experimentally obtained and Lorentzian fitted Raman spectra at 120 K and 100 K.

The whole range Raman spectra of CdTe18 at 80 K with experimentally obtained and Lorentzian fitted curves are given in Figure 5.20. As seen in Raman spectra of sample, Te specific modes created a broad peak at 80 K and overlapped each other. E and A_1-symmetry modes of Te observed at 109.81 cm^{-1} (FWHM; 10.79 cm^{-1}) and at 132.43 cm^{-1} (FWHM; 14.23 cm^{-1}) at 80 K, respectively. The intensity of second-order LO phonon mode was increased with respect to first order LO phonon mode when compared to measured temperatures at 120 K and 100 K. It was also seen that 2LO/LO ratio was 1.66 at 80 K. First order LO phonon mode was observed at 177.64 cm^{-1} (FWHM; 3.83 cm^{-1}) and the overtone of LO phonon mode was observed at 346.92 cm^{-1} (FWHM; 3.38 cm^{-1}). The band at 152.59 cm^{-1} with FWHM value of 3.79 cm^{-1} was attributed to first order TO phonon mode of CdTe at 80 K.

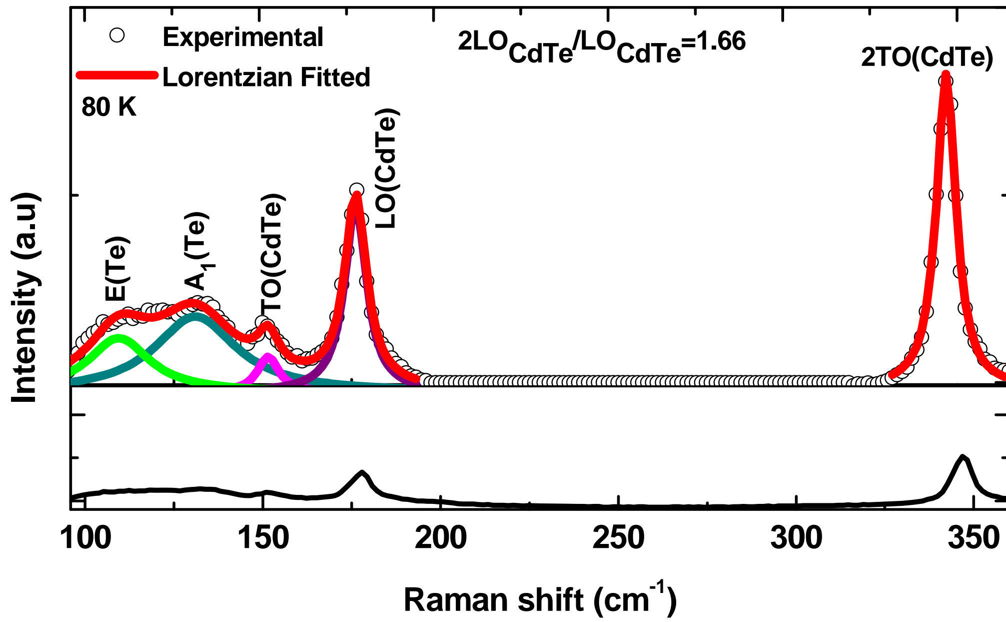

Figure 5.20. Experimentally obtained and Lorentzian fitted the whole range Raman spectra of CdTe18 at 80 K.

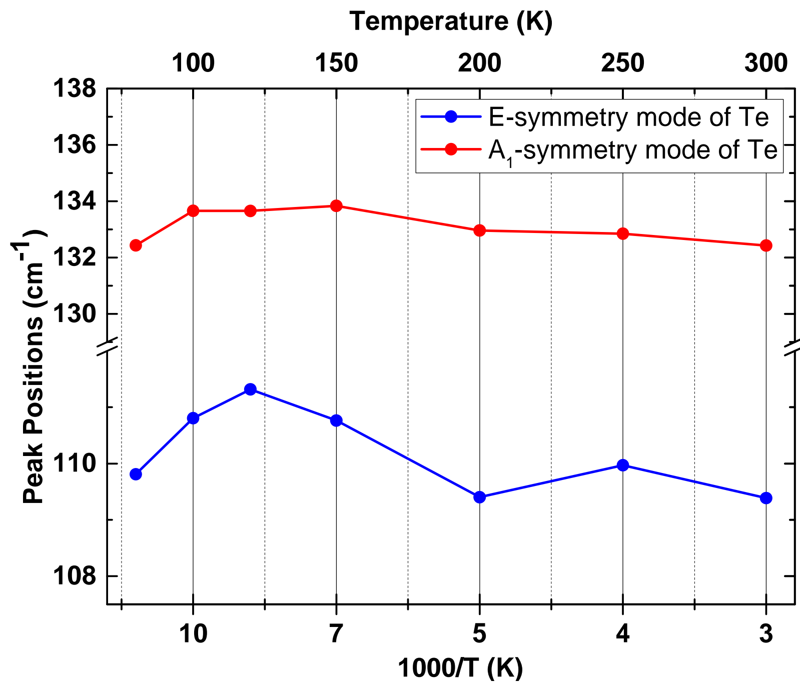

Figure 5.21. The change of Te specific E-symmetry and A_1-symmetry modes with the temperature for CdTe18 sample.

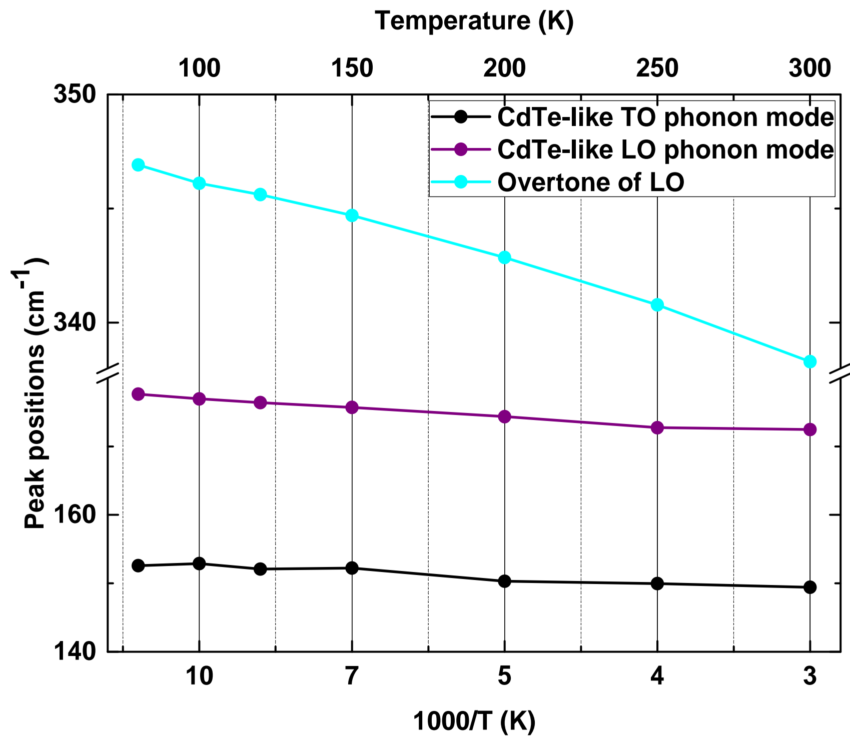

Figure 5.22. The change of CdTe-like TO, LO and 2LO phonon modes with the temperature for CdTe18 sample.

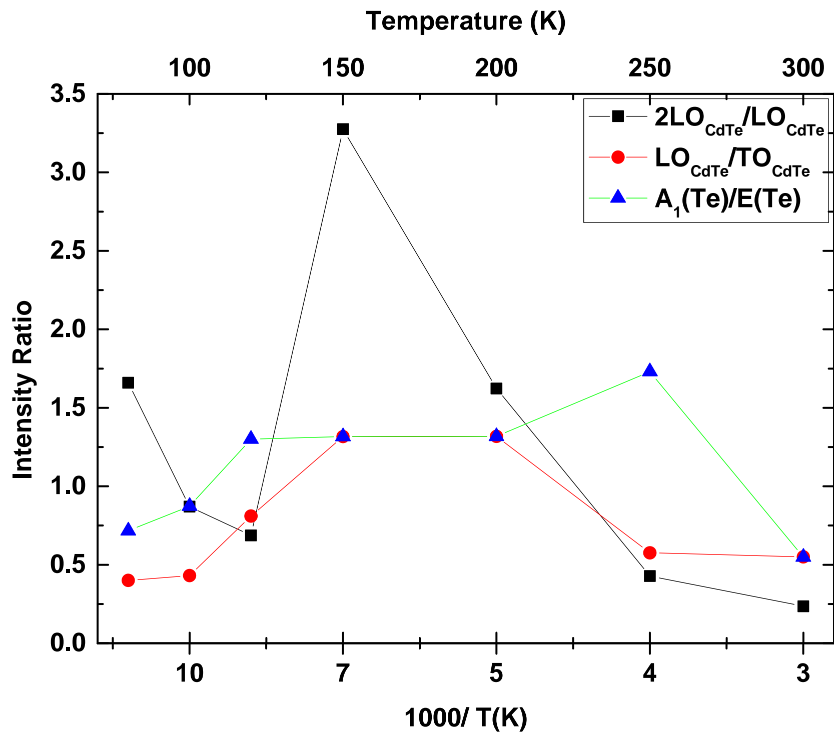

Figure 5.23. The change of calculated intensity ratios of observed phonon modes for CdTe18 sample.

In Figure 5.24, the change of Raman spectra depending on various temperatures for sample CdTe23 are shown. Despite 2.098 μm calculated thickness by FTIR transmittance curve, CdTe-like Raman active modes can be hardly resolved for all measured temperatures due to high intensity of GaAs-like Raman active modes. In order to observe the intensity and position changes of CdTe-like phonon modes, the spectra are normalized to Raman active TO phonon mode of GaAs (Figure 5.25). CdTe-like TO and LO phonon modes observed at 141.95 cm^{-1} and at 164.66 cm^{-1} at room temperature. TO Raman active phonon mode of CdTe shifted to higher frequencies by 0.83 cm^{-1}, 4.02 cm^{-1}, 10.33 cm^{-1}, 6.2 cm^{-1}, 3.31 cm^{-1} and 4.54 cm^{-1} at 250K, 200 K, 150 K, 120 K, 100 K and 80 K. On the other hand, CdTe-like LO Raman active mode shifted to higher frequencies by 2.47 cm^{-1}, 3.3 cm^{-1}, 7.01 cm^{-1}, 6.59 cm^{-1} and 7.42 cm^{-1} at 250 K, 200 K, 150 K, 100 K and 80 K that LO phonon mode position stayed constant at 150 K and 120 K. The band at 127.05 cm^{-1} has been assigned to A_1 symmetry mode of Te at 300 K which shifted to higher frequencies by 2.9 cm^{-1} (250 K), 5.38 cm^{-1} (200 K), 2.9 cm^{-1} (150 K and 120 K), 1.65 cm^{-1} (100 K) and 2.9 cm^{-1} (80 K). The most dominant Raman active modes for CdTe23 sample are GaAs-like first-order TO and LO phonon modes which observed respectively at 269.49 cm^{-1} and 293.04 cm^{-1} at room temprerature.

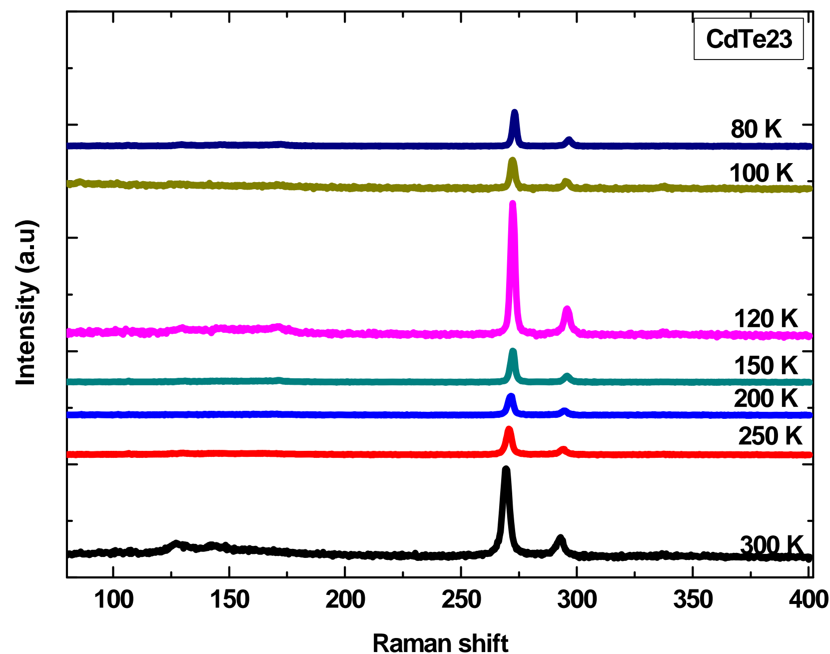

Figure 5.24. Temperature dependent Raman spectra of CdTe23 sample under 488 nm excitation.

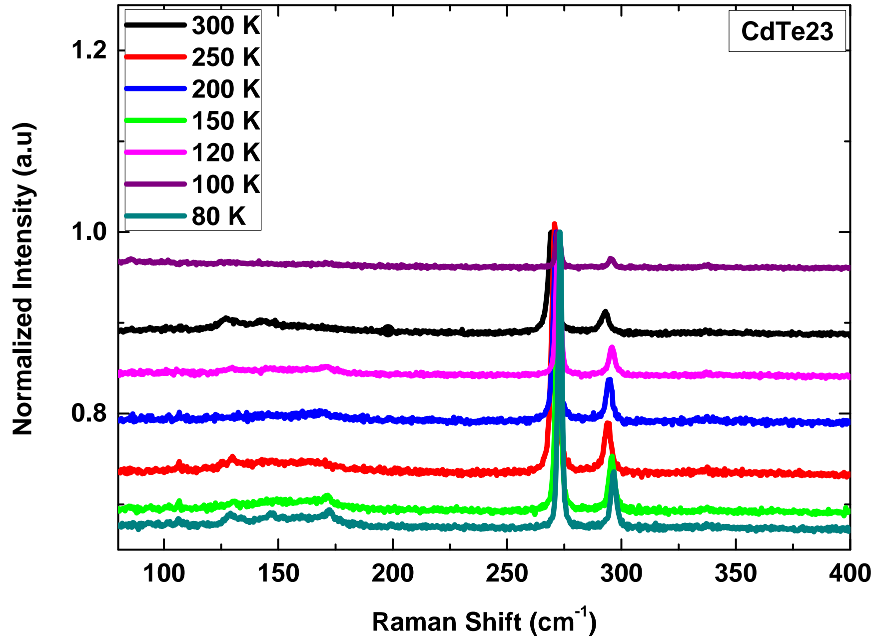

Figure 5.25. Raman scattering spectra of CdTe23 at various temperatures. The spectra were normalized to Raman active TO phonon mode of GaAs.

In order to investigate the CdTe-like Raman active and Te-related phonon modes in more detail, the experimentally obtained Raman peaks of CdTe23 sample at different temperatures fitted with Lorentzian fitting. The whole range Raman spectra of CdTe23 at 300 K and 250 K with experimentally obtained and Lorentzian fitted curves are given in Figure 5.26. At 300 K, E-symmetry mode of Te was not observed which gave rise a small peak at 106.54 cm^{-1} with FWHM value of 1.92 cm^{-1} at 250 K. The band at 127.84 cm^{-1} (FWHM; 5.16 cm^{-1}) and 129.58 cm^{-1} (FWHM; 4.64 cm^{-1}) attributed to A_1 symmetry mode of Te at 300 K and 250 K, respectively. This mode was more intense at 300 K compare to 250 K. Raman active CdTe-like TO and LO phonon modes observed at 143.77 cm^{-1} (FWHM; 6.95 cm^{-1}) and 161.92 cm^{-1} (FWHM; 11.49 cm^{-1}) at 300 K, respectively. CdTe-like TO and LO phonon modes shifted to higher frequencies respectively by 1.22 cm^{-1} and 2.51 cm^{-1} at 250 K. Overtone of LO became observable at 250 K with 340.05 cm^{-1} (FWHM; 30.29 cm^{-1}) peak position. The intensity ratio of CdTe-like 2LO phonon peak to 1LO phonon peak was found as 0.71 at 250 K.

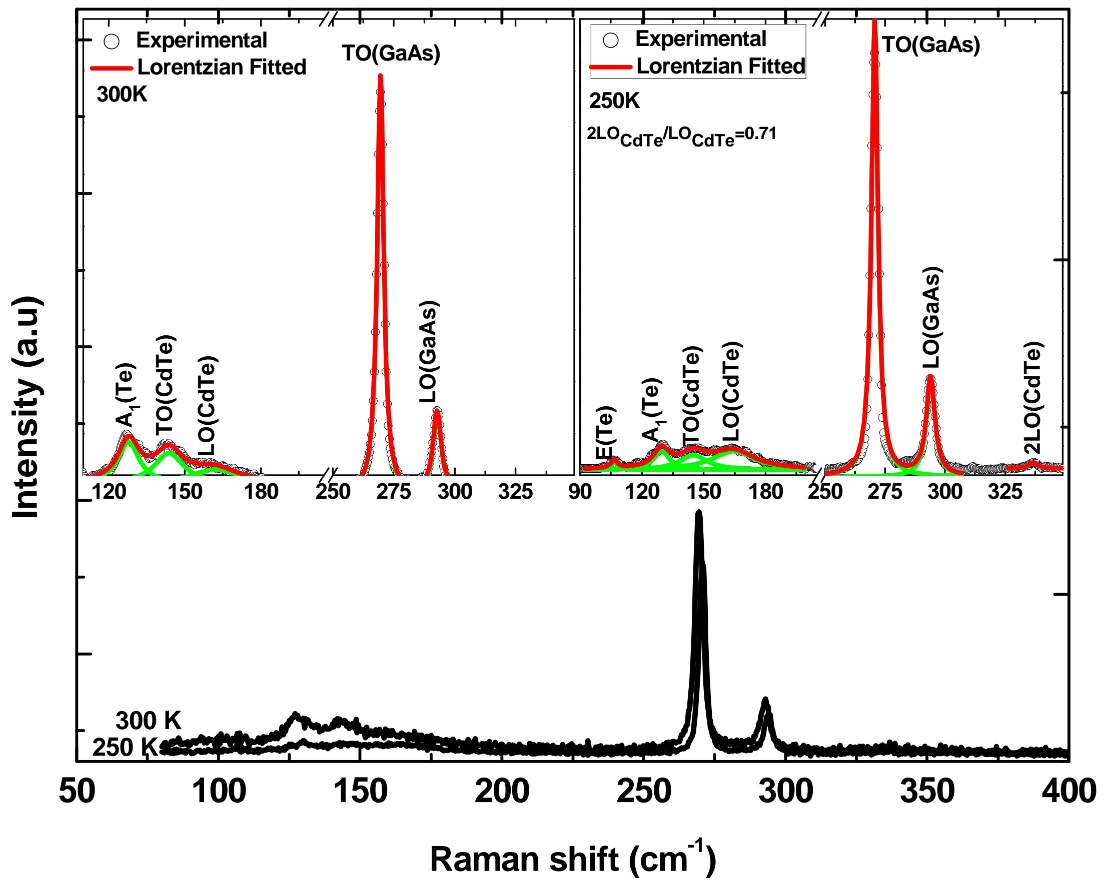

Figure 5.26. The whole range Raman spectra of CdTe23 at 300 K and 250 K. The insets show experimentally obtained and Lorentzian fitted Raman spectra at 300 K and 250 K.

Experimentally obtained and Lorentzian fitted Raman spectra of CdTe23 sample at 200 K and at 150 K are shown in Figure 5.27. Overtone of LO phonon mode of CdTe was not observed for two measured temperatures. In addition, Te-related symmetry modes were only observable at 150 K with respect to 200 K. The band at 130.12 cm^{-1} assigned as A_1 symmetry mode of Te which have a FWHM value of 1.67 cm^{-1}. Raman active CdTe-like TO and LO modes observed as a broad peak for two temperatures that TO phonon mode of CdTe observed at 146.48 cm^{-1} (FWHM; 19.68 cm^{-1}) at 200 K and shifted to 152.92 cm^{-1} (FWHM; 28.42 cm^{-1}) at 150 K. The band at 168.34 cm^{-1} (FWHM; 7.24 cm^{-1}) attributed to CdTe-like LO phonon mode at 200 K and it shifted to 171.09 cm^{-1} (FWHM; 2.91 cm^{-1}) at 150 K. Likely to other measured temperatures, the most dominant modes were Raman active modes of GaAs that TO phonon mode observed respectively at 271.43 cm^{-1} (FWHM; 1.49 cm^{-1}) and at 272.34 cm^{-1} (FWHM; 1.19 cm^{-1}) for 200 K and 150 K temperatures. In addition, GaAs-like LO phonon mode observed at 294.61 cm^{-1}

(FWHM; 2.19 cm^{-1}) at 200 K which is shifted to higher frequency by 1.18 cm^{-1} (FWHM; 1.76 cm^{-1}) at 150 K.

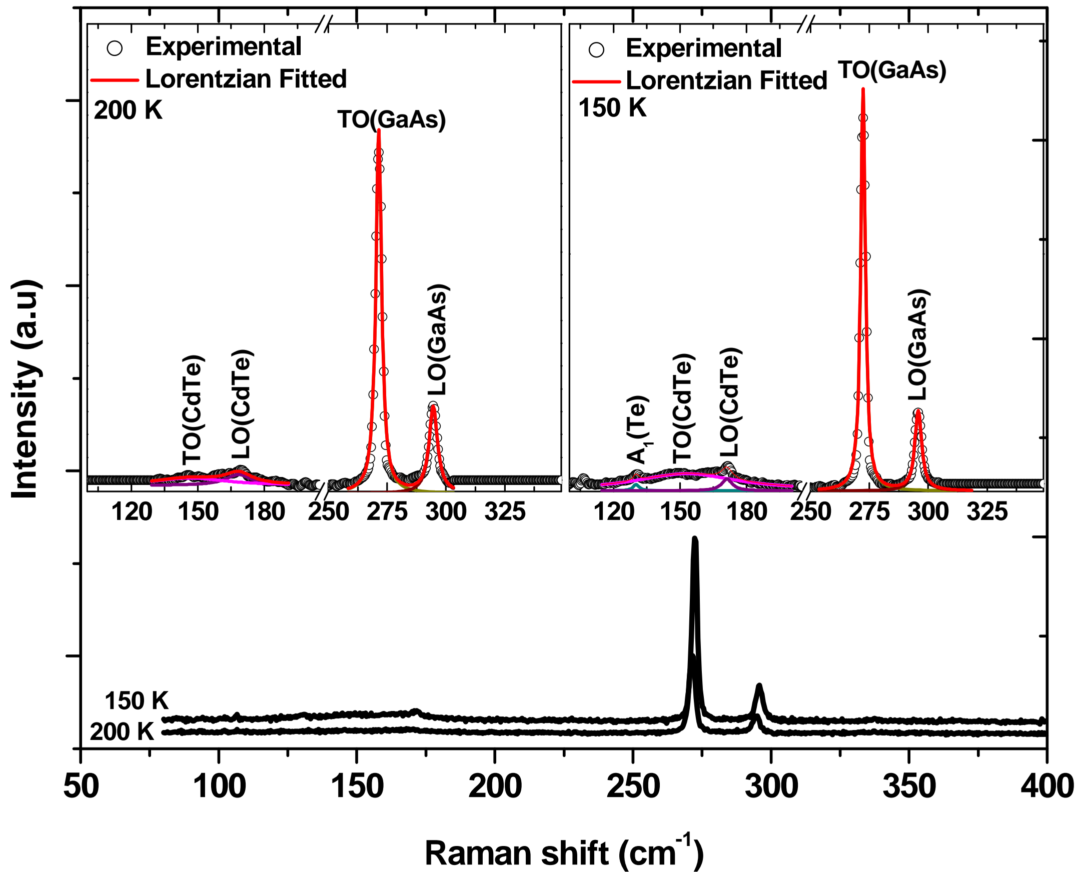

Figure 5.27. The whole range Raman spectra of CdTe23 at 200 K and 150 K. The insets show experimentally obtained and Lorentzian fitted Raman spectra at 200 K and 150 K.

The Raman spectra of CdTe23 sample at 120 K and 100 K are given in Figure 5.28. Both first order first-order and second-order LO Raman active mode of CdTe observed, however, first-order TO Raman active mode could not resolved with Lorentzian fitting at 120 K. At 120 K, CdTe-like first order and second-order LO phonon modes observed at 169.49 cm^{-1} (FWHM; 9.18 cm^{-1}) and 337.39 cm^{-1} (FWHM; 2.85 cm^{-1}), respectively that the calculated 2LO/LO ratio was 1.046. The peak at 129.14 cm^{-1} (FWHM; 3.63 cm^{-1}) attributed to Te-specific A_1 symmetry mode at 120 K which is shifted to 130.18 cm^{-1} and observed as a broad peak with FWHM value of 19.05 cm^{-1} at 100 K. Both GaAs-like TO and LO Raman active modes observed at two measured temperatures.

An additional peak observed at 286.15 cm^{-1} with FWHM value of 2.38 cm^{-1} at 120 K which attributed to SO phonon mode of GaAs.

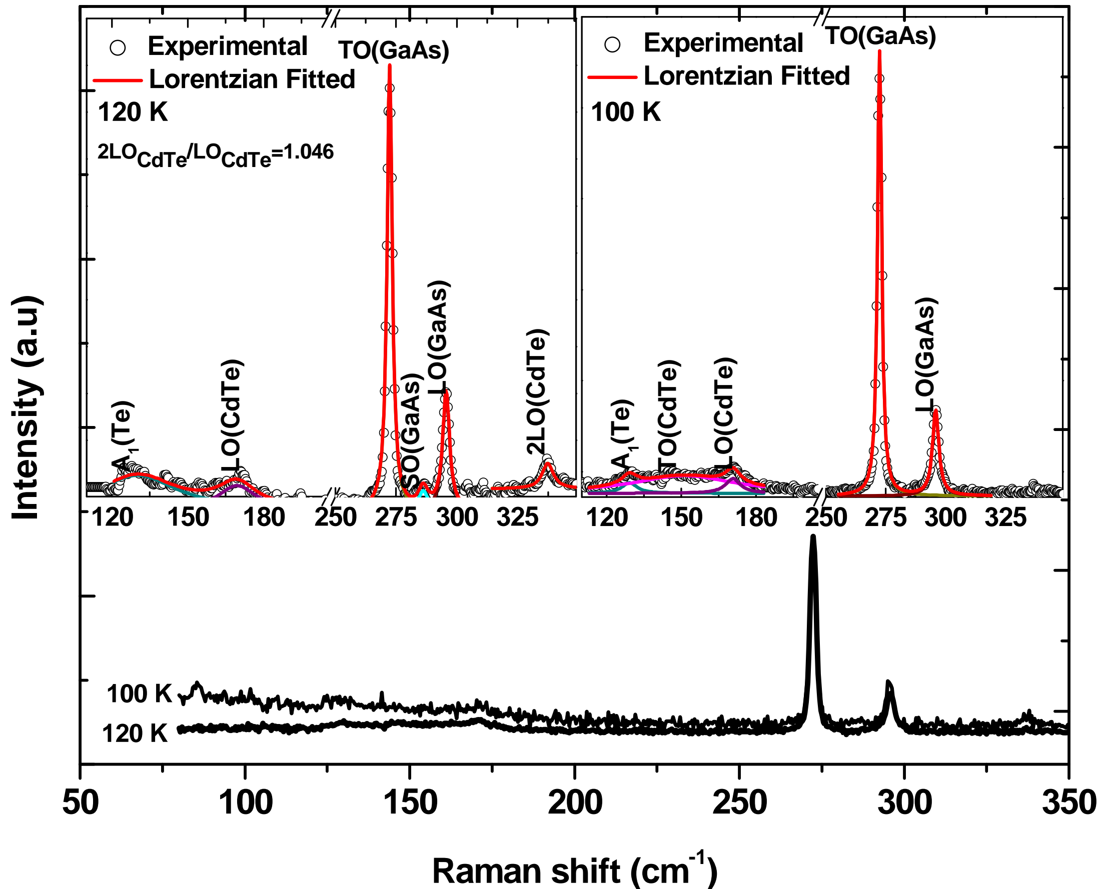

Figure 5.28. The whole range Raman spectra of CdTe23 at 120 K and 100 K. The insets show experimentally obtained and Lorentzian fitted Raman spectra at 120 K and 100 K.

The whole range experimentally obtained and Lorentzian fitted curves Raman spectra of CdTe23 at 80 K are given in Figure 5.29. Likely to Raman spectrum of sample at 100 K, second order LO phonon mode of CdTe layer couldn't observed at 80 K. The most dominant Raman active modes are belonging to GaAs that TO phonon mode of GaAs observed at 273.17 cm^{-1} (FWHM; 0.87 cm^{-1}) and GaAs-related LO phonon mode observed at 296.53 cm^{-1} (FWHM; 1.48 cm^{-1}). CdTe-like TO and LO phonon modes observed at 146.65 cm^{-1} and 172.17 cm^{-1} with FWHM values of 1.69 cm^{-1} and 2.12 cm^{-1},

respectively. The band at 129.20 cm^{-1} attributed to A_1 symmetry mode of Te that Te-specific E-symmetry mode could not observed at 80 K.

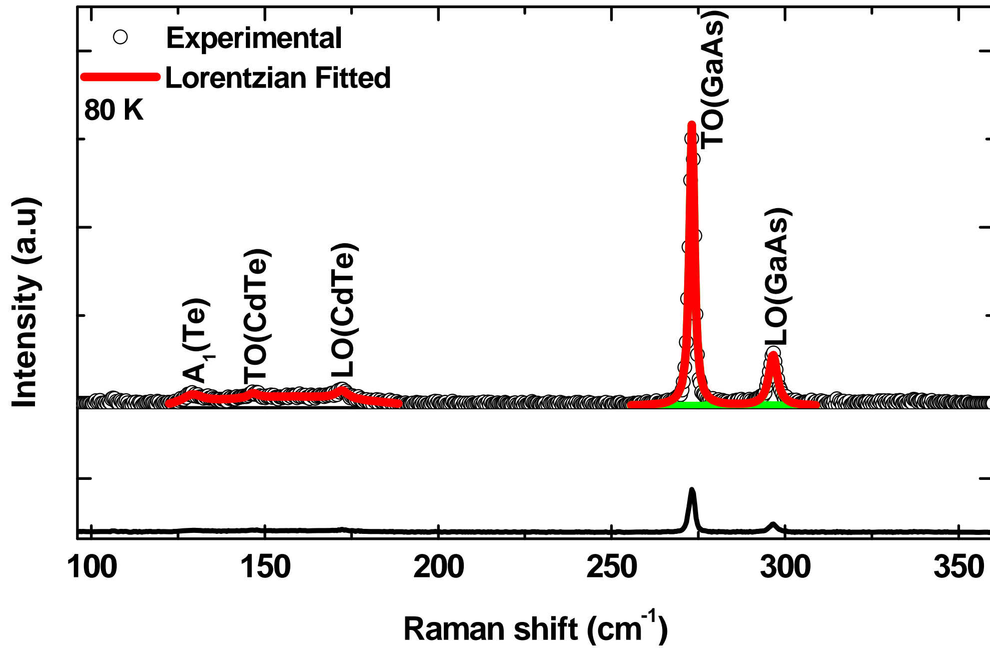

Figure 5.29. Expeimentally obtained and Lorentzian fitted the whole range Raman spectra of CdTe23 at 80 K.

Temperature dependent Raman spectra and the normalized Raman spectra to first-order CdTe-like LO phonon mode of CdTe24 sample are given in Figure 5.30 and Figure 5.31, respectively. GaAs-related phonon modes were not observed for CdTe24 sample. Likely to sample CdTe18, the intensity of the second-order CdTe-like LO phonon mode increases as temperature decreases. As clearly seen, the first order Raman active modes of CdTe and Te-specific modes forms a broad peak at lower temperatures. CdTe-like first order TO phonon mode observed at 143.19 cm^{-1} at room temperature and it shifted to lower frequency by 1.66 cm^{-1} for 250 K and shifted to higher frequencies respectively by 1.65 cm^{-1}, 2.07 cm^{-1}, 2.9 cm^{-1}, 2.48 cm^{-1} and 1.24 cm^{-1} for 200 K, 150 K, 120 K, 100 K, 80 K.

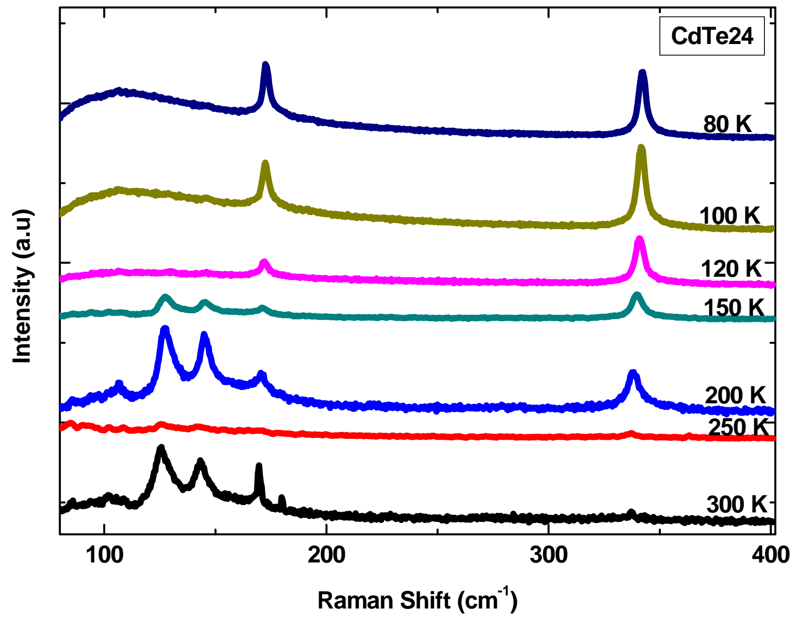

Figure 5.30. Temperature dependent Raman spectra of CdTe24 sample under 488 nm excitation.

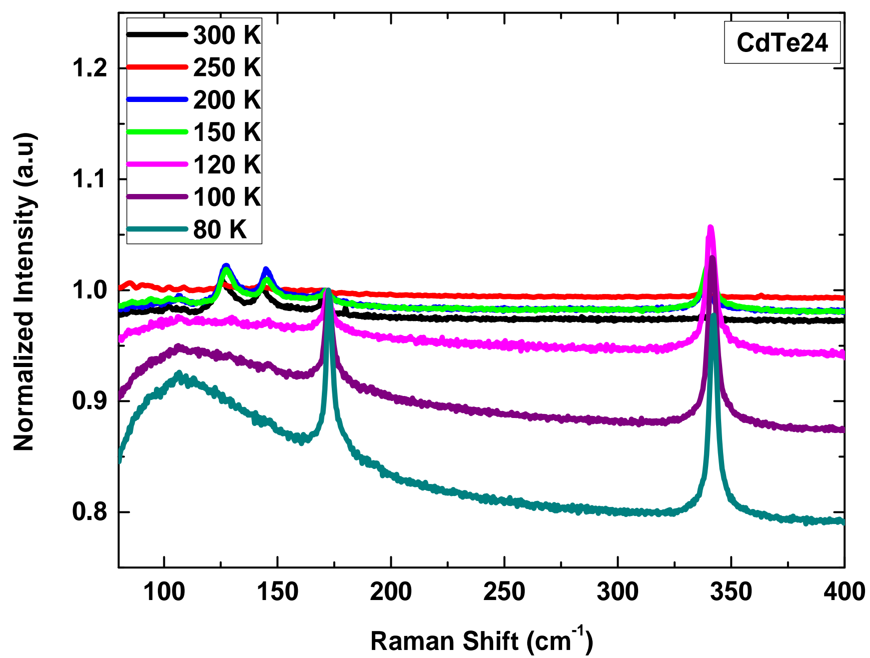

Figure 5.31. Raman scattering spectra of CdTe24 at various temperatures. The spectra were normalized to first-order TO phonon mode of CdTe.

First order and second order LO Raman active modes observed respectively at 169.61 cm^{-1} and 337.09 cm^{-1} at 300 K. 2LO phonon mode position stayed constant at 250 K, but it shifted to 338.31 cm^{-1}, 339.52 cm^{-1}, 340.73 cm^{-1}, 341.54 cm^{-1}, 342.34 cm^{-1} at 200 K, 150 K, 120 K, 100 K and 80 K, respectively.

The band at 125.80 cm^{-1} attributed to A_1 symmetry mode which is also shifted to higher frequencies by 1.66 cm^{-1}, 1.67 cm^{-1}, 4.15 cm^{-1}, 2.91 cm^{-1} at 200 K, 150 K, 120 K and 100 K and shifted to lower frequency by 0.41 cm^{-1} at 250 K. Te-specific A_1 symmetry mode at 80 K could not obtained experimental data.

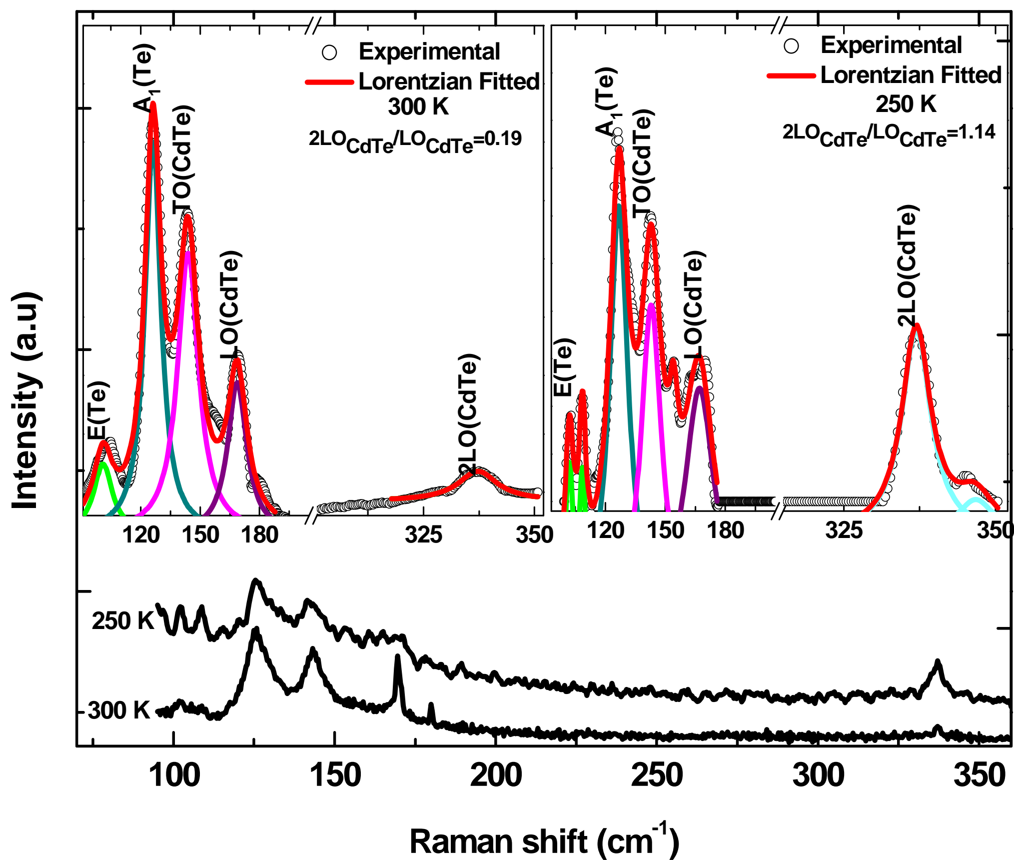

Figure 5.32. The whole range Raman spectra of CdTe24 at 300 K and 250 K. The insets show experimentally obtained and Lorentzian fitted Raman spectra at 300 K and 250 K.

The whole range compared and Lorentzian fitted Raman spectra of CdTe24 sample at 300 K and 250 K are given in Figure 5.32. As clearly seen, the intensity of Raman active modes of CdTe and Te-related modes decreases as measurement

temperature decreases. However, overtone of CdTe-like LO phonon mode intensity increases when temperature was decreased to 250 K. 2LO phonon mode of CdTe observed at 337.22 cm^{-1} (FWHM; 5.39 cm^{-1}) at room temperature and it shifted to 336.94 cm^{-1} (FWHM; 2.92 cm^{-1}) at 250 K. An additional peak observed as a shoulder of 2LO phonon mode at 346.73 cm^{-1}, but the origin of this peak couldn't understood. The first-order TO and LO phonon modes observed at 143.93 cm^{-1} and 168.74 cm^{-1} with FWHM values of 6.44 cm^{-1} and 5.89 cm^{-1} at 300 K, respectively. TO Raman active mode shifted to a higher frequency by 10.18 cm^{-1} and LO phonon mode shifted to a lower frequency by 1.63 cm^{-1} at 250 K. A_1 symmetry mode of Te observed for two temperatures with high intensities at 126.22 cm^{-1} (300 K) and 126.76 cm^{-1} (250 K). Unlikely to CdTe18 and CdTe23 samples, E-symmetry mode splitted into two peaks at 250 K which observed at 102.09 cm^{-1} (FWHM; 2.69 cm^{-1}) and 108.59 cm^{-1} (FWHM; 2.09 cm^{-1}). At 300 K, E-symmetry mode broadened at 101.04 cm^{-1} with FWHM value of 5.88 cm^{-1}. The 2LO/LO intensity ratio calculated as 0.19 and 1.14 at 300 K and 250 K.

The whole range experimentally obtained and Lorentzian fitted curves Raman spectra of CdTe24 at 200 K and 150 K are given in Figure 5.33. Likely to Raman spectrum at 250 K, E-symmetry mode splitted into two peaks one at 101.99 cm^{-1} (FWHM; 2.68 cm^{-1}) and the other at 107.86 cm^{-1} (FWHM; 3.14 cm^{-1}) at 150 K. This peak was observed as a single broad peak at 106.48 cm^{-1} with FWHM value of 6.99 cm^{-1} at 200 K. The peak at 127.93 cm^{-1} (FWHM; 4.88 cm^{-1}) attributed to A_1 symmetry mode of Te at 200 K and it became sharper and shifted to 127.85 cm^{-1} (FWHM; 3.61 cm^{-1}) at 150 K. Raman active CdTe-like TO phonon mode observed at 145.64 cm^{-1} and 145.80 cm^{-1} for 200 K and 150 K measured temperatures. At 200 K, CdTe-like LO phonon mode broadened at 168.81 cm^{-1} with FWHM value of 11.22 cm^{-1} with respect to 150 K measurement temperature. At 150 K, LO phonon mode of CdTe shifted to 170.21 cm^{-1} with FWHM of 6.78 cm^{-1}. In addition, 2LO phonon mode observed at 338.39 at 200 K and it shifted to a higher frequency by approximately 1.49 cm^{-1} at 150 K. At 150 K, the intensity of second-order LO phonon mode increased with respect to Raman spectrum at 200 K. The intensity ratio of 2LO and LO found by fitted curves as 1.25 and 3.48 at 200 K and at 150 K, respectively.

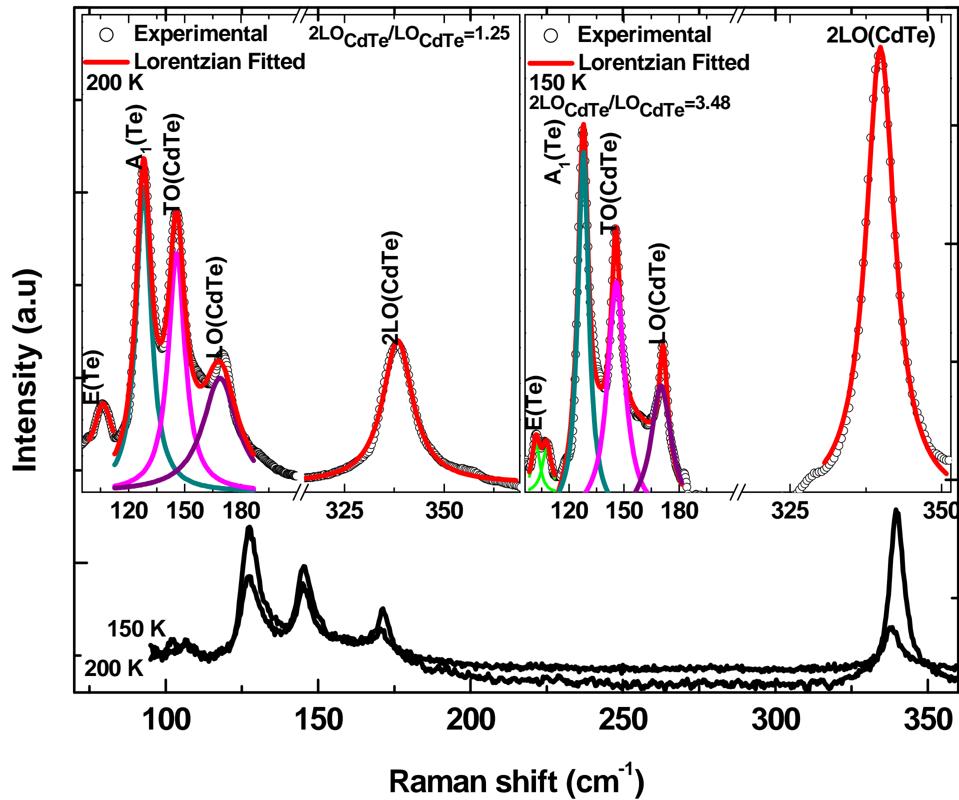

Figure 5.33. The whole range Raman spectra of CdTe24 at 200 K and 150 K. The insets show experimentally obtained and Lorentzian fitted Raman spectra at 200 K and 150 K.

The compared Raman spectra of CdTe24 sample at 120 K and 100 K are given in Figure 5.34. As seen in the Figure, at 100 K, Te specific modes and TO Raman active mode of CdTe are completely broadened and the intensity of first-order LO phonon mode of CdTe increased with respect to 120 K. Te-related A_1 and E symmetry modes observed in both Raman spectrum. E-symmetry mode observed at 106.48 cm^{-1} (FWHM; 6.99 cm^{-1}) at 120 K which shifted to a higher frequency by 0.76 cm^{-1} (FWHM; 7.02 cm^{-1}) at 100 K. The peak at 125.95 cm^{-1} with FWHM of 13.19 cm^{-1} attributed to A_1 symmetry mode of Te at 120 K which broadened with 21.38 cm^{-1} FWHM value and shifted to 125.72 cm^{-1} at 100 K. Raman active CdTe-like TO phonon mode observed at 147.68 cm^{-1} and 146.49 cm^{-1} for 120 K and 100 K measured temperatures. First-order and second order LO phonon modes of CdTe layer were observed at 172.17 cm^{-1} (FWHM; 2.84 cm^{-1}) and 341.06 cm^{-1} (FWHM; 2.59 cm^{-1}) at 120 K, respectively. LO phonon mode of CdTe shifted to a higher frequency by 0.99 cm^{-1} with 2.00 cm^{-1} FWHM value at 100 K. 2LO phonon mode of CdTe also shifted to 341.69 cm^{-1} with FWHM value of 2.17 cm^{-1} at 100 K. The

intensity ratio of 2LO and LO were found by fitted curves as 3.17 and 1.87 at 120 K and 100 K, respectively.

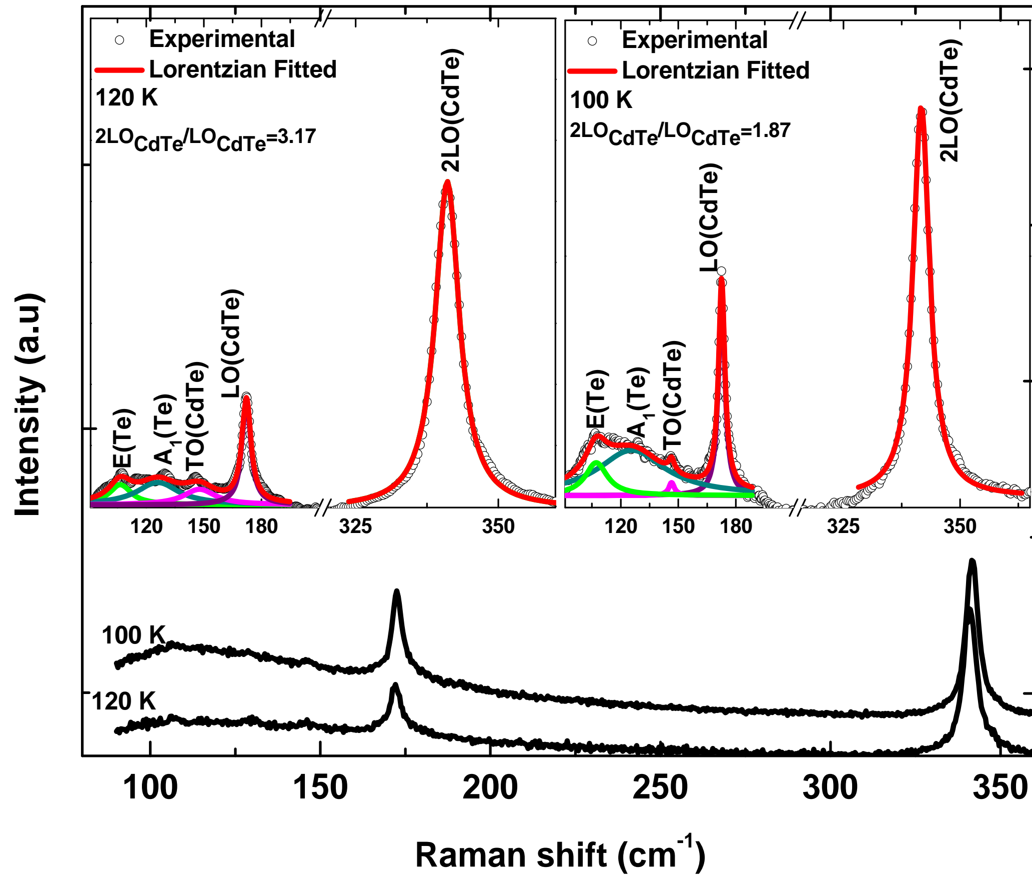

Figure 5.34. The whole range Raman spectra of CdTe24 at 100 K and 120 K. The insets show experimentally obtained and Lorentzian fitted Raman spectra at 100 K and 120 K.

Lorentzian fitted and experimentally obtained Raman spectrum of CdTe24 at 80 K is shown in Figure 5.35. As seen in Raman spectrum, Te specific modes and first order TO phonon mode of CdTe were observed as a broad peak that they became observable with Lorentzian fitting. The peaks at 106.31 cm^{-1} (FWHM; 10.40 cm^{-1}) and 122.12 cm^{-1} (FWHM; 13.95 cm^{-1}) attributed to E and A_1-symmetry modes of Te, respectively. First order LO phonon mode was observed at 172.88 cm^{-1} (FWHM; 1.69 cm^{-1}) and the overtone of LO phonon mode observed at 342.19 cm^{-1} (FWHM; 2.00 cm^{-1}). The band at 140.44 cm^{-1} with FWHM value of 8.72 cm^{-1} attributed to first order TO phonon mode of

CdTe at 80 K. 2LO/LO ratio calculated using Lorentzian fitting results and found as 1.27 at 80 K.

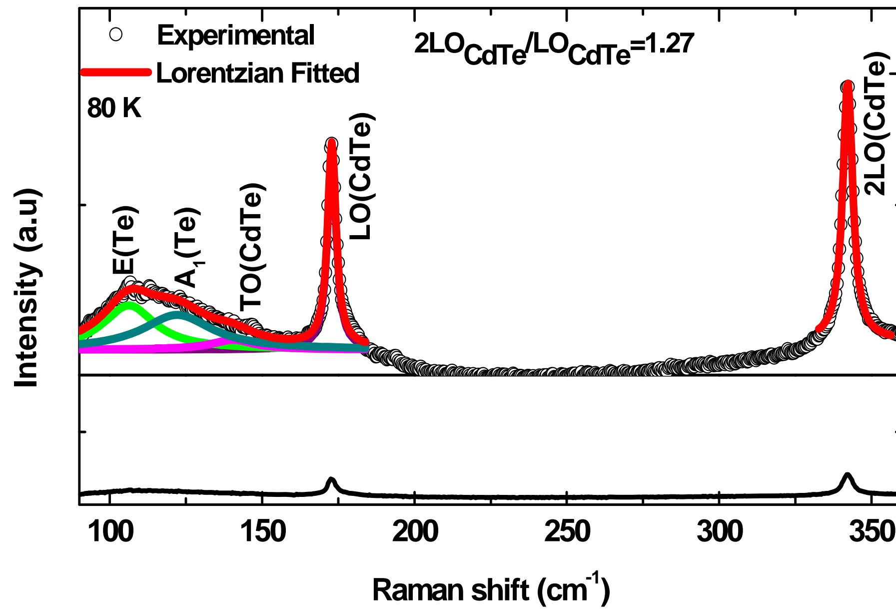

Figure 5.35. Experimentally obtained and Lorentzian fitted the whole range Raman spectra of CdTe24 at 80 K.

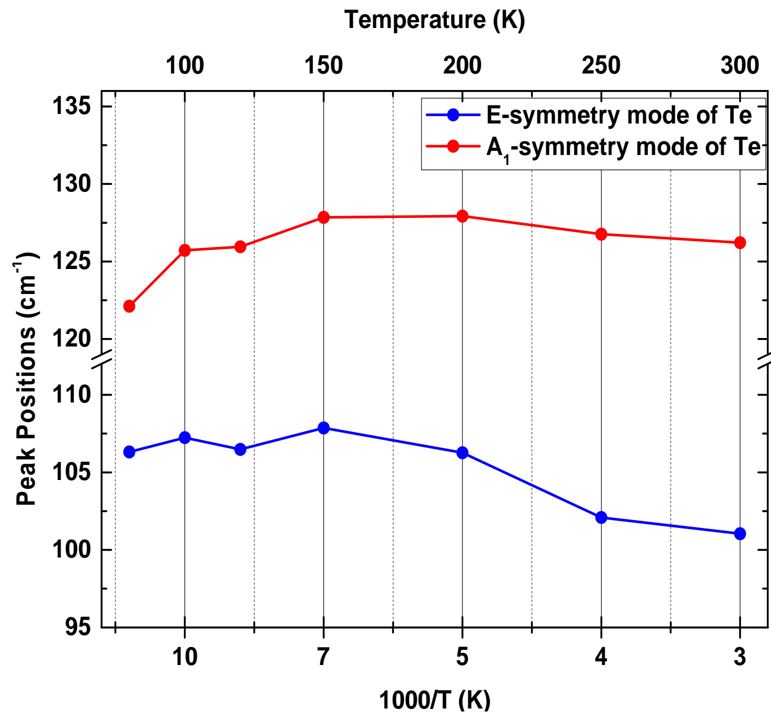

Figure 5.36. Variation of Te specific E-symmetry and A_1-symmetry modes with the temperature for CdTe24 sample.

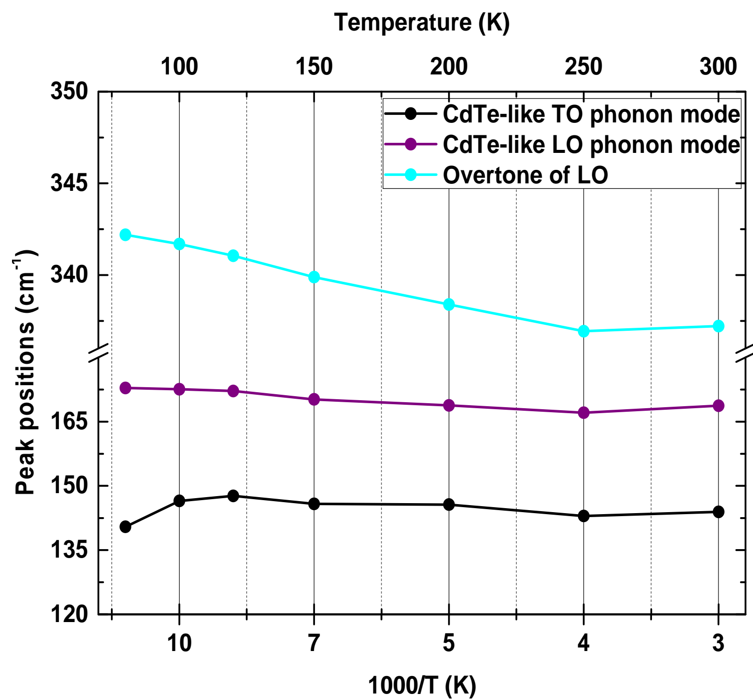

Figure 5.37. The change of CdTe-like TO, LO and 2LO phonon modes depending on the temperature for CdTe24 sample.

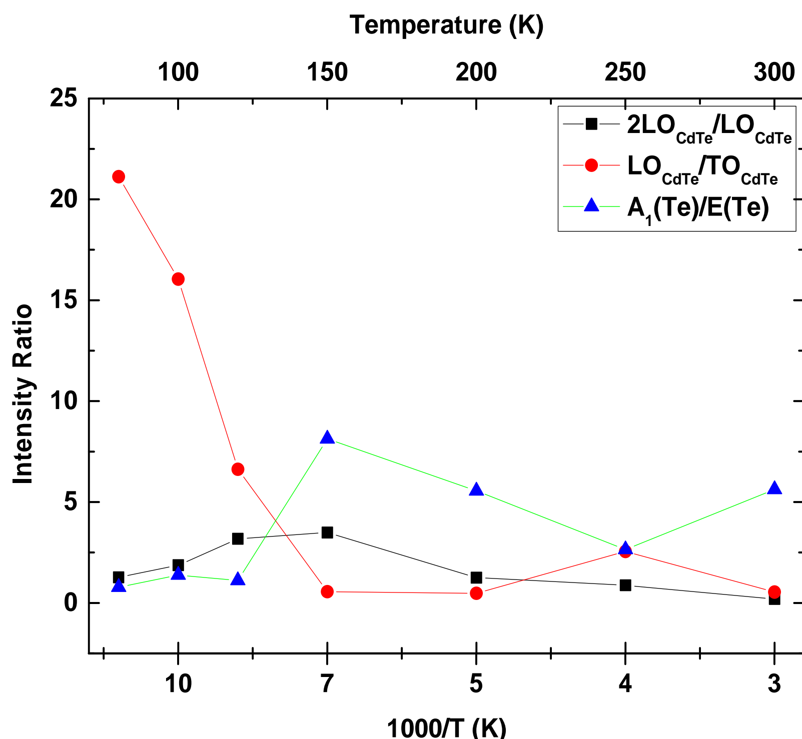

Figure 5.38. The change of calculated intensity ratios of observed phonon modes for CdTe24 sample

5.3. Dislocation Density Analysis

Etch pit formation and assessment is a major way to determine crystal quality of epitaxial films which gives a clear observation of dislocations per unit area, hence it is called Etch Pit Density (EPD). Etch pit formation is also referred as dislocation decoration etch and produces various geometrical shapes on the surface such as triangular, wedge shaped, fish shaped and others which gives information about the type of the dislocation [209, 210]. The etch pits are formed near dislocations, because the etch velocity is higher near the dislocation due to strain field of dislocation than the other parts. Etch pit geometry and the etch rate depend on the film orientation and the thickness [211]. It is important for pits to be in adequate size to be easily observed by optical means which can be controlled by etching time and etch rate.

There are many reported defect etching methods for Cd-based compounds such as Inoue, Everson, Nakagawa, Benson, Chen and Hahnert-Shenk, Schaake. Everson defect decoration technique was first developed by W. J. Everson and based on hydrofluoric acid, nitric acid and lactic acid mixtures [212]. It was reported that Everson method

produces successful dislocation decorations on both (111) and (211) planes [212, 213]. Nakagawa solution is hydrofluoric acid and hydrogen peroxide based which was first reported by Nakagawa and co-workers. Unlikely to Everson, Nakagawa and Inoue methods was useful for (111)A face which are generally used for polarity determination [214, 215]. Inoue solutions divided into two categories as E-Ag1 and E-Ag2 depending on the concentration of silver solution that both of them consists of acidic solutions of potassium dichromate [215]. Benson method was developed in early 2008 by Benson who reported that successful pits can be formed with smooth surface. Benson etch contains the mixture of hydrochloric, hydrofluoric, nitric and chromic acids which diluted by deionized water [216]. On the other hand, Chen technique consists of the mixture of nitric and hydrochloric acids containing potassium dichromate which produces pits on (110), (100), (111)A and (111)B planes [217]. Hahnert-Shenk method described by Chen and also Hahnert and Shenk which consists of hydrofluoric acid instead of nitric acid and produces pits on (111)A, (111)B, (110) and (511) surfaces [218].

In this work; Everson and Benson defect decoration techniques were used in varying volume ratios and implementation times to obtain the dislocation distribution across the CdTe films and to determine the densities of dislocations of the MBE grown CdTe/GaAs (211)B epitaxial films. The number etch pits were counted manually and the dislocation density of CdTe films calculated per unit. Nomarski phase-contrast microscopy, scanning electron microscopy (SEM) and atomic force microscopy (AFM) were used to evaluate surface morphologies of Everson and Benson etched CdTe/GaAs (211)B films. The sizes of the etch pits were determined via both AFM and SEM techniques. Etch depths were determined by AFM profile analysis in tapping mode. EDX analysis were also performed to obtain elemental analysis of etch pits. Etchant solutions with volume ratios and implementation times are summarized in Table 5.3. All mixtures were prepared in polypropylene beakers and etches were performed at room temperature in class-100 cleanroom environment and followed by rinsing immediately deionized water and dried by N_2 blower.

Table 5.3. Chemical composition, volume ratios, implementation times of performed defect decoration methods.

Sample IDs	Method and Chemical Composition	Volume Ratios	Etch Times (s)
CdTe18-1	Everson ($HF:HNO_3$:Lactic acid)	0.5:4:25	30
CdTe18-2		1:4:50	40
CdTe18-3		1:4:25	30
CdTe23-1	Everson $HF:HNO_3$:Lactic acid	0.5:4:25	30
CdTe23-2		1:4:50	40
CdTe23-3		1:4:25	30
CdTe23-4		1:4:25	60
CdTe23-5	Benson ($H_2O:HF:HCl:HNO_3:CrO_3$)	300ml:10ml:10ml:10ml:8g	10
CdTe24-1	Everson ($HF:HNO_3$:Lactic acid)	0.5:4:25	30
CdTe24-2		1:4:50	40
CdTe24-3		1:4:25	20

As seen in Table 5.3, CdTe18 sample etched by Everson dislocation decoration methods in various ratios and implementation times to reveal dislocations on the sample surface. SEM micrograph, AFM 2D and 3D topographic images and profile analyses of Everson etched ($0.5HF:4HNO_3$:25Lactic acid) CdTe18-1 sample are given in Figure 5.39.

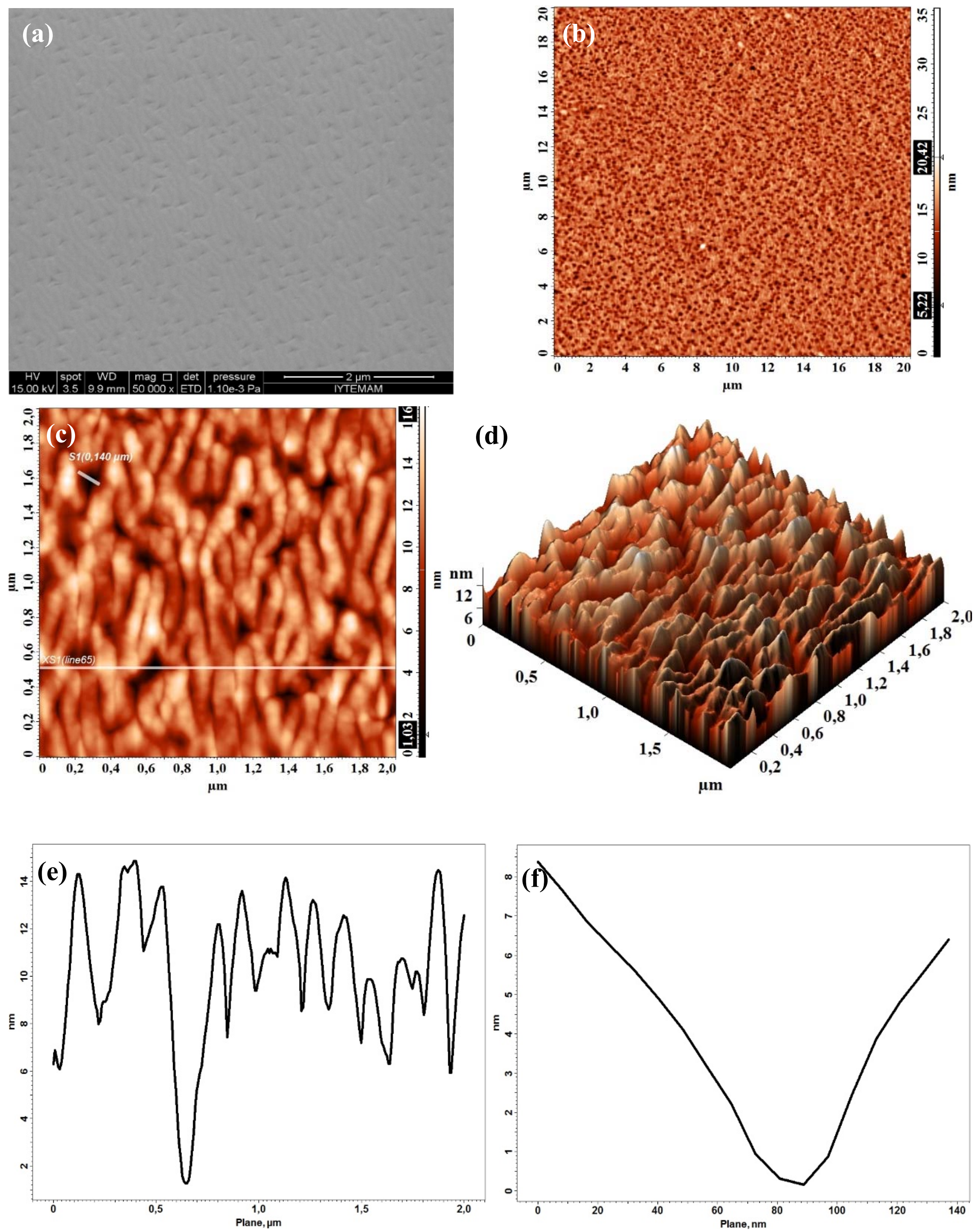

Figure 5.39. (a) SEM micrograph with 50 000 magnifications, (b) and (c) are AFM 2D Topographic image from 20x20 μm^2 and 2x2 μm^2 scanned areas, (d) AFM 3D Topographic image and (e) and (f) are profile line analysis of XS1 (line 65) and S1 line of 0,140 µm width of Everson defect decorated CdTe18-1 sample.

SEM micrograph and AFM topographic images of CdTe18-1 sample showed that the etch pits formed with a triangular shape which have approximately 0.14 μm width and the measured etch depth was 12 nm. The measured RMS roughness of CdTe18 sample was reduced to 2.05 nm, after the Everson decoration method was performed for 30 s. However, the size of pit features were not large enough to observe with Nomarski microscope (Figure 5.43) that pits are only seen as small dots on the surface of CdTe film. Etch pit density (EPD) of Everson etched CdTe18-1 sample determined from SEM image and found as 8.8×10^{8} cm^{-2}.

In order to obtain larger size pits, implementation time of Everson etch was increased to 40 s, and the volume ratio of the mixture was also changed to 1HF:4HNO_3:50Lactic acid. The AFM 2D and 3D topographic images of 10x10 μm^2 and 2x2μm^2 scanned areas and profile analyses are given in Figure 5.40, after the Everson decoration method was performed on the sample. The RMS roughness of sample CdTe18-2 was increased to 3.47 nm in comparison with CdTe18-1. Triangular shapes of pits became clear with approximately 0.16 μm size and 18 nm depth. SEM images of the sample CdTe18-2 showed that twinned-triangular shapes was formed on the some parts of the sample (Figure 5.41).

The calculated width of twinned-triangular shapes reach the size of 3 μm. Elemental EDX analyses were also performed on twinned pits, atomic and weight percentages of Cd, Te, Ga and As elements are listed in Figure 5.41 for selected areas of both regular and pit formed on the sample. EDX analyses showed that atomic percentages of Ga and As elements increased as expected. However, it can be predicted that the etch depths of pits are low for twinned-triangular shapes due to the small amount of increment of Ga and As elements with respect to regular surface. EPD value for CdTe18-2 sample increased to 9.2×10^{8} cm^{-2} with increasing HF and Lactic acid volume ratios and also implementation time.

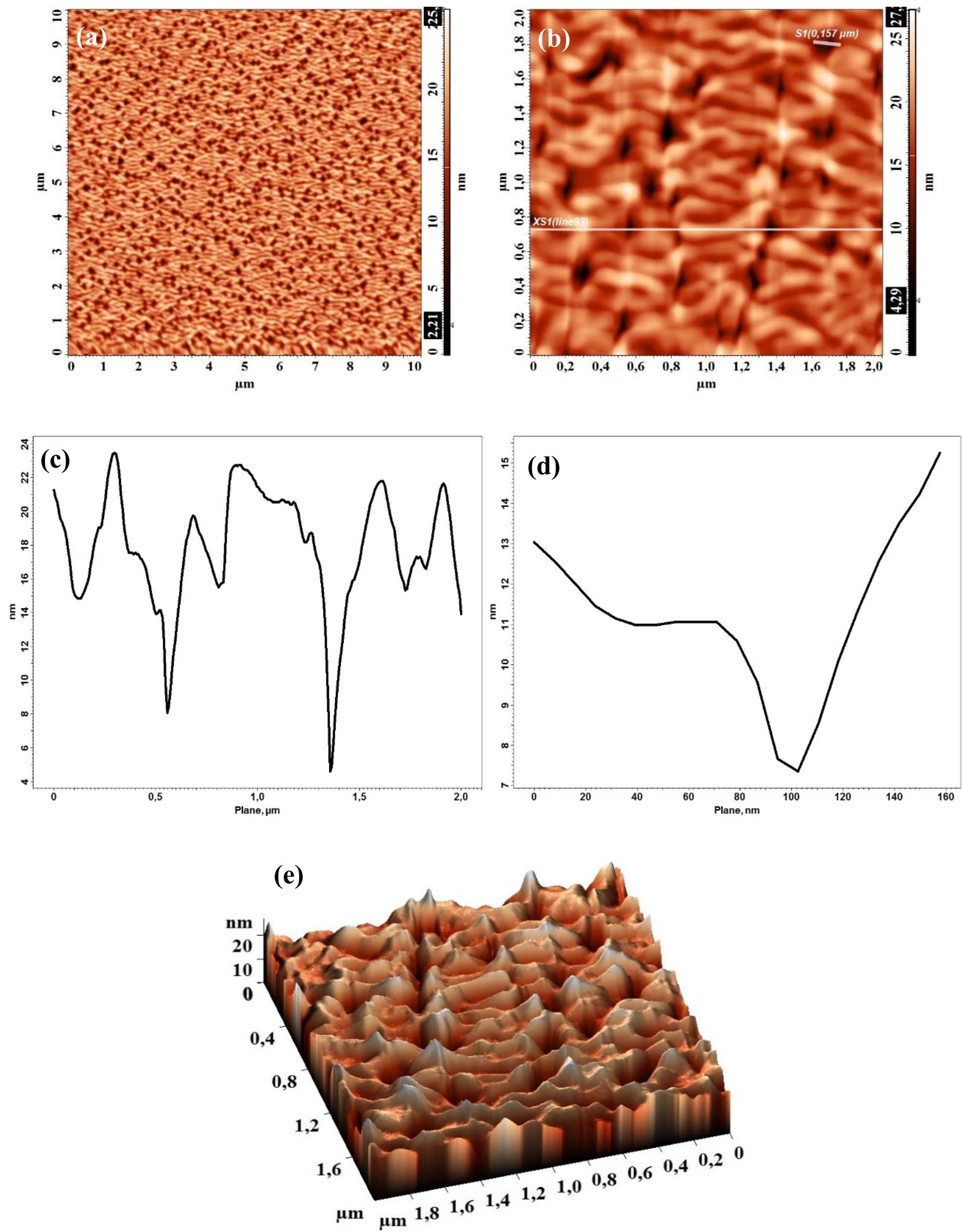

Figure 5.40. (a) and (b) are AFM 2D Topographic image from 20x20 µm^2 and 2x2 µm^2 scanned areas, (e) AFM 3D Topographic image and (c) and (d) are profile line analysis of XS1 (line 93) and (d) S1 line of 0,157 µm width of Everson defect decorated CdTe18-2 sample.

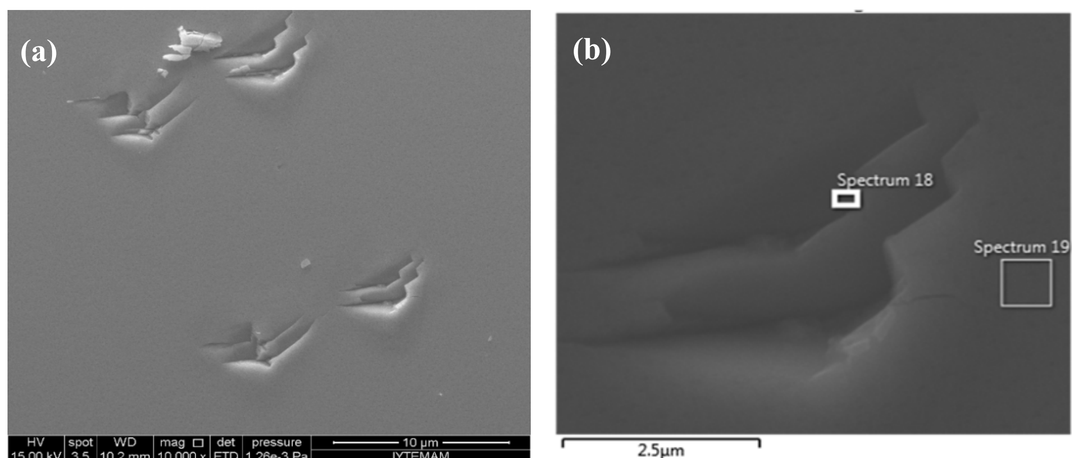

Element	Weight %	Atomic %
Spectrum 18		
Cd	45.36	45.72
Te	46.75	41.50
Ga	7.50	12.19
As	0.39	0.59

Element	Weight %	Atomic %
Spectrum 19		
Cd	45.41	46.66
Te	49.35	44.66
Ga	5.24	8.68
As	0.00	0.00

Figure 5.41. SEM micrographs of sample CdTe18-2 with 10 000 and 2500 magnifications where spectra show the region that EDX analysis were performed in SEM image and the tables show the percentage distributions of Cd, Te, Ga and As in spectrum 18 and 19.

AFM 2D and 3D topographic images and SEM micrograph with 100 000 magnification of Everson etched sample CdTe18-3 with 1HF:4HNO_3:25Lactic acid for 30 s are shown in Figure 5.42. As clearly seen from SEM micrograph and AFM profile analyses, triangular shapes could not observed due to short implementation time of 30 s and reduced volume ratio of lactic acid of 25 in comparison with sample CdTe18-2. Particules developed on the sample surface with heights of 6 nm which can be associated with undeveloped defect decorations. Pits were shallow with approximately 2 nm depths and the surface was smooth with 1.56 nm RMS roughness.

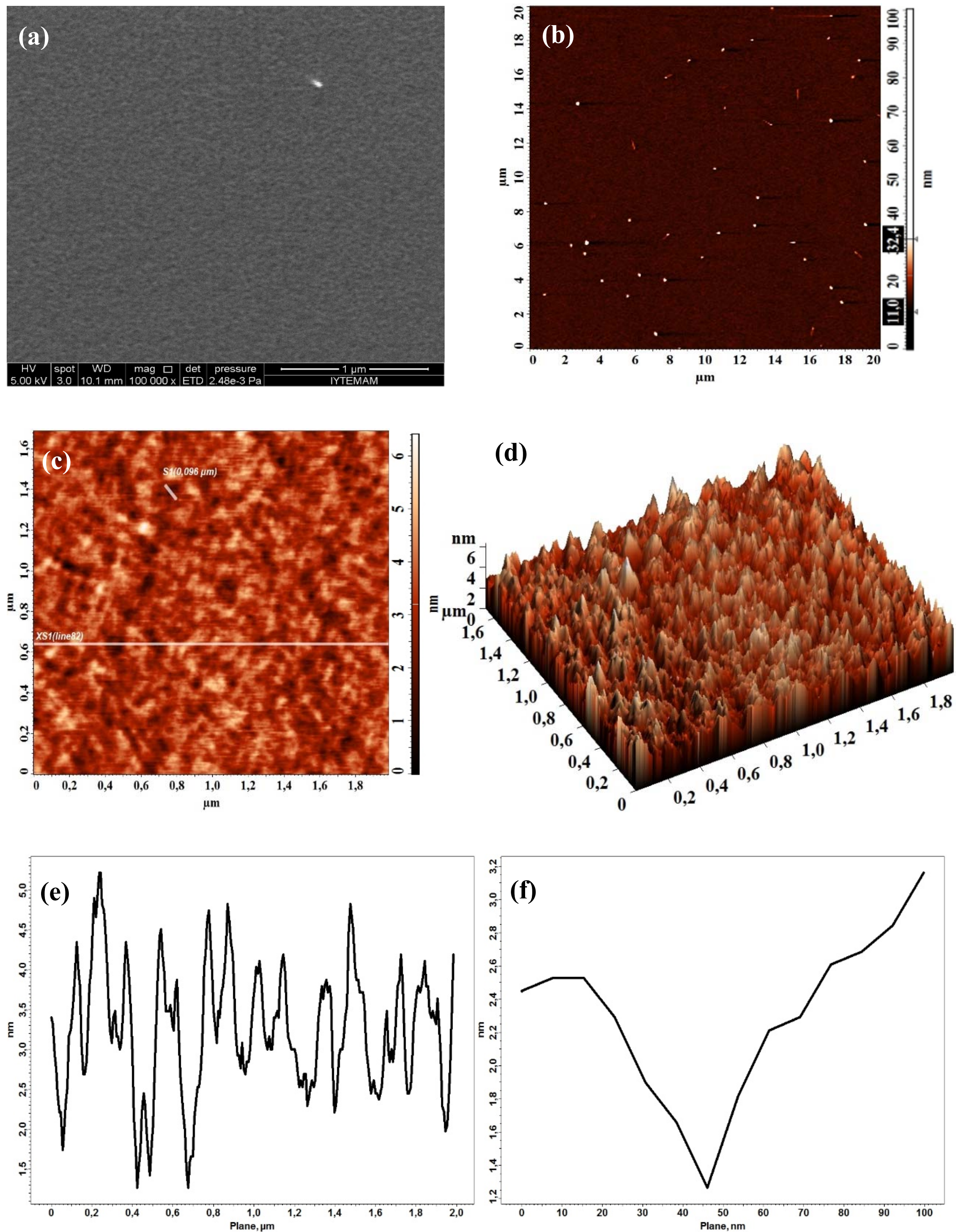

Figure 5.42. (a) SEM micrograph with 100 000 magnifications, (b) and (c) are AFM 2D Topographic image from 20x20 µm^2 and 2x1.7 µm^2 scanned areas, (d) AFM 3D Topographic image and (e) and (f) are profile line analysis of XS1 (line 82) and S1 line of 0,096 µm width of Everson defect decorated CdTe18-3 sample.

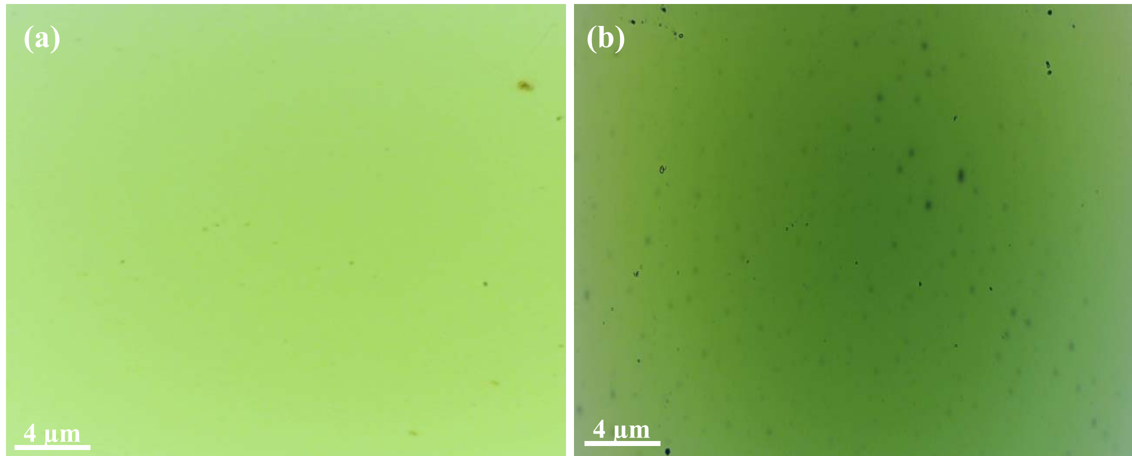

Figure 5.43. Nomarski images of CdTe18 sample (a) before dislocation decoration and (b) after Everson etch with 0.5HF+4HNO3+25Lactic acid mixture during 30 s.

CdTe23 sample etched by Everson dislocation decoration methods in various ratios and implementation times to reveal dislocations on the surface. In addition, Benson etch technique was performed to confirm Everson EPD measurements. SEM micrograph, AFM 2D and 3D topographic images and profile analyses of Everson etched CdTe23-1 sample are given in Figure 5.44. SEM micrograph and AFM topographic images clearly shows that Everson dislocation decoration technique with 0.5HF:4HNO_3:25Lactic acid volume ratios and 25 s implementation time did not formed observable etch pits on the surface.

Pits on the surface were not distributed homogenously across the surface and reached maximum depth of only 1.5 nm. The RMS roughness value increased to 1.36 nm after Everson etch. However, despite low RMS roughness value, the CdTe23-1 sample surface did not show a smooth surface characteristic. AFM profile analyses showed that particules formed on the surface with approximately 2 nm heights.

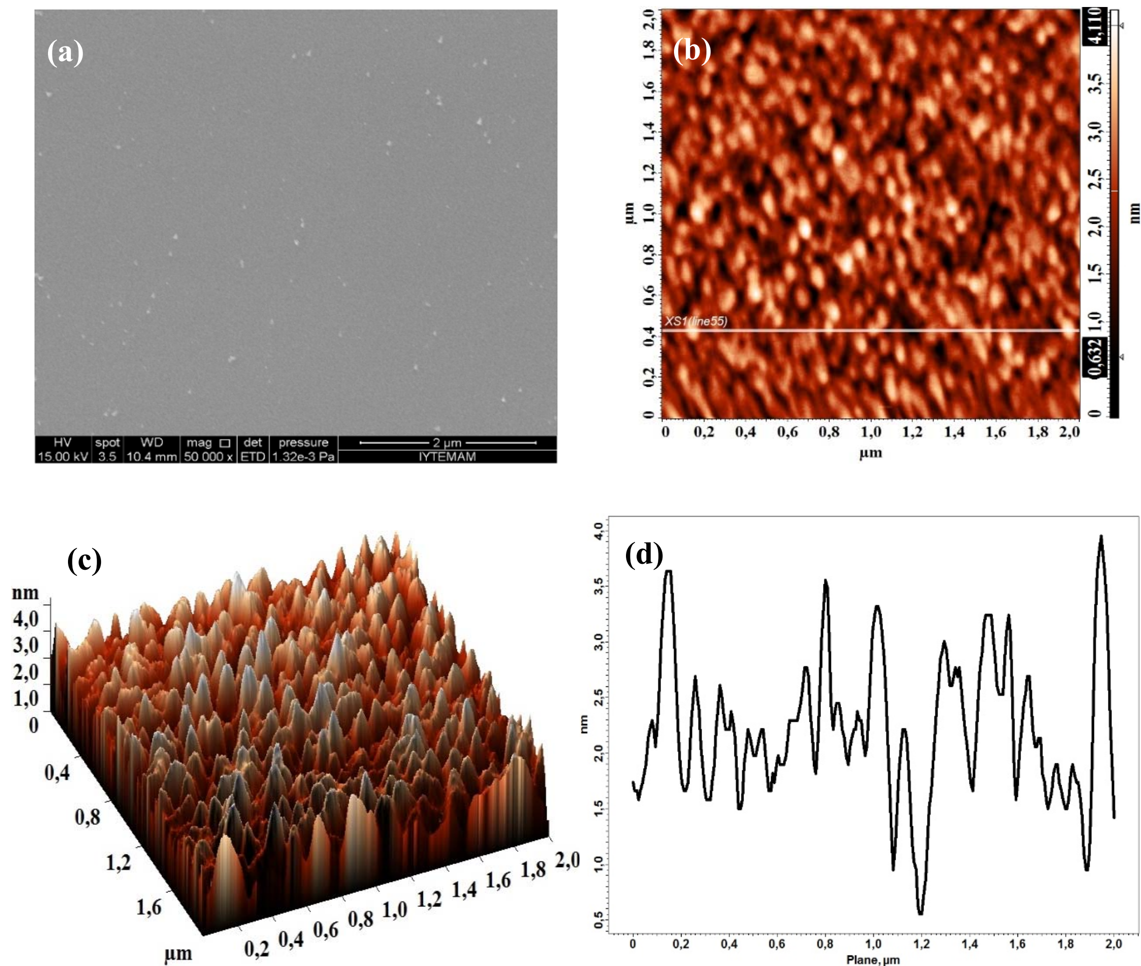

Figure 5.44. Everson etched CdTe23-1 sample of (a) SEM micrograph with 50 000 magnification, (b) AFM 2D Topographic image, (c) AFM 3D Topographic image and (d) Profile line analyse of XS1 (line 55).

In order to obtain etch pits related to threading dislocations, implementation time of Everson etch was increased to 40 s, and the volume ratio of the mixture was also changed to 1HF:4HNO_3:50Lactic acid for sample CdTe23-2. The AFM 2D and 3D topographic images of CdTe23-2 sample for scanned 10x10 µm^2 and 2x2µm^2 scanned areas and profile analyses were given in Figure 5.45. The RMS roughness of sample CdTe23-2 was decreased to 0.68 nm with respect to CdTe23-1. Likely to CdTe23-1, the Everson etch technique was not successful despite changing volume ratios and implementation times of etchant. However, the etch pits became to distribute homogenously with approximately 2 nm depths and 0.13 µm widths.

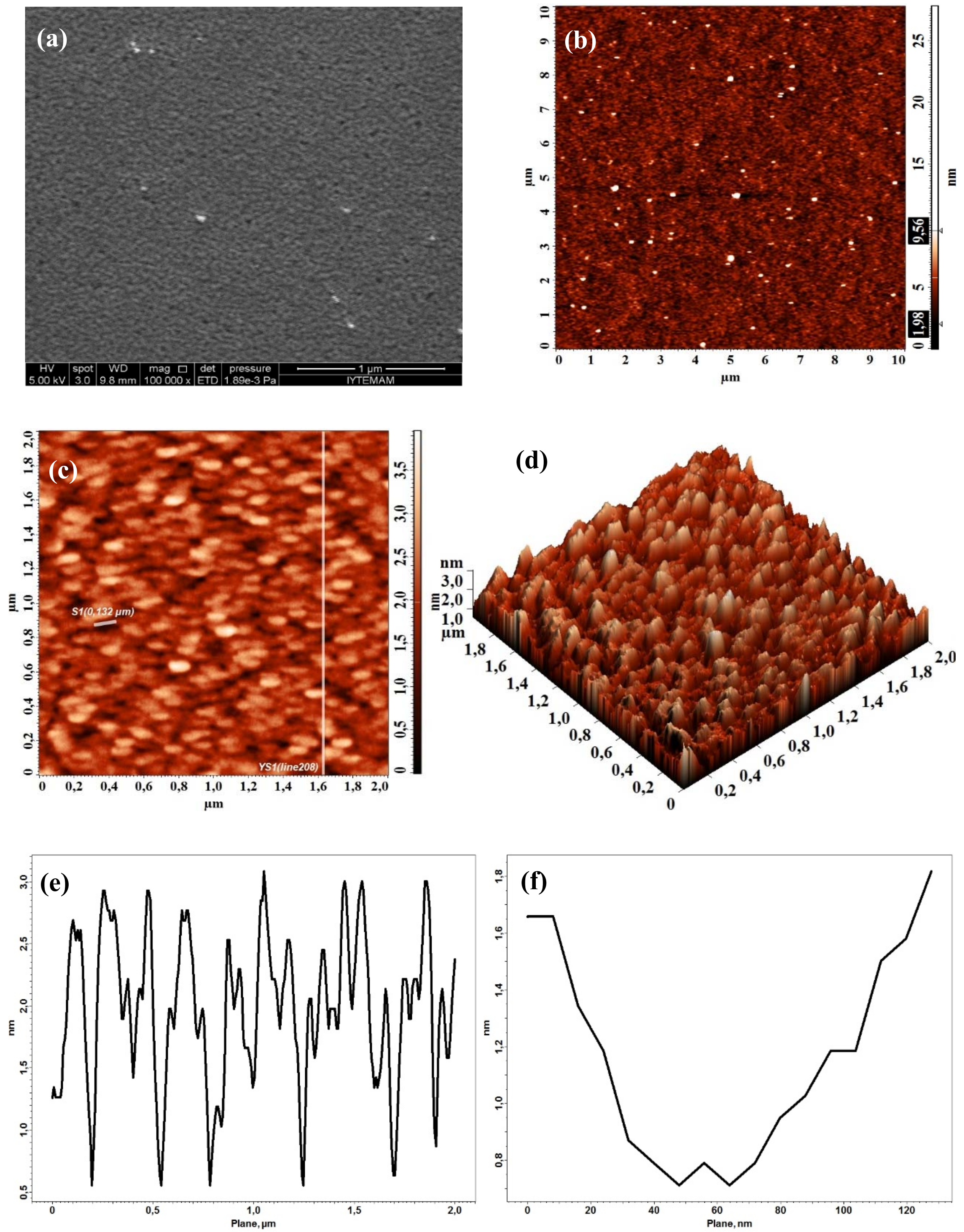

Figure 5.45. Everson etched CdTe23-2 sample of (a) SEM micrograph with 100 000 magnification, (b) and (c) are AFM 2D Topographic images, (c) AFM 3D Topographic image, (d) Profile line analyses of YS1 (line 208) and (e) S1 line of 0,132 µm width.

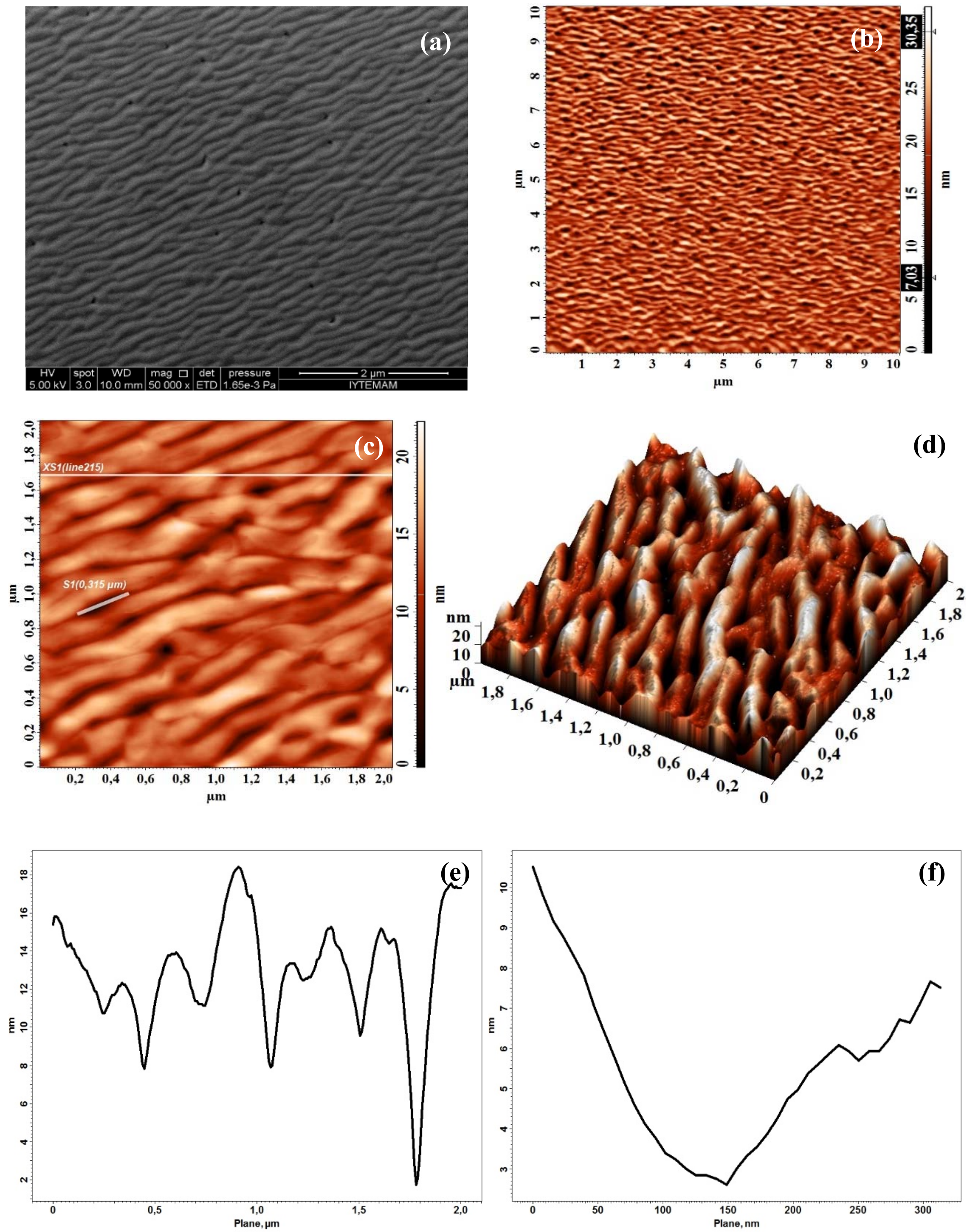

Figure 5.46. (a) SEM micrograph with 50 000 magnification, (b) and (c) are AFM 2D Topographic images, (d) AFM 3D Topographic image, (e) Profile line analyses of XS1 (line 215) and (f) S1 line of 0,315 µm width of Everson etched CdTe23-3 sample.

The AFM 2D and 3D topographic images for scanned 10 μm^2 and 2 μm^2 scanned areas and profile analyses were given in Figure 5.46 for sample CdTe23-3. This time, the

mixture performed for 30 s and the volume ratio of Everson etchant changed to 1HF:4HNO_3:25Lactic acid. The RMS roughness of sample CdTe23-3 was increased to 2.01 nm with respect to CdTe23-1 and CdTe23-2 samples. As clearly seen in SEM image of sample, small triangular-like shapes with approximately 0.32 μm widths and approximately 8-10 nm depths formed on the sample surface. EPD value for this sample found 5.3 x 10^7 cm^{-2} which is our best result threading dislocation density value within all CdTe samples.

In order to obtain larger-size pits, implementation time of Everson etch was increased to 60 s for sample CdTe23-4. The RMS roughness value was measured as 1.68 nm which was decreased in comparison with CdTe23-3 sample.However, triangular shapes were not observed via SEM micrography, AFM 2D topographic imaging and Nomarski microscopy (Figure 5.47 and Figure 5.48).

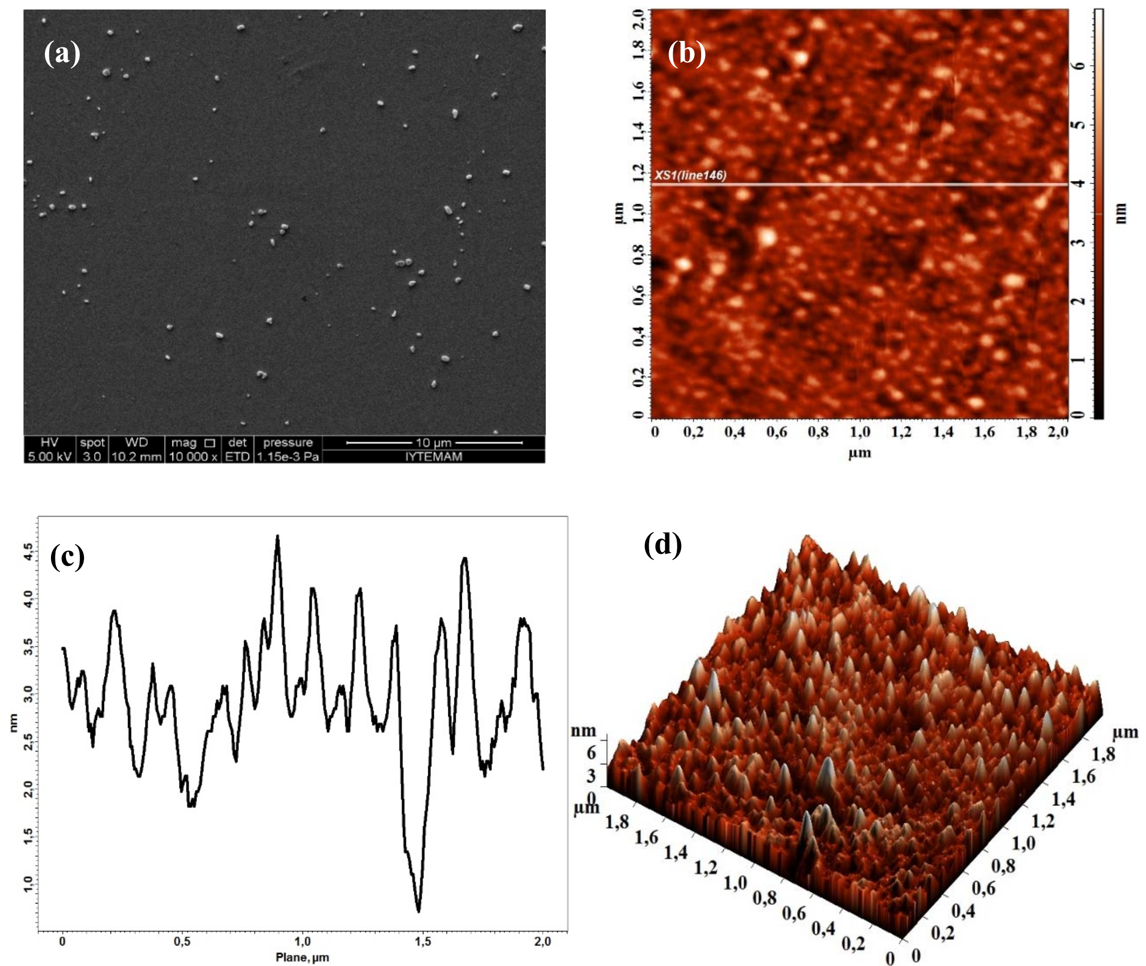

Figure 5.47. (a) SEM micrograph with 10 000 magnification, (b) AFM 2D Topographic image, (c) Profile line analysis of XS1 (line 146) and (d) AFM 3D Topographic image of Everson etched CdTe23-4 sample

Benson dislocation decoration etch technique was performed for sample CdTe23 to compare the EPD values with Everson etch technique. However, CrO_3 could not decomposed in the mixture that volume ratio of CrO_3 was less than 8 gr. Benson etchant implemented only 10 s due to spuming of the surface at higher implementation periods. AFM topographic images and profile analyses for Benson etched CdTe23-5 sample are shown in Figure 5.50.

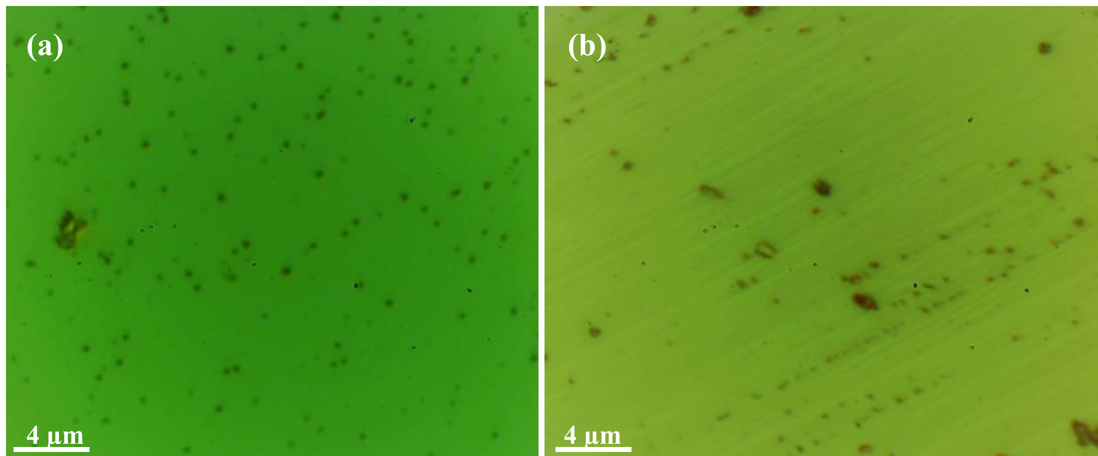

Figure 5.48. Nomarski images of CdTe23 sample (a) before dislocation decoration and (b) after Everson etch with 1HF+4HNO3+25Lactic acid mixture during 60 s.

The RMS roughness was obtained as 8.91 nm for 20x20 μm^2 scanned area. As seen in AFM topographic images, particulates formed with approximately 35 nm heights and pits formed with 0.21 µm widths and 8 nm depths on the sample surface. In addition, to investigate atomic distributions on the CdTe23-5 sample surface, EDX analyses performed (Figure 5.50). According to atomic percentages in EDX spectra, Cd and Te elements were not observed. Therefore we can say that Benson etch completely removed CdTe layer from the surface.

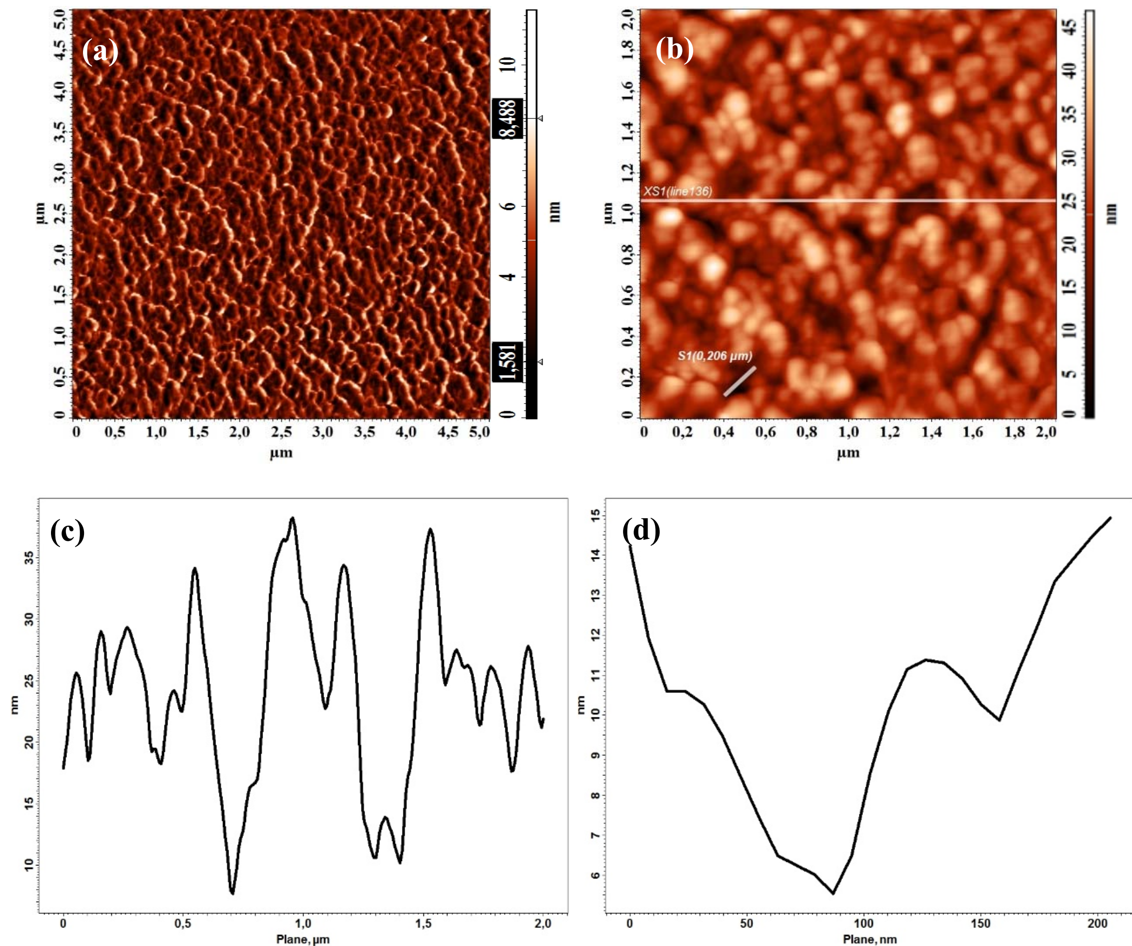

Figure 5.49. Benson decoration etched CdTe23-5 sample of (a) and (b) AFM 2D Topographic images for 5 µm^2 and 2 µm^2 scanned areas , (c) and (d) Profile line analysis of XS1 (line 136) and S1 line of 0,206 µm width

CdTe24 sample etched also by Everson dislocation decoration methods in various ratios and implementation times to reveal dislocations. As seen in AFM topographic images and SEM micrographs of sample CdTe24-1, the etch pits were in the form of triangular shapes with approximately maximum 0.24 µm width and 18 nm depths (Figure 5.51 and Figure 5.52). However, the dimensions and the depths of triangular shapes distributed inhomogeneously on the sample surface.

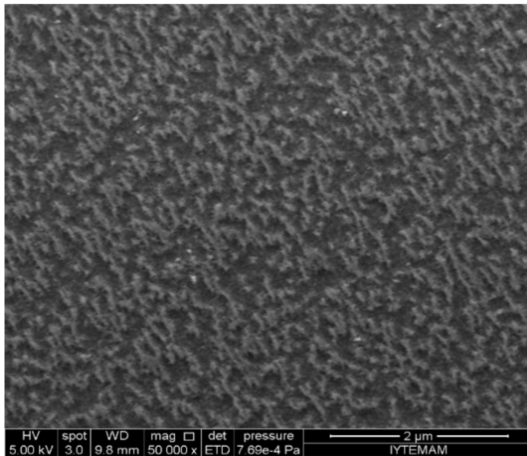

Element	Weight %	Atomic %
Ga	48.22	43.84
As	48.99	41.44
C	2.79	14.72

Figure 5.50. SEM micrograph of CdTe23-5 with 50 000 magnifications and EDX elemental analyses results.

The measured RMS roughness of CdTe24-1 sample was increased to 2.11 nm, after the Everson decoration method was performed for 30 s. EPD for this sample calculated as 1.7 x 10^8 cm^{-2}. The EDX spectra from a triangular shape (spectrum 14 in Figure 5.52) showed that concentration of Ga element is higher at that location than the areas without shapes. In addition to Ga element, As was also observed in small amounts in the triangular shaped areas.

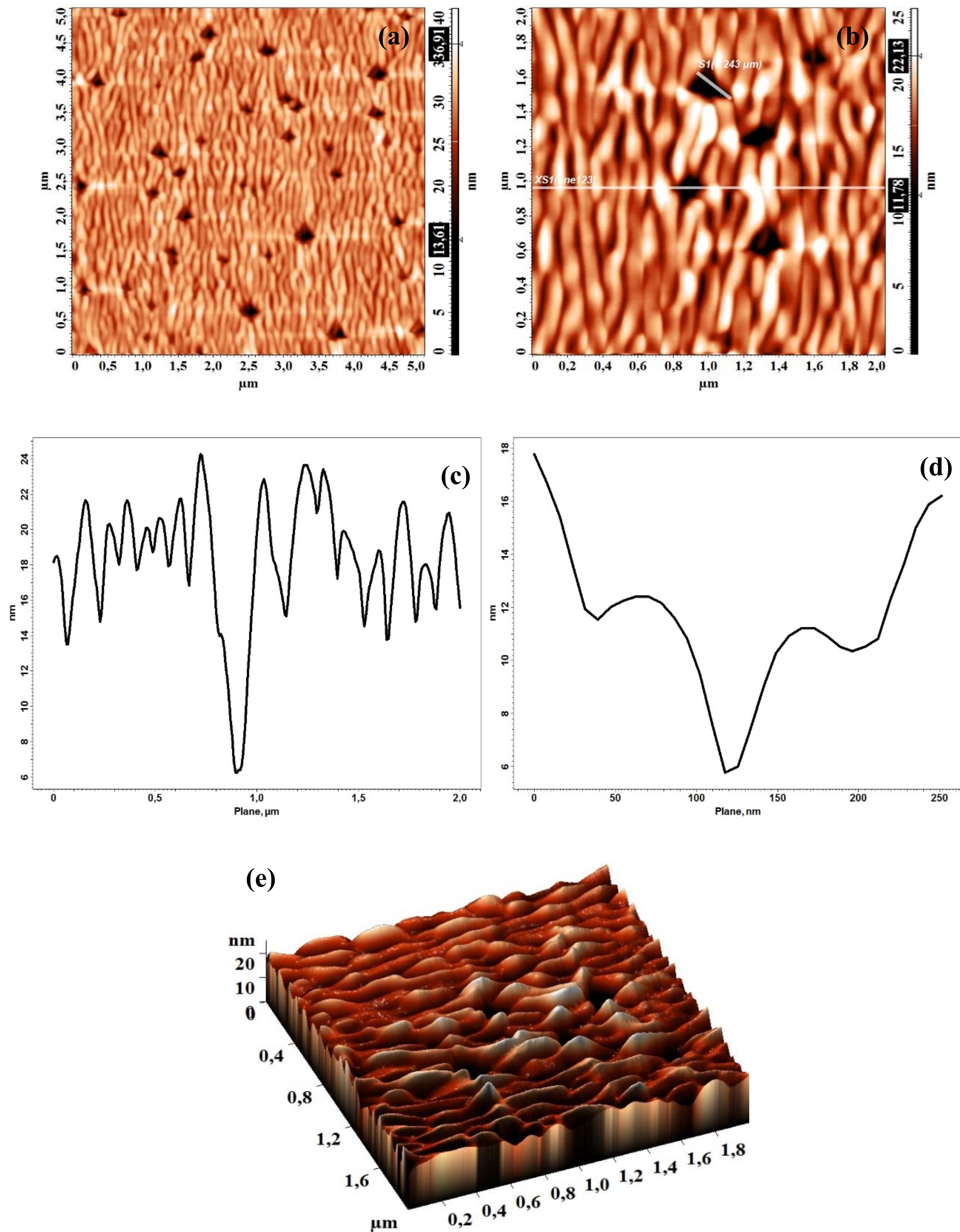

Figure 5.51. Everson etched CdTe24-1 sample of AFM 2D topographic images for (a) 5x5 μm^2 scanned area and (b) 2 μm^2 scanned area, (c) Profile line analyses of XS1 (line 123), (d) S1 line of 0,243 µm width and (e) AFM 3D topographic image.

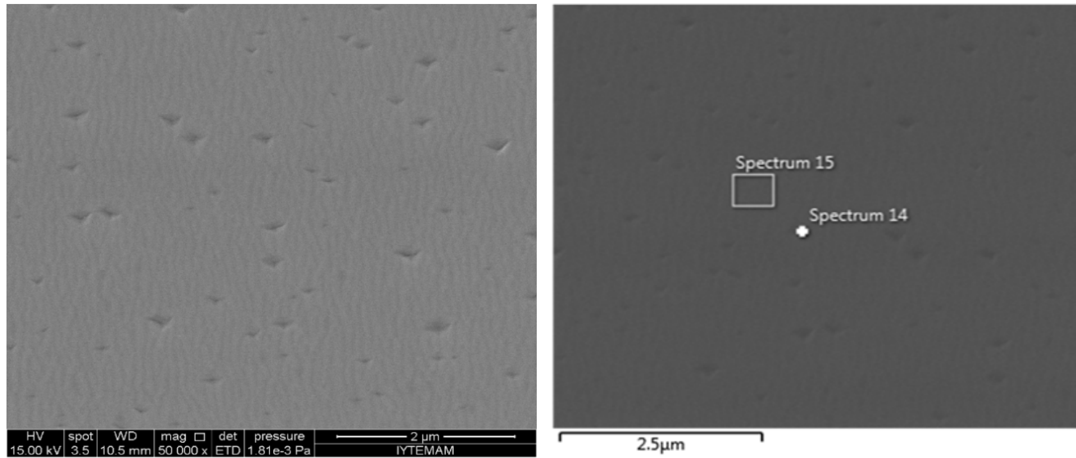

Element	Weight %	Atomic %
Spectrum 14		
Cd	46.18	47.18
Te	47.88	43.09
Ga	5.49	9.04
As	0.45	0.69

Element	Weight %	Atomic %
Spectrum 15		
Cd	45.83	46.99
Te	48.75	44.04
Ga	5.42	8.97
As	0.00	0.00

Figure 5.52. Everson etched CdTe24-1 sample of SEM micrographs with 50 000 and 2 500 magnifications and EDX analyses results in spectrums 14 and 15.

AFM topographic images and profile analyses for sample CdTe24-2 are given in Figure 5.53. For this time, Everson dislocation decoration etch performed for 40 s and the volume ratio of mixture changed to 1HF:4HNO_3:50Lactic acid. The RMS roughness value measured as 2.25 nm which was close to RMS roughness value of sample CdTe24-1. Similar to CdTe24-1, the etch pits are formed as triangular shapes with approximately maximum 0.24 µm width and 20 nm depths. Changing implementation time and volume ratio of etchant did not change the calculated EPD value which was found as 1.7 x 10^8 cm^{-2}, again. SEM micrographs with various magnifications are shown in Figure 5.54. Despite triangular shapes observed in both AFM and SEM images, Ga and As elements were observed in scanned areas of pits via EDX analyses.

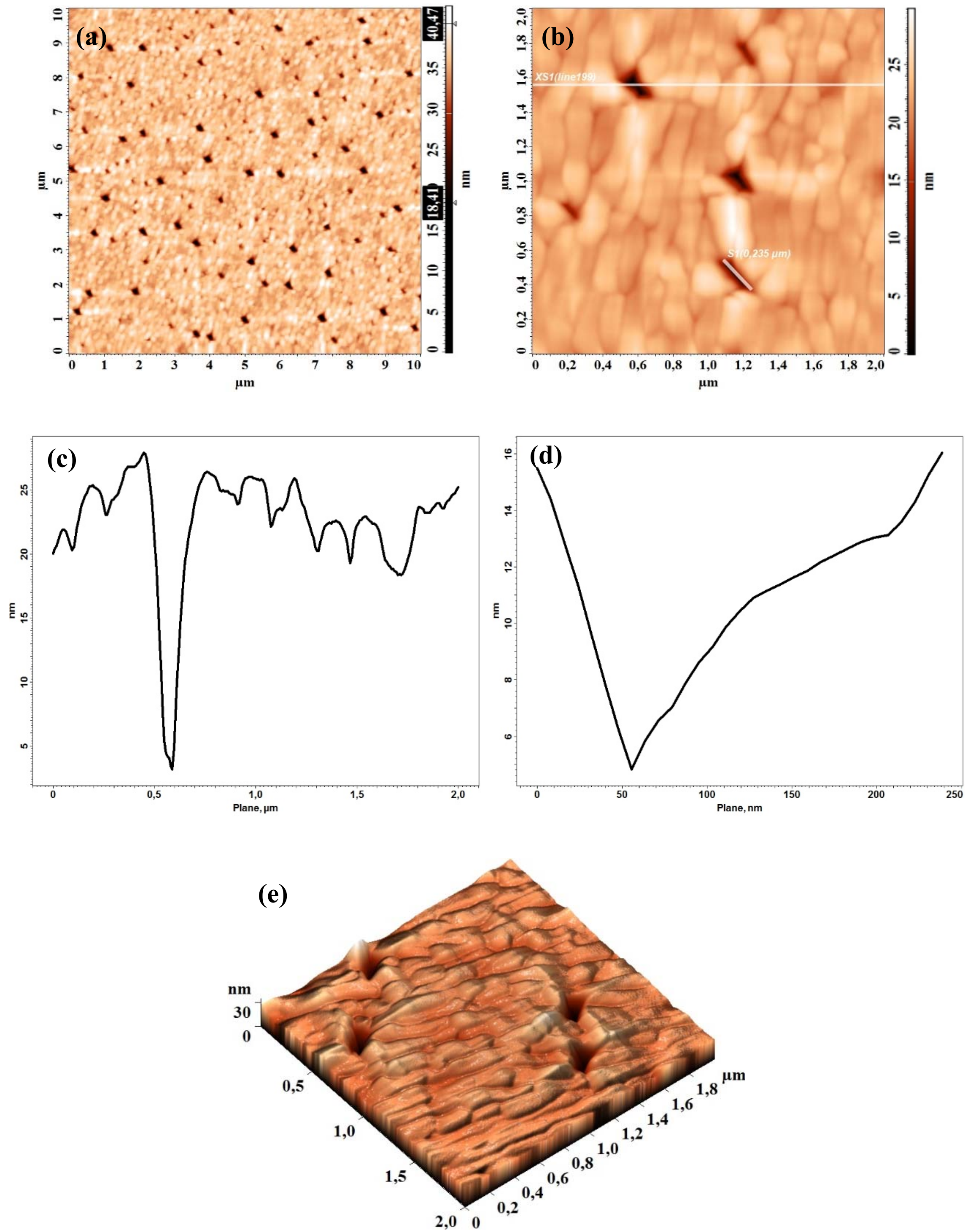

Figure 5.53. Everson etched CdTe24-2 sample of AFM 2D topographic images for (a) 10x10 μm^2 scanned area and (b) 2 μm^2 scanned area, (c) Profile line analyses of XS1 (line 199), (d) S1 line of 0,235 µm width and (e) AFM 3D topographic image.

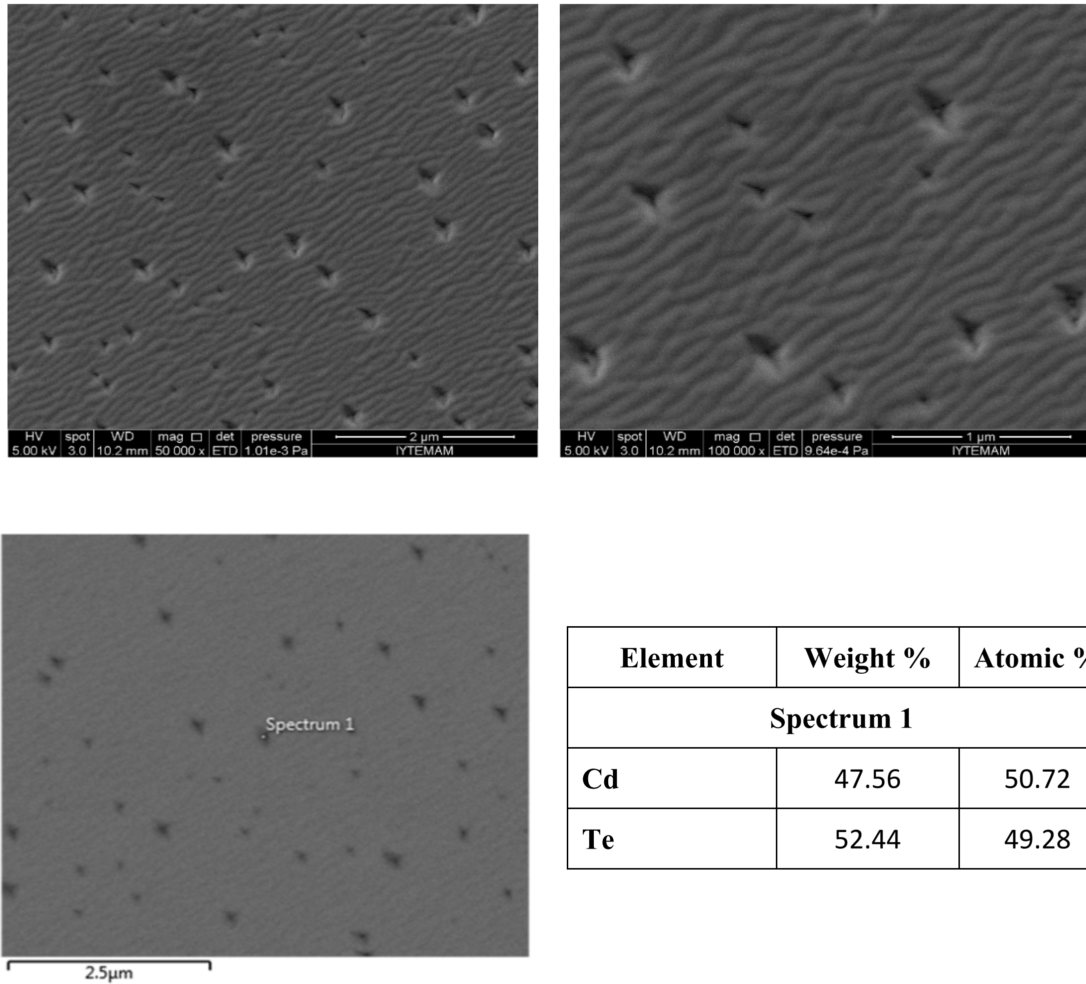

Element	Weight %	Atomic %
Spectrum 1		
Cd	47.56	50.72
Te	52.44	49.28

Figure 5.54. SEM micrographs of CdTe24-2 with 50 000, 100 000 and 2 500 magnifications and table shows EDX spectrum results in 2 500 magnification SEM image.

In order to obtain larger-size pits, HF volume ratio in sample CdTe24-1 increased from 0.5 to 1 for sample CdTe24-3. However, the mixture implemented only for 20 s due to spuming of the surface at higher implementation periods. It was observed that 20 s etching time was enough for this sample to achieve proper triangular shapes on the surface. Calculated EPD value for this sample was reduced to 1.2 x 10^{8} cm^{-2} after increasing HF volume ratio in the mixture and decreasing implementation time to 20 s. AFM topographic images with profile analysis and SEM micrographs with EDX analysis results are given in Figure 5.55 and Figure 5.56, respectively. Highest etch depths and sizes were observed for this sample with approximately 80 nm depth and 0.71 µm width. The RMS roughness of CdTe24-3 was increased to 26.01 nm with comparison to CdTe24-1 and CdTe24-2 samples. The EDX spectra from a triangular shape (spectrum 2

in Figure 5.56) showed that atomic percentages of Ga and As were higher for deeply etched areas. EPD values were counted using SEM micrographs (Figure 5.57).

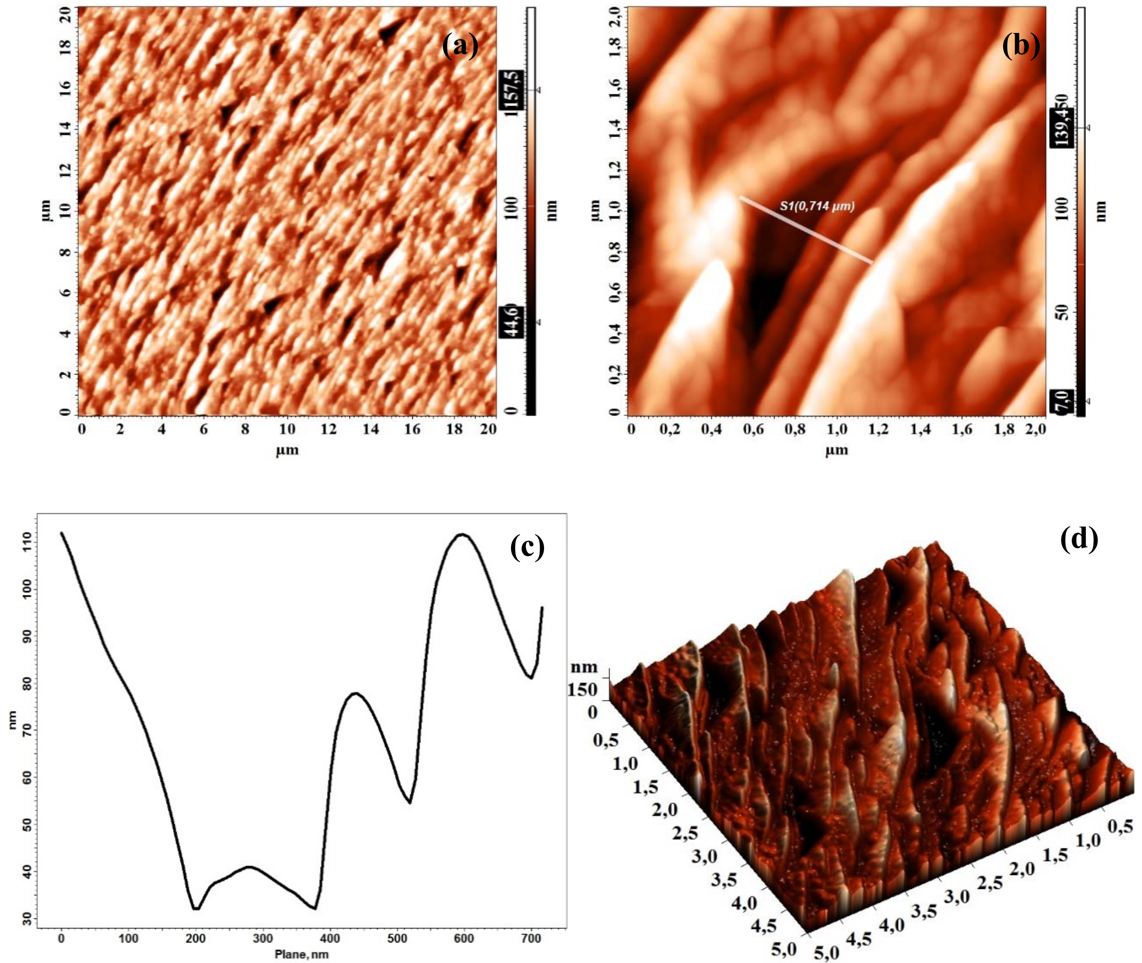

Figure 5.55. Everson etched CdTe24-3 sample of AFM 2D topographic images for (a) 20x20 μm^2 scanned area and (b) 2 μm^2 scanned area, (c) Profile line analyses of S1 line of 0.714 μm width and (d) AFM 3D topographic image.

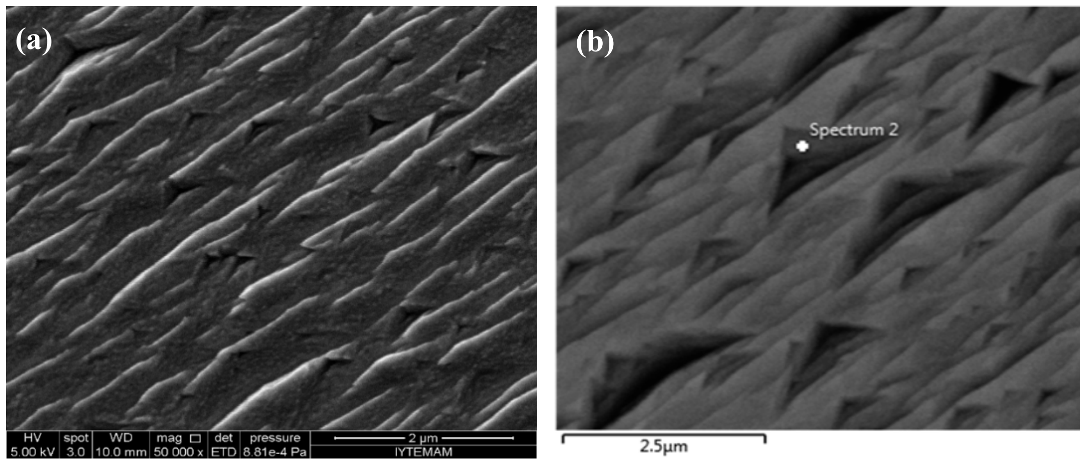

Element	Weight %	Atomic %
Spectrum 2		
Cd	38.28	37.52
Te	47.79	41.27
Ga	6.46	10.21
As	7.48	11.00

Figure 5.56. SEM micrographs of CdTe24-3 with (a) 50 000 and (b) 2 500 magnifications, and EDX analyses results of spectrum 2 in (b).

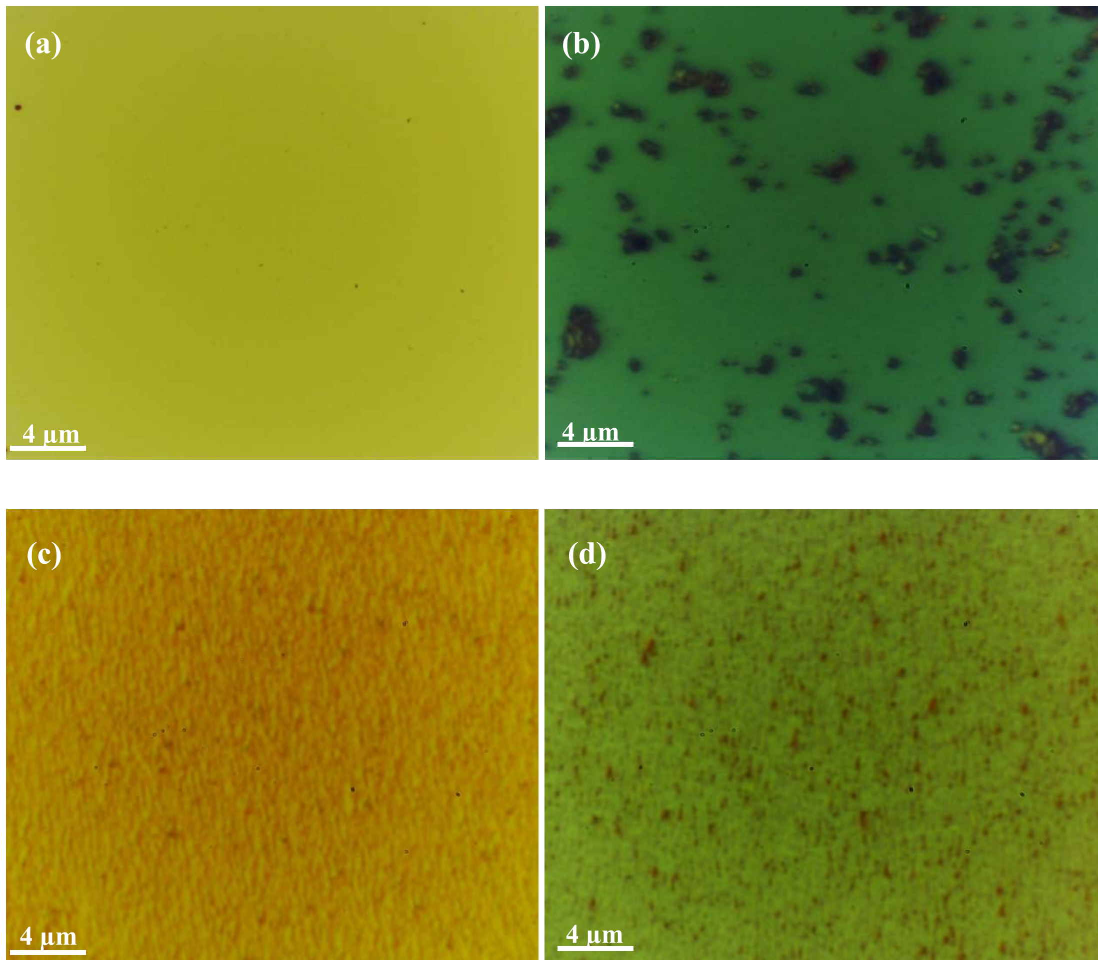

Figure 5.57. Nomarski images of CdTe24 sample (a) before dislocation decoration, after Everson etch with (b) 1HF+4HNO3+50Lactic acid mixture for 40 s, (c) and (d) 1HF+4HNO3+25Lactic acid mixture for 20 s.

In order to examine the distribution of Raman active phonon modes of CdTe and GaAs and also Te-related symmetry modes intensities for etched CdTe24-2 sample, (x, y) Raman mapping technique was used. In Figure 5.58, optical microscope image of 10x10 µm^2 scanned area of CdTe24-2 and Raman intensity change of observed phonon modes in Raman spectrum are shown. As seen in optical microscope image, it is hard to observe the etch pits due to maximum 0.24 µm width. To obtain more accurate results, Raman mapping implemented with 0.20 µm shifts on the examined surface.

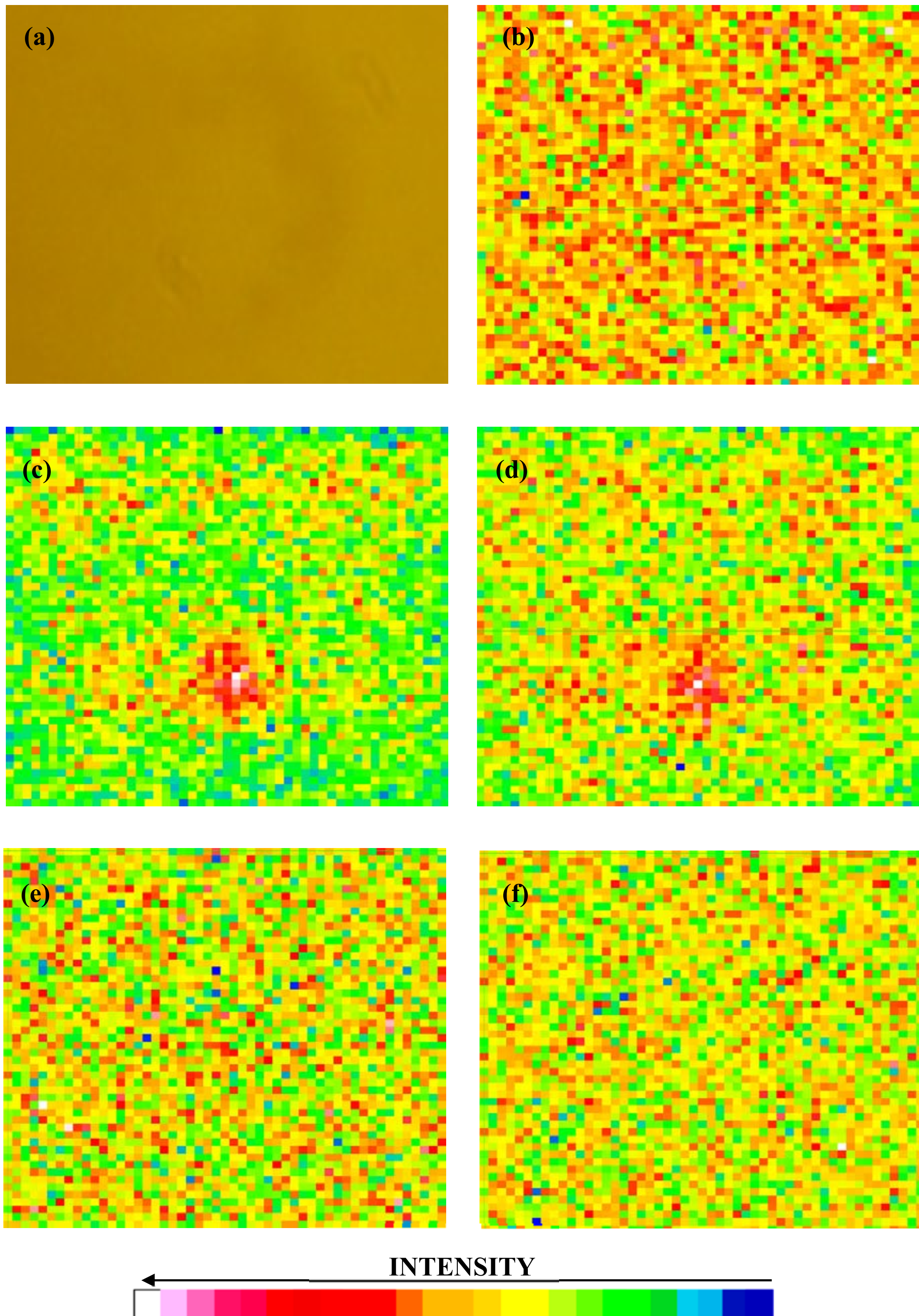

Figure 5.58. a) Optical microscope image of 10 μmx10 μm scanned area on sample CdTe24-2, Raman intensity change of (b) A_1-symmetry mode, (c) CdTe-like TO phonon mode, (d) CdTe-like LO phonon mode, (e) GaAs-like TO phonon mode and (f) GaAs-like LO phonon mode.

Te-specific E-symmetry mode were not observed during mapping in Raman spectra, but A_1-symmetry mode intensity was high for scanned area. In addition, CdTe-like TO-phonon mode and LO-phonon mode intensities were higher for an area which shows unetched areas by Everson decoration method. However, the same results were not obtained via the change of GaAs-like Raman active modes intensities which show inconsistent distribution.

CHAPTER 6

CONCLUSIONS

The main focus of this study was to investigate the defect structures of Molecular Beam Epitaxial (MBE) grown CdTe epitaxial films on GaAs(211)B wafers by various structural and optical characterization techniques.

Prior to MBE growth; piranha solution (H_2SO_4:H_2O_2:H_2O)-based wet-chemical etching and oxide removal processes using diluted hydrofluoric acid (HF:H_2O) performed at various volume ratios and implementation times to understand the effects of surface treatment by wet-cleaning procedure and the change of chemical composition of epiready GaAs wafers.

Before and after wet chemical etching, the surface morphologies of GaAs(211)B wafers were characterized by SEM and AFM. Before wet-chemical etching, the root mean square (RMS) roughnesses of wafers were found to be approximately 0.45 nm. The highest RMS roughness was found for G1C1-B2 sample which was etched with 2:1:1 volume ratio of piranha solution for 120 s. The best RMS roughness obtained for G1C1-E3 sample which was etched with 3:0.75:1 volume ratio of piranha solution for 30 s. In order to examine the chemical composition of piranha etched GaAs surface, Energy Dispersive X-ray Spectroscopy (EDX) was used. Despite the fact that it was expected to be As-rich surface after etching, surfaces of GaAs samples were slightly Ga-rich, except G1C1-A1 sample. In addition, atomic percentages of the elements for scanned areas showed that there were carbon contaminations on the sample surfaces due to degreasing processes by acetone and methanol. Besides the carbon contaminations, most GaAs surfaces had oxidation due to deionized water, hydrogen peroxide and sulfuric acid in etchant solution.

Oxide removal process performed for only two volume ratios for 60 s. The RMS roughness was found as 0.78 nm for G2W24A sample before etching with HF: H_2O (1:8) and after etching it increased to 0.94 nm. For G2W25A sample, the RMS roughness decreased from 1.09 nm to 0.62 nm due to increase in volume ratio of hydrofluoric acid in the etchant. Oxide structures of GaAs(211)B samples were studied via Raman scattering techniques at room temperature. The Raman spectra of the samples were

excited with an emission of $Ar^{(+)}$ laser with 488 nm wavelength. In addition to transverse and longitudinal optical Raman active modes of GaAs, vibrational modes belonging to Ga_2O_3 and As_2O_3 species, As-related defect modes and f_2 mode of As_4 were observed in Raman spectra of samples. To investigate the distribution of As_2O_3 vibrational mode intensities on the GaAs surface, two dimensional (x, y) map collected by Raman spectroscopy. As_2O_3 mode were more intense for darker detected areas on the sample surface. It was observed that oxide components of gallium and arsenic completely removed from the surface, after oxide removal procedure. These results indicates that the both 1:5 and 1:8 volume ratios of diluted hydrofluoric acid and also 60 s implementation time gave optimum conditions to remove the protective oxide layer of GaAs wafer surface by wet-chemical method.

Subsequent to growth of CdTe(211)B epitaxial films on GaAs(211)B wafers, the quality of CdTe layers were investigated via various characterization techniques. The surface morphologies were observed by AFM and SEM techniques. The RMS roughnesses were found 3.89 nm, 3.18 nm and 1.18 nm for CdTe films. SEM-EDX and EDX mapping techniques also performed to assess the chemical composition and the distribution of Cd, Te, Ga and As elements on the surface of CdTe layer. EDX analyses showed that the atomic percentage of Cd and Te are lower than Ga and As elements for CdTe23 sample. SEM micrographs in back-scattered electron (BSE) mode was used to estimate the CdTe layer thickness. It was observed that MBE-grown CdTe layer thicknesses were approximately 1 µm. Despite the lower atomic percentages of Cd and Te elements for CdTe23, the estimated CdTe layer thickness was approximately 2 µm. In addition, X-ray triple axis rocking curve (XR-DCRC) measurements performed to investigate the crystalline quality of MBE grown CdTe(211)B epitaxial films. The best (211)B CdTe/(211)B GaAs films grown in this study was CdTe24 sample with 190 arcsec $FWHM_{\theta}$. X-ray reflectivity measurements also performed for sample CdTe18 to confirm the thickness and roughness of grown layers. It was obtained that CdTe18 has CdTe layer with 1.018 µm thickness and 2.801 nm roughness.

Fourier Transform spectroscopy (FTRs) and UV/VIS/NIR spectrometer were used to obtain the transmittance curve and to calculate the thickness of CdTe layers. The thicknesses of CdTe layers was calculated 1.078 µm, 2.098 µm and 1.085 µm from intensity oscillations in the transmittance spectrum. To obtain refractive index and extinction coefficient of CdTe films ex-situ spectroscopic ellipsometry (SE) was used. Obtained layer thicknesses by SE coincide with FTIR calculated values except CdTe23.

In order to investigate Te precipitates and the quality of CdTe layers, Raman scattering experiments were performed under 488 nm excitation wavelength at various temperatures between 300 K and 80 K. To examine the quality of CdTe layers, the intensity ratio of second order (2LO) and first order (LO) longitudinal phonon modes was calculated at various temperatures. The results indicates that the intensity ratios changes non-linearly with measurement temperature. It was observed that Te-specific A_1 and E symmetry modes and transverse optical phonon mode of CdTe form a broad peak as the measurement temperature decreases. The first order longitudinal optical phonon mode intensity increases more rapidly than its overtone up to 150 K. Second order longitudinal optical phonon mode intensity reach its maximum value at 150 K. This non-linear change of 2LO and LO phonon mode intensity ratios might indicate the low crystal quality layers. In addition, A_1 symmetry of elemental Te in Raman spectra shows also poor quality layers with Te precipitates on the grown CdTe layers. This results were in agreement with both AFM and X-ray triple axis rocking curve measurements that growth related defects can be seen obviously in AFM topographic images. Despite 2 μm calculated layer thickness by intensity oscillations in the transmittance curve of CdTe23 sample, CdTe-like Raman active modes could be hardly resolved in all temperature range due to higher intensities of GaAs-like TO and LO phonon modes. Te-specific E-symmetry mode could not observed for this sample which indicates Te-flux was not sufficient during growth. This result were in agreement with EDX and SE measurements. This indicates that optimal growth conditions such as growth temperature and cell fluxes could not achieved.

Finally, Everson defect decoration technique was applied in various volume ratios and implementation times to understand the dislocation distribution across the films and to determine the areal densities of dislocations of epitaxial CdTe films. AFM, SEM and Nomarski phase contrast microscopy were used to evaluate the etch pits. Etch depths were determined via AFM profile analyses. The best EPD value obtained were 5.3×10^7 cm^{-2} with approximately 10 nm pit depth. In addition, to examine the distribution of CdTe-like and GaAs-like Raman phonon mode intensities, two-dimensional (x, y) Raman mapping technique was used. However, GaAs-like phonon mode intensities showed inconsistent distribution compared to CdTe-like first order phonon modes.

Future works related to this work include optical characterizations such as Raman and pholuminescence measurements to examine Te-related defects and localized defect levels. The behavior of E and A_1 symmetry modes of elemental Te depending on temperature will be studied in detail. With this background and perspective, we aim to

continue our work to improve the quality of CdTe layers by optimizing the growth parameters, such as growth temperature and cell fluxes. In addition, periodic annealing will be performed to improve the crystal quality, type and density of impurities as a function of annealing cyle will be investigated by photoluminescence measurements.

REFERENCES

1. Lawson, W., et al., Preparation and properties of HgTe and mixed crystals of HgTe-CdTe. Journal of Physics and Chemistry of Solids, 1959. 9(3): p. 325-329.

2. Kasap, S., et al., Mercury Cadmium Telluride: Growth, Properties and Applications. Vol. 38. 2011: Wiley. com.

3. Wald, F., Applications of CdTe. A review. Revue de Physique Appliquée, 1977. 12(2): p. 277-290.

4. Chadi, D., et al., Reflectivities and electronic band structures of CdTe and HgTe. Physical Review B, 1972. 5(8): p. 3058.

5. Yu, P.Y. and M. Cardona, Fundamentals of semiconductors: physics and materials properties. 1999: Springer Berlin etc.

6. Kane, E.O., Energy band structure in p-type Germanium and Silicon. Journal of Physics and Chemistry of Solids, 1956. 1(1): p. 82-99.

7. Camassel, J., et al., Temperature dependance of the fundamental absorption edge in CdTe. Solid State Communications, 1973. 13(1): p. 63-68.

8. Palatnik, L., V. Sorokin, and V. Marincheva, Conversion of the Hexagonal Form Into the Cubic During the Natural Ageing of CdTe Films. Izvest. Akad. Nauk SSSR Neorg. Materialy, 1974. 10(3): p. 413-417.

9. Yezhovsky, Y.K. and I. Kalinkin, Epitaxy of cadmium telluride in a quasi-closed cell. Thin Solid Films, 1973. 18(1): p. 127-136.

10. Ueda, R., Synthesis and epitaxial growth of CdTe films by neutral and ionized beams. Journal of Crystal Growth, 1975. 31: p. 333-338.

11. Douglas, B.E. and S.-M. Ho, Structure and chemistry of crystalline solids. Vol. 222. 2006: Springer New York.

12. Zanio, K. and F.H. Pollak, Semiconductors and Semimetals, Vol. 13 (Cadmium Telluride). Physics Today, 1978. 31: p. 53.

13. Williams, M., R. Tomlinson, and M. Hampshire, X-ray determination of the lattice parameters and thermal expansion of cadmium telluride in the temperature range 20–420 C. Solid State Communications, 1969. 7(24): p. 1831-1832.

14. Strauss, A., The physical properties of cadmium telluride. Revue de Physique Appliquée, 1977. 12(2): p. 167-184.

15. Cruz, L. and R. de Avillez, The formation of CdTe thin films by the stacked elemental layer method. Superficies y vacío, 1999(9): p. 92-95.

16. Davis, P. and T. Shilliday, Some optical properties of cadmium telluride. Physical Review, 1960. 118(4): p. 1020.

17. Bowden, C.H.a.S.; Available from: http://pveducation.org/pvcdrom/pn-junction/absorption-coefficient.

18. Marple, D. and H. Ehrenreich, Dielectric constant behavior near band edges in CdTe and Ge. Physical Review Letters, 1962. 8(3): p. 87.

19. Albin, D., et al. Comparison study of close-spaced sublimated and chemical bath deposited cds films: effects on cdte solar cells. in Photovoltaic Specialists Conference, 1997., Conference Record of the Twenty-Sixth IEEE. 1997. IEEE.

20. Alias, M., et al., The Role of Annealing Temperature on the Optical Properties of Thermally Deposited CdTe Films.

21. Johnson, C., G. Sherman, and R. Weil, Far infrared measurement of the dielectric properties of GaAs and CdTe at 300 K and 8 K. Applied optics, 1969. 8(8): p. 1667-1671.

22. Garlick, G., J. Hough, and R. Fatehally, The Nature of Binding in Cadmium Telluride. Proceedings of the Physical Society, 1958. 72(5): p. 925.

23. Yamada, S., On the Electrical and Optical Properties of p-type Cadmium Telluride Crystals. Journal of the Physical Society op Japan, 1960. 15(11).

24. Fisher, P. and H. Fan, Optical and Magneto-Optical Absorption Effects of Group III Impurities in Germanium. Physical Review Letters, 1959. 2(11): p. 456.

25. Dubrovskii, G., Optical properties of CdTe. Soviet. Phys. Solid State, 1961. 3: p. 1305.

26. Nobel, D.d., Philips Res. Rep. 14 361 Nobel D 1959. Philips Res. Rep, 1959. 14: p. 430.

27. Planker, K. and E. Kauer, Bestimmung der effektiven Masse freier Ladungsträger in Halbleitern aus der Ultra-rot absorption. Z. Angew. Phys, 1960. 12: p. 425.

28. Wiedemann, E., Ueber Fluorescenz und Phosphorescenz I. Abhandlung. Annalen der Physik, 1888. 270(7): p. 446-463.

29. Chandra, B. and J. Zink, Triboluminescence and the dynamics of crystal fracture. Physical Review B, 1980. 21(2): p. 816.

30. Leverenz, H.W., An introduction to luminescence of solids. 1950: Wiley.

31. Stokes, G.G., On the change of refrangibility of light. Philosophical Transactions of the Royal Society of London, 1852. 142: p. 463-562.

32. Lambropoulos, C., et al. Simulation studies of CdTe pixel detectors. in Nuclear Science Symposium Conference Record, 2008. NSS'08. IEEE. 2008. IEEE.

33. Fox, A.M., Optical properties of solids. Vol. 3. 2001: Oxford university press.

34. Giles, N., et al., Optical properties of undoped and iodine-doped CdTe. Journal of electronic materials, 1995. 24(5): p. 691-696.

35. Fistul, V.I., Heavily doped semiconductors. American Journal of Physics, 1969. 37: p. 1291-1292.

36. Bebb, H.B. and E. Williams, Photoluminescence I: theory. Semiconductors and semimetals, 1972. 8: p. 181-320.

37. Lampert, M.A., Mobile and immobile effective-mass-particle complexes in nonmetallic solids. Physical Review Letters, 1958. 1(12): p. 450.

38. Sharma, R. and S. Rodriguez, Theory of excitons bound to ionized impurities in semiconductors. Physical Review, 1967. 153(3): p. 823.

39. Thomas, D., J. Hopfield, and W. Augustyniak, Kinetics of radiative recombination at randomly distributed donors and acceptors. Physical Review, 1965. 140(1A): p. A202.

40. Hopfield, J. The quantum chemistry of bound exciton complexes. in Proceedings of the 7th International Conference on the Physics of Semiconductors. Paris: Dunod. 1964.

41. Rubio-Ponce, A., D. Olguín, and I. Hernández-Calderón, Calculation of the effective masses of II-VI semiconductor compounds.

42. Pelant, I. and J. Valenta, Luminescence spectroscopy of semiconductors. 2012: Oxford University Press.

43. Molva, E., et al., Acceptor states in CdTe and comparison with ZnTe. General trends. Physical Review B, 1984. 30(6): p. 3344.

44. Molva, E., et al., Photoluminescence studies in N, P, As implanted cadmium telluride. Solid state communications, 1983. 48(11): p. 955-960.

45. Gold, J.S., et al., Photoluminescence from heteroepitaxial (211) B CdTe grown on (211) B GaAs by molecular beam epitaxy. Journal of applied physics, 1993. 74(11): p. 6866-6871.

46. Francou, J., K. Saminadayar, and J. Pautrat, Shallow donors in CdTe. Physical Review B, 1990. 41(17): p. 12035.

47. Amirtharaj, P., et al., Electrolyte electroreflectance study of laser annealing effects on the CdTe/Hg< inf> 0.8</inf> Cd< inf> 0.2</inf> Te (111) system. Applied Physics Letters, 1982. 41(9): p. 860-862.

48. Lee, J., et al., Room-temperature band-edge photoluminescence from cadmium telluride. Physical Review B, 1994. 49(3): p. 1668.

49. Gupta, A., et al. Visible and x-ray spectroscopy studies of defects in CdTe. in Photovoltaic Specialists Conference, 2002. Conference Record of the Twenty-Ninth IEEE. 2002. IEEE.

50. Luo, M., Transition-Metal Ions in II-VI Semiconductors: ZnSe and ZnTe. 2006, West Virginia University.

51. Furstenberg, R. and J.O. White, Photoluminescence study of the 1.3–1.55 eV defect band in CdTe. Journal of crystal growth, 2007. 305(1): p. 228-236.

52. Guo, S.-p., et al., Study of molecular beam epitaxial growth and optical characteristics of HgCdTe. Acta Physica Sinica (Overseas Edition), 1996. 5(5): p. 370.

53. Lee, J., Photoluminescence study of cadmium zinc telluride grown by using the vertical Bridgman technique. JOURNAL OF THE KOREAN PHYSICAL SOCIETY, 2000. 36(1): p. 60-62.

54. Dean, P., G. Williams, and G. Blackmore, Novel type of optical transition observed in MBE grown CdTe. Journal of Physics D: Applied Physics, 1984. 17(11): p. 2291.

55. Giles-Taylor, N., et al., Photoluminescence of CdTe: A comparison of bulk and epitaxial material. Journal of Vacuum Science & Technology A: Vacuum, Surfaces, and Films, 1985. 3(1): p. 76-82.

56. Beattie, A.R., Quantum efficiency in InSb. Journal of Physics and Chemistry of Solids, 1962. 23(8): p. 1049-1056.

57. Altermatt, P.P., et al., Assessment and parameterisation of Coulomb-enhanced Auger recombination coefficients in lowly injected crystalline silicon. Journal of applied physics, 1997. 82(10): p. 4938-4944.

58. Shockley, W. and W. Read Jr, Statistics of the recombinations of holes and electrons. Physical Review, 1952. 87(5): p. 835.

59. Hall, R.N., Electron-hole recombination in germanium. Physical Review, 1952. 87(2): p. 387.

60. Li, S.S., Semiconductor physical electronics. 2006: Springer Berlin.

61. Kiran, R., Optimization of the Mercury Cadmium Telluride Surface and Its Characterization by Electrical and Optical Techniques. 2008: ProQuest.

62. Emelie, P.-Y., HgCdTe Auger-Suppressed Infrared Detectors Under Non-Equilibrium Operation. 2009, The University of Michigan.

63. Kim, C., et al., Temperature dependence of the optical properties of CdTe. Physical Review B, 1997. 56(8): p. 4786.

64. Sporken, R., et al., Molecular beam epitaxy and characterization of HgCdTe (111) B on Si (100). Applied physics letters, 1991. 59(1): p. 81-83.

65. Bridgman, P., The viscosity of liquids under pressure. Proceedings of the National Academy of Sciences of the United States of America, 1925. 11(10): p. 603.

66. Stephen C. Bates, K.S.K. High Temperature Transparent Furnace Development Available from: http://www.tvu.com/PHighTTFweb.html.

67. Kyle, N.R., Growth of Semi-Insulating Cadmium Telluride. Journal of The Electrochemical Society, 1971. 118(11): p. 1790-1797.

68. Watson, C., Structural defects in CdTe and related materials. 1993, Durham University.

69. Lu, Y.-C., et al., Effect of vibrational stirring on the quality of Bridgman-grown CdTe. Journal of crystal growth, 1990. 102(4): p. 807-813.

70. Raiskin, E. and J. Butler, CdTe low level gamma detectors based on a new crystal growth method. Nuclear Science, IEEE Transactions on, 1988. 35(1): p. 81-84.

71. Szeles, C., et al. Semi-insulating CdZnTe with improved structural perfection for radiation detector applications. in International Symposium on Optical Science and Technology. 2001. International Society for Optics and Photonics.

72. Zanio, K. and F.H. Pollak, Semiconductors and Semimetals, Vol. 13 (Cadmium Telluride). Physics Today, 2008. 31(8): p. 53-54.

73. Czochralski, J., Ein neues Verfahren zur Messung der Kristallisationsgeschwindigheit der Metalle. Z. phys. Chemie., 1918. 92: p. 219-221.

74. Teal, G.K., Methods Of Producing Semiconductive. 1955, Google Patents.

75. Holt, D. and B. Yacobi, Semiconducting materials. 1951.

76. Von Neida, A., L. Oster, and J. Nielsen, Liquid encapsulated growth of GaP from non-stoichiometric melts. Journal of Crystal Growth, 1972. 13: p. 647-650.

77. Hyder, S. and C. Holloway, In-situ synthesis and growth of indium phosphide. Journal of Electronic Materials, 1983. 12(3): p. 575-585.

78. AuCoin, T., et al., Liquid Encapsulated Compounding And Czochralski Growth Of Semi-Insulating Gallium-Arsenide. Solid State Technology, 1979. 22(1): p. 59-&.

79. Hacskaylo, M., Method for growing crystals. 1981, Google Patents.

80. Weinstein, M., S. Axelrod, and A. Mlavsky, The Travelling Solvent Method of Crystal Growth. 1962, Air Force Cambridge Research Labs Hanscom Afb Ma.

81. Dost, S. and B. Lent, Single Crystal Growth of Semiconductors from Metallic Solutions. 2006: Elsevier.

82. Triboulet, R. and P. Siffert, CdTe and Related Compounds; Physics, Defects, Hetero-and Nano-structures, Crystal Growth, Surfaces and Applications: Physics, CdTe-based Nanostructures, CdTe-based Semimagnetic Semiconductors, Defects. 2009: Access Online via Elsevier.

83. Scheel, H.J., T. Fukuda, and J. Wiley, Crystal growth technology. 2003: Wiley Online Library.

84. Cho, A., M. Panish, and I. Hayashi. Molecular beam epitaxy of GaAs, AlxGa1-xAs and GaP. in Proc. Symp. GaAs and Related Compounds. 1970.

85. Herman, M.A. and H. Sitter, Molecular beam epitaxy: fundamentals and current status. 1989: Springer-Verlag Berlin.

86. Zacharia, R., Desorption of gases from graphitic and porous carbon surfaces. Ph. Dr. Thesis, Freien Universität Berlin, Berlin, Germany, 2004.

87. Manasevit, H.M., Applied Physics Letters, 1968. 12: p. 1530.

88. Sze, P., et al., Characteristics of MOCVD-grown high-quality CdTe layers on GaAs substrates. Active and passive electronic components, 1995. 18(4): p. 247-258.

89. Rao, S., et al., High-Quality (211) B CdTe on (211) Si Substrates Using Metalorganic Vapor-Phase Epitaxy. Journal of electronic materials, 2011. 40(8): p. 1790-1794.

90. Mitra, P., F. Case, and M. Reine, Progress in MOVPE of HgCdTe for advanced infrared detectors. Journal of electronic materials, 1998. 27(6): p. 510-520.

91. Zilko, J.L., Metal organic chemical vapor deposition: technology and equipment. Handbook of Thin Film Deposition Processes and Techniques, 2001: p. 151.

92. Antson, J. and T. Suntola, Method for producing compound thin films. 1977, Google Patents.

93. Grubbs, R., N. Steinmetz, and S. George, Gas phase reaction products during tungsten atomic layer deposition using WF 6 and Si 2 H 6. Journal of Vacuum Science & Technology B: Microelectronics and Nanometer Structures, 2004. 22(4): p. 1811-1821.

94. Bisengaliev, R., et al., Molecular layering of 2D films and superlattices based on II–VI compounds. Physics of the Solid State, 1998. 40(5): p. 754-755.

95. Ezhovskii, Y.K. and A. Klyuikov, Atomic-Layer Epitaxy of Cadmium Chalcogenides on Gallium Arsenide. RUSSIAN JOURNAL OF APPLIED CHEMISTRY C/C OF ZHURNAL PRIKLADNOI KHIMII, 2000. 73(6): p. 933-936.

96. Sitter, H. and W. Faschinger, Ultra high vacuum atomic layer epitaxy of CdTe. Thin solid films, 1993. 225(1): p. 250-255.

97. Smith, H.M. and A. Turner, Vacuum deposited thin films using a ruby laser. Applied Optics, 1965. 4(1): p. 147-148.

98. Dijkkamp, D., et al., Preparation of Y-Ba-Cu oxide superconductor thin films using pulsed laser evaporation from high Tc bulk material. Applied Physics Letters, 1987. 51(8): p. 619-621.

99. Wang, K., Laser Based Fabrication of Graphene. 2013.

100. Oszwaldowski, M., et al., Pulsed laser deposition of II–VI semiconductor thin films and their layered structures. Journal of alloys and Compounds, 2004. 371(1): p. 164-167.

101. Neretina, S., et al., The role of lattice mismatch in the deposition of CdTe thin films. Journal of electronic materials, 2006. 35(6): p. 1224-1230.

102. Neretina, S., et al., Evolution of wurtzite CdTe through the formation of cluster assembled films. Applied physics letters, 2006. 89(13): p. 133101.

103. Lopez-Otero, A., Hot wall epitaxy. Thin solid films, 1978. 49(1): p. 3-57.

104. Mullins, J., et al., Crystal growth of large-diameter bulk CdTe on GaAs wafer seed plates. Journal of Crystal Growth, 2008. 310(7): p. 2058-2061.

105. Jiang, Q., et al., Hetero-epitaxial crystal growth of CdTe on GaAs substrates. Journal of Crystal Growth, 2008. 310(7): p. 1652-1656.

106. Lalev, G.M., et al., Hot wall epitaxy of high-quality CdTe/Si (111). Journal of crystal growth, 2003. 256(1): p. 20-26.

107. Carmody, M., et al., Recent progress in MBE growth of CdTe and HgCdTe on (211) B GaAs substrates. Journal of electronic materials, 2012. 41(10): p. 2719-2724.

108. Dhanaraj, G., K. Byrappa, and V. Prasad, Springer handbook of crystal growth. 2010: Springer.

109. Carmody, M., et al., Status of LWIR HgCdTe-on-Silicon FPA Technology. Journal of Electronic Materials, 2008. 37(9): p. 1184-1188.

110. Jacobs, R., et al., Relevance of thermal mismatch in large-area composite substrates for HgCdTe heteroepitaxy. Journal of Electronic Materials, 2008. 37(9): p. 1480-1487.

111. Xin-Hao Zhao, M.J.D., Jing Lu, Shi Liu, David J. Smith, Yong-Hang Zhang, Structural and Optical Properties of High Quality CdTe and CdTe/MgCdTe Double Heterostructures Grown on InSb Substrates using MBE, in The US Workshop on the Physics & Chemistry of II-VI materials. 2013.

112. Dhanaraj G., B.K., Prasad V., Dudley, M., Springer Handbook of Crystal Growth. 2010.

113. Wang, X., et al., Microstructure of Heteroepitaxial ZnTe Grown by Molecular Beam Epitaxy on Si (211) Substrates. Journal of electronic materials, 2011. 40(8): p. 1860-1866.

114. Lo, Y., et al., Growth of CdTe films on silicon by molecular beam epitaxy. Journal of Applied Physics, 1983. 54(7): p. 4238-4240.

115. Sporken, R., et al., Molecular beam epitaxial growth of CdTe and HgCdTe on Si (100). Applied Physics Letters, 1989. 55(18): p. 1879-1881.

116. Rujirawat, S., et al., High quality large-area CdTe (211) B on Si (211) grown by molecular beam epitaxy. Applied physics letters, 1997. 71(13): p. 1810-1812.

117. Chen, Y., et al., MBE-Grown ZnTe/Si, a Low-Cost Composite Substrate. Journal of electronic materials, 2012. 41(10): p. 2917-2924.

118. Koestner, R. and H. Schaake, Kinetics of molecular-beam epitaxial HgCdTe growth. Journal of Vacuum Science & Technology A: Vacuum, Surfaces, and Films, 1988. 6(4): p. 2834-2839.

119. Lennon, C., et al., Real-Time In Situ Monitoring of GaAs (211) Oxide Desorption and CdTe Growth by Spectroscopic Ellipsometry. Journal of electronic materials, 2012. 41(10): p. 2965-2970.

120. Jacobs, R., et al., Comparative study of thermal mismatch effects in CdTe/Si, CdTe/Ge, and CdTe/GaAs composite structures.

121. Chung, Y.-w., Introduction to materials science and engineering. 2007: CRC Press.

122. Berding, M., Native defects in CdTe. Physical Review B, 1999. 60(12): p. 8943.

123. Boukerche, M., et al., The doping of mercury cadmium telluride grown by molecular-beam epitaxy. Journal of Vacuum Science & Technology A: Vacuum, Surfaces, and Films, 1988. 6(4): p. 2830-2833.

124. Vydyanath, H., J. Ellsworth, and C. Devaney, Electrical activity, mode of incorporation and distribution coefficient of group V elements in Hg1− xCdxTe grown from tellurium rich liquid phase epitxial growth solutions. Journal of electronic materials, 1987. 16(1): p. 13-25.

125. Wu, O.K., D.N. Jamba, and G.S. Kamath, Growth and properties of In-and As-doped HgCdTe by MBE. Journal of crystal growth, 1993. 127(1): p. 365-370.

126. Vydyanath, H., Lattice Defects in Semiconducting Hg1− x Cd x Te Alloys I. Defect Structure of Undoped and Copper Doped. Journal of The Electrochemical Society, 1981. 128(12): p. 2609-2619.

127. Destefanis, G., Indium ion implantation in Hg< inf> 0.78</inf> Cd< inf> 0.22</inf> Te/CdTe. Journal of Vacuum Science & Technology A: Vacuum, Surfaces, and Films, 1985. 3(1): p. 171-175.

128. M. Hage-Ali, P.S., Semiconductors and Semimetals. Vol. 43. 1995: Academic Press.

129. Soundararajan, R., et al., Study of defect levels in CdTe using thermoelectric effect spectroscopy. Journal of electronic materials, 2006. 35(6): p. 1333-1340.

130. Ayers, J.E., Heteroepitaxy of semiconductors: theory, growth, and characterization. 2007: CRC press.

131. Bimberg, D., M. Grundmann, and N.N. Ledentsov, Quantum dot heterostructures. Vol. 471973882. 1999: John Wiley Chichester.

132. Port, R.I., Structural defects in MOVPE grown CdTe/GaAs. 1995, Durham University.

133. Rujirawat, S., The CdTe/Si (111): As interface. 2000, University of Illinois at Chicago.

134. Smith, W.F., Principles of materials science and engineering. 1986.

135. Askeland, D.R., P.P. Fulay, and W.J. Wright, The Science and Engineering of Materials: Si Edition. 2011: CengageBrain. com.

136. Al-Jassim, M., et al., TEM, AFM, and cathodoluminescence characterization of CdTe thin films. Thin solid films, 2001. 387(1): p. 246-250.

137. Zhao, W., et al., Microstructural Characterization of CdTe (211) B/ZnTe/Si (211) Heterostructures Grown by Molecular Beam Epitaxy. Journal of electronic materials, 2011. 40(8): p. 1733-1737.

138. Kakani, S., Material science. 2006: New Age International.

139. Szeles, C. and M.C. Driver. Growth and properties of semi-insulating CdZnTe for radiation detector applications. in SPIE's International Symposium on Optical Science, Engineering, and Instrumentation. 1998. International Society for Optics and Photonics.

140. VEECO, GEN20 MBE System User Manual

141. Davies, G. and D. Williams, III-V MBE growth systems. The technology and physics of molecular beam epitaxy, 1985: p. 17.

142. Knodle, W.S. and R. Chow, Molecular Beam Epitaxy: Equipment and Practice. Handbook of Thin Film Deposition Processes and Techniques, 2001: p. 381.

143. VEECO. Available from: http://www.veeco.com/effusion-cells,-valved-crackers,-and-gas-injectors.aspx.

144. Lüth, H., Solid surfaces, interfaces and thin films. Vol. 8431. 2010: Springer.

145. Van Der Wagt, J.P.A., Reflection High-Energy Electron Diffraction During Molecular-Beam Epitaxy. 1994, Stanford University.

146. Raman, C.V., A new radiation. Indian Journal of physics, 1928. 2: p. 387-398.

147. Smith, E. and G. Dent, Modern Raman spectroscopy: a practical approach. 2005: John Wiley & Sons.

148. Christensen, N., Electronic structure of GaAs under strain. Physical Review B, 1984. 30(10): p. 5753.

149. Cardona, M., N. Christensen, and G. Fasol, Relativistic band structure and spin-orbit splitting of zinc-blende-type semiconductors. Physical Review B, 1988. 38(3): p. 1806.

150. Strauch, D. and B. Dorner, Phonon dispersion in GaAs. Journal of Physics: Condensed Matter, 1990. 2(6): p. 1457.

151. Kagaya, H.M.S., Phys. Status Solidi, 1984.

152. Loudon, R., The Raman effect in crystals. Advances in Physics, 1964. 13(52): p. 423-482.

153. Chaves, A. and S. Porto, Generalized Lyddane-Sachs-Teller relation. Solid State Communications, 1973. 13(7): p. 865-868.

154. Poulet, H., Sur certaines anomalies de l'effet Raman dans les cristaux. 1955.

155. Birman, J.L., Theory of infrared and Raman processes in crystals: selection rules in diamond and zincblende. Physical Review, 1963. 131(4): p. 1489.

156. Parmenter, R., Symmetry properties of the energy bands of the zinc blende structure. Physical Review, 1955. 100(2): p. 573.

157. Alencar, A., V. Freire, and G. Farias, The Electron-Phonon Interaction in Semiconductor Films with Interfacial Charges. Brazilian Journal of Physics, 1997. 27: p. 240-243.

158. Spirkoska, D., G. Abstreiter, and A.F. i Morral, Size and environment dependence of surface phonon modes of gallium arsenide nanowires as measured by Raman spectroscopy. Nanotechnology, 2008. 19(43): p. 435704.

159. Trommer, R. and M. Cardona, Resonant Raman Scattering in GaAs. Physical Review B, 1978. 17(4): p. 1865.

160. Kwok, S., et al., Raman scattering from heavily doped (311) GaAs: Si grown by molecular beam epitaxy. Journal of applied physics, 1992. 72(1): p. 285-286.

161. Arguello, C., D. Rousseau, and S.P.d.S. Porto, First-order Raman effect in wurtzite-type crystals. Physical Review, 1969. 181(3): p. 1351.

162. McCluskey, M., Local vibrational modes of impurities in semiconductors. Journal of Applied Physics, 2000. 87(8): p. 3593-3617.

163. Jiang, D.-S., et al., A Raman scattering study of GaAs: As films lifted off GaAs substrate. Journal of Physics D: Applied Physics, 1999. 32(6): p. 629.

164. Amirtharaj, P. and F.H. Pollak, Raman scattering study of the properties and removal of excess Te on CdTe surfaces. Applied Physics Letters, 1984. 45(7): p. 789-791.

165. Pine, A. and G. Dresselhaus, Raman spectra and lattice dynamics of tellurium. Physical Review B, 1971. 4(2): p. 356.

166. Levy, M., et al., Characterization of CdTe substrates and MOCVD Cd< sub> 1−x</sub> Zn< sub> x</sub> Te epilayers. Journal of crystal growth, 1999. 197(3): p. 626-629.

167. Zitter, R., Raman detection of tellurium layers on surfaces of CdTe. Surface Science, 1971. 28(1): p. 335-338.

168. Harada, H. and S.-i. Narita, Lattice Vibration Spectra of Zn x Cd1-x Te Alloys. Journal of the Physical Society of Japan, 1971. 30(6): p. 1628-1639.

169. Olego, D., P. Raccah, and J. Faurie, Compositional dependence of the Raman frequencies and line shapes of Cd 1-x Zn x Te determined with films grown by molecular-beam epitaxy. Physical Review B, 1986. 33(6): p. 3819.

170. Batalla, E., E. Koteles, and W. Datars, Far-infrared absorption in CdTe. Canadian Journal of Physics, 1977. 55(22): p. 2013-2018.

171. Saucedo, E., et al., Simulation and characterization of CdTe: Bi crystals grown by the Markov method. Journal of Crystal Growth, 2005. 275(1): p. e471-e477.

172. Parker, T., J. Birch, and C. Mok, A critical point analysis of multi-phonon structure in the far infrared dielectric response of CdTe. Solid State Communications, 1980. 36(7): p. 581-584.

173. Prabakar, K., S.K. Narayandass, and D. Mangalaraj, Structural, optical and Raman scattering studies on polycrystalline Cd< sub> 0.8</sub> Zn< sub> 0.2</sub> Te thin films prepared by vacuum evaporation. Physica B: Condensed Matter, 2003. 328(3): p. 355-362.

174. Prabakar, K., et al., Microstructure, Raman and optical studies on Cd< sub> 0.6</sub> Zn< sub> 0.4</sub> Te thin films. Materials Science and Engineering: B, 2004. 107(1): p. 99-105.

175. Gorska, M. and W. Nazarewicz, Application of the Random-Element Isodisplacement Model to Long-Wavelength Optical Phonons in CdSexTe1− x Mixed Crystals. physica status solidi (b), 1974. 65(1): p. 193-202.

176. Tatarkiewicz, J., A. Witowski, and E. Jahne, Hydrogen vibrations in CdTe. physica status solidi (b), 1987. 142(2): p. K101-K104.

177. Sciacca, M.D., et al., Host-isotope fine structure of local and gap modes of substitutional impurities in zinc-blende and wurtzite II-VI semiconductors. Physical Review B, 1996. 53(19): p. 12878.

178. Onari, S., M. Miura, and K. Matsuishi, Raman spectroscopic studies on bismuth nanoparticles prepared by laser ablation technique. Applied surface science, 2002. 197: p. 615-618.

179. Lu, W., et al., Local and Quasi-Local Modes of Fe and Zn in CdTe. physica status solidi (b), 1988. 147(2): p. 767-778.

180. Talwar, D., Z. Feng, and P. Becla, Impurity-induced phonon disordering in Cd 1-x Zn x Te ternary alloys. Physical Review B, 1993. 48(23): p. 17064.

181. Michelson, A.A., XXVIII. Visibility of interference-fringes in the focus of a telescope. The London, Edinburgh, and Dublin Philosophical Magazine and Journal of Science, 1891. 31(190): p. 256-259.

182. Cooley, J.W. and J.W. Tukey, An algorithm for the machine calculation of complex Fourier series. Mathematics of computation, 1965. 19(90): p. 297-301.

183. Tarhan, E., Fourier transform infrared spectroscopy of III-V compound semiconductors. 2004.

184. Bell, R., Introductory Fourier Transform Spectroscopy (Academic, New York, 1972). Chap. 12: p. 159-166.

185. Smith, B.C., Fundamentals of Fourier transform infrared spectroscopy. 2011: CRC press.

186. Jaggi, N. and D. Vij, Fourier transform infrared spectroscopy, in Handbook of Applied Solid State Spectroscopy. 2006, Springer. p. 411-450.

187. Nomarski, G., Interferential polarizing device for study of phase objects. 1960, Google Patents.

188. Murphy, D.B. and M.W. Davidson, Fundamentals of light microscopy and electronic imaging. 2012: John Wiley & Sons.

189. Duncan, D.D., et al., Quantitative Carré differential interference contrast microscopy to assess phase and amplitude. JOSA A, 2011. 28(6): p. 1297-1306.

190. Binnig, G., C.F. Quate, and C. Gerber, Atomic force microscope. Physical review letters, 1986. 56(9): p. 930.

191. Balthazar, J.M., et al., On an overview of nonlinear and chaotic behavior and their controls of an atomic force microscopy (afm) vibrating problem. Nonlinearity, bifurcation and chaos: Theory and Applications, 2012. 1: p. 45-68.

192. Seo, Y. and W. Jhe, Atomic force microscopy and spectroscopy. Reports on Progress in Physics, 2008. 71(1): p. 016101.

193. Giessibl, F.J., Advances in atomic force microscopy. Reviews of modern physics, 2003. 75(3): p. 949.

194. Israelachvili, J.N., Intermolecular and Surface Forces: With Applications to Colloidal and Biological Systems (Colloid Science). 1992, Academic press London.

195. Sarid, D., Scanning force microscopy. 1991: Oxford University Press.

196. Gadelmawla, E., et al., Roughness parameters. Journal of Materials Processing Technology, 2002. 123(1): p. 133-145.

197. Knoll, M., Aufladepototentiel une Sekündaremission elektronbestrahlter Körper. Zeitschrift fur technische Physik, 1935. 16: p. 467-475.

198. Stanton, A., Wilhelm Conrad Röntgen on a new kind of rays: translation of a paper read before the Würzburg Physical and Medical Society, 1895. Nature, 1896. 53(1896): p. 274-276.

199. Baca, A.G. and C.I. Ashby, Fabrication of GaAs devices. 2005: IET.

200. Bertrand, P., XPS study of chemically etched GaAs and InP. Journal of Vacuum Science and Technology, 1981. 18(1): p. 28-33.

201. Song, J., et al., Wet chemical cleaning process of GaAs substrate for ready-to-use. Journal of crystal growth, 2004. 264(1): p. 98-103.

202. Liu, H., et al., The phase identification of the H_2SO_4-etched GaAs by X-ray diffraction. Materials chemistry and physics, 1999. 61(2): p. 117-123.

203. Lu, Z., et al., Damage profile of ion-implanted GaAs by x-ray photoelectron spectroscopy. Applied Physics Letters, 1989. 55(9): p. 846-848.

204. Lockwood, D., Raman Spectroscopy of Oxides of GaAs Formed in Solution. Journal of Solution Chemistry, 2000. 29(10): p. 1039-1046.

205. Allwood, D., et al., Monitoring epiready semiconductor wafers. Thin Solid Films, 2002. 412(1): p. 76-83.

206. Herms, M., K. Roth, and G. Irmer, Composition of arsenic and phosphorus vapour in different annealing geometries determined by Raman spectroscopy. Journal of crystal growth, 1998. 186(1): p. 166-174.

207. Brumbach, S.B. and G.M. Rosenblatt, In—Cavity Laser Raman Spectroscopy of Vapors at Elevated Temperatures. As_4 and As_4O_6. The Journal of Chemical Physics, 2003. 56(6): p. 3110-3117.

208. Ozin, G., Gas-phase Raman spectroscopy of phosphorus, arsenic, and saturated sulphur vapours. Journal of the Chemical Society D: Chemical Communications, 1969(22): p. 1325-1327.

209. Yang, J., et al., Traces of HgCdTe defects as revealed by etch pits. Journal of Electronic Materials, 2008. 37(9): p. 1241-1246.

210. Farrell, S., et al., Comparison of the Schaake and Benson Etches to Delineate Dislocations in HgCdTe Layers. Journal of electronic materials, 2013. 42(11): p. 3097-3102.

211. Ivanits'ka, V., et al., Chemical etching of CdTe in aqueous solutions of H2O2-HI-citric acid. Journal of Electronic Materials, 2007. 36(8): p. 1021-1024.

212. Everson, W., et al., Etch pit characterization of CdTe and CdZnTe substrates for use in mercury cadmium telluride epitaxy. Journal of electronic materials, 1995. 24(5): p. 505-510.

213. Bhattacharya, P., S. Mahajan, and H. Kamimura, Comprehensive Semiconductor Science and Technology: Online version. Vol. 1. 2011: Newnes.

214. Capper, P., Properties of narrow gap cadmium based compounds. 1994: Iet.

215. Lu, Y.C., et al., Etch pit studies in CdTe crystals. Journal of Vacuum Science & Technology A, 1985. 3(1): p. 264-270.

216. Farrell, S., et al., Effect of Cycle Annealing Parameters on Dislocation Density Reduction for HgCdTe on Si. Journal of electronic materials, 2011. 40(8): p. 1727-1732.

217. Chen, J.-S., Etchant for revealing dislocations in II-VI compounds. 1990, Google Patents.

218. Hähnert, I. and M. Schenk, New defect etchants for CdTe and $Hg_{1-x}Cd_xTe$. Journal of crystal growth, 1990. 101(1): p. 251-255.